NMR STUDIES OF CHEMICAL EXCHANGE IN SOLUTION AND SOLIDS

NUCLEAR MAGNETIC RESONANCE STUDIES OF CHEMICAL EXCHANGE IN SOLUTION AND SIMULATION OF CHEMICAL EXCHANGE IN ROTATING SOLIDS

By

PAUL HAZENDONK

B.Sc., M.Sc.

A Thesis

Submitted to the School of Graduate Studies

in Partial Fulfilment of the Requirements

for the Degree

Doctor of Philosophy

McMaster University

© Copyright by Paul Hazendonk, 2000

DOCTOR OF PHILOSOPHY(2000)
(Chemistry)

McMASTER UNIVERSITY
Hamilton, Ontario

TITLE: Nuclear Magnetic Resonance Studies of Chemical Exchange in Solution and Simulation of Chemical Exchange in Rotating Solids

AUTHOR: Paul Hazendonk, B.Sc. (University of Winnipeg)
M.Sc. (University of Manitoba)

SUPERVISOR: Professor A. D. Bain

NUMBER OF PAGES: xvii, 275

Abstract

The primary objective of the following work is to advance the study of dynamic processes in molecules by Nuclear Magnetic Resonance. Rate measurements by NMR give rise to activation parameters of unprecedented accuracy. We have had much success with small molecules in solution phase and would like to extend these methods to larger molecules and to the solid phase.

Two studies into small molecules found: substantial entropies of activation for furfural in a series of solvents and that measured substituent effects on amide barriers could not be explained simply by Atoms in Molecules methodologies. Exchange rates measurements were made on two large sample systems: DADS which has five observable conformations, and TRH is proline-containing tripeptide with two conformations. Complete lineshape analysis and selective inversion experiments provided for reliable activation parameters.

Currently lineshape simulation methods for exchanging multispin systems undergoing magic-angle spinning using full theory are not available. Using the time-independent Floquet approach it was possible to do such simulations. Since this method involves large matrices an efficient numerical method was developed. A sparse implementation of a stable formulation of the dual Lanczos algorithm made these simulations possible on a realistic time scale. The CPMAS spectra of doubly-^{13}C-labelled dimethylsulfone were successfully simulated for a series of temperatures and rotor speeds.

Acknowledgements

I would like to express my deepest gratitude to my supervisor Dr. A. D. Bain, for his guidance and support over the duration of my studies. I also want to recognise Dr. R. S. Dumont for his continued encouragement and help. I would like to thank the Chemistry Department for giving me the opportunity to study at McMaster, and their financial support. I am also grateful to NSERC for financial support over the first two years.

For helpful instruction and guidance in the NMR laboratory I am thankful to Dr. D. Hughes, B. Sayer, and Dr. H. Grondey (Toronto).

To my fellow students I am grateful for providing a healthy environment conducive to study and research, *etc.* In particular I would like to thank Fernando Martin, Bernhard Pointner, and Michael Gerken for their continued companionship and stimulating dialogue.

Last but not least, I would like to thank my family and Clare for their support and patience throughout the years of my studies.

Table of Contents

Part III
Simulation of Coupled Spin Systems in Rotating Solids Undergoing Chemical Exchange by Application of Sparse Matrix Methods to Floquet Theory.

List of Figures

List of Tables

Chapter 1

Objectives and Overview

Objectives

The primary goal of this thesis is to develop and improve methods for measuring chemical exchange rates. Much attention has been devoted to solution phase Nuclear Magnetic Resonance (NMR) spectroscopy, where the temperature range over which rates are measured can be greatly extended, giving rise to activation parameters of unprecedented accuracy. The implications of this advance have not yet been fully investigated and are the primary focus of the first two projects. Accurate rate measurements are mainly achieved with one-dimensional (1D) techniques, which are not well suited to studies of large complicated spins systems. Thus additional studies consider the feasibility of two-dimensional (2D) techniques to aid the application of 1D methods to large systems. These systems have either many spins, or exchange between many sites, resulting in complicated spectra. 2D NMR methods are used to assign the spectrum, making complete lineshape analysis possible. The last area of interest is extending techniques commonly used in the solution phase, in particular lineshape analysis, to the solid phase. Simulation of exchanging multispin systems undergoing magic angle spinning, (MAS), is a challenge computationally. The final two projects entail the development of new numerical techniques permitting sufficiently rapid

simulation of MAS spectra to fit all the parameters of an exchanging spin system in the solid state.

Some background on NMR

NMR spectroscopy provides a vast array of techniques indispensable to chemistry. It is most commonly used to determine molecular structure in the solution phase. With development of 2D techniques it has become possible to determine structures of very large systems. As a result the NMR spectrometer is a routine tool of organic and biological chemistry, alongside mass spectrometry and x-ray crystallography. NMR is sensitive to dynamic processes, and as such has been exploited to measure the associated rates. Dynamic NMR measurements have determined a wealth of kinetic data, providing valuable insights into the energetics of dynamic processes in the 10 to 80 kJ/mol range.

The basic NMR experiment requires that a sample be placed in a strong magnetic field. Nuclei that posses a magnetic moment, will either align (tilted slightly) with or against the field, giving rise to a net induced magnetisation, in the magnetic field direction. The tilted nuclear magnetic moments precess at the Larmor frequency, about the applied field direction. They are not in phase with one another, leaving no net magnetisation perpendicular to the field direction. When the nuclei are subjected to a resonant radio frequency pulse, this bulk magnetisation is tipped into the plane perpendicular to the magnetic field direction. The bulk magnetisation then rotates in this plane at the Larmor frequency. The magnetisation slowly relaxes back to alignment

along the field. The z-component of the magnetisation relaxes by a process called spin-lattice relaxation, at a rate of $1/T_1$. If a coil is placed in the plane, the transverse component of the oscillating magnetisation of the sample induces current in the coil, which is the NMR signal. This transverse component dephases, causing the signal to decay at a rate of $1/T_2$.

The NMR signal is a decaying sinusoidal function, which can be expressed in the frequency domain via Fourier transformation. The corresponding spectrum is composed of signals at characteristic frequencies (chemical shifts), which may be split into complex patterns due to indirect spin-spin coupling. These spectral parameters are dependent on molecular structure which is the key to the use of NMR for structure determination.

One-dimensional techniques are most routinely used. Often it suffices to obtain a ^{1}H and ^{13}C spectrum to determine the structure of a small organic molecule. A simple chemical modification can readily be observed in the NMR spectrum as a change in the spectrum. These techniques are very useful to synthetic chemistry, since fast verification of structural modifications can be obtained in a non-destructive manner. In addition, today's instruments are relatively easy to use, even by a non-specialist.

2D NMR

The larger the molecule, the more complicated and crowded the spectrum becomes. At some stage it is necessary to simplify the spectrum by expanding the spectrum into a second frequency dimension. In 2D NMR there are two frequency axes of the same or two different types of nuclei. Peaks in the spectrum represent correlations, which are due to interactions between two spins. Correlation Spectroscopy (COSY), employs correlations based on the homonuclear indirect spin-spin-coupling interaction, and is used in assigning spin systems. When two nuclei are physically close, they are strongly dipolar coupled, which results in cross relaxation, wherein magnetisation is exchanged between them. A 2D experiment exploiting this interaction is called Nuclear Overhauser Effect Spectroscopy (NOESY). It provides an invaluable tool for determining three-dimensional structure.

Two-dimensional NMR techniques have made it possible to determine structure of very large chemical systems. For instance it is now routinely used to determine secondary, tertiary and quaternary structural features of proteins. In the N-H region of the NOESY spectrum of a protein α–helical and β-sheet character give characteristic correlations. A NOESY cross -peak between residues far away in sequence number can indicate folds in the protein, which place the two residues in close proximity. Using the COSY and NOESY methods, the assignment of substructures of a large natural product can also be made. The chemical shift and coupling constants can be used to determine geometric features such as ring pucker and stereochemistry. These subspectra can be

pieced together using an experiment based on long-range heteronuclear correlations, such as Heteronuclear Multiple Bond Correlation spectroscopy (HMBC), to obtain the complete structure.

Solid State NMR

The resonance frequency of a nucleus depends on its local electronic environment and also on the orientation and strength of the applied magnetic field. In other words the chemical shift of a nucleus is a tensorial property (a 3×3 matrix). In liquids, random molecular tumbling leaves only an averaged effect and thus a single resonance frequency. In the solid state with powder materials, the orientational dependence manifests itself by giving rise to spectra comprised of broad signals. Often other interactions, such as direct dipole-dipole coupling, which is averaged away in liquids, can be seen for solids. The dipolar-coupling interaction depends on the orientation and length of the internuclear vector between the nuclei involved, and is responsible for further broadening the signal. In favourable situations these tensorial parameters can be measured to give valuable information about the structure of the system. Although the technique does not lend itself to large systems, it does provide much more insight into the electronic structure about a nucleus than with solution phase NMR.

It is possible to significantly reduce the broadening of the spectrum and consequently improve the signal to noise ratio by rapidly rotating the sample about an axis at the magic angle with respect to the applied magnetic field. Sample rotation removes leading terms in the orientation dependence of the signal, which can reduce the

spectrum to a single sharp line. The result is generally a series of rotational side bands, which are much sharper than the original "powder pattern". One- and two-dimensional techniques have been developed with magic angle spinning (MAS), which are analogous to solution phase experiments.

Solid state NMR is particularly useful in the analysis of amorphous solids for which X-ray methods are not applicable. It is used in the analysis of organometallic, organic, biological and polymer molecules. Recent advances include Rotational-Echo Double-Resonance-based (REDOR) experiments, which measure selected dipole-dipole couplings and thus provide inter-nuclear distance information under high-resolution conditions. This experiment is now seeing wide application in studies of selectively labelled proteins and polymers.

Dynamic NMR

When a molecule undergoes some sort of rearrangement in which the local environment of the nuclei are changed, thereby changing spectral parameters, the process is NMR-observable and the rate can be measured accurately. In NMR terminology, such a process is known as chemical exchange. Isomerisation processes, such a nitrogen inversion, hindered rotation about a partial double bond, ring inversion, silane migrations, carbonyl rearrangements in metal complexes, take place in an energy regime which can be investigated using Dynamic NMR techniques.

Take the dimethylformamide molecule as an example. There are two distinct chemical environments for the methyl hydrogens. They are either *cis* or *trans* to the

carbonyl oxygen, each with a distinct chemical shift. The nitrogen-carbon bond of dimethylformamide has partial double-bond character, with a barrier to rotation of approximately 75 kJ/mol. This means that at room temperature, the rotation occurs at a rate of roughly 0.3 s^{-1}.

As the temperature is increased the lines start to broaden. When the rate is much larger than the difference in the two resonance frequencies, the lines coalesce into one. Upon further increase in temperature (and hence rate), the one line becomes narrow. The single resonance frequency, observed in the limit of fast exchange, is the average of the two original frequencies.

Methods for measuring chemical exchange rates depend on the exchange regime. For slow exchange, when $k << \Delta\nu$, rates are measured using T_1 based experiments. Lineshape analysis applies to intermediate exchange, where k is of the same order of magnitude as $\Delta\nu$. Accurate T_2 measurements are used in the fast-exchange regime after coalescence, where $k >> \Delta\nu$.

Slow exchange corresponds to exchange rates comparable to, or smaller than, the relaxation rate, $1/T_1$. In this case, the rates are measured by selective inversion or exchange spectroscopy (EXSY). The former is a modification of an experiment used to measure T_1's. One resonance is selectively perturbed and the relaxation behaviour of the entire system is observed. Numerical modelling of the relaxation behaviour with independently measured relaxation rates gives the exchange rates. The latter experiment is a 2D version of the selective inversion experiment, implemented identically to NOESY, when cross-peaks appear due to a chemical exchange process. The ratio of the

cross-peak to the diagonal peak is related to the exchange rate. For accurate rates it is often preferable to use selective inversion experiments if possible. However, mechanistic information is more readily available using EXSY.

Past the slow-exchange limit the lineshape is very sensitive to the exchange rate. Spectra are simulated for many rate values, and matched to experimental spectra, obtained at different temperatures.

In the fast-exchange regime, past coalescence, the spectra become insensitive to increases in exchange rate. However, the exchange contribution to $1/T_2$ (the dephasing rate) remains the largest, well into this regime. An accurate measurement of both T_2 and T_1, gives accurate rates past coalescence. The trick is to obtain an accurate T_2 value, independent of other linebroadening factors. One experiment where this is possible is the offset-saturation experiment. The spectral line of interest is subjected to irradiation at different frequencies from resonance. The line intensity as a function of frequency has a dip like form, whose width at half height is directly related to the ratio T_1/T_2. Therefore by measuring T_1 independently one can get an accurate value for T_2, which in turn gives the exchange rate.

Barriers are determined from a series of rate measurements over a range of temperatures, using the Eyring equation. With the Eyring equation approach, ln(r/T) is plotted as a function of 1/T to give a slope of $-\Delta H^{\dagger}/R$ and an intercept of $\ln(k_b/h) + \Delta S^{\dagger}/R$, where $\Delta H^{\dagger}$ and $\Delta S^{\dagger}$ are the enthalpy and entropy of activation; r is the rate, R is the ideal gas constant, h is the Planck constant, and k_b is the Boltzmann constant. Activation entropies are obtained by extrapolating to $1/T = 0$. However there can be

large extrapolation errors due to small errors in slope. To minimise extrapolation error, it is essential to have data over as large a temperature range as possible. Combining the three rate measurement techniques described provides a sufficiently large temperature range to obtain activation entropies of unprecedented accuracy.

Part 1 ***Accurate Activation Parameters for Dynamic Processes Studied by NMR Using a Three-Experiment Approach.***

Using a combination of three experiments to measure exchange rate in the slow-, intermediate- and fast-exchange regimes, it is possible to collect rate data over a large temperature range, giving very accurate activation parameters. The enthalpies of activation are usually determined to within 1 kJ/mol and the error in activation entropies lie within 5 J/mol K. As a result realistic comparisons with calculated values of enthalpies are now possible. Measured activation entropies can now be used to extract useful characteristics of exchange process transition states.

The new technology permits investigation of questions previously beyond reach. For example, solution phase studies often assume that the activation entropies of unimolecular processes are insignificant and their effects can be ignored. Under what conditions is this assumption valid? Even if the activation entropy of the molecule is zero, can the same be assumed for the solvent? The first study (chapter 3) attempts to answer some of these questions by investigating the solvent effect on the internal rotational barrier of furfural, in aprotic and hydrogen bonding solvents. The barriers are computed using molecular orbital calculations including the contribution of the reaction

field from the solvent. These computed barriers are compared with those determined experimentally. The activation entropies are interpreted in terms of solvent-solute interactions.

Recent theoretical studies have suggested that the barrier in amides should be considered as a special case of amine inversion without appealing to loss of resonance stabilisation between the nitrogen and oxygen. Past determinations of substituent effects on barriers of this type are based on rate measurements over small temperature ranges and thus were reported as free energies. Ideally comparisons with computations should be made with activation enthalpies, with the contribution of activation entropy removed. The second study (chapter 4) describes accurate determinations of the substituent effect on the amide activation enthalpy of the amide process in series of spirofused-oxadiazolines. Molecular orbital calculations are performed for three of the derivatives. The Atoms in Molecules (AIM) protocol is used to probe the atomic contributions to the barrier and to describe the effects of different substituents on the carbonyl carbon. Atomic properties such as populations and energies of the amide C, O and N were computed. The behaviour seen in formamide was recovered theoretically, but there was no simple explanation of the substituent effect.

Part II *Application of 1D NMR Methods to the Measurement of Exchange Rates of Large Spin Systems.*

Accurate rate measurements on large spin systems pose a significant experimental challenge. One-dimensional DNMR methods give the most accurate results. However, spectral overlap and the need for a complete assignment of the spin systems, impede their application. The 2D method for measuring exchange, EXSY, overcomes these difficulties but is less accurate and more time consuming. For large coupled spins systems with multiple sites, exchange cross-peaks are hard to integrate. In addition, often the signal to noise ratio is poor due to the short mixing times required, to avoid second-order peaks.

Two-dimensional techniques, such as COSY, NOESY, and HMBC, are very useful in assigning the spin system. In addition, selective 1D techniques can be used to get subspectra of isolated spin systems, making it possible to obtain their spectral parameters separately. This raises the question that if complete assignments of complicated exchanging spin systems is feasible, using 2D techniques, to what extent can 1D methods then be used to measure rates accurately? Is it possible to obtain measurements over a large range in temperature?

The main objective is to obtain accurate activation parameters of large spin systems undergoing exchange between multiple sites. Each study looks into a different aspect of this problem. The first study (chapter 5) looks into N,N'-[Dimethyl-(2,2'-dithiobisacetyl)]ethylenediamine (DADS), a ten-membered ring existing in five observable conformations. The ring contains one disulfide and two amide fragments. There are four active processes observed where the barriers are to be determined for each.

The second study (chapter 6) concerns the dynamics of a tripeptide, Thyrotropin-releasing hormone (TRH), containing a proline ring with two possible conformations. In this case the exchange mechanism is trivial. However, the complete assignment of the spectrum and measurement of the spectral parameters pose a significant challenge. In this case, the pH catalysis of the barrier is investigated and the validity of histidine participation in the catalysis is evaluated.

In both studies total assignments of all the conformations and measurement of all their spectral parameters is achieved using a combination of COSY, NOSY and HMBC spectra. Selective TOCSY spectra were used to obtain subspectra of the amino acid residues of TRH in both conformations. These were simulated to obtain the spectral parameters. To establish the exchange mechanism of DADS, EXSY methods were employed. Total lineshape analysis was possible for DADS. For TRH, lineshape analysis was performed using only the histidine signals. In both cases there were well resolved, unobscured signals allowing selective inversion rate measurements. For both DADS and TRH, rate measurements were possible over large ranges in temperature (*c.a.* 60 to 100 °C) in order to get accurate activation parameters.

Part III *Simulation of Coupled Spin Systems in Rotating Solids Undergoing Chemical Exchange by the Application of Sparse Matrix Methods to Floquet Theory*

Considerable attention has been given to chemical exchange in the solid state. However, extracting rate parameters from the spectra is very involved, especially under magic angle spinning conditions. Often only one interaction is considered in the Hamiltonian, such as the chemical shielding anisotropy, dipolar, or quadrupolar coupling. Combined terms require special circumstances in order to solve the problem easily.

The main complication is that the Hamiltonian, under magic angle spinning, becomes time-dependent. This necessitates quite a different theoretical approach than that used to treat static Hamiltonians. The problem is only simple when the terms in the Hamiltonian commute with each other for all time. Otherwise, traditional methods require that the Hamiltonian be treated as time-independent over small time steps. Short time propagators are computed, using an average Hamiltonian for each time step, then applied in succession to a spin state. Another approach converts the time-dependent Hamiltonian to a time-independent form. This is achieved by expanding the Hamiltonian as a Fourier series, which gives rise to an effectively time-independent Hamiltonian acting on a combined Fourier-spin space called Floquet space. The Floquet Hamiltonian is much larger than the original Hamiltonian. The main difference is that one has to perform only one diagonalisation of a large matrix as opposed to many of a much smaller matrix.

Using standard numerical techniques the Floquet method is not more efficient than the time step method, since diagonalisation requires $O(N^3)$ operations (N is the order

of the matrix). If a numerical method were available which scales more favourably than $O(N^3)$ then the approach would be much more desirable. Sparse matrix methods such as Lanczos tridiagonalisation make this possible. This method scales at least as $O(N^2)$ and in favourable situations it approaches O(N).

The Lanczos method exploits the inherent sparsity of the Liouvillian. Sparsity means that most of the matrix elements are zero. In NMR, the number of nonzero elements scales only as the order of the matrix, with increasing spin system size or number of sites. The Lanczos algorithm converts the Liouvillian to a tridiagonal form, in N_L iterations, where N_L is near the order of the matrix or significantly smaller. The algorithm consists of iterated sparse-matrix vector multiplications, each scaling as O(N). The conversion to the Lanczos representation thus entails $O(N \times N_L)$ operations. In addition, the spectrum can be computed directly in the time domain in the tridiagonal form using standard numerical methods, which scale as O(N) for each frequency. The spectrum evaluation thus requires $O(N \times N_v)$ operations where N_v is the number of frequencies. The entire calculation requires $O(N \times N_L) + O(N \times N_v)$ operations, which in most circumstances is near $O(N^2)$.

The objective of the last two studies is to develop the Lanczos method, initially applying it to the simulation of solution phase spectra (chapter 7), then to the simulation of MAS spectra of exchanging multispin systems (chapter 8). The scaling properties are investigated in detail in the solution phase study, and are compared with standard numerical methods. Next the Lanczos method is implemented with Floquet theory to simulate MAS spectra of exchanging multispin systems. Doubly ^{13}C-labeled

dimethylsulfone is used as a test case, where both the CSA and dipolar terms are included in the simulation.

Chapter 2

Theory of NMR

A brief history of dynamic NMR

Nuclear magnetic resonance was discovered in 1946 by Bloch *et al.*[1-3] and Purcell *et al.*[4] independently. Not long afterwards most of the familiar features of chemical NMR spectroscopy such as chemical shielding[5-7] and indirect coupling[8-10] were discovered. During this time Gutowsky realised the importance of chemical exchange effects on NMR spectra when studying the ^{1}H, ^{19}F, and ^{31}P spectra of inorganic phosphorus and boron compounds[11] and ^{1}H spectra of aqueous solutions of acids.[12] In the former they ascribed the lack of indirect spin-spin coupling interactions to a chemical exchange. In the latter study, the proton signal was a single line, and not separated into many lines each corresponding to a species in solution. He attributed this to a fast exchange process where the proton line is at a frequency that is a weighted average of the signals of the proton in different species in the absence of exchange.

Chemical exchange falls into three rate regimes, slow, intermediate, and fast, in which different experimental methods were developed for optimum rate measurements. In the slow-exchange regime the rate is of the same order of magnitude as the spin-lattice relaxation rate, $1/T_1$. Consequently magnetisation transfer experiments are used in this

regime. In the intermediate-exchange regime, the rate is of the same order of magnitude as the frequency difference of the exchanging lines. As a result the spectrum becomes very sensitive to the rate, and thus rate measurements are made by lineshape simulations. As the rate increases the lines become too narrow for lineshape methods. In this fast-exchange regime exchange rates are determined from the spin-spin relaxation rate, $1/T_2$.

The NMR lineshape was initially calculated using a modification of the Bloch equations including chemical exchange.[13-15] This treatment was extended for two-site unequally-populated exchange. From this treatment, expressions were developed to obtain the rate from the linewidth in the slow- and fast-exchange limit, and from the coalescence temperature.[16,17] Later Sack extended this approach to multiple sites.[18] This classical approach however is not generally applicable to coupled systems which require a quantum mechanical treatment.

Using density matrix theory,[19] Kaplan[20] and Alexander[21,22] described exchange of coupled spin systems under steady state conditions. The density matrix description of chemical exchange has been the subject of numerous reviews by Lynden-Bell,[23] Buckley,[24] Johnson,[25] and others.[26,27] A complete density matrix formulation of coupled chemical exchange, based on the Liouville representation of quantum mechanics, was developed by Binsch *et al.*, which is the underlying theoretical approach of much of the simulation software to date.[28,29]

Reeves and Shaw showed that the NMR of a two uncoupled exchanging spins can be decomposed into two Lorentzian lines.[30] Thinking along these lines, and using the "direct method" of calculating the NMR transition,[31] Bain and Duns generalised the

concept of the NMR transition. It can always be thought of as a Lorentzian line, even for strongly coupled system undergoing exchange, each with a phase, width, frequency and intensity.[32-34] They were able to convey a clear and intuitive picture of the concept of the NMR transition.

Slow exchange rate measurements can be made by perturbing the spin system and observing its relaxation back to equilibrium. In 1964, in days of Continuous Wave (CW) NMR, Forsen and Hoffman[35] were the first to perform magnetisation transfer experiments. For a two-site exchange, one line was saturated with a strong rf-field, and the other line was observed with a weak rf-field. Using McConnell's formulation of the modified Bloch equations[14] saturation transfer to the observed line was modelled under different experimental situations. This method was extended to multiple non-equivalent sites.[36] Upon the advent of Fourier Transform NMR, in 1975, Dahlquist *et al.* used the concept of magnetisation transfer in the selective inversion experiment,[37] where the magnetisation of one site was inverted by 180° and both magnetisations were observed after a delay period. This approach proved to give more reliable exchange rates.

To analyse selective inversion data properly, the relaxation behaviour of the spin system has to be modelled numerically. In the past, analytical forms were derived, by making various simplifying assumptions, in order to make data analysis tractable. When computer resources became more widely available, Led and Gesmar, in 1986, numerically modelled the data of a multiple site selective inversion experiment.[38] McClung *et al.* formulated the selective inversion between multiple sites such that different mechanistic pathways can be tested.[39] His methods were adapted by Bain and

Cramer,[40-42] where the relaxation of any non-equilibrium state can be modelled, for various mechanistic pathways.

In the fast exchange-regime, when the line is too narrow to allow for reliable rate measurements by lineshape analysis, one needs an accurate way to measure T_2. Spin-echo experiments make this possible. Hahn discovered the spin-echo in 1953,[15,43] after applying two consecutive 90° pulses. Later in 1954, Carr and Purcell[44] suggested the use of a 180° pulse for the second pulse at short delay times. Further modifications were proposed by Meiboom and Gill,[45] where the 180^0 pulse is 90^0 out of phase with the initial 90^0 pulse. This reduces error due to pulse phase error and B_1 inhomogeneity. Woessner was the first to suggest the use of spin-echo methods to study chemical exchange. He used the Bloch-McConnell approach to predict the first echo amplitude in all three exchange regimes for a two-site uncoupled exchange.[46] Later Allerhand and Gutowsky,[47] as well as Bloom[48] derived analytical expressions for consecutive echo amplitudes in a CPMG pulse train, for the two-spin two-site equally-populated exchange. Allerhand and Gutowsky numerically simulated consecutive echo amplitudes of coupled spin systems undergoing chemical exchange using density matrix methods.[49,50] The main problem with spin-echo measurements is their lack of selectivity. For large spin systems, these methods become impracticable. An alternative, selective method was suggested by Bain and Duns, known as a steady-state offset saturation experiment. This experiment allows for simultaneous measurement of both T_1 and T_2,[51] and is also insensitive to coherent dephasing mechanisms.

Two-dimensional NMR techniques for measuring exchange rates are based on the concept of magnetisation transfer. In fact Exchange Spectroscopy, EXSY, can be thought of as the 2D adaptation of the selective inversion. The basic pulse sequence is 90^0-t_1-90^0-t_m- 90^0-t_2 initially proposed by Jeener *et al.*[52,53] The first pulse creates x-y magnetisation, which evolves for a period t_1. The second pulse aligns this transverse magnetisation along the z-axis. Magnetisation transfer occurs via cross-relaxation and exchange mechanisms during the mixing time. The last pulse returns the magnetisation back to the transverse plane where it is then observed. Exchange is seen as a cross-peak at the frequencies of the two sites involved. The main utility of this experiment is the acquisition of qualitative information such as the exchange mechanism. Accurate rate measurements are cumbersome, especially for coupled systems. The signal of the cross- and diagonal-peaks are very difficult to integrate due to poor signal to noise and their complex shapes. Accurate rate measurements via EXSY are also very time consuming since spectra are required for several mixing times. Numerical methods have been developed to analyse the intensity data of EXSY spectra, even for complex exchange mechanisms.[54,55] In practice it requires too much effort and time to get rate data comparable to selective inversion, consequently it should be considered as a last resort.

This survey of the history of DNMR served to introduce some of the basic concepts and issues in the development of the experimental methods. The following treatment is meant to introduce the basic concepts of NMR, starting with the classical theory, and continues with a quantum mechanical treatment. A time-dependent quantum mechanical description follows, introducing the density matrix. The theory of chemical

exchange is developed using the superspin formulation of Liouville space. The chapter ends with a section introducing solid state NMR, and magic-angle spinning (MAS).

The theory of NMR

An atomic nucleus is a charged structure, which has an intrinsic angular momentum,[56] **L**, that is quantised according to its angular momentum quantum number I.

$$\mathbf{L} = \hbar\sqrt{I(I+I)} \tag{2.1}$$

I takes on integral or half integral values ranging between 0 and 6 depending on the structure of the nucleus. Associated with the angular momentum is a magnetic moment $\mu = \gamma\mathbf{P}$ where γ is the magnetogyric ratio. Thus

$$\mu = \gamma\hbar\sqrt{I(I+I)} \tag{2.2}$$

When subjected to a magnetic field, $\mathbf{B_0}$, the magnetic moment can take on a discrete number of orientations with respect to the field. For example, a spin-1/2 nucleus in a magnetic field can either align itself with or against the field at a given angle. Figure 2.1 illustrates the general case. Thus, if the field orientation is taken to be the z direction the magnetic moment of a spin-1/2 nucleus has z components, $\mu_z = \gamma\hbar/2$ or $-\gamma\hbar/2$. In general, μ can have any one of 2I +1 orientations, with $\mu_z = m_I\gamma\hbar$, where m_I= -I, (-I +1),...,I is known as the magnetic quantum number.

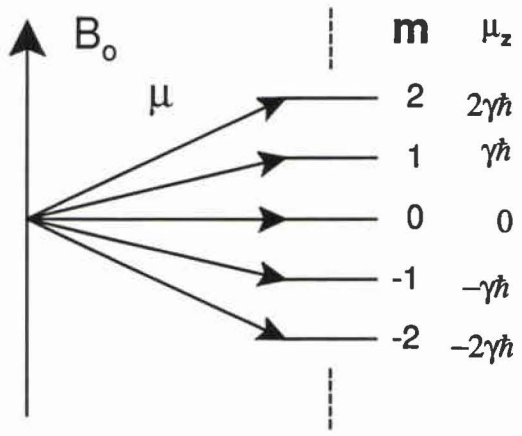

Figure 2.1 Orientation of the magnetic moment, μ, with respect to the applied magnetic field $\mathbf{B}_0$.

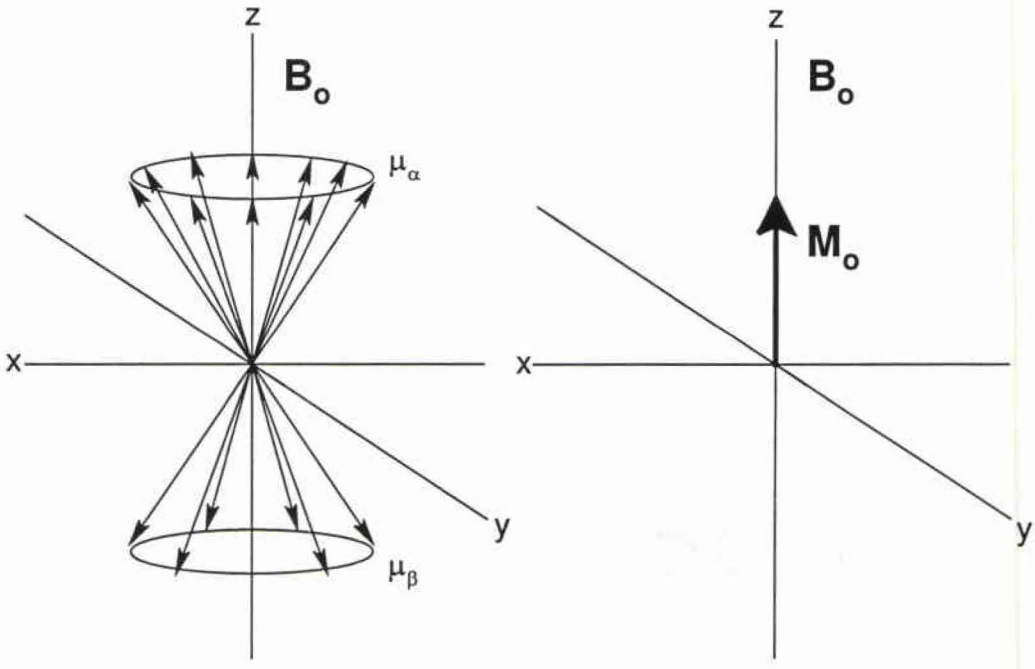

Figure 2.2 The bulk magnetic moment is the result of the vector sum of individual nuclear magnetic moment randomly distributed about a cone oriented either with or against the field.

The energy of a magnetic moment in a magnetic field, along the z-axis, is

$$E = \mu \cdot \mathbf{B} = -\mu_z B_o = -m\gamma\hbar B_o, \tag{2.3}$$

which gives rise to 2I +1 energy levels equally spaced by $\gamma\hbar B_0$. The corresponding transition frequency ($\Delta m_I = \pm 1$) $\nu_L = -\gamma B_o/2\pi$ is known as the Larmor frequency, which in the classical view is the frequency at which the magnetic moment precesses around the axis defined by $\mathbf{B}_o$.

A large collection of nuclei will have an induced macroscopic magnetic moment, M_o, that is aligned with the field and has no net x or y component. The Boltzmann distribution, as in eqn. (2.4), requires that the equilibrium population in the lower energy level, α, be slightly larger than in the higher level, β. The change in energy is small compared to the thermal energy, consequently the high temperature approximation can be invoked as shown in the right hand side of eqn. (2.4). At equilibrium, there is no net x or y component since the nuclei are precessing incoherently and thus are randomly distributed along the surface of a double cone as in figure 2.2.

$$\frac{N_\beta}{N_\alpha} = \exp\left[-\frac{\Delta E}{k_b T}\right] = \exp\left[\frac{-\gamma\hbar B_o}{k_b T}\right] \doteq 1 - \frac{\gamma\hbar B_o}{k_b T} \tag{2.4}$$

Relaxation

The process by which the populations of the two energy levels reach equilibrium is called spin-lattice relaxation, since the energy is dissipated into the local environment (*i.e.* the lattice). The energy of the system is dependent only on the sum of all the z-component of the magnetic moments. Consequently the rate at which the system returns to thermal equilibrium depends only on the z-component of the magnetisation. It is assumed to be characterised by the time constant T_1 as in eqn (2.5).[1-3]

$$\frac{dM_z}{dt} = -\frac{M_z - M_o}{T_1} \tag{2.5}$$

Relaxation of the x and y components is really a dephasing process. The rate at which this phase coherence between spins is lost is known as the spin-spin relaxation. This dephasing rate is characterised by the time constant,T_2, as in eqn (2.6).

$$\frac{dM_{x,y}}{dt} = -\frac{M_{x,y}}{T_2} \tag{2.6}$$

The Bloch equations

The response of the magnetisation vector to an applied magnetic field B(t) is governed by eqn. (2.7).

$$\frac{d(M_x, M_y, M_z)}{dt} = \gamma(M_x, M_y, M_z) \times (B_x(t), B_y(t), B_z) + \left(\frac{M_x}{T_2}, \frac{M_y}{T_2}, \frac{M_z - M_o}{T_1}\right) \quad (2.7)$$

$B_x(t) = B_1 \cos\omega t$, $B_y(t) = B_1 \sin\omega t$, $B_z = B_o$, and T_1 and T_2 are the spin-lattice and spin-spin relaxation time constants. This is a set of coupled first-order differential equations as shown in eqn. (2.8).[1-3]

$$\begin{aligned}
\frac{dM_x}{dt} &= \gamma(M_y B_o + M_z B_1 \sin\omega t) - \frac{M_x}{T_2} \\
\frac{dM_y}{dt} &= \gamma(M_z B_1 \cos\omega t - M_x B_o) - \frac{M_y}{T_2} \\
\frac{dM_z}{dt} &= \gamma(M_x B_1 \sin\omega t - M_y B_1 \cos\omega t) - \frac{M_z - M_o}{T_1}
\end{aligned} \quad (2.8)$$

At this stage a transformation is made to a system that rotates about the z-axis at angular velocity ω. This rotating frame contains two orthogonal components of the magnetisation, $u = M_x \cos\omega t - M_y \sin\omega t$ and $v = -M_x \sin\omega t - M_y \cos\omega t$, which are in the plane perpendicular to B_0, where u is along the B_1 direction. The equations can now be rewritten as

$$\begin{aligned}
\frac{du}{dt} + \frac{u}{T_2} + (\omega_o - \omega)v &= 0 \\
\frac{dv}{dt} + \frac{v}{T_2} + (\omega_o - \omega)u + \gamma B_1 M_z &= 0 \\
\frac{dM_z}{dt} + \frac{M_z - M_o}{T_1} - \gamma B_1 v &= 0
\end{aligned} \quad (2.9)$$

where $\omega_o=\gamma B_o$. By assuming that the system is in a steady state, meaning that the time derivative of the magnetisation components are zero, the system of equations can be solved for u, v and M_z.(eqn (2.10)).

$$u = M_o \frac{\gamma B_1 T_2^2(\omega_o - \omega)}{1 + T_2^2(\omega_o - \omega)^2 + \gamma^2 B_1^2 T_1 T_2}$$

$$v = -M_o \frac{\gamma B_1 T_2}{1 + T_2^2(\omega_o - \omega)^2 + \gamma^2 B_1^2 T_1 T_2}$$

$$M_z = M_o \frac{1 + T_2^2(\omega_o - \omega)^2}{1 + T_2^2(\omega_o - \omega)^2 + \gamma^2 B_1^2 T_1 T_2} \qquad (2.10)$$

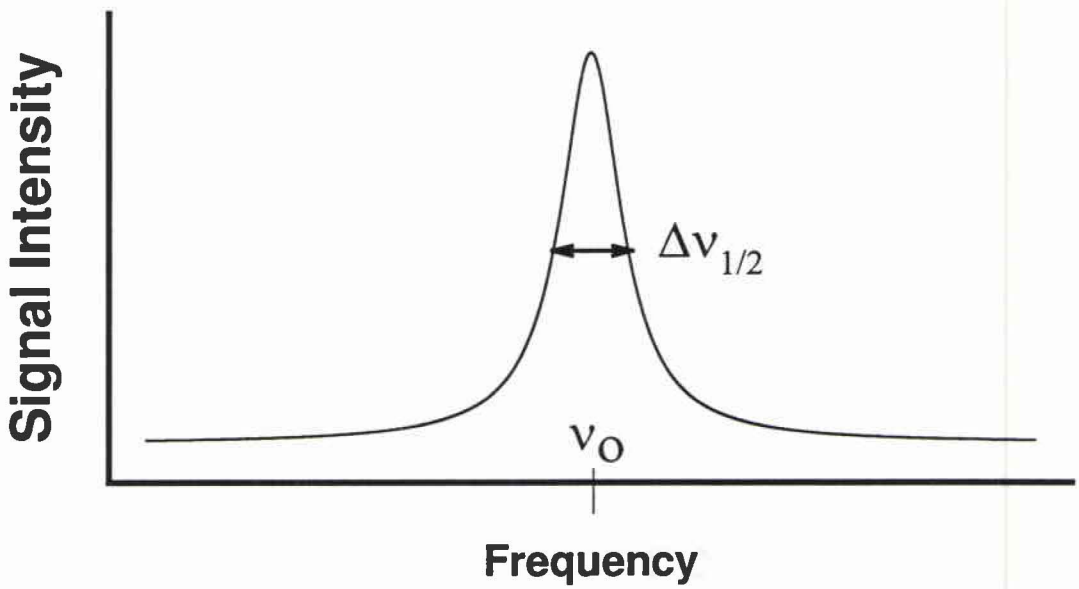

Figure 2.3 The Lorentzian lineshape is centred at the resonance frequency ν_o, and has width $\Delta\nu_{1/2} = 1/\pi T_2$. It is also called the absorption lineshape.

Under non-saturating conditions, for which $\gamma B_1 << (T_1 T_2)^{-1}$, the expression for v becomes

$$v \propto -M_o \gamma B_1 \frac{T_2}{1 + 4\pi^2 T_2^2 (\nu_o - \nu)^2}, \tag{2.11}$$

where $\nu=\omega/2\pi$ and $\nu_o=\omega_o/2\pi$. This is the absorption line, which is shaped like a Lorentzian function, shown in figure 2.3.

Pulse NMR

To describe the behaviour of the bulk magnetisation during the pulse NMR experiment, it is instructive to explore the rotating frame as introduced in deriving the Bloch equations. In this frame the x- and y-axes rotate at the irradiation frequency ν, so that $\mathbf{B}_1$ is static and lies along the y-axis. The field along the z-axis is $\mathbf{B}_o - 2\pi\nu/\gamma$. The effective field is the vector sum of $\mathbf{B}_{eff} = \mathbf{B}_1 + \mathbf{B}_o - 2\pi\nu/\gamma$. At resonance $\mathbf{B}_{eff} = \mathbf{B}_1$, which causes the bulk magnetisation to precess about the y-axis. The angle of precession is $\varphi=\gamma B_1 \tau$ for a pulse of duration τ and thus the transverse component of the magnetisation becomes $M_0 \sin\varphi$. Subsequent to the pulse, this transverse component is detected as a decaying sinusoidal signal. The signal is called a free induction decay (FID) which is of the form (figure 2.4)

$$FID = e^{i(2\pi\nu_o t + \varphi)} e^{-t/T_2}. \tag{2.12}$$

The spectrum is obtained by taking the Fourier transform of the FID as follows

$$S(\nu) \propto \int_0^{+\infty} [FID] e^{-i2\pi\nu t} dt$$

$$= \int_0^{+\infty} e^{i(2\pi\nu_o t+\varphi)} e^{-t/T_2} e^{-i2\pi\nu t} dt$$

$$= e^{i\varphi} \int_0^{+\infty} e^{[i2\pi(\nu_o-\nu)-1/T_2]t} dt \qquad (2.13)$$

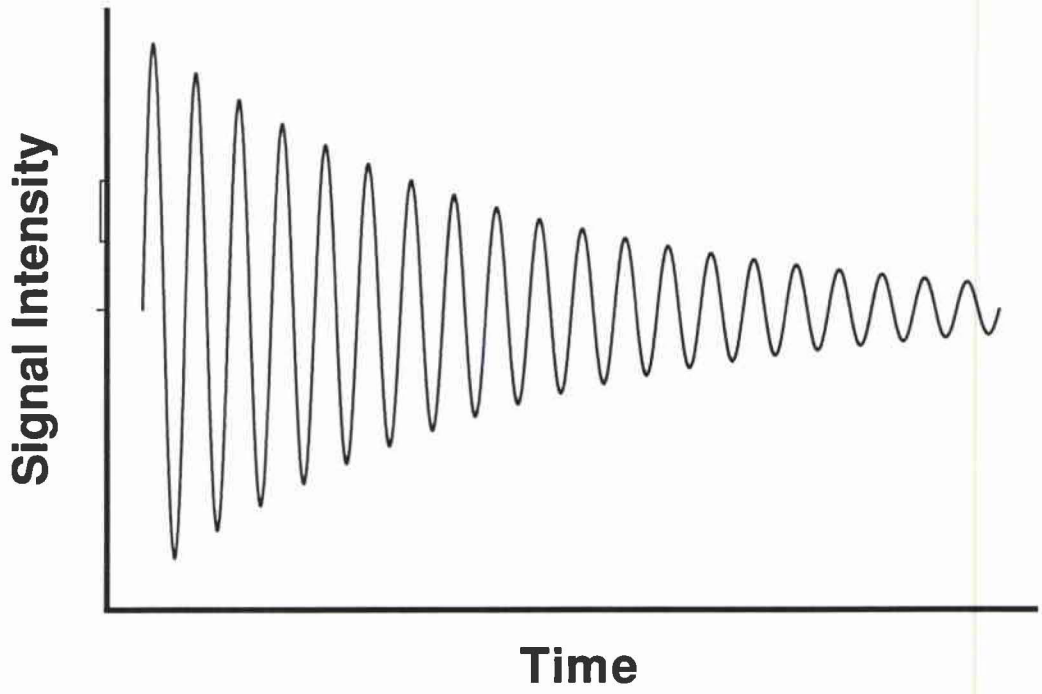

Figure 2.4 The free induction decay (FID) signal, is a sinusoidal function, oscillating at ν_o, and decaying at a rate determined by T_2.

This integral is solved

$$= e^{i\varphi} \frac{e^{[i2\pi(\nu_o-\nu)-1/T_2]t}\Big]_0^{\infty}}{i2\pi(\nu_o - \nu) + 1/T_2} = e^{i\varphi} \frac{i2\pi(\nu_o - \nu) + 1/T_2}{4\pi^2(\nu_o - \nu)^2 + 1/T_2^2}$$

$$= e^{i\varphi} \left(\frac{2\pi i(\nu_o - \nu)T_2^2}{4\pi T_2^2(\nu_o - \nu)^2 + 1} + \frac{T_2}{4\pi T_2^2(\nu_o - \nu)^2 + 1} \right)$$

$$= e^{i\varphi} \, (iD(\nu) + A(\nu))$$
$$= A(\nu)\cos\varphi - D(\nu)\sin\varphi + i\,(D(\nu)\cos\varphi + A(\nu)\sin\varphi) \quad (2.14)$$

where A(ν) and D(ν) are the absorption and dispersion lineshapes, and φ is the relative phase between the pulse and the detector.

The chemical shift and indirect spin-spin coupling.

The resonance frequency of a nucleus is influenced by its local electronic environment. The magnetic field gives rise to electron currents in the surrounding electron density, which in turn give rise to magnetic fields that counteract the imposed field.[57] In other words, the electrons shield the nucleus from the magnetic field. The degree of shielding is proportional to the strength of the applied field. Therefore the effective field experienced by the nucleus is $B = B_0 - \sigma B_0$, where σ is called the chemical shielding constant. Each nucleus in a unique chemical environment will have a unique value of σ. In general, shielding depends on the orientation of the electron density with the magnetic field and thus should really be treated as a tensorial property. In the solution phase, however, rapid isotropic tumbling causes this orientation dependence to be averaged to a scalar value.

The resonance frequencies of nuclei are affected by the states of nearby nuclei, through indirect spin-spin coupling.[57] The magnetic moment of one nucleus polarises the local electronic environment. This electron-spin polarisation is channelled through the local electron density to electronic environments surrounding other nuclei causing those nuclei to be polarised. These effects manifest themselves as splitting in the NMR lines.

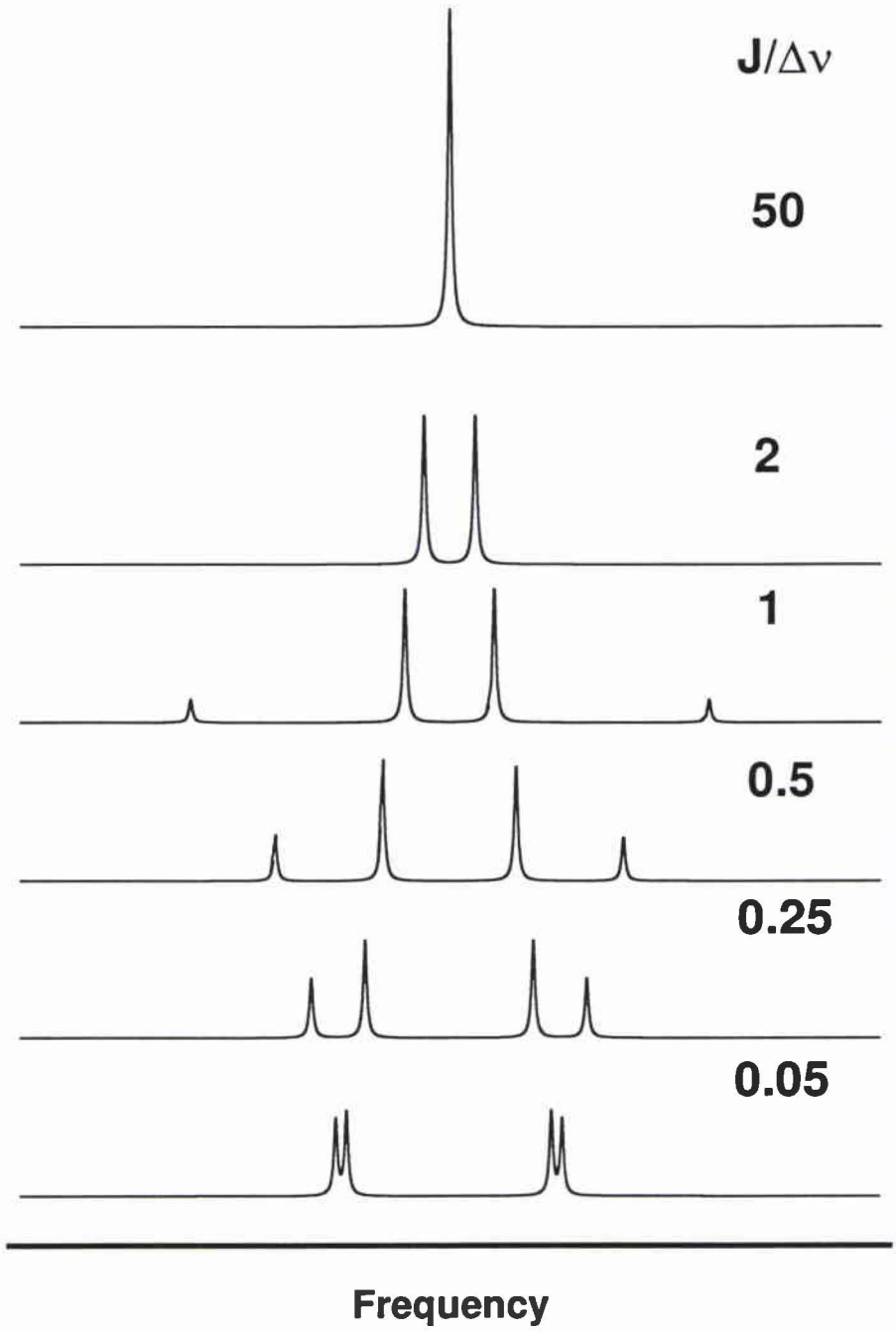

Figure 2.5 The spectrum of a two-spin-1/2 system initially as a first-order AX system and gradually becoming a second-order AB. In this case $\Delta\nu$ is kept constant and J is increased.

For example consider two coupled spin-1/2 nuclei A and B. The resonance frequency of A is split into two lines corresponding to the two possible spin orientations of B. The same is true for B. So the spectrum contains two sets of two lines split by the indirect spin-spin coupling constant J_{AB} centred at ν_A and ν_B, as in the bottom of figure 2.5.[58]

The magnitudes of the spin-spin coupling constants are independent of the magnetic field strength and are highly dependent on molecular structure. For example the coupling between the protons in H_2 is large and positive at 209 Hz.[57] Couplings between two protons on the same carbon of a methylene group range between –8 to –20 Hz. In substituted ethanes the three bond coupling constants are functions of the dihedral angle between the C-H bonds. This relationship was characterised by Karplus[59] as $J = A + B\cos(\theta) + C\cos(2\theta)$, where A B and C are empirically determined. In general, coupling constants change sign with each additional bond and decrease in magnitude.

A quantum mechanical treatment

To simulate spectra of real spin systems, a quantum mechanical approach is required. Before this can be discussed the operators involved should be introduced. A single spin-1/2 nucleus in a magnetic field has two possible states $|1/2,1/2\rangle = \alpha$ and $|1/2,-1/2\rangle = \beta$ such that $I_z \alpha = \hbar/2\, \alpha$ and $I_z \beta = -\hbar/2\, \beta$. In matrix form (*i.e.* in the α, β representation) $\mathbf{I}_z$ is given by

$$\mathbf{I}_z = \frac{\hbar}{2}\begin{bmatrix} 1 & 0 \\ 0 & -1 \end{bmatrix} \tag{2.15}$$

Similarly, the square of the magnitude of the angular momentum corresponds to the operator $\mathbf{I}^2 = \mathbf{I}_x^2 + \mathbf{I}_y^2 + \mathbf{I}_z^2$, where $\langle\alpha|\mathbf{I}^2|\alpha\rangle = \langle\beta|\mathbf{I}^2|\beta\rangle = \hbar^2/2(1/2+1) = \hbar^2 3/4$, given in matrix form as

$$\mathbf{I}^2 = \frac{3\hbar^2}{4}\begin{bmatrix} 1 & 0 \\ 0 & 1 \end{bmatrix} \tag{2.16}$$

All the properties of the spin operators can be deduced from the commutation relations between spin operators. These are

$$\begin{aligned} [\mathbf{I}_x, \mathbf{I}_y] &= i\mathbf{I}_z \\ [\mathbf{I}_y, \mathbf{I}_z] &= i\mathbf{I}_x \\ [\mathbf{I}_z, \mathbf{I}_x] &= i\mathbf{I}_y \end{aligned} \tag{2.17}$$

These imply that none of $\mathbf{I}_x$, $\mathbf{I}_y$ or $\mathbf{I}_z$ have simultaneous eigenstates. However, since $[\mathbf{I}^2, \mathbf{I}_{x,y,z}]=0$, $\mathbf{I}^2$ and one of $\mathbf{I}_{x,y,x}$ have simultaneous eigenstates. Quantisation can occur along any axis, with states that are completely determined by the eigenvalues of $\mathbf{I}_i$ and $\mathbf{I}^2$.

There is complete uncertainty regarding angular momentum along the two remaining axes. We choose the z-axis.

The raising and lowering operators, $\mathbf{I}_+ = \mathbf{I}_x + i\mathbf{I}_y$ and $\mathbf{I}_- = \mathbf{I}_x - i\mathbf{I}_y$, obey the commutation relationships

$$\begin{aligned} [\mathbf{I}_+, \mathbf{I}_z] &= -\mathbf{I}_+ \\ [\mathbf{I}_-, \mathbf{I}_z] &= \mathbf{I}_- \\ [\mathbf{I}+, \mathbf{I}_-] &= 2\mathbf{I}_z \end{aligned} \tag{2.18}$$

$\mathbf{I}_+$ increases the magnetic quantum number, which determines the eigenvalue of $\mathbf{I}_z$, by one unit. To see this, consider the commutator $[\mathbf{I}_+, \mathbf{I}_z]$ acting on state |I,m>

$$(\mathbf{I}_+\mathbf{I}_z - \mathbf{I}_z\mathbf{I}_+) \mid I,m\rangle = -\mathbf{I}_+ \mid I,m\rangle \tag{2.19}$$

$$m\mathbf{I}_+ \mid I,m\rangle - \mathbf{I}_z\mathbf{I}_+ \mid I,m\rangle = -\mathbf{I}_+ \mid I,m\rangle$$

$$m\mathbf{I}_+ \mid I,m\rangle + \mathbf{I}_+ \mid I,m\rangle = \mathbf{I}_z\mathbf{I}_+ \mid I,m\rangle$$

$$(m+1)\{\mathbf{I}_+ \mid I,m\rangle\} = \mathbf{I}_z\{\mathbf{I}_+ \mid I,m\rangle\}$$

Since the eigenvalue of state $\{\mathbf{I}_+|I,m>\}$ is m+1, $\{\mathbf{I}_+|I,m>\}$ must be |I,m+1>, to within a multiplicative constant. The magnetic quantum number is thereby raised by 1. A similar argument can be made for $\mathbf{I}_-$ showing that $\{\mathbf{I}_-|I,m>\}$ is just |I,m-1> (again to within a multiplicative constant).

The NMR Hamiltonian for solution NMR contains chemical shift and coupling terms only

$$\begin{aligned}\mathbf{H} &= \sum_i h\gamma B_o(1-\sigma_i)\mathbf{I}_z^i + \sum_{i<j} J_{i,j}\mathbf{I}^i \cdot \mathbf{I}^j \\ &= -\hbar^{-1}\sum_i (v_i - v_o)\mathbf{I}_z^i + \sum_{i<j} J_{i,j}\left[\mathbf{I}_z^i\mathbf{I}_z^j + \frac{J_{i,j}}{2}(\mathbf{I}_+^i\mathbf{I}_-^j + \mathbf{I}_-^i\mathbf{I}_+^j)\right]\end{aligned} \tag{2.20}$$

Using a product basis, $|\psi> = |I,m>_1|I,m>_2|I,m>_3\ldots|I,m>_n$, the matrix form of the Hamiltonian is derived. Take, for example, a two spin-1/2 system with chemical shifts ν_A and ν_B and coupling constant J_{AB}. The Hamiltonian is just

$$\mathbf{H} = v_A\mathbf{I}_z^A + v_B\mathbf{I}_z^B + J_{A,B}\mathbf{I}_z^A\mathbf{I}_z^B + \frac{J_{A,B}}{2}(\mathbf{I}_+^A\mathbf{I}_-^B + \mathbf{I}_-^A\mathbf{I}_+^B) \tag{2.21}$$

There are four possible product functions, $\alpha\alpha$, $\alpha\beta$, $\beta\alpha$ and $\beta\beta$, from which the Hamiltonian matrix, $<\Psi_i|H|\Psi_j>$, is constructed as

$$\begin{bmatrix} \frac{1}{2}\Sigma_{A,B} + \frac{J_{AB}}{4} & 0 & 0 & 0 \\ 0 & \frac{1}{2}\Delta_{A,B} - \frac{J_{AB}}{4} & \frac{J_{AB}}{2} & 0 \\ 0 & \frac{J_{AB}}{2} & -\frac{1}{2}\Delta_{A,B} - \frac{J_{AB}}{4} & 0 \\ 0 & 0 & 0 & -\frac{1}{2}\Sigma_{A,B} + \frac{J_{AB}}{4} \end{bmatrix}, \tag{2.22}$$

where $\Sigma_{A,B} = \nu_A + \nu_B$ and $\Delta_{A,B} = \nu_A - \nu_B$. Diagonalising this matrix gives the energies of the system and the resulting eigenvectors give the stationary states. Here, the Hamiltonian is block diagonal - only a 2×2 matrix needs to be diagonalised. The energy levels and eigenfunctions are[58]

$$
\begin{aligned}
\Psi_1 &= \alpha\alpha & E_1 &= \frac{1}{2}\Sigma_{A,B} + \frac{J_{AB}}{4} \\
\Psi_2 &= \alpha\beta\cos\theta + \beta\alpha\sin\theta & E_2 &= \frac{1}{2}[(\Delta_{A,B})^2 + J_{AB}^2]^{1/2} - \frac{J_{AB}}{4} \\
\Psi_3 &= -\alpha\beta\sin\theta + \beta\alpha\cos\theta & E_3 &= -\frac{1}{2}[(\Delta_{A,B})^2 + J_{AB}^2]^{1/2} - \frac{J_{AB}}{4} \\
\Psi_4 &= \beta\beta & E_4 &= \frac{1}{2}\Sigma_{A,B} + \frac{J_{AB}}{4}
\end{aligned}
\quad , \qquad (2.23)
$$

where $\sin 2\theta = J_{A,B}\Delta_{A,B}^{-1}$. The energy diagram is shown in figure 2.6. The line intensity in the spectrum is computed from the transition moment between states differing by ± 1 unit in m. The frequency is computed from the energy difference. According to time-dependent perturbation theory, the transition moment is given by $\langle\Psi_i|\mathbf{I}_\pm|\Psi_j\rangle$. The perturbation is the raising or lowering operator in the rotating wave approximation. For this example the transition intensities are shown in table 2.1.

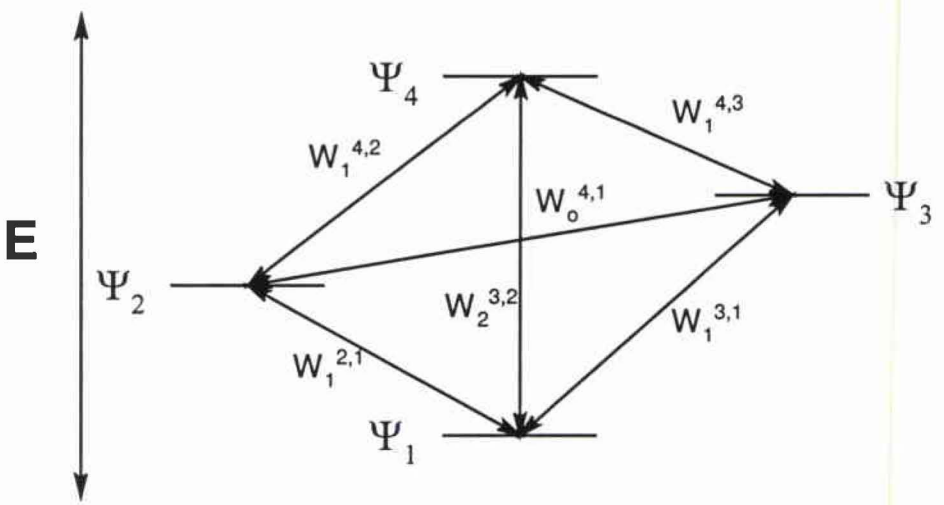

Figure 2.6 The energy level diagram for a two-spin-1/2 system.

Table 2.1

The relative intensities and energies of the transitions in a two-spin-1/2 system.[58]

Transition	*Δm*	*Energy relative to* $(\nu_A+\nu_B)/2$	*Relative intensity*
3 to 1	1	$J/2 + C$	1- sin 2θ
4 to 2	1	$-J/2 + C$	1+ sin 2θ
2 to 1	1	$J/2 - C$	1+ sin 2θ
4 to 3	1	$-J/2 - C$	1- sin 2θ
3 to 2	0	2C	0
4 to 1	2	$(\nu_A+\nu_B)/2$	0

First- and second-order behaviour

Notice that as the ratio of J/Δν increases, the outer lines of the spectrum decrease in intensity while the inner lines increase, and eventually the spectrum collapses into one line (see figure 2.5). This behaviour is called second-order behaviour and is the result of off-diagonal elements in the Hamiltonian. In first-order spectra, the off-diagonal elements are small enough to be ignored. In this case, the product basis is the eigenbasis. First-order spectra are simple and can be approximated using the n+1 rule. Specifically, for spin-1/2 systems, the number of lines in a multiplet is equal to the number of magnetically equivalent coupled partners plus one. The intensity pattern is determined by the binomial distribution, in other words, Pascal's triangle. For each set of coupled partners there is a unique splitting. For example take an A_3MX_2, the multiplet corresponding to the M nucleus is split into a 1:3:3:1 quartet due to the 3 magnetically equivalent A nuclei. Each of these lines is further split into a 1:2:1 triplet due to the 2 X

nuclei. Second-order spectra are more complicated for large systems, and thus have to be computed numerically. Figure 2.5 illustrates the transition from first-order behaviour of a 2 spin-1/2 system, an AX system, to various stages of second-order behaviour, an AB system. Eventually the system collapses into a singlet where the system can be regarded as an A_2 system.

A time-dependent quantum mechanical treatment

Quantum theory describes the time evolution of a spin system, needed to predict 2D spectra.[60] The effects of chemical exchange,[61] and the treatment of solid state spectra under MAS conditions, are also provided by quantum theory.[62-64] A proper treatment requires handling of collections of states (an ensemble), as opposed to one state described by Ψ, since the NMR experiment is performed on a bulk material containing a large number of nuclei in different spin states. In such a treatment, one follows the evolution of all possible states at once in terms of state populations and intensities of transition between them. The collection of states is described by a density matrix, ρ, which is constructed from the operators, $|\Psi\rangle\langle\Psi|$. In what follows, we develop the density matrix starting with the time-dependent Schrödinger equation.

The state of a spin system changes in time according to the time-dependent Schrödinger equation,

$$i\hbar \frac{d \mid \Psi(t)\rangle}{dt} = \mathbf{H} \mid \Psi(t)\rangle, \tag{2.24}$$

which has the solution (provided that the Hamiltonian is time-independent)

$$\mid \Psi(t)\rangle = \exp\left(-\frac{i\mathbf{H}t}{\hbar}\right) \mid \Psi(0)\rangle = \mathbf{U}(t) \mid \Psi(0)\rangle, \tag{2.25}$$

where **U**(t) is a unitary transformation which propagates the state through time. In terms of a time-independent basis, the state is represented by a set of time-dependent coefficients. Specifically

$$\psi(t) = \sum_i C_i(t)\varphi_i\,, \tag{2.26}$$

where $\sum_i |C_i(t)|^2 = 1$. In general, the $C_i(t)$ are complex.

Consider the time development of an observable **O**

$$\begin{aligned}
\mathbf{O}(t) &= \langle \exp\left(\frac{-i\mathbf{H}t}{\hbar}\right)\Psi \,|\mathbf{O}|\, \exp\left(\frac{-i\mathbf{H}t}{\hbar}\right)\Psi\rangle \\
&= \left\langle C_\alpha(t)\alpha + C_\beta(t)\beta\right| \mathbf{O} \left|C_\alpha(t)\alpha + C_\beta(t)\beta\right\rangle \\
&= \begin{bmatrix} C_\alpha^*(t) & C_\beta^*(t)\end{bmatrix}\begin{bmatrix}\langle\alpha|\mathbf{O}|\alpha\rangle & \langle\alpha|\mathbf{O}|\beta\rangle \\ \langle\beta|\mathbf{O}|\alpha\rangle & \langle\beta|\mathbf{O}|\beta\rangle\end{bmatrix}\begin{bmatrix}C_\alpha(t) \\ C_\alpha(t)\end{bmatrix} \\
&= C_\alpha^*(t)C_\alpha(t)O_{\alpha\alpha} + C_\beta^*(t)C_\alpha(t)O_{\beta\alpha} \\
&\qquad + C_\alpha^*(t)C_\beta(t)O_{\alpha\beta} + C_\alpha^*(t)C_\beta(t)O_{\beta\beta} \\
&= Tr\begin{bmatrix} C_\alpha^*(t)C_\alpha(t) & C_\beta^*(t)C_\alpha(t) \\ C_\alpha^*(t)C_\beta(t) & C_\beta^*(t)C_\beta(t)\end{bmatrix}\begin{bmatrix}O_{\alpha\alpha} & O_{\alpha\beta} \\ O_{\beta\alpha} & O_{\beta\beta}\end{bmatrix}
\end{aligned} \tag{2.27}$$

Now consider a matrix $\rho = |\Psi\rangle\langle\Psi|$ which is a projection operator of one state onto another.

$$\rho = |\Psi(t)\rangle\langle\Psi(t)| = \begin{bmatrix}C_\alpha(t)|\alpha\rangle \\ C_\beta(t)|\beta\rangle\end{bmatrix}\begin{bmatrix}C_\alpha^*(t)\langle\alpha| & C_\beta^*(t)\langle\beta|\end{bmatrix}$$

$$= \begin{bmatrix}C_\alpha(t)C_\alpha^*(t)|\alpha\rangle\langle\alpha| & C_\alpha(t)C_\beta^*(t)|\alpha\rangle\langle\beta| \\ C_\beta(t)C_\alpha^*(t)|\beta\rangle\langle\alpha| & C_\beta(t)C_\beta^*(t)|\beta\rangle\langle\beta|\end{bmatrix} = \begin{bmatrix}C_\alpha(t)C_\alpha^*(t) & C_\alpha(t)C_\beta^*(t) \\ C_\beta(t)C_\alpha^*(t) & C_\beta(t)C_\beta^*(t)\end{bmatrix} \tag{2.28}$$

$\rho = |\Psi\rangle\langle\Psi|$ is the density matrix for one quantum state (a pure state). In general $\langle \mathbf{O}(t) \rangle = Tr\left(\rho^T(t)\mathbf{O}\right)$, where the time-dependent density matrix is constructed from a sum of time evolving pure states (an ensemble). (T indicates the adjoint of the matrix) The matrix representation of this ensemble is seen in eqn.(2.28), except that the matrix elements have a more general form. Each component of the density matrix can be viewed as a basis element. The diagonal terms are always real and positive and can be viewed as populations. The off-diagonal elements are related to transition intensities.

Consider a single spin-1/2 nucleus in a magnetic field $\mathbf{B_o}$. The difference in equilibrium energy level populations is $\Delta n = N(\gamma\hbar B_o/k_bT)$. This gives an equilibrium density matrix of the form,

$$\rho = \begin{bmatrix} 1+\Delta n/2 & 0 \\ 0 & 1-\Delta n/2 \end{bmatrix} = \begin{bmatrix} 1 & 0 \\ 0 & 1 \end{bmatrix} + \Delta n \begin{bmatrix} 1/2 & 0 \\ 0 & -1/2 \end{bmatrix} = \mathbf{1} + \Delta n \mathbf{I}_z \quad (2.29)$$

Since **1** exhibits no time dependence, it is usually dropped from the formalism and the equilibrium density matrix is take to be $\mathbf{I}_z$. At equilibrium, there is induced magnetisation along the z-axis – there are no components along the x- and y-axis. This agrees with the classical picture described earlier.

The effect of a pulse

The effect of a pulse on a density matrix is now considered. When a resonant pulse is applied the axis of precession changes from the applied static field to the $\mathbf{B}_1$ field of the pulse. The axis of precession is determined by the phase of the pulse. Thus, if a 90^0 pulse is applied along the y axis, we expect the magnetisation to rotate to the x-axis. (*i.e.* $\mathbf{I}_z$ goes to $\mathbf{I}_x$). The propagator that describes the rotation is $\exp\left[-i\gamma B_1 \tau \mathbf{I}_y\right]$= $1\cos(\gamma B_1\tau) - I_x\sin(\gamma B_1\tau)$,[60] where $\gamma B_1\tau = 90^\circ$. In other words the corresponding rotation matrix looks like

$$\exp\left[i\beta \mathbf{I}_y\right] = \exp\left[i\beta \sigma_y\right] = 1\cos(\beta/2) + i\,\sigma_y \sin(\beta/2)$$

$$= \begin{bmatrix} \cos(\beta/2) & \sin(\beta/2) \\ -\sin(\beta/2) & \cos(\beta/2) \end{bmatrix} \tag{2.30}$$

The effect of a pulse on $\mathbf{I}_z$ is computed as

$$\exp\left[-i\beta \mathbf{I}_y\right] \mathbf{I}_z \exp\left[i\beta \mathbf{I}_y\right]$$

Substituting the appropriate matrices gives

$$\begin{bmatrix} \cos(\beta/2) & \sin(\beta/2) \\ -\sin(\beta/2) & \cos(\beta/2) \end{bmatrix} \begin{bmatrix} 1/2 & 0 \\ 0 & -1/2 \end{bmatrix} \begin{bmatrix} \cos(\beta/2) & \sin(\beta/2) \\ -\sin(\beta/2) & \cos(\beta/2) \end{bmatrix} \tag{2.31}$$

$$= 1/2 \begin{bmatrix} \cos^2(\beta/2) - \sin^2(\beta/2) & 2\cos(\beta/2)\sin(\beta/2) \\ 2\cos(\beta/2)\sin(\beta/2) & -\cos^2(\beta/2) + \sin^2(\beta/2) \end{bmatrix}$$

$$= 1/2 \begin{bmatrix} \cos(\beta) & \sin(\beta) \\ \sin(\beta) & -\cos(\beta) \end{bmatrix} = \mathbf{I}_z \cos\beta + \mathbf{I}_x \sin\beta$$

When β is 90° $\mathbf{I_z}$ is transformed to $\mathbf{I_x}$, as expected.

Evolution

During a delay the spin system evolves according to the spin Hamiltonian. In the case of a single spin, $\mathbf{H} = \omega \mathbf{I_z}$. Taking the initial density matrix after an initial 90°_{y} pulse to be $\mathbf{I_x}$, the evolution of ρ is computed as

$$\rho(t) = \exp\left[-i\omega \mathbf{I}_z\right] \mathbf{I}_x \exp\left[+i\omega \mathbf{I}_z\right]$$

The rotation matrix for this propagator is $\mathbf{1}\cos(\omega t/2) - i\sigma_z \sin(\omega t/2)$. Substituting the appropriate matrices the expression for $\rho(t)$ becomes

$$1/2\begin{bmatrix} \exp(-i\omega t/2) & 0 \\ 0 & \exp(i\omega t/2) \end{bmatrix}\begin{bmatrix} 0 & 1 \\ 1 & 0 \end{bmatrix}\begin{bmatrix} \exp(i\omega t/2) & 0 \\ 0 & \exp(-i\omega t/2) \end{bmatrix}$$

$$= \cos(\omega t)\mathbf{I_x} + \sin(\omega t)\mathbf{I_y} \qquad (2.32)$$

Here we see how the x and y components oscillate at the Larmor frequency as seen in the classical picture.

The Liouville representation and Superspin formalism

To incorporate the effects of relaxation and dynamic processes on NMR spectra, it is convenient to change to the Liouville representation.[19] In this formulation the density matrix is a vector, in a matrix basis. Operators acting on vectors of this type are called super-operators, since they act on operators.

Applying the time-dependent Schrödinger equation to the density matrix (in case of a pure state)

$$\begin{aligned}\frac{\partial}{\partial t}\rho(t) &= \frac{\partial}{\partial t}|\Psi(t)\rangle\langle\Psi(t)| = \left|\frac{\partial}{\partial t}\Psi(t)\right\rangle\langle\Psi(t)| + |\Psi(t)\rangle\left\langle\frac{\partial}{\partial t}\Psi(t)\right| \\ &= -i\mathbf{H}|\Psi(t)\rangle\langle\Psi(t)| + i|\Psi(t)\rangle\langle\Psi(t)|\mathbf{H} = -i\mathbf{H}\rho(t) + i\rho(t)\mathbf{H}. \\ &= -i[\mathbf{H},\rho(t)]\end{aligned} \tag{2.33}$$

This expression can be restated such that ρ(t) is a vector and the action of taking the commutator with the Hamiltonian, [, **H**] is a super-operator **L** as follows

$$\frac{\partial}{\partial t}\rho(t) = -i\mathbf{L}\rho(t) \tag{2.34}$$

This is a simple set of first-order differential equations, which have solutions of the form

$$\rho(t) = \exp\left[-i\,\mathbf{L}t\right]\rho(o) \tag{2.35}$$

The way in which to think of ρ as a vector is by expanding it as a linear combination of basis matrices. For example

$$\rho = \begin{bmatrix}\rho_{\alpha\alpha} & \rho_{\alpha\beta}\\ \rho_{\beta\alpha} & \rho_{\beta\beta}\end{bmatrix} = \rho_{\alpha\alpha}\begin{bmatrix}1 & 0\\ 0 & 0\end{bmatrix} + \rho_{\alpha\beta}\begin{bmatrix}0 & 1\\ 0 & 0\end{bmatrix} + \rho_{\beta\alpha}\begin{bmatrix}0 & 0\\ 1 & 0\end{bmatrix} + \rho_{\beta\beta}\begin{bmatrix}0 & 0\\ 0 & 1\end{bmatrix} \tag{2.36}$$

thus in this basis ρ becomes[62]

$$\begin{bmatrix} \rho_{\alpha\alpha} \\ \rho_{\alpha\beta} \\ \rho_{\beta\alpha} \\ \rho_{\beta\beta} \end{bmatrix}.$$

A basis set including $\mathbf{I_x}$, $\mathbf{I_y}$, $\mathbf{I_z}$ and **1** can also be used yielding

$$\begin{aligned} \rho &= \frac{1}{2}(\rho_{\alpha\alpha} + \rho_{\beta\beta})\begin{bmatrix} 1 & 0 \\ 0 & 1 \end{bmatrix} + \frac{1}{2}(\rho_{\alpha\alpha} - \rho_{\beta\beta})\begin{bmatrix} 1 & 0 \\ 0 & -1 \end{bmatrix} \\ &\quad + \frac{1}{2}(\rho_{\alpha\beta} + \rho_{\beta\alpha})\begin{bmatrix} 0 & 1 \\ 1 & 0 \end{bmatrix} + \frac{i}{2}(\rho_{\alpha\beta} - \rho_{\beta\alpha})\begin{bmatrix} 0 & -i \\ i & 0 \end{bmatrix} \\ &= \frac{1}{2}(\rho_{\alpha\alpha} + \rho_{\beta\beta})\mathbf{1} + \frac{1}{2}(\rho_{\alpha\alpha} - \rho_{\beta\beta})\mathbf{I_z} + \frac{1}{2}(\rho_{\alpha\beta} + \rho_{\beta\alpha})\mathbf{I_x} \\ &\quad + \frac{i}{2}(\rho_{\alpha\beta} - \rho_{\beta\alpha})\mathbf{I_y} \end{aligned} \tag{2.37}$$

forming the vector

$$\begin{bmatrix} \rho_{\alpha\alpha} + \rho_{\beta\beta} \\ \rho_{\alpha\alpha} - \rho_{\beta\beta} \\ \rho_{\alpha\beta} + \rho_{\beta\alpha} \\ i(\rho_{\alpha\beta} - \rho_{\beta\alpha}) \end{bmatrix} = \begin{bmatrix} \rho_o \\ \rho_z \\ \rho_x \\ \rho_y \end{bmatrix}.$$

Instead of using $\mathbf{I_x}$, $\mathbf{I_y}$ they can be replaced by $\mathbf{I_+} = \frac{1}{2}(\mathbf{I_x} + i\mathbf{I_y})$ and $\mathbf{I_-} = \frac{1}{2}(\mathbf{I_x} - i\mathbf{I_y})$,

$$\begin{aligned} \rho &= \rho_0\begin{bmatrix} 1 & 0 \\ 0 & 1 \end{bmatrix} + \rho_z\begin{bmatrix} 1 & 0 \\ 0 & -1 \end{bmatrix} + (\rho_x + i\rho_y)\begin{bmatrix} 0 & 1 \\ 0 & 0 \end{bmatrix} + (\rho_x - i\rho_y)\begin{bmatrix} 0 & 0 \\ 1 & 0 \end{bmatrix} \\ &= \rho_0\mathbf{1} + \rho_z\mathbf{I_z} + (\rho_x + i\rho_y)\mathbf{I_+} + (\rho_x - i\rho_y)\mathbf{I_-} \end{aligned}$$

$$= \begin{bmatrix} \rho_0 \\ \rho_z \\ \rho_x + i\rho_y \\ \rho_x - i\rho_y \end{bmatrix} = \begin{bmatrix} \rho_0 \\ \rho_z \\ \rho_+ \\ \rho_- \end{bmatrix} = \begin{bmatrix} \rho_{\alpha\alpha} + \rho_{\beta\beta} \\ \rho_{\alpha\alpha} - \rho_{\beta\beta} \\ \rho_{\beta\alpha} \\ \rho_{\alpha\beta} \end{bmatrix} \tag{2.38}$$

In this space, operators form the basis functions. This particular basis is called the superspin basis, where $(1/\sqrt{2})\mathbf{1} = |0)$, $(\sqrt{2})\mathbf{I_z} = |I_0)$, $\mathbf{I}_+ = |I_{+1})$ and $\mathbf{I}_- = |I_{-1})$.[65] A super-operator acts on these operators as $\mathbf{L} \mid \mathbf{I}_i) = [\mathbf{H}, \mathbf{I}_i]$. For example, if $H=\omega_o \mathbf{I_z}$, then

$$\begin{aligned} \mathbf{L} \mid 0) &= \left[\omega_o \mathbf{I}_z, (1/\sqrt{2})\mathbf{1}\right] = 0 \\ \mathbf{L} \mid \mathbf{I}_0) &= [\omega_o \mathbf{I}_z, (\sqrt{2})\mathbf{I}_z] = 0 \\ \mathbf{L} \mid \mathbf{I}_{+1}) &= [\omega_o \mathbf{I}_z, \mathbf{I}_+] = \omega_o \mathbf{I}_+ = \omega_o \mid \mathbf{I}_{+1}) \\ \mathbf{L} \mid \mathbf{I}_{-1}) &= [\omega_o \mathbf{I}_z, \mathbf{I}_-] = -\omega_o \mathbf{I}_- = -\omega_o \mid \mathbf{I}_{-1}) \end{aligned} \tag{2.39}$$

Note that the |0) component is time-independent as a consequence of normalisation of the density matrix. It commutes with any Hamiltonian, and its coefficients can be taken to be zero. The system thus reduces to a three-component vector.

The matrix elements $(\mathbf{I}_i \mid \mathbf{L} \mid \mathbf{I}_j)$ are computed using the trace relation $(\mathbf{I}_i \mid \mathbf{L} \mid \mathbf{I}_j) = Tr[\mathbf{I}_i^* [\mathbf{H}, \mathbf{I}_j]]$. For example, $(\mathbf{I}_{+1} \mid \mathbf{L} \mid \mathbf{I}_{+1}) = Tr[\mathbf{I}_- [\mathbf{H}, \mathbf{I}_+]]$. The matrix representation of the Liouvillian for $\mathbf{H} = \omega_o \mathbf{I_z}$ is

$$\mathbf{L} = \begin{bmatrix} \omega_o & 0 & 0 \\ 0 & 0 & 0 \\ 0 & 0 & -\omega_o \end{bmatrix}, \tag{2.40}$$

and the expression for $\rho(t)$ becomes

$$\begin{bmatrix} \rho_{+1}(t) \\ \rho_0(t) \\ \rho_{-1}(t) \end{bmatrix} = \begin{bmatrix} \exp(-i\omega_o t) & 0 & 0 \\ 0 & 1 & 0 \\ 0 & 0 & \exp(i\omega_o t) \end{bmatrix} \begin{bmatrix} \rho_{+1}(0) \\ \rho_0(0) \\ \rho_{-1}(0) \end{bmatrix} \tag{2.41}$$

From the above expression $\rho_{+1}(t)$ represents the component of the magnetisation which rotates in the x-y plane (*i.e.* single quantum coherence), while $\rho_0(t)$ is the z-magnetisation.

The NMR signal is the expectation value of the operator $\mathbf{I}_+$. In other words $S(\omega)=(\mathbf{I}_+|\rho(t))$ which is just the $|\mathbf{I}_{+1})$ component of $\rho(t)$ (*i.e.* $\rho_{+1}(t)$).

Relaxation and exchange

In order to simulate spectra, which include effects of chemical exchange and relaxation it is necessary to introduce two additional super-operators in the master equation. The resulting time-dependent state is given by[60]

$$\rho(t) = \exp[(-i\mathbf{L} - \mathbf{R} - \mathbf{K})t]\rho(0), \tag{2.42}$$

where $\rho(t)$ belongs to a direct product space of spin and nuclear configuration space. The matrix $i\mathbf{L} + \mathbf{R} + \mathbf{K}$ is diagonalised giving the diagonal eigenvalue matrix, Λ, and the matrix of eigenvectors $\mathbf{U}$. The signal is computed as

$$\begin{aligned} S(t) &= (\mathbf{I}_{1+} \mid \mathbf{U}^{-1} \exp[-\Lambda t]\mathbf{U}\mathbf{F}_{1+}) \\ &= \sum_j (\mathbf{U}^{-1}\mathbf{I}_{1+})_j^* (\mathbf{U}\mathbf{F}_{1+})_j \exp\left[-\lambda_j t\right] \end{aligned} \tag{2.43}$$

where $\mathbf{I}_{1+}$ is the detector function and $\mathbf{F}_{1+}$ is the sum of the $\mathbf{I}_{1+}$ weighted by the equilibrium populations (*i.e.* $\rho(0)$).[32-34] Each term in this sum is a transition, which is of

the form of a decaying sinusoidal function. The amplitude of each transition is the product of two terms. The first term $(\mathbf{U}^{-1}\mathbf{I}_{1+})^{*}_{j}$ is a measure of how efficiently the receiver senses xy magnetisation. The second term, $(\mathbf{UF}_{1+})_{j}$, is a measure of xy-magnetisation made available from the initial z-magnetisations.

The relaxation super-operator, $\mathbf{R}$, describes how the density matrix returns to equilibrium from a non-equilibrium state, as follows

$$\rho(t) - \rho(\infty) = \exp[-\mathbf{R}t][\rho(0) - \rho(\infty)] \tag{2.44}$$

A simple implementation uses a diagonal form of $\mathbf{R}$, where x and y magnetisation decay as $1/T_2$ and z-magnetisations as $1/T_1$. Therefore $\mathbf{R}$ is of the form:

$$\mathbf{R} = \begin{bmatrix} 1/T_2 & 0 & 0 \\ 0 & 1/T_1 & 0 \\ 0 & 0 & 1/T_2 \end{bmatrix}$$

$$\begin{bmatrix} \rho_{+1}(t) - \rho_{+1}(\infty) \\ \rho_0(t) - \rho_0(\infty) \\ \rho_{-1}(t) - \rho_{-1}(\infty) \end{bmatrix} = \begin{bmatrix} \exp(-t/T_2) & 0 & 0 \\ 0 & \exp(-t/T_1) & 0 \\ 0 & 0 & \exp(-t/T_2) \end{bmatrix} \begin{bmatrix} \rho_{+1}(0) - \rho_{+1}(\infty) \\ \rho_0(0) - \rho_0(\infty) \\ \rho_{-1}(0) - \rho_{-1}(\infty) \end{bmatrix} \tag{2.45}$$

The exchange super-operator connects the same coherences between different conformational species. The system's state belongs to a direct product space of spin states and conformations. For example if there are two equally populated species, the block form of the master equation is

$$\begin{bmatrix} \rho_1(t) \\ \rho_2(t) \end{bmatrix} = \exp\left[-i\begin{bmatrix} \mathbf{L}_1 & 0 \\ 0 & \mathbf{L}_2 \end{bmatrix} + \begin{bmatrix} \mathbf{R}_1 & 0 \\ 0 & \mathbf{R}_2 \end{bmatrix} + k\begin{bmatrix} -1 & 1 \\ 1 & -1 \end{bmatrix}\right]. \tag{2.46}$$

Keeping track of only the $\rho_{+1}(t)$ components[34,66,67]

$$\begin{bmatrix}\rho_{+1}^1(t)\\ \rho_{+1}^2(t)\end{bmatrix} = \exp\left[-i\begin{bmatrix}\omega_o^1 & 0\\ 0 & \omega_o^2\end{bmatrix} - \begin{bmatrix}1/T_2^1 & 0\\ 0 & 1/T_2^2\end{bmatrix} + \begin{bmatrix}-k & k\\ k & -k\end{bmatrix}\right] t \begin{bmatrix}\rho_{+1}^1(0)\\ \rho_{+1}^2(0)\end{bmatrix}$$

$$= \exp\begin{bmatrix}-i\omega_o^1 - 1/T_2^1 - k & k\\ k & -i\omega_o^2 - 1/T_2^2 - k\end{bmatrix} t \begin{bmatrix}\rho_{+1}^1(0)\\ \rho_{+1}^2(0)\end{bmatrix}.$$

Assuming that $\delta = \left(\omega_o^1 - \omega_o^2\right)/2$ and $1/T_2^1 = 1/T_2^2 = 1/T_2$, simplifies the system of equations. The eigenvalues of the Liouvillian are

$$\lambda = -\left(\frac{1}{T_2} + k\right) \pm \sqrt{k^2 - \delta^2}\,, \tag{2.47}$$

which are either complex or pure real. During slow exchange, $k < \delta$, so the eigenvalues are complex. The corresponding eigenvector matrix is

$$\mathbf{U} = \begin{pmatrix} k & i(\sqrt{\delta^2 - k^2} + \delta) \\ -i(\sqrt{\delta^2 - k^2} + \delta) & k \end{pmatrix}. \tag{2.48}$$

The expression for the NMR signal is derived in general for the 2x2 case as follows:

$$\mathbf{U} = \begin{pmatrix} a & b \\ c & d \end{pmatrix}; \mathbf{U}^{-1} = \frac{1}{\det \mathbf{U}} \begin{pmatrix} d & -b \\ -c & a \end{pmatrix}$$

$$S(t) = \frac{(a+c)(d-b)}{\det \mathbf{U}} e^{\lambda_1 t} + \frac{(b+d)(-c+a)}{\det \mathbf{U}} e^{\lambda_2 t}$$

For the slow exchange case, the NMR signal is:

$$S(t) = \left[1 + ik\frac{\sqrt{\delta^2 - k^2}}{\delta^2 - k^2}\right] e^{\left[-\left(\frac{1}{T_2}+k\right)+i\sqrt{\delta^2-k^2}\right]t} + \left[1 - ik\frac{\sqrt{\delta^2 - k^2}}{\delta^2 - k^2}\right] e^{\left[-\left(\frac{1}{T_2}+k\right)-i\sqrt{\delta^2-k^2}\right]t} \tag{2.49}$$

This spectrum is comprised of two lines of equal intensity, with linewidths of $1/T_2 + k$. Their frequencies and phases are $\pm\sqrt{\delta^2 - k^2}$ and $tan\left(\pm k\sqrt{\delta^2 - k^2}\right)$, respectively (see figure 2.7). Thus, while in the slow-exchange regime as the rate increases, the lines broaden, the chemical shift difference increases, the phase angle increases, and the amplitudes do not change.

In the fast-exchange regime $k > \delta$, thus $k - \delta$ is positive, which implies that the eigenvalues are now pure real. The corresponding matrix of eigenvectors is

$$U = \begin{pmatrix} \sqrt{\delta^2 - k^2} - i\delta & -\sqrt{\delta^2 - k^2} - i\delta \\ k & k \end{pmatrix}, \tag{2.50}$$

from which the expression for the signal is:

$$s(t) = \left[1 + k\frac{\sqrt{k^2 - \delta^2}}{k^2 - \delta^2}\right] e^{\left[-\left(\frac{1}{T_2}+k\right)+\sqrt{k^2-\delta^2}\right]t} + \left[1 - k\frac{\sqrt{k^2 - \delta^2}}{k^2 - \delta^2}\right] e^{\left[-\left(\frac{1}{T_2}+k\right)-\sqrt{k^2-\delta^2}\right]t}. \tag{2.51}$$

The above expression implies that that both lines have the same frequency, and have zero phase(see figure 2.8). The second term represents a line with negative intensity, which decreases in absolute intensity, and broadens with increasing rate. The other line has positive intensity, which increases and becomes narrower with increasing rate. In the

limit of infinite rate the second term disappears, the first doubles its intensity and has a width of $1/T_2$.

A similar approach can be taken to look into the selective inversion of a two-site uncoupled exchange. Following the z-magnetisations, we start with the initial state, where the magnetisation of one site in inverted, and the other is unperturbed, *i.e.* eqn. (2.46) becomes

$$\begin{bmatrix} \rho_0^1(t) - \rho_0^1(\infty) \\ \rho_0^2(t) - \rho_0^2(\infty) \end{bmatrix} = \exp\begin{bmatrix} -k - 1/T_1^1 & k \\ k & -k - 1/T_1^2 \end{bmatrix} \begin{bmatrix} \rho_{+1}^1(0) - \rho_{+1}^1(\infty) \\ \rho_{+1}^2(0) - \rho_{+1}^2(\infty) \end{bmatrix}. \qquad (2.52)$$

where we take $\rho_0^1(0) - \rho_0^1(\infty) = -2M_o$ and $\rho_0^2(0) - \rho_0^2(\infty) = 0$. Assuming equally-populated exchange and $T_1^1 = T_1^2$, the eigenvalues are $2k - 1/T_1$ and $-1/T_1$ with the corresponding eigenvectors, $1/\sqrt{2}\begin{pmatrix} -1 & 1 \end{pmatrix}$ and $1/\sqrt{2}\begin{pmatrix} 1 & 1 \end{pmatrix}$. The general solution is

$$\begin{aligned} \rho_0^1(t) - \rho_0^1(\infty) &= 1/2\left[\exp\left(-t/T_1\right) + \exp\left(-\left[2k + 1/T_1\right]t\right)\right]\left[\rho_{+1}^1(0) - \rho_{+1}^1(\infty)\right] \\ &\quad +1/2\left[\exp\left(-t/T_1\right) - \exp\left(-\left[2k + 1/T_1\right]t\right)\right]\left[\rho_{+2}^1(0) - \rho_{+2}^1(\infty)\right] \\ \rho_0^2(t) - \rho_0^2(\infty) &= 1/2\left[\exp\left(-t/T_1\right) - \exp\left(-\left[2k + 1/T_1\right]t\right)\right]\left[\rho_{+1}^1(0) - \rho_{+1}^1(\infty)\right] \\ &\quad +1/2\left[\exp\left(-t/T_1\right) + \exp\left(-\left[2k + 1/T_1\right]t\right)\right]\left[\rho_{+2}^1(0) - \rho_{+2}^1(\infty)\right] \end{aligned} \qquad (2.53)$$

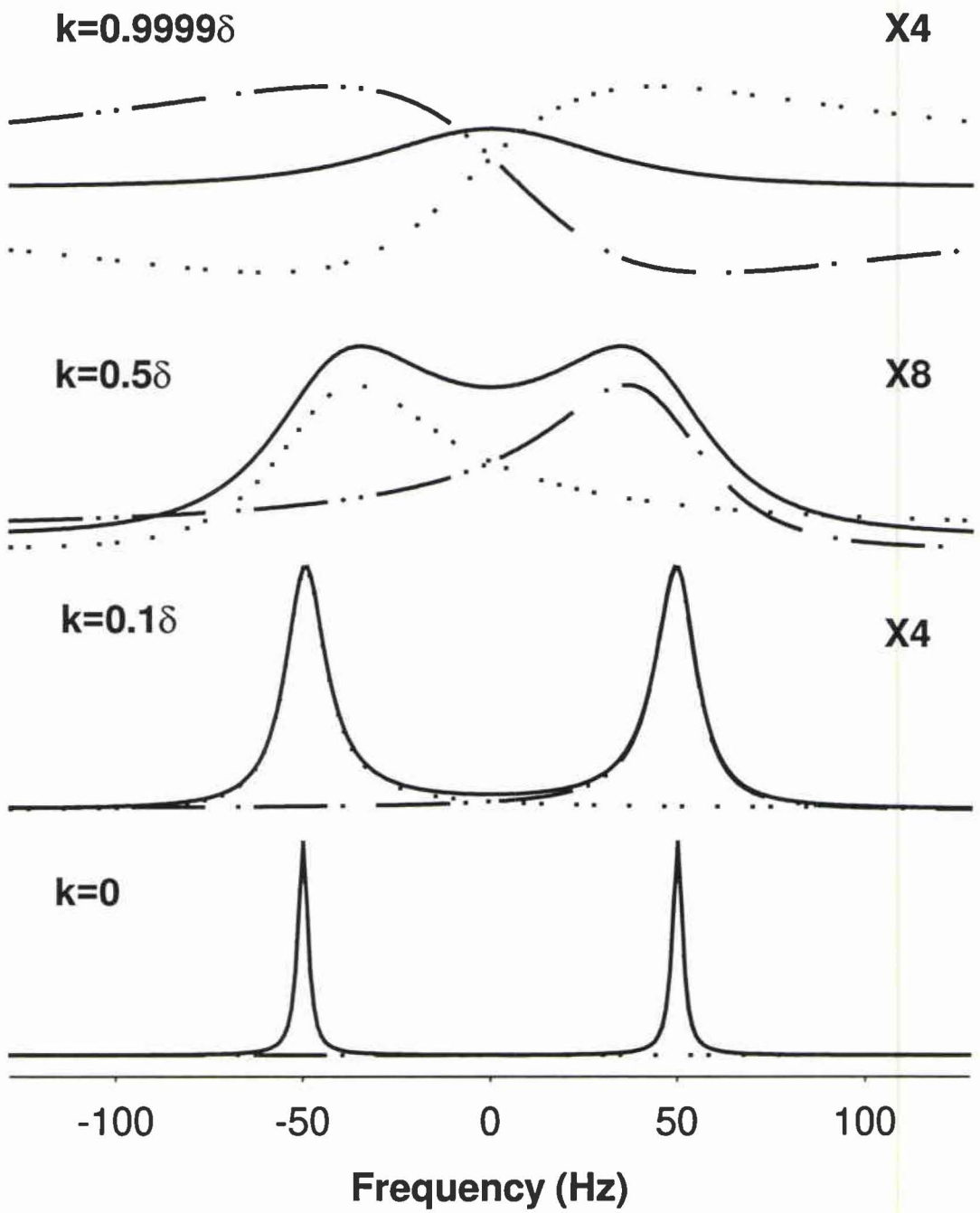

Figure 2.7 Lineshapes in the slow- to intermediate- exchange regimes. The lineshape is composed of two line, initially in phase, that rotate out of phase with increasing rate up to 180^0. As the rate increases both lines broaden. The rate, k, is given as a multiple of the frequency difference, δ.

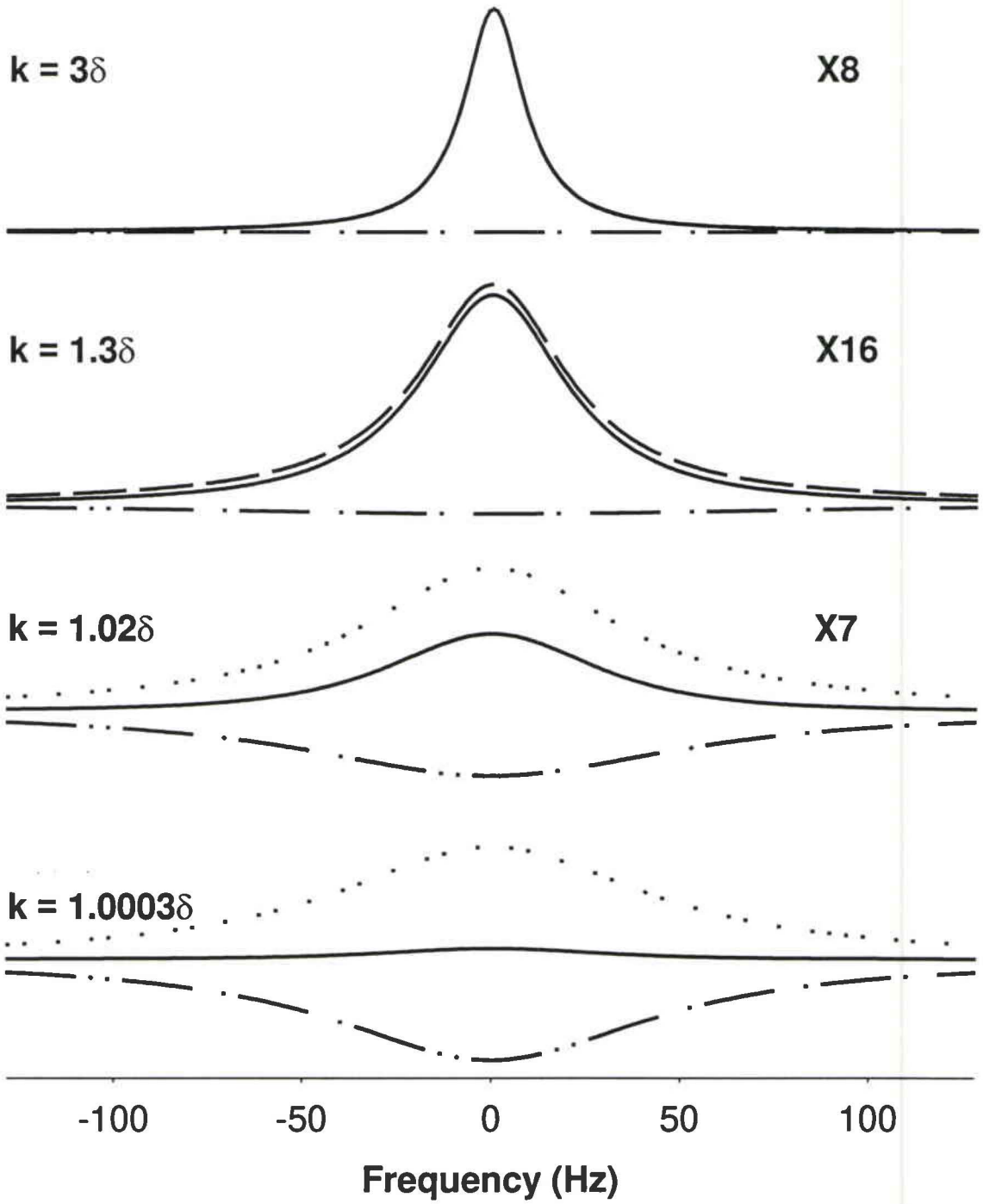

Figure 2.8 Lineshapes in the intermediate- to fast-exchange regimes. The lineshape is composed of two line 180^0 out of phase. As the rate increases one line narrows, while the other one broadens until it effectively disappears. The rate, k, is given as a multiple of the frequency difference, δ.

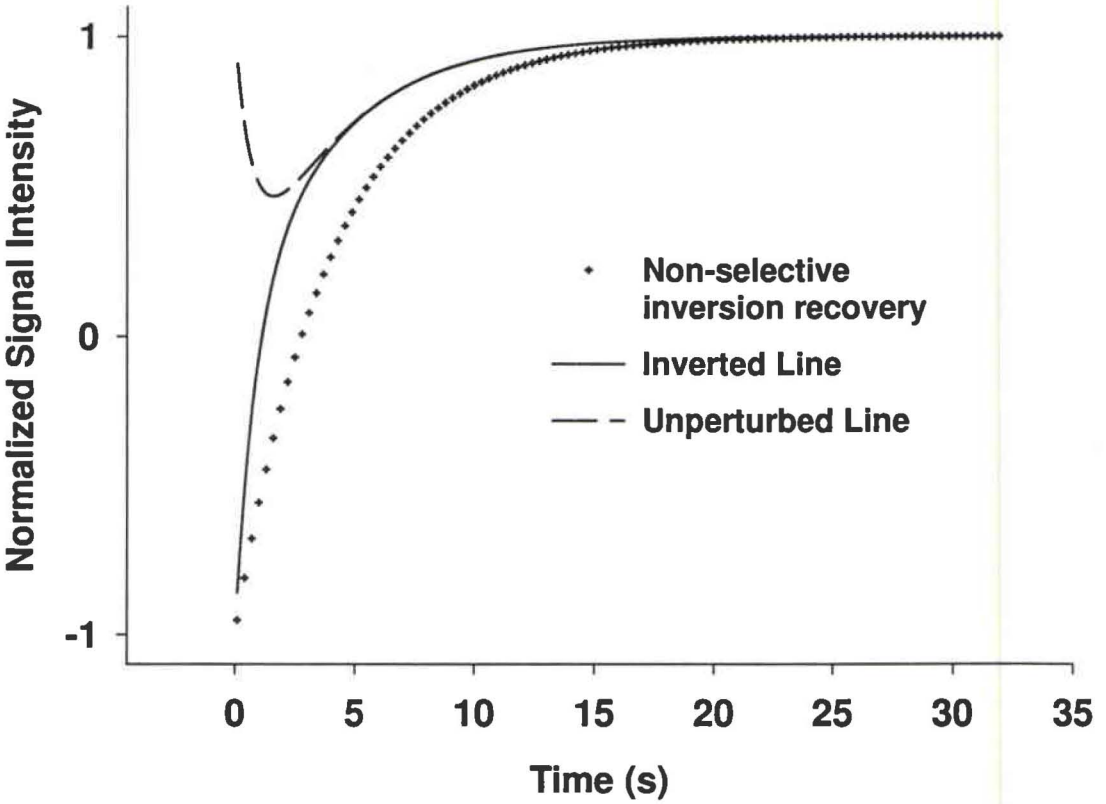

Figure 2.9 Two-site equally-populated selective inversion. The inverted line (solid) relaxes more rapidly than the non-selectively inverted line (cross hairs). Notice that the unperturbed line (dashed line) exhibits a transient response. The exchange rate is 0.5 s^{-1} the relaxation time is 4 s.

Therefore, with the initial conditions above we get,

$$\rho_0^1(t) = \left[1 - \exp\left(-t/T_1\right) - \exp\left(-\left[2k + 1/T_1\right]t\right)\right][M_o]$$
$$\rho_0^2(t) = \left[1 - \exp\left(-t/T_1\right) + \exp\left(-\left[2k + 1/T_1\right]t\right)\right][M_o] \tag{2.54}$$

which implies that the inverted spin relaxes via both the exchange and spin-lattice relaxation.(see figure 2.9) Notice also that exchange between the inverted and non-inverted magnetisation, causes a transient response in the non-inverted line.

Solid State NMR

The spectral parameters in the Hamiltonian, in general, depend on orientation in some fashion.[62,63] For instance the degree of shielding that a nucleus experiences depends on the orientation of the surrounding electron density with the magnetic field. The dipole-dipole interaction depends on the relative orientation of the two nuclei involved. Thus the spectrum is different for each orientation. For powder samples the spectra of each crystal orientation contributes to the total spectrum, giving rise to broad envelopes, called powder patterns.(see figure 2.10)

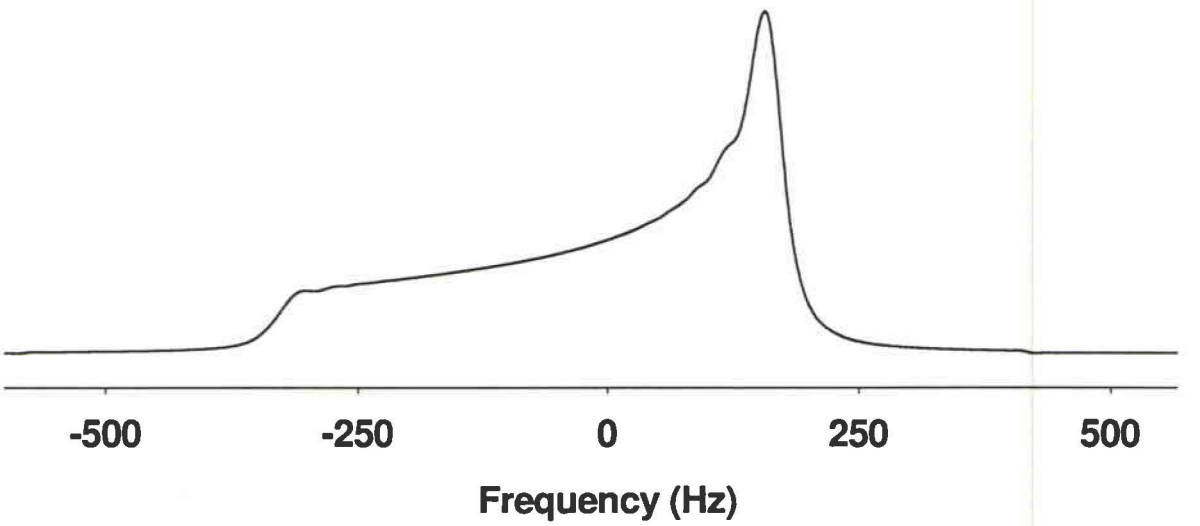

Figure 2.10 Powder pattern for a cylindrically-symmetric chemical shielding tensor.

Each interaction in the Hamiltonian has a corresponding tensor, $\mathbf{R}$, where the term has the general form[62]

$$\mathbf{H} = C\,\mathbf{I}\cdot\mathbf{R}\cdot\mathbf{A}, \tag{2.55}$$

Here, **I** and **A** are vector operators, and C is a combination of appropriate physical constants. For instance, the degree of shielding at the nucleus can be determined along three mutual orthogonal directions. These directions and shielding parameters are sufficient to describe the shielding with respect to any orientation with the field. Thus the shielding term in the Hamiltonian becomes[62]

$$\mathbf{H} = \gamma\hbar(\mathbf{I} \cdot \sigma \cdot \mathbf{B}). \tag{2.56}$$

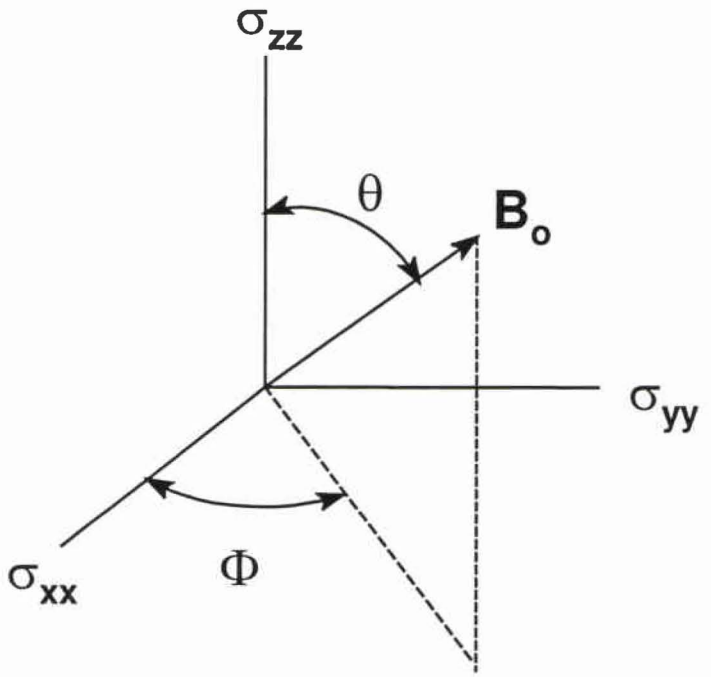

Figure 2.11 Coordinates of the magnetic field as seen in the principal axis system (PAS) of the chemical shielding tensor.

The shielding tensor is diagonal in the principal axis representation, where it has principal components, σ_{xx}, σ_{yy}, σ_{zz} and the relative orientation with the laboratory frame is given by three Euler angles, α, β, γ. Alternatively, the magnetic field direction in this

frame can be described by the polar angles θ and Φ, as seen in figure 2.11. The z component of the CSA tensor in the laboratory frame is given by[62]

$$\begin{aligned}\sigma_{zz}^{Lab} &= \sigma_{xx}\sin^2\theta\cos^2\phi + \sigma_{yy}\sin^2\theta\sin^2\phi + \sigma_{zz}\cos^2\theta \\ &= \sigma_{iso} + \frac{\sigma_{zz}-\sigma_{iso}}{2}(3\cos^2\theta - 1) + \frac{1}{2}\eta\sigma_{zz}\sin^2\theta\cos 2\phi\end{aligned} \tag{2.57}$$

where $\sigma_{iso} = Tr[\sigma]/3$ and $\eta = (\sigma_{xx} - \sigma_{yy})/\sigma_{zz}$, are the isotropic component and asymmetry parameter of the CSA tensor, respectively.

Dipole-dipole interactions involve two spins and depend on the orientation of their internuclear vector, $\mathbf{r}_{jk}$. The energy of two interacting magnetic dipoles is given as[62,68]

$$E_D = \frac{\mu_o}{4\pi}\left[\frac{\mu_j \cdot \mu_k}{r_{jk}^3} - \frac{3(\mu_j \cdot \mathbf{r}_{jk})(\mu_k \cdot \mathbf{r}_{jk})}{r_{jk}^5}\right], \tag{2.58}$$

where μ_i's are the dipole moments. The corresponding term in the Hamiltonian is of the form

$$\mathbf{H} = \frac{\gamma_j\gamma_k\hbar^2}{r_{jk}^3}\frac{\mu_o}{4\pi}(\mathbf{I}_j \cdot \mathbf{D} \cdot \mathbf{I}_k) = K(\mathbf{I}_j \cdot \mathbf{D} \cdot \mathbf{I}_k), \tag{2.59}$$

where $\mathbf{D}$ is the dipole tensor, which is of the form

$$\mathbf{D} = \frac{1}{r^2}\begin{bmatrix}(r^2-3x^2) & -3xy & -3xz \\ -3xy & (r^2-3y^2) & -3yz \\ -3xz & -3yz & (r^2-3z^2)\end{bmatrix} \tag{2.60}$$

Using spherical polar coordinates the Hamiltonian can be expressed in what is commonly referred to as the dipolar alphabet[57]

$$\mathbf{H} = K(A + B + C + D + E + F) \tag{2.61}$$

where A to F are combinations of spin and spatial operators. For homonuclear spin systems in a strong magnetic field, this Hamiltonian in commonly truncated to include only the terms that commute with the Zeeman term, A and B, given in eqn. (2.61).

$$\begin{aligned} A &= \mathbf{I}_z^j \mathbf{I}_z^k (3\cos^2\theta - 1) \\ B &= \frac{1}{4}\left[\mathbf{I}_+^j \mathbf{I}_-^k + \mathbf{I}_-^j \mathbf{I}_+^k\right](3\cos^2\theta - 1) \end{aligned} \tag{2.62}$$

The Hamiltonian in the solid state also contains terms due to indirect coupling, J, and quadrupolar coupling. The indirect coupling is often not observed in solids, since such interactions are small on the frequency scale of these experiments. The quadrupolar-interaction[69] is a self-coupling term, where the electric quadrupole moment of the nucleus interacts with the electric field gradient at the nucleus. The quadrupole-coupling interaction will not be considered in this work since a proper treatment requires a combined Zeeman-quadrupolar interaction frame, further complicating the problem.

Magic angle spinning

The broad featureless bands of powder samples can be converted to a series of narrow side bands by spinning the sample at a certain angle with respect to the magnetic field - as in figure 2.12. This angle is called the magic angle and is equal to $\cos^{-1}[(1/3)^{1/2}]$, which effectively removes the leading orientationally-dependent terms, in equations (2.57) and (2.62).[70-72] In other words, spinning rapidly (faster than the frequency scale of the interaction) at this angle, effectively averages the angle θ to the magic angle for all orientations (see R. K. Harris appendix 5).[57] Often the spinning speed required to achieve this averaging effect can not be attained. Consequently, a side band pattern emerges, with line spacing equal to the spinning speed (see figure 2.13). The intensity patterns of these side bands depend on the tensor parameters.

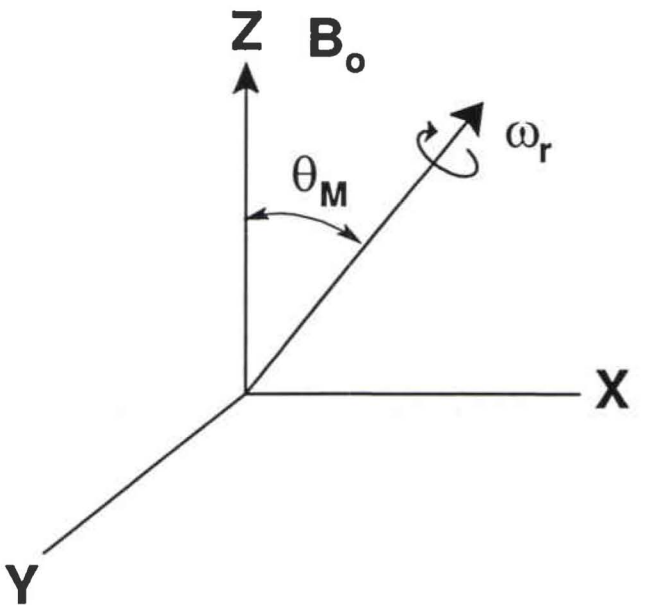

Figure 2.12 Magic angle spinning shown in the laboratory frame. $\mathbf{B_o}$ is along the z-axis, rotation axis make and angle with the z-axis which is the magic angle, θ_M. The spinning speed is ω_r

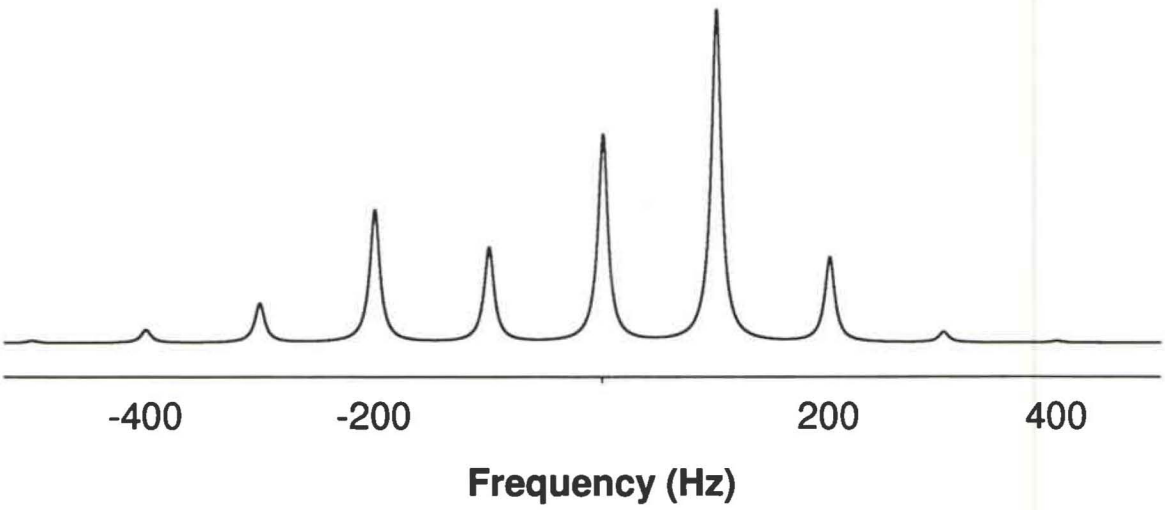

Figure 2.13 The MAS spectrum of the powder pattern shown in figure 2.10, where the spinning speed in 100 Hz.

It is generally convenient to work in the laboratory frame, in the interaction representation where the orientation of **B** determines the axis of quantisation and the Zeeman term is eliminated. However for this treatment a transformation to the rotor frame is required, where the spinning axis becomes the z-axis. In this frame rotation is expressed around the z-axis by the Euler angle α. The α dependence of the Hamiltonian is due to the α dependence of its constituent tensors. In the case of tensor **M** (a generic tensor which could be CSA, dipole-dipole coupling, *etc*), the α dependence can be expressed as[73]

$$\mathbf{M}(\alpha) = \mathbf{R}(\alpha)\mathbf{M}\mathbf{R}(\alpha)^{T} \tag{2.63}$$

where **R**(α) is the rotation matrix

$$\mathbf{R}(\alpha) = \begin{pmatrix} \cos\alpha & -\sin\alpha & 0 \\ \sin\alpha & \cos\alpha & 0 \\ 0 & 0 & 1 \end{pmatrix}.$$

It is convenient to express $\mathbf{R}(\alpha)$ as

$$\begin{aligned} \mathbf{R}(\alpha) &= \begin{pmatrix} 0 & 0 & 0 \\ 0 & 0 & 0 \\ 0 & 0 & 1 \end{pmatrix} + \frac{e^{i\alpha}}{2}\begin{pmatrix} 1 & i & 0 \\ -i & 1 & 0 \\ 0 & 0 & 0 \end{pmatrix} + \frac{e^{-i\alpha}}{2}\begin{pmatrix} 1 & -i & 0 \\ i & 1 & 0 \\ 0 & 0 & 0 \end{pmatrix} \\ &= A + e^{i\alpha}B + e^{-i\alpha}B^T \end{aligned} \tag{2.64}$$

Placing eqn. (2.64) into eqn. (2.63) the five term Fourier series is derived for $\mathbf{M}(\alpha)$.

$$\mathbf{M}(\alpha) = \sum_{j=-2}^{2} \mathbf{M}_j e^{ij\alpha}$$

where

$$\mathbf{M}_0 = \begin{pmatrix} (M_{11}+M_{22})/2 & 0 & 0 \\ 0 & (M_{11}+M_{22})/2 & 0 \\ 0 & 0 & M_{33} \end{pmatrix}, \tag{2.65}$$

$$\mathbf{M}_{\pm 1} = \begin{pmatrix} 0 & 0 & (M_{31} \pm iM_{32})/2 \\ 0 & 0 & (M_{32} \mp iM_{31})/2 \\ (M_{31} \pm iM_{32})/2 & (M_{32} \mp iM_{31})/2 & 0 \end{pmatrix} \tag{2.66}$$

and

$$\mathbf{M}_{\pm 2} = \begin{pmatrix} (M_{11} - M_{22} \pm 2iM_{12})/4 & (\mp i(M_{11} - M_{22}) + 2M_{12})/4 & 0 \\ (\mp i(M_{11} - M_{22}) + 2M_{12})/4 & (-M_{11} + M_{22} \mp 2iM_{12})/4 & 0 \\ 0 & 0 & 0 \end{pmatrix} \tag{2.67}$$

are given in terms of the elements of $\mathbf{M}$. The Fourier components can be evaluated in this manner for each term of the Hamiltonian and separately accumulated to construct the Fourier components of the full Hamiltonian. This is possible because the Hamiltonian is linear in its constituent tensors. These Fourier components can be separately transformed back to the Zeeman frame for use in simulation.

Conclusions

The purpose of this chapter was to give an overview of the basic concepts of NMR to a reader that is not familiar with the subject. The intention was to start with the basic ideas of magnetic resonance and build up to a time-dependent-quantum-mechanical treatment, required for chemical exchange. It also served to outline the particular formalisms and notation to be used in the following work. The concept of MAS was only introduced in a precursory fashion, since it will be more thoroughly developed in chapter 8. There the reader will be introduced to Floquet theory, which is adapted to a time dependent-quantum-mechanical approach to simulating chemical exchange in solids undergoing MAS. Theoretical concepts other than those related to NMR will be introduced where they are applied.

References

1) Bloch, F.; Hansen, W.W.; Packard, M.E. *Phys.Rev.* **1946**, *69*, 127-127.

2) Bloch, F. *Phys.Rev.* **1946**, *70*, 460-474.

3) Bloch, F.; Hansen, P.E.; Packard, M.E. *Phys.Rev.* **1946**, *70*, 474-485.

4) Purcell, E.M.; Torrey, H.C.; Pound, R.V. *Phys.Rev.* **1946**, *69*, 37-38.

5) Arnold, J.T.; Dharmatti, S.S.; Packard, M.E. *J.Chem.Phys.* **1951**, *19* , 507-507.

6) Dickinson, W.C. *Phys.Rev.* **1950**, *77*, 736-737.

7) Proctor, W.G.; Yu, F.C. *Phys.Rev.* **1950**, *77*, 717-717.

8) Gutowsky, H.S.; McCall, D.W.; Slichter, C.P. *Phys.Rev.* **1951**, *84*, 589-590.

9) Hahn, E.L.; Maxwell, D.E. *Phys.Rev.* **1951**, *84*, 1246-1247.

10) Gutowsky, H.S.; McCall, D.W.; Slichter, C.P. *Phys.Rev.* **1951**, *84*, 589-590.

11) Gutowsky, H.S.; McCall, D.W.; Slichter, C.P. *J.Chem.Phys.* **1953**, *21*, 279-292.

12) Gutowsky, H.S.; Saika, A. *J.Chem.Phys.* **1953**, *21*, 1688-1694.

13) Gutowsky, H.S.; Holm, C.H. *J.Chem.Phys.* **1956**, *25*, 1228-1234.

14) McConnell, H.M. *J.Chem.Phys.* **1958**, *28*, 430-431.

15) Hahn, E.L.; Maxwell, D.E. *Phys.Rev.* **1952**, *88*, 1070-1084.

16) Piette, L.H.; Anderson, W.A. *J.Chem.Phys.* **1959**, *30*, 899-908.

17) Loewenstein, A.; Connor, T.M. *Berichte der Bunsen-Gesellschaft* **1963**, *67*, 280-295.

18) Sack, R.A. *Mol.Phys.* **1958**, *1*, 163-167.

19) Fano, U. *Rev.Mod.Phys.* **1957**, *29*, 74-93.

20) Kaplan, J.I. *J.Chem.Phys.* **1958**, *28*, 278-282.

21) Alexander, S. *J.Chem.Phys.* **1962**, *37*, 967-974.

22) Alexander, S. *J.Chem.Phys.* **1962**, *37*, 974-980.

23) Lynden-Bell, R.M. *Prog.Nucl.Magn.Reson.Spectrosc.* **1967**, *2*, 163-204.

24) Buckley, P.D.; Jolley, K.W.; Pinder, D.N. *Prog.Nucl.Magn.Reson.Spectrosc.* **1975**, *10*, 1-26.

25) Johnson, C.S. *Advances in Magnetic Resonance* **1965**, *1*, 33-102.

26) Pyper, N.C. *Mol.Phys.* **1971**, *21*, 1-33.

27) Szymanski, S.; Witanowski, M.; Gryff-Keller, A.M.In *Annual reports on NMR spectroscopy*; Webb, G.A., Ed.; Academic Press: London, 1978; pp 227-289.

28) Kleier, D.A.; Binsch, G. *J.Magn.Reson.* **1970**, *3*, 146-160.

29) Binsch, G. *J.Am.Chem.Soc.* **1969**, *91*, 1304-1309.

30) Reeves, L.W.; Shaw, K.N. *Can.J.Chem.* **1970**, *48*, 3641-3653.

31) Banwell, C.N.; Primas, H. *Mol.Phys.* **1963**, *6*, 225-256.

32) Bain, A.D.; Fletcher, D.A.; Hazendonk, P. *Concepts Magn.Reson.* **1998**, *10*, 85-98.

33) Bain, A.D.; Duns, G.J. *Can.J.Chem.* **1996**, *74*, 819-824.

34) Bain, A.D.; Duns, G.J. *J.Magn.Reson.* **1995**, *112 A*, 258-260.

35) Forsen, S.; Hoffman, R.A. *J.Chem.Phys.* **1963**, *39*, 2892-2901.

36) Forsen, S.; Hoffman, R.A. *J.Chem.Phys.* **1964**, *40*, 1189-1196.

37) Dahlquist, F.W.; Longmuir, K.J.; DuVernet, R.B. *J.Magn.Reson.* **1975**, *17*, 406-410.

38) Gesmar, H.; Led, J.J. *J.Magn.Reson.* **1986**, *68*, 95-101.

39) Muhandiram, D.R.; McClung, R.E.D. *J.Magn.Reson.* **1987**, *71*, 187-192.

40) Bain, A.D.; Cramer, J.A. *J.Magn.Reson.* **1993**, *103 A*, 217-222.

41) Bain, A.D.; Cramer, J.A. *J.Phys.Chem.* **1993**, *97*, 2884-2887.

42) Bain, A.D.; Cramer, J.A. *J.Magn.Reson.* **1996**, *118 A*, 21-27.

43) Hahn, E.L. *Phys.Rev.* **1950**, *80*, 580-594.

44) Carr, H.Y.; Purcell, E.M. *Phys.Rev.* **1954**, *94*, 630-638.

45) Meiboom, S.; Gill, D. *Review of Scientific Instruments* **1958**, *29*, 688-691.

46) Woessner, D.E. *J.Chem.Phys.* **1961**, *35*, 41-48.

47) Allerhand, A.; Gutowsky, H.S. *J.Chem.Phys.* **1965**, *42*, 1587-1599.

48) Bax, A.; Freeman, R. *J.Magn.Reson.* **1981**, *44*, 542-561.

49) Allerhand, A.; Gutowsky, H.S. *J.Chem.Phys.* **1965**, *42*, 4203-4212.

50) Gutowsky, H.S.; Vold, R.L.; Wells, E.J. *J.Chem.Phys.* **1965**, *43*, 4107-4126.

51) Bain, A.D.; Duns, G.J. *J.Magn.Reson.* **1994**, *109 A*, 56-64.

52) Jeener, J.; Meier, B.H.; Bachmann, P.; Ernst, R.R. *J.Chem.Phys.* **1979**, *71*, 4546-4553.

53) Macura, S.; Huang, Y.; Suter, D.; Ernst, R.R. *J.Magn.Reson.* **1981**, *43*, 259-281.

54) Johnston, E.R.; Dellwo, M.J.; Hendrix, J. *J.Magn.Reson.* **1986**, *66*, 399-409.

55) Perrin, C.L.; Engler, R.E. *J.Magn.Reson.* **1996**, *123 A*, 188-195.

56) Pauli, W. *Naturwiss.* **1924**, *12*, 741

57) Harris, R.K.*Nuclear Magnetic Resonance Spectroscopy*; Pitman Books Limited: London, 1983;

58) Pople, J.A.; Schneider, W.G.; Bernstein, H.J.*High-Resolution Nuclear Magnetic Resonance*; McGraw-Hill Book Company, Inc.: New York, 1959;

59) Karplus, M. *J.Am.Chem.Soc.* **1963**, *85*, 2870-2871.

60) Ernst, Richard R., Bodenhausen, Geoffrey, and Wokaun, Alexander. Principles of nuclear magnetic resonance in one and two dimensions. 202-205. 1987. Oxford, Oxford University Press.

61) Jackman, L.M.; Cotton, F.A.*Dynamic Nuclear Magnetic Resonance Spectroscopy*; Academic Press: New York, 1975;

62) Munowitz, M.*Coherence and NMR*; John Wiley & Sons: New York, 1988;

63) Mehring, M.*Principles of High Resolution NMR in Solids*; Springer-Verlag: Berlin, 1983;

64) Maricq, M.M.; Waugh, J.S. *J.Chem.Phys.* **1978**, *70*, 3300-3316.

65) Bain, A.D. *Prog.Nucl.Magn.Reson.Spectrosc.* **1988**, *20*, 295-315.

66) Bain, A.D.In *Encyclopedia of Spectroscopy and Spectrometry*; Lindon, J., Tranter, G., Holmes, J., Eds.; Academic Press: London, 1999;

67) Bain, A.D.In *Encyclopedia of Chemical Physics and Physical Chemistry*; Moore, J.H., Spencer, N.D., Eds.; Institute of Physics: Philadelphia, 1999;

68) Pake, G.E. *J.Chem.Phys.* **1948**, *16*, 327-336.

69) Pound, R.V. *Phys.Rev.* **1950**, *79*, 685-702.

70) Lowe, I.J. *Phys.Rev.Lett.* **1959**, *2*, 285-287.

71) Andrew, E.R.; Newing, R.A. *Proc.Phys.Soc.A* **1958**, *72*, 959-972.

72) Andrew, E.R.; Bradbury, A.; Eades, R.G. *Nature (London)* **1958**, *182* , 1659-1659.

73) Hazendonk, P.; Dumont, R.S.; Grondey, H.; Harrison, P.H.M.; Bain, A.D. *J.Magn.Reson.*, submitted.

Part I

Accurate Activation Parameters for Dynamic Processes Studied by NMR Using a Three-Experiment Approach.

Overview

NMR is one of the most common methods employed in measuring energetic barriers to dynamic processes in molecules. Various experiments have been developed to measure chemical exchange rates based on T_1 and T_2 methods, spectral simulation, or two-dimensional techniques. Each technique is optimal to a given range of rates, and thus should be applied between specific temperature limits. Many studies employ just one type of experiment, thereby constraining rate data to a narrow temperature range, thus compromising the accuracy of the activation parameters derived from them.

The temperature range over which rate measurements are made can be increased by using a combination of techniques, where each is optimum for a particular rate regime. In the slow exchange regime, the exchange rate is of the same order of magnitude as the spin-lattice relaxation rate, $1/T_1$, and thus can be determined by modelling the relaxation dynamics of the spin system. When the rate is of the same order as the frequency difference between the lines in question, the appearance of the line becomes strongly dependent on the exchange rate. In this case it is best to simulate the spectrum to measure the rate. After

coalescence, when the spectral lines become narrow, the exchange rate is best determined by measuring T_2. An accurate way to do this is the modelling of the saturation behaviour of the spectral line as a function of the resonance off-set. This gives a value for T_2 independent of coherent dephasing mechanisms.

Using the combination of selective inversion, lineshape analysis and off-resonance saturation it is possible to measure rates over as many as six orders of magnitude. The selective inversion experiment provides rates where lineshape methods would normally overestimate them due to linebroadening factors. Similarly, these linebroadening factors cause lineshape analysis to underestimate rates in the fast exchange regime. The off-resonance saturation experiment gives T_2's which are insensitive to these effects and lead to more accurate rates. As a result, accurate rates are now available in the slow, intermediate and fast exchange regime. Consequently, the temperature range is extended to a point at which the free energy can be confidently separated into its contributions from enthalpy and entropy. The error in these activation parameters are, *ca.* 1 $kJmol^{-1}$ for $\Delta H^{\dagger}$ and *ca.* 6 $Jmol^{-1}K^{-1}$ for $\Delta S^{\dagger}$.

The literature contains many barriers that are reported as free energies, but these are very difficult to compare with enthalpies available from computations. Many of these barriers are of unimolecular processes. The activation entropy is assumed to be insignificant and thereby the free energy is equated to the enthalpy. Is this a valid assumption in the liquid phase? Even if there is no significant activation entropy inherent to the molecule, is it valid to assume that the entropy change of the solvent is not important?

The study in chapter 3 attempts to tackle this question by characterising the effect of

solvent on the internal rotational barrier of the aldehyde group on furfural. Using this three experiment approach, rates were measured over temperatures ranging from 190 K to 310 K in three solvents. The solvents were chosen to be different in the way they interact with the solute. For example, toluene is an aprotic solvent with a small dielectric constant. On the other hand, acetone and methanol have large dielectric constants, and could potentially participate in some type of direct interaction with the solute owing to their large dipole moments and ability to form hydrogen bonds. The enthalpy of activation obtained from experiment was compared to the results of the molecular orbital calculations, which include the solvent effect via the Onsager's reaction field model, and Tomasi's polarized continuum model. The activation entropies are discussed in terms of solvent-solute interactions.

Substituent effects on rotational barriers are often small, and thus accurate rate measurements are required to obtain reliable energy differences between barriers. These in turn can be compared with calculations. Significant contributions from activation entropies make these comparisons difficult, especially in the solution phase. Recent theoretical work has suggested that the origin of the barrier in amides resides in the energetics of the nitrogen pyramidalisation, rather than being due to the loss of resonance stabilisation between the oxygen and the nitrogen. In other words, it should be thought of as a nitrogen inversion rather than a hindered rotation. Chapter 4 details a study performed on a series of seven substituted, spirofused oxadiazolines. Exchange rates were measured over large temperature ranges and barriers were obtained for all seven derivatives in two solvents. The barriers for three derivatives were computed, and compared with the enthalpies of activation. The electron density functions were analysed using Atoms in Molecules

methods. The substituent effect on the barrier is discussed in terms of these atomic contributions to the barrier and the redistribution of electrons between O, N and C.

Careful rate measurements over a large temperature range have allowed the determination of small, statistically significant activation entropies. Those reported in the following two chapters are the most accurate to date, by NMR methods. These measurements have shed some light in yet-not-fully-understood contributions of small activation entropies, from either solvent or inherent to the molecule, on rotational barriers of small molecules.

Chapter 3

Solvent Effects on the Internal Rotational Barrier in Furfural. NMR Measurements and *Ab-Initio* Molecular Orbital Methods Using Continuum Models.

(Based on an article by A. D. Bain and P. Hazendonk published in the Journal of Physical Chemistry volume 101A pages 7182 to 7188 in 1997.[1])

Introduction

Rotations of chemical bonds in molecules are seldom "free". In other words there is always some barrier to rotation, which can furthermore depend on solvent. Studies into the effects of solvent on these processes are primarily concerned with experimental measurements or computational predictions. Measurements are achieved mainly by nuclear magnetic resonance (NMR), microwave and infrared (IR) spectroscopies. Barriers are computed using molecular orbital calculations of the solute in the presence of the reaction field due to the solvent. The main aim of this study is the comparison of the most recent methods of measurement with prediction, on a sample system.

Usually NMR rate measurements are made with lineshape fitting procedures.[2-10] Due to limits on the temperature range over which rate measurements can be made, barriers are often reported as $\Delta G^{\dagger}$.[9,11-15] To compare these barriers with calculations, which give $\Delta H^{\dagger}$, $\Delta S^{\dagger}$ is often assumed to be zero.[9,16] This assumption is not unreasonable since these are unimolecular processes. However, there are cases where $\Delta S^{\dagger}$ is experimentally observed to be significantly non-zero.[17,18]

Calculations of internal rotational barriers in solvent usually include continuum models,[19-22] which compute the electrostatic contribution to the free energy of solvation. The total energy is just a combination of the free energy of solvation with the gas phase energy. To make the model more complete, the electrostatic solvation energy is often accompanied by contributions from cavitation and dispersion energies.[21,23] Recently the electrostatic interaction has been incorporated into the Fock operator of the solute, including it in the self-consistent cycles which optimise the electron density, thus allowing the solute to be polarized by the solvent field.[24-26] Second derivatives of this Self-Consistent Reaction Field energy, with respect to the nuclear coordinates, are now readily determined, making transition state searches and frequency calculations possible.[27,28] With these developments, barriers in liquid phase are as readily obtained as in gas phase, with some additional computational effort. It should be stressed however that these methodologies do not account for direct solute-solvent interactions.

In order to obtain good experimental values of $\Delta H^{\dagger}$ and $\Delta S^{\dagger}$, rate measurements are needed over as wide a range as possible. Recently this laboratory developed a technique which employs three complementary NMR experiments.[6,8,29-33] These, when combined, are capable of generating rate data over 6 orders of magnitude, corresponding to temperature ranges ca. 150°C. Measurements made on furfural in acetone revealed that the $\Delta H^{\dagger}$ was much smaller than previously seen in polar solvents and a large negative $\Delta S^{\dagger}$ was observed.[30] The Gibbs free energy of activation ,$\Delta G^{\dagger}(298)$, was in line with the previous experimental and theoretical studies. Consequently, the assumption that the entropy of activation is zero is not always justified and thus the direct interpretation of $\Delta G^{\dagger}$ as $\Delta H^{\dagger}$ can

be misleading.

This study will compare barriers calculated by recently developed computational methodologies with those measured by the most accurate NMR methods for furfural in toluene, acetone and methanol. Measurements will be carried out with the three NMR experiment technique, and computations will employ Self-Consistent Reaction Field (SCRF) methods using the Onsager[24-26] and Tomasi's Isodensity surface Polarised Continuum (IPC) models.[34,35] The importance of considering $\Delta S^{\dagger}$ will be discussed.

Methodology

Rate measurements

The most common way to measure rates by NMR involves lineshape methods. The rates so obtained are only accurate when the lineshape in question is broad,[9,29,30] which occurs only when the line width is dominated by the contribution from exchange, with other line broadening factors being small or negligible by comparison. In the extreme ranges of measurement, both when the rates are slow and fast, the lines are narrow, thus linebroadening factors become significant.[36] As a result the rates may be overestimated in the slow- and underestimated in the fast-exchange regimes, giving rise to systematic errors in $\Delta H^{\dagger}$ and $\Delta S^{\dagger}$. Therefore it is necessary to make additional measurements in the slow- and fast-exchange regimes, which are independent of these broadening effects.

In the slow-exchange regime, where the conformer life-time is of the same order of magnitude as the spin-lattice relaxation times of the observed nuclei, the rate can be measured using the selective inversion experiment.[32,33,37,38] The line corresponding to one

site is inverted selectively, and the relaxation of both lines is observed. The exchange rate can be extracted by fitting the data to the set of differential equations which describe the relaxation and exchange behaviour.

In the fast exchange regime T_2 is measured independently of the magnetic field inhomogeneities using the offset-saturation experiment.[31] The decoupler is tuned near the spectral line, which is irradiated for a period long enough to establish a steady state. After a short delay an FID is acquired. A plot of the partially saturated line intensity as a function of offset frequency exhibits a dip,[39] when approaching resonance, whose width at half depth is $\gamma B_2(T_1/T_2)^{1/2}$. With independent measurements of T_1 and the γB_2, T_2 can be determined, which in turn is directly related to the rate.[4]

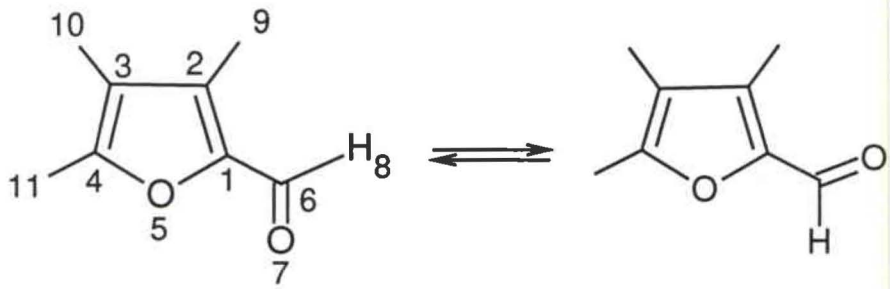

O,O-*cis* O,O-*trans*

Figure 3.1 Isomerisation of Furfural between its O,O-*cis* to O,O-*trans* froms.

Solvent calculations

The barrier to interconversion between the O,O-*cis* and O,O-*trans* forms of furfural (figure 3.1) will be computed in gas and solvent phase up to mp2/6-31g** level. With both the gas phase and SCRF calculations, the transition state geometries will be determined at saddle points in the energy surface with respect to the reaction coordinates. The SCRF techniques will employ the Onsager and the IPC models. Both these models assume the solute is in a cavity of a given shape which is surrounded by a polarisable continuous medium with dielectric constant ε.[19-22,24-26,40] The solute electron density polarises the medium, causing the medium to impose an inhomogeneous electric field onto the solvent, leading to a net stabilisation. The reaction field can polarise the solute, altering the electric field it produces which in turn changes the reaction field itself, and so on, leading to higher order corrections to the solvation energy. The two solvent models differ mainly in the way the reaction field is modelled.

The Onsager model assumes a perturbation to the Hamiltonian of the isolated solute molecule based on the interaction energy between the molecular dipole (**μ**) and the reaction field (**R**), $\mathbf{H_1} = -\boldsymbol{\mu}\cdot\mathbf{R}$.[24] The reaction field is related to the molecular dipole and the cavity radius (a_o) as:

$$R = g\mu \;\; ; \;\; g = \frac{2\,(\varepsilon - 1)}{(2\varepsilon + 1)a_o^3} \tag{3.1}$$

The cavity radius is usually based on the molar volume of the solute. The interaction energy term can be included directly into the Fock matrix as:

$$F_{\lambda\sigma} = F^o_{\lambda\sigma} - g\,\mu < \phi_\lambda \mid \mu \mid \phi_\sigma > \tag{3.2}$$

where ϕ_λ and ϕ_σ are basis functions.[24] In SCRF calculations the molecular dipole moment is not computed as an expectation value, but is computed as a derivative of the solute energy with respect to a uniform electric field.[24] The total energy including the contribution due to solvent polarization is:

$$E = < \Psi \mid H_o \mid \Psi > - \frac{1}{2} \mu \cdot R \tag{3.3}$$

where Ψ is the full wave function. First and second order energy derivatives with respect to nuclear coordinates are easily obtained for geometry optimisations and transition state searches.[27]

The implementation of the Tomasi model considered in this study is based on the Apparent Surface Charge approach.[20] Initially the electric field, $\mathbf{E_s}$, from the solute charge density induces a dipole density distribution **P(r)** in the continuum.[22]

$$P(r) = (1 - \varepsilon)\, E\,(r) = (1 - \varepsilon)(E_s\,(r) + E_p(r)) \tag{3.4}$$

where **E(r)** is the total electric field at **r** including the contribution from the dipoles themselves. Gauss's law is applied such that the potential from the solvent dipole field can be described as arising from a charge density on the surface of the cavity by:

$$\sigma(r_s) = -\frac{(\varepsilon - 1)}{4\pi\varepsilon} [E_o(r_s) + E_p\,(r_s)] \cdot n\,(r_s) \tag{3.5}$$

where $\mathbf{n(r_s)}$ is the vector normal to the cavity surface at a point on the surface $\mathbf{r_s}$.[21] The potential from this surface charge distribution is included in the solute Hamiltonian, $\mathbf{H_0}$, for Self Consistent Isodensity Polarised Continuum calculations. In equation (3.6) the

Hamiltonian is made up of three parts, the isolated solute molecule Hamiltonian, $\mathbf{H_o}$, the contribution of the solute electron density, and nuclei to the reaction field potential.[34]

$$H = H_o - \sum_i \oint \frac{\sigma_p(r_s)\, dr_s}{|r_i - r_s|} + \sum_n Z_n \oint \frac{\sigma_p(r_s)\, dr_s}{|R_n - r_s|} \tag{3.6}$$

The Onsager method is simpler than the Tomasi method, and is not expected to be as accurate. It restricts the electrostatic energy to the dipole-induced-dipole contribution and ignores higher order terms.[20] Due to its simplicity, its main advantage is that computations can be performed quickly. Its main disadvantage is that its conventional implementation is restricted to using spherical and ellipsoidal cavity shapes. The results are also dependent on cavity dimensions, often making interpretation of the results arbitrary.[24] The Tomasi model includes the higher-order electrostatic terms, therefore it should give more accurate electrostatic contributions to the solvation energy.[20] Its main disadvantage is that it requires much more computational effort than the Onsager method, needing as much as 50% additional cpu time.[34] Its main advantage is its ability to use arbitrary cavity shapes, reflecting the actual structure of the solute. Despite the different advantages and disadvantages of both methods, both performed equally well in studies into the solvent effect on the *gauche-trans* ratios of 1,2-dichloro-ethane.[24,34]

A brief overview of the literature on furfural

Experiments on furfural have focused mainly on the relative conformer stabilities.[41-64] After some initial confusion,[61] the O,O-*trans* form was seen to predominate in gas phase[59] and a transition occurs to the O,O-*cis* in media with ε greater than 5 C^2/Nm^2.[23,41,44,47,58,64] Theoretical studies employing both classical reaction field and SCRF methodologies reproduce this trend closely.[23,24,58,63,64] The gas phase energy difference is 6.3 kJ/mol.[64]

Measurements of the barrier in furfural are rare. To date barriers are known only in the gas phase and a few solvents. Microwave experiments by Mönnig and infrared measurements by Miller gave gas phase barriers of 34 and 25 kJ/mol, respectively.[60] In solution they are 44 kJ/mol for dimethyl ether, 46 kJ/mol for neat solution.[64] Studies predicting this barrier in solvent are restricted to Abraham and Siverns,[64] Birnstock,[23] Benassi,[63] and In-Suk Han,[65] who found that the barriers increased with increasing dielectric constant, as was seen experimentally. The results of Abraham and Han agree closely with experiment. Bennassi's analysis, which includes contributions from cavitation and dispersion energies, overemphasises this effect tremendously. Birstock's approach, similar to that of Bennasi's, predicts a barrier around 50.2 kJ/mol in tetrachloromethane [23], which is large compared to 43.9 kJ/mol measured in dimethyl ether. The more recent study by Han use single point Onsager SCRF calculations with mp2/6-31+g** geometries giving barriers of 38.6 kJ/mol in gas phase, and 46.8 kJ/mol in a medium with ε = 78.54 C^2/Nm^2.

Experimental

Furfural was purchased from Aldrich and was used without further purification. Samples, of approximately 5 mol. %, were prepared in toluene-d_8, acetone-d_6, and methanol-d_4. These were degassed with 5 freeze-pump-thaw cycles, and were sealed under vacuum. Tetramethylsilane was used as an internal chemical shift and line-width reference.

All ^{1}H NMR measurements were performed on a Bruker AC-300 spectrometer using a 5 mm four-nucleus probe. Temperature control was maintained to within ±0.5 °C using a BVT 2000 temperature controller, and was monitored periodically by inserting a copper/constantan thermocouple in a 5 mm NMR tube into the probe.

The selective inversion experiments were carried out employing the RD - $\pi/2$ - τ - $\pi/2$ - VD -- $\pi/2$ - Acq. pulse sequence, similar to jump-return solvent suppression.[66] The carrier frequency was set to the resonance to be inverted, typically the major site. The delay, τ, was set to $1/(2\Delta\nu_{cis\text{-}trans})$, where $\Delta\nu_{cis\text{-}trans}$ is the frequency difference between the *cis* and *trans* signal, which varied with solvent from 50 Hz in acetone to 120 Hz in toluene. The variable delays, VD, were chosen from a range of 10 ms to 10 s, and the relaxation delay was typically 20 seconds. Line intensity measurements of this data were obtained via the XWINNMR package, and were analysed with CIFIT, a program developed in this laboratory based on the SIFIT program written by R.E.D. McClung and R. Muhandiram.[67] The main difference between the two programs is the way in which they formulate the partial derivatives of the eigenvectors with respect to the parameters. These derivatives are required for the optimisation routine.[68]

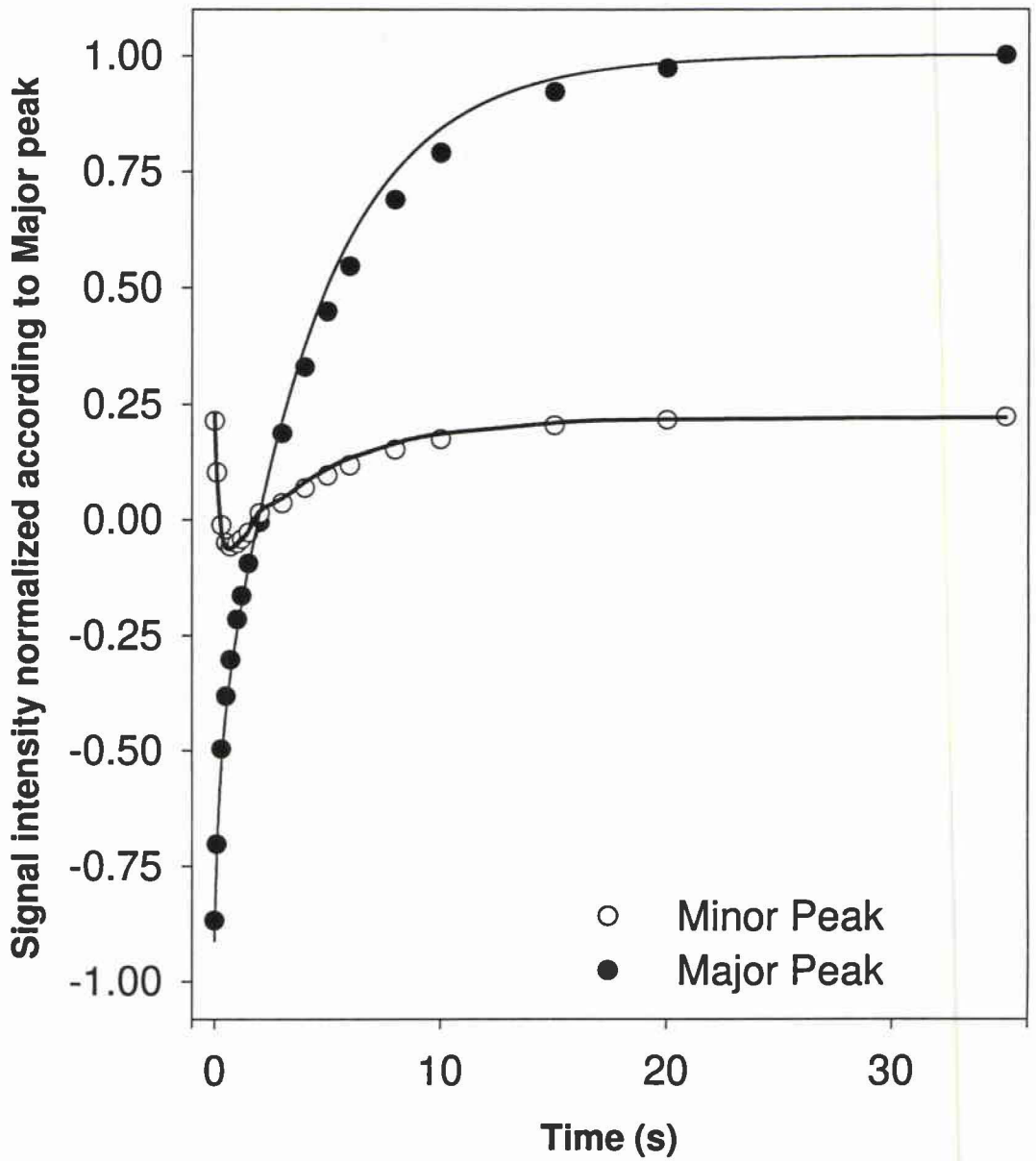

Figure 3.2 Selective inversion of the major aldehyde proton resonance of furfural in toluene-d_8 at 185 K. Notice the transient behaviour in the minor resonance. The lines represent best fit curves based on multivariable non-linear regression analysis performed by the CIFIT program.

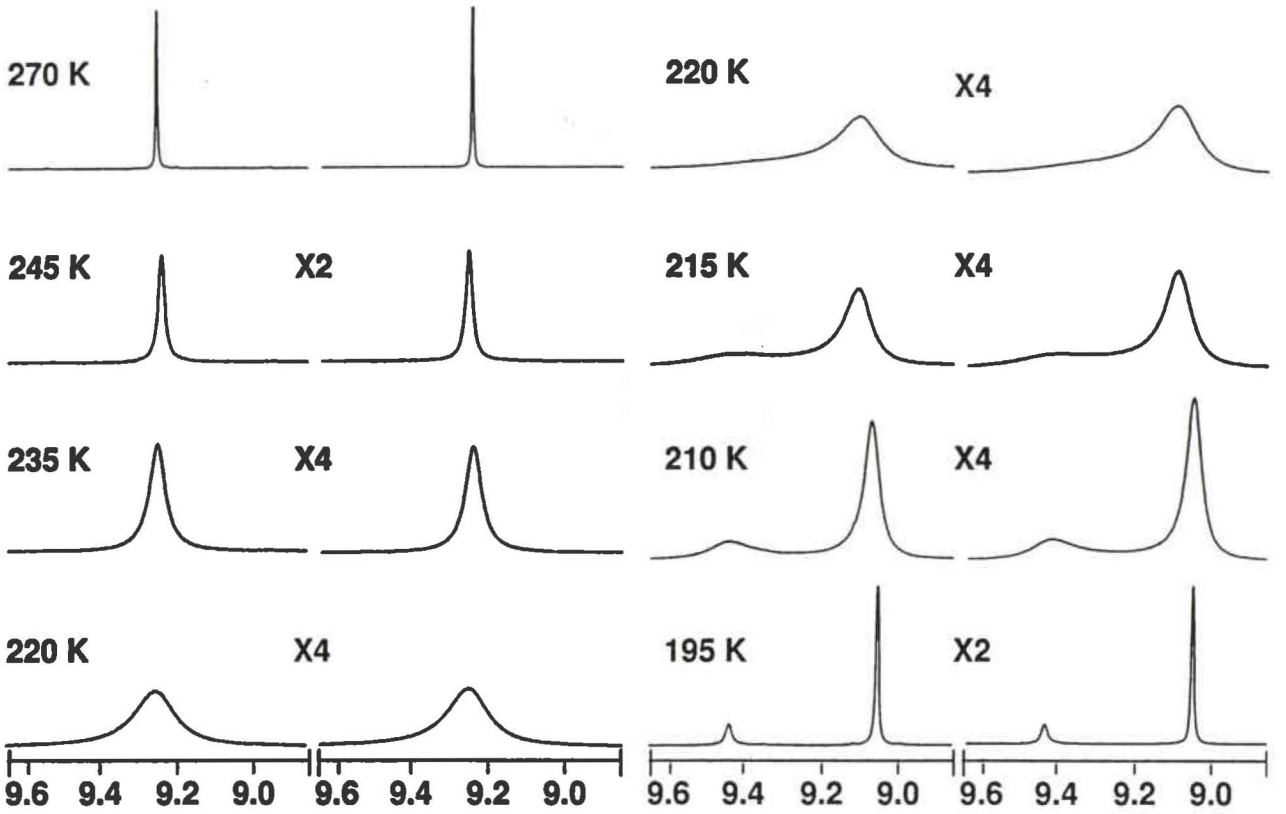

Figure 3.3 Lineshape analysis on the aldehyde proton signal of furfural toluene-d_8 from 195 to 270 K. Experimental spectra are on the left, and simulated spectra are on the right.

Line shape analysis was performed with MEX. MEX is a program that simulates lineshapes of exchanging systems without scalar coupling. The simulated spectra are directly imported into XWINNMR and compared with experiment using the dual display mode.(see figure 3.3)

The off-resonance saturation experiments, described in previous work,[30,31] were performed, using the proton homodecoupler set to high power providing a saturating field. The field strength of the decoupler was calibrated using the single-spin double-resonance experiment, with the TMS signal.[38] The values for $\gamma B_2/2\pi$ were typically 30 to 40 Hz. The T_1 for the aldehyde signal ranged from 5 to 40 s with increasing temperature, consequently the irradiation periods required in the off-resonance saturation experiment ranged over 30 to 200 s. The preacquisition delay was set to typically $0.1 \times T_1$, and thus ranged from 0.5 to 4 s. The free induction decays were obtained with a $\pi/2$ pulse using 6 kHz spectral widths. Decoupler frequencies were chosen with emphasis on the region where the width at half-height of the curve of intensity as a function of off-set frequency was expected. An average of 35 frequencies were used.

The intensities, relative to that furthest from resonance, were analysed using DIPPER, a multivariable non-linear least-squares fitting program which optimises the parameters line intensity, saturating field strength, and T1/T2, to a mathematical model of a saturated line intensity after a short delay (see figure 3.4). Values for T_1 and T_2 were obtained in this manner. Separate inversion-recovery experiments were carried out at each temperature to obtain an independent value of T_1

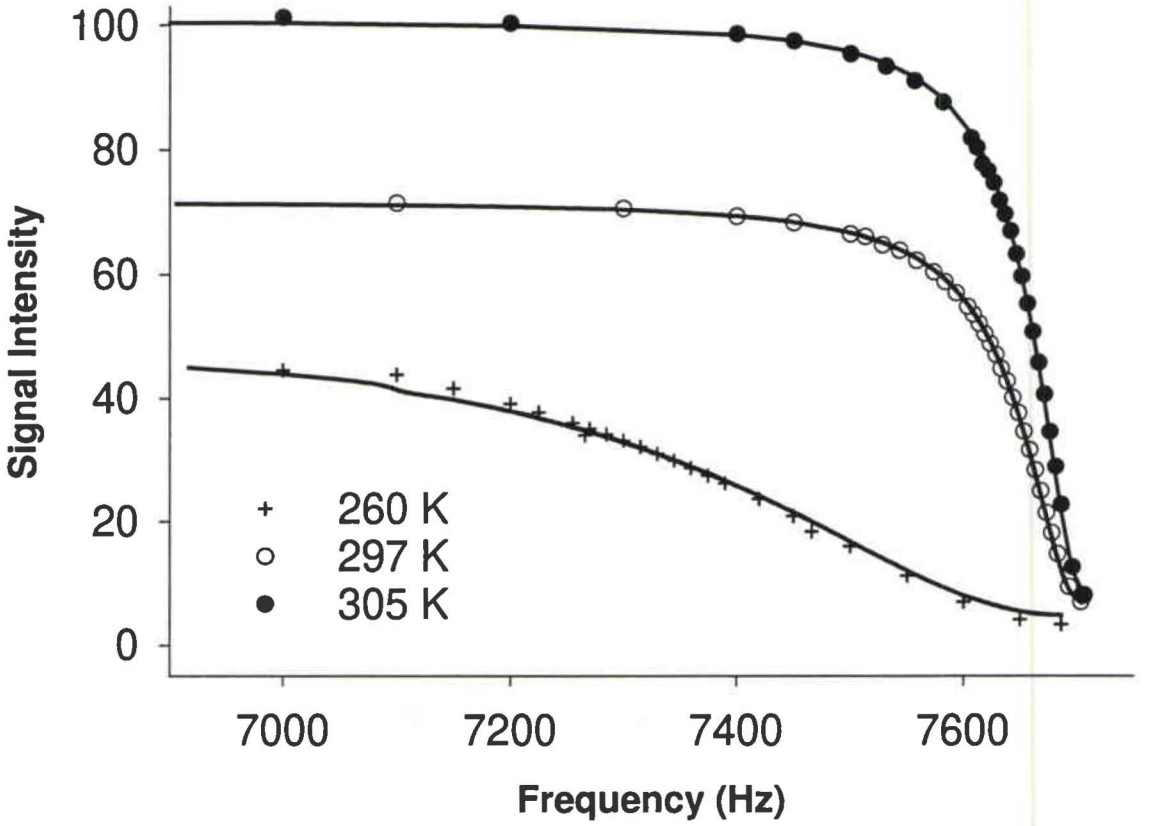

Figure 3.4 Offset-saturation data of the aldehyde proton of furfural at 260, 297 and 305 K in toluene-d_8. The line is the best-fit curve based on a multivariable non-linear regression analysis implemented in the DIPPER program.

Restricted Hatree-Fock calculations were performed using Gaussian 94[69] with an IBM RS 6000 470 series computer. Optimum states of both the *cis* and *trans* conformers were computed to mp2/6-31g** level. Transition state calculations were performed using the QST3 method of searching for saddle points in the energy surface, available in Gaussian 94. Self-consistent-reaction field computations were done with the Onsager and Isodensity Surface Polarised Continuum model. Both the optimum and transition geometries were determined with the SCIPC method to 6-31g level and up to 6-31g** level for the Onsager

SCRF approach. The dielectric constants employed were 20.7 32.63 and 0.38 C^2/Nm^2 for acetone, methanol and toluene, respectively.[70] With gas phase geometries from 6-31g** and mp2/6-31g**, single point SCRF computations were performed via both models at 6-31g** and mp/6-31g** levels. The cavity radius was 3.70 A.[24]

Results

The rate constants at various temperatures for the *cis-trans* process, k_{c-t}, in toluene, acetone, and methanol are given in table 3.1 along with their equilibrium constants. The equilibrium constants were obtained by extrapolating low temperature values to room temperature values using the van't Hoff isochore. In toluene and methanol, significant entropy differences, (ΔS^o), between the *cis* and *trans* forms were observed. The equilibrium constants at low temperature were determined by integration of the spectral lines, and those at room temperature were given by Bertran and others.[45,58,64] The Eyring plots are shown in figure 3.5. The relative error in rate constants, at 95% confidence, are below 10% for all three methods. The thermodynamic parameters, for both k_{c-t} and k_{t-c}, obtained from the Eyring plots are given in table 3.2 and 3.3. Values for k_{t-c} were computed from the corresponding k_{t-c} and equilibrium constant.

By moving the origin to the average 1000/T value any covariance between the error in the slope and that of the intercept is removed.[29] The error in the $\Delta H^\dagger$ was taken directly from the regression error in the slope (Δm). The error in $\Delta S^\dagger$ was computed with the regression error in the intercept (Δy) and slope using:

$$R * \sqrt{\Delta m^2 x^2 + \Delta y^2} \qquad (3.7)$$

where x is the average of 1000/T.

The removal of the covariance between the error of the slope and the intercept can be shown as follows. For N pairs of x_i and y_i, we define the statistical parameters:

$$S_x = \sum_{i=1}^{N} x_i \ , \ S_y = \sum_{i=1}^{N} y_i \ , S_{xx} = \sum_{i=1}^{N} x_i^2 \ \text{and} \ S_{xy} = \sum_{i=1}^{N} x_i \, y_i \, . \tag{3.8}$$

The best fit values of the slope and the intercept are

$$m = \frac{NS_{xy} - S_x S_y}{NS_{xx} - S_x^2} \ \text{and} \ b = \frac{S_{xx} S_y - S_x S_{xy}}{NS_{xx} - S_x^2} \, . \tag{3.9}$$

The variance of the regression is

$$S_R = \frac{\sum_{i=1}^{N} (y_i - mx_i - b)^2}{N - 2} \, . \tag{3.10}$$

The variances of the slope and the intercept are given as

$$\text{var}(m) = \frac{S_R N}{NS_{xx} - S_x^2} \ \text{and} \ \text{var}(b) = \frac{S_R S_{xx}}{NS_{xx} - S_x^2} \, , \tag{3.11}$$

and the covariance between them is

$$\text{cov}(m, b) = \frac{-S_R S_x}{NS_{xx} - S_x^2} \, . \tag{3.12}$$

Therefore if a set of x_i were chosen such that $S_x = 0$, the covariance between the slope and the intercept dissapears. This is achieved by subtracting the mean of x_i from x_i and the variance of y can be expressed as:

$$\mathrm{var}(y_i) = (x_i - \overline{x})^2 \,\mathrm{var}(m) + \mathrm{var}(b), \tag{3.13}$$

which is analogous to eqn. (3.7).

The total and relative calculated electronic energies along with the electric dipole moments of all three geometries of furfural are shown in table 3.4. All relative energies are reported with respect to the energy of the O,O-*trans* form. The mp2/6-31g** geometries of the *cis*, *trans* and transition forms are given in table 3.5. The results from the self-consistent IPC/6-31g calculations with geometry optimisation are shown in table 3.6. The stabilisation due to the solvent for each geometry is reported with respect to the corresponding gas phase value. The predicted barriers at the 6-31g level with geometry optimisation are given in table 3.7. These barriers were corrected using mp2/6-31g** gas phase relative conformer stabilities and SC-IPC/6-31g stabilisation energies, and are seen in table 3.9. Barriers from the Onsager and IPC single point calculations at 6-31g** and mp2/6-31g** are given in table 3.8. These were performed with 6-31g** and mp2/6-31g** gas phase geometries. The ICP mp2/6-31g** results are depicted in figure 3.6 and are compared with measured barriers in figure 3.7. Onsager SCRF calculations with geometry optimisations indicated no significant change in gas and liquid phase geometries using $\varepsilon = 32.63\ C^2/Nm^2$.

Table 3.1

Summary of temperature, rate and equilibrium constant data for furfural in toluene, acetone and methanol, as obtained from the NMR analyses.

Toluene				Acetone			Methanol		
T[a]	k_{c-t}[b]	K[c]	E[d]	k_{c-t}	K	E	k_{c-t}	K	E
177				0.20	0.10	si			
180							0.18	0.17	si
182				0.44	0.10	si			
185	0.88	0.24	si				0.63	0.18	si
190	1.89	0.26	si	1.60	0.11	si	1.13	0.19	si
195				3.25	0.13	ls			
200	10.0	0.30	ls						
205	23.0	0.31	ls	11.3	0.15	ls	16.0	0.21	ls
210	40.0	0.33	ls	30.0	0.20	ls	28.6	0.22	ls
215	80.0	0.35	ls	46.8	0.28	ls	51.8	0.23	ls
220	135	0.37	ls				88.5	0.24	ls
225	225	0.39	ls				150	0.24	ls
230	415	0.41	ls	110	0.30	T	258	0.25	ls
235	715	0.42	ls	260	0.31	T	417	0.26	ls
240	1200	0.44	ls	403	0.32	T	630	0.27	ls
245	1980	0.46	ls				922	0.28	ls
250	3150	0.48	ls	819	0.33	T	2217	0.28	T
260	11300	0.52	T				5150	0.29	T
262.5				2680	0.35	T			
275				7290	0.37	T			
282.5				11400	0.38	T			
292.5				17800	0.39	T			
297	23700	0.65	T						
300				31100	0.40	T			
305	38800	0.68	T						
310				43800	0.41	T	17300	0.36	T
317.5				61400	0.42	T			

[a]All temperatures are given in Kelvin. [b]All rates are *cis* to *trans* rates and are given in s^{-1}. The error in the rates is approximately 10%. [c]Equilibrium constants were calculated from integration values of the *cis* and *trans* aldehyde proton signal in the low temperature spectra. At room temperature the equilibrium constants were

taken from the literature. The intermediate values were obtained by extrapolation with the van't Hoff Isochore. [d]The columns with heading E, indicate with which experiment the rate was measured. (si, selective inversion; ls, line shape, and T, is the off-set saturation experiment)

Table 3.2

Activation parameters of furfural in three solvents, determined by NMR chemical exchange measurements.

Solvent	$\Delta H^{\dagger}_{ct}$	$\Delta H^{\dagger}_{tc}$	$\Delta S^{\dagger}_{ct}$	$\Delta S^{\dagger}_{tc}$	$\Delta G^{\dagger}_{ct}$	$\Delta G^{\dagger}_{tc}$
Toluene	48.6[a]	44.6	20[b]	10	42.7[c]	41.7
Acetone	40.2	35.0	-26	-36	47.8	45.8
Methanol	46.4	43.8	5	5	44.9	42.2

[a]All enthalpies are given in kJ/mol. The error is taken directly from the regression error of the slope of the Eyring plot, and is approximately 1 kJ/mol at the 95% confidence. [b]All entropies are given in J/molK. The error, including the contribution from the uncertainty in the slope of the Eyring plot, is approximately 6 J/molK at the 95% confidence. [c]All Gibbs free energies are given in kJ/molK and are evaluated at 298 K.

Table 3.3

Thermodynamic parameters of furfural in three solvents, determined by NMR measurements.

Solvent	ΔH^{o}	ΔS^{o}	ΔG^{o}	K_{eq}
Toluene	4.0[a]	10[b]	1.1[c]	0.64[d]
Acetone	5.1	10	2.0	0.45
Methanol	2.6	0	2.7	0.33

[a]All enthalpies are given in kJ/mol. These values were obtained by extrapolating the measured values, by NMR, at low temperature to room temperature values, in the literature based on nmr coupling constants and dielectric constant measurements, using the van't Hoff Isochore. [b]All entropies are given in J/molK. [c]All Gibbs free energies are given in kJ/mol and are evaluated at 298 K. [d]Equilibrium constants are *trans/cis* and are evaluated at 298 K.

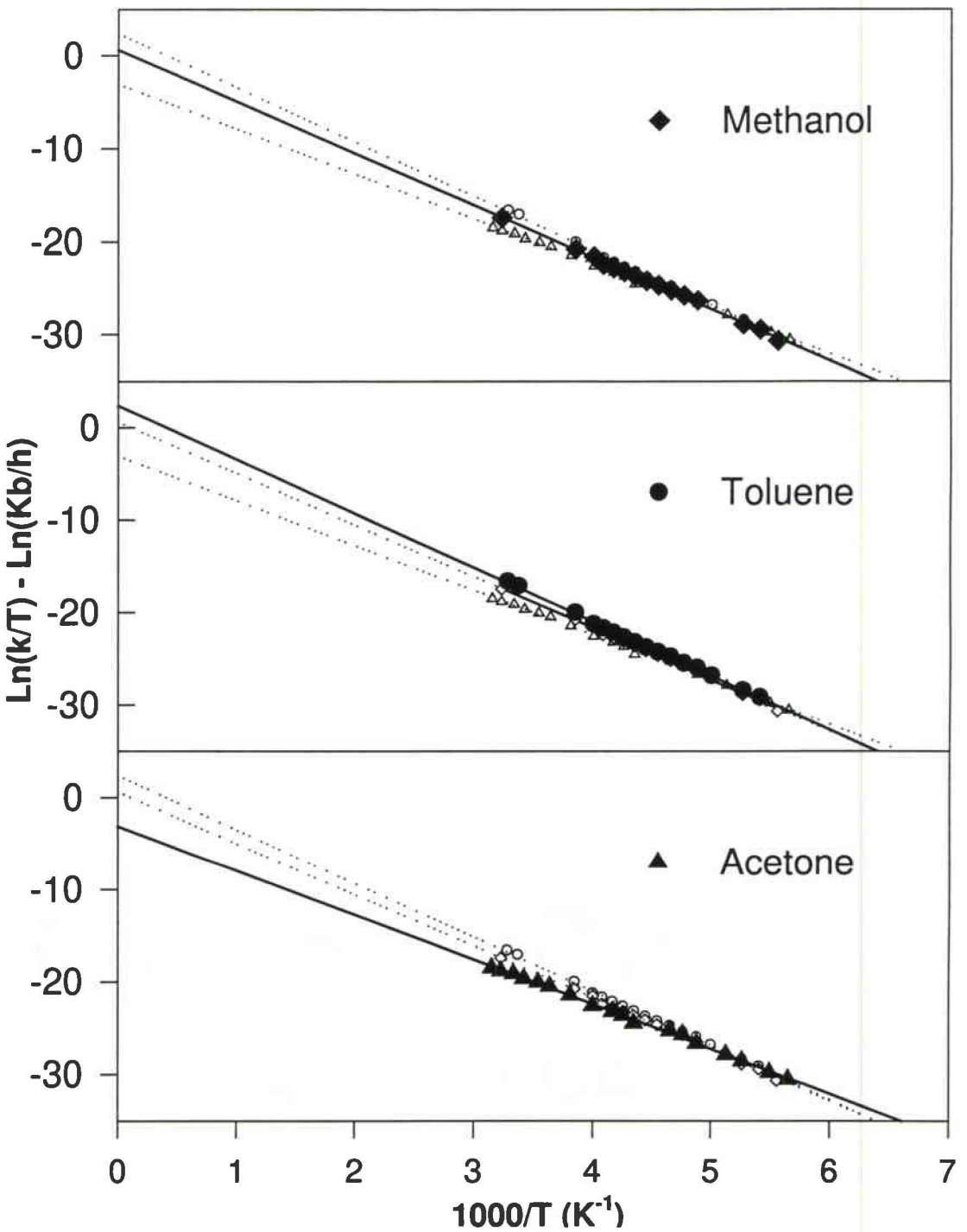

Figure 3.5 Eyring plots of the rate data in Methanol (top, ◆), Toluene (middle, ●) and Acetone (bottom, ▲), each with the remaining plots in the background.

Table 3.4
Energies and dipole moments of the three conformations of furfural obtained from molecular orbital calculations.

Basis	Property	O,O-*trans*	O,O-*cis*	Transition State
	E	-336.98218[a]	-336.98095	-336.97218
Sto-3g	ΔE_{trans}	0[b]	3.23	26.24
	μ	1.83[c]	2.41	1.81
	E	-341.20051	-341.19605	-341.18158
6-31g	ΔE_{trans}	0	11.69	49.69
	μ	3.98	5.21	3.92
	E	-341.36407	-341.36202	-341.34666
6-31g**	ΔE_{trans}	0	5.38	45.71
	μ	3.50	4.32	3.21
	E	-342.37083	-342.36927	-341.35311
mp2/6-31g**	ΔE_{trans}	0	4.09	46.52
	μ	3.87	4.75	3.43

[a]All total energies are given in Hartrees. [b]All relative energies are given in kJ/mol. [c]All electric dipole moments given in Debyes.

Table 3.5

Geometries of the *cis*, *trans* and transition forms of furfural as determined by mp2/6-31g** calculations.

Parameter	*cis*	*trans*	†	Parameter	*cis*	*trans*	†
C1-C2	1.379	1.377	1.369	C1-C6-O7	124.6	122.9	122.5
C2-C3	1.418	1.417	1.427	C1-C6-H8	113.5	114.9	116.7
C3-C4	1.371	1.372	1.366	C1-C2-H9	125.9	125.2	126.2
C4-O5	1.360	1.361	1.368	C2-C3-H10	127.8	127.6	127.4
C1-C6	1.457	1.458	1.493	C3-C4-H11	133.4	133.6	134.0
C6-O7	1.227	1.229	1.224	C1-C2-C3-C4	0.0	0.0	-0.2
C6-H8	1.104	1.103	1.102	C2-C3-C4-O5	0.0	0.0	0.0
C2-H9	1.078	1.077	1.077	C3-C2-C1-C6	180.0	180.0	181.0
C3-H10	1.076	1.077	1.076	C2-C1-C6-O7	180.0	0.0	91.7
C4-H11	1.076	1.076	1.075	C2-C1-C6-H8	0.0	180.0	-88.3
C1-C2-C3	106.4	106.3	106.1	O5-C1-C2-H9	180.0	180.0	179.9
C2-C3-C4	106.0	106.4	106.4	C1-C2-C3-H10	180.0	180.0	179.6
C3-C4-O5	110.9	110.6	110.4	C2-C3-C4-H11	180.0	180.0	180.0
C2-C1-C6	131.5	133.1	133.6				

All geometries were allowed to fully relax. Bond lengths are given in angstroms, and angles are given in degrees.

Table 3.6

Solvent calculations with the Self-Consistent-Isodensity surface Polarised Continuum model to 6-31g level on the *cis*, *trans* and transitions forms of furfural.(see figure 3.6)

Medium	Property	O,O-*cis*	O,O-*trans*	Transition state
Gas	E[a]	-341.1961	-341.2005	-341.1816
Toluene	E	-341.2029	-341.2057	-341.1868
	ΔE[b]	-17.87	-13.56	-13.64
Acetone	E	-341.2104	-341.2108	-341.1923
	ΔE	-37.79	-27.15	-28.18
Methanol	E	-341.2109	-341.2111	-341.1927
	ΔE	-39.04	-27.90	-29.08

[a]Total energies including the stabilisation due to solvent. These are reported in Hartrees. [b]Energies energies relative to gas phase. These are reported in kJ/mol.

Table 3.7

Barrier to internal rotation of the aldehyde group, E(*cis*) - E(*trans*) and electric dipole moments of furfural as predicted by SCIPC HF/6-31g calculations.

	Δ*Et*†[a]	Δ*Ec*†	Δ*Etc*	μ_{cis}[b]	μ_{trans}	$\mu_{\dagger}$
Gas	49.96[c]	38.00	11.69	5.21	3.98	3.92
Toluene	49.61	42.23	7.37	5.94	4.50	4.32
Acetone	48.66	47.61	1.05	6.77	5.03	4.75
MeOH	48.52	47.97	0.55	6.82	5.06	4.77

[a]The change in energy between the transition state (†) and the *trans* conformer (*t*)(*c* stands for the *cis* conformer). [b]Molecular dipoles computed in solvent field. All dipoles are given in Debyes.

Table 3.8

Single point self-consistent ICP and Onsager calculations employing gas phase geometries from 6-31g** and mp2/6-31g** calculations.

	SCIPC HF/6-31g**[a]			SCIPC mp2/6-31g**[b]		
Solvent	ΔE^{rf}	ΔE^{cf}	ΔE^{tc}	ΔE^{rf}	ΔE^{cf}	ΔE^{tc}
Gas[c]	45.71[d]	40.33	-5.38	46.51[e]	42.42	-4.09
Toluene	45.64	43.26	-2.38	46.53	44.36	-2.17
Acetone	44.86	46.51	1.66	46.17	46.01	0.23
Methanol	44.79	46.72	1.93	46.13	46.52	0.39
	Onsager HF/6-31g**[f]			Onsager mp2/6-31g**[g]		
Solvent	ΔE^{rf}	ΔE^{cf}	ΔE^{tc}	ΔE^{rf}	ΔE^{cf}	ΔE^{tc}
Gas	45.71[d]	40.33	-5.38	46.51[e]	42.42	-4.09
Toluene	46.40	43.06	-3.34	48.74	47.51	-1.23
Acetone	47.46	46.44	-1.02	52.48	54.74	2.26
Methanol	47.54	46.67	-0.87	52.76	55.25	2.48

[a]Single point SCRF calculations using 6-31g** basis, HF/6-31g** gas phase geometries and the Isodensity surface Polarized Continuum model. [b]Single point mp2 SCRF calculations using 6-31g** basis, mp2/6-31g** gas phase geometries and the Isodensity surface Polarized Continuum model. [c]Gas phase energies at 6-31g** level. [d]All energies are given in kJ/mol. [e]Gas phase energies at mp2/6-31g** level. [f]Single point SCRF calculations using 6-31g** basis, HF/6-31g** gas phase geometries and the Onsager model. [g]Single point mp2 SCRF calculations using 6-31g** basis, mp2/6-31g** gas phase geometries and the Onsager model.

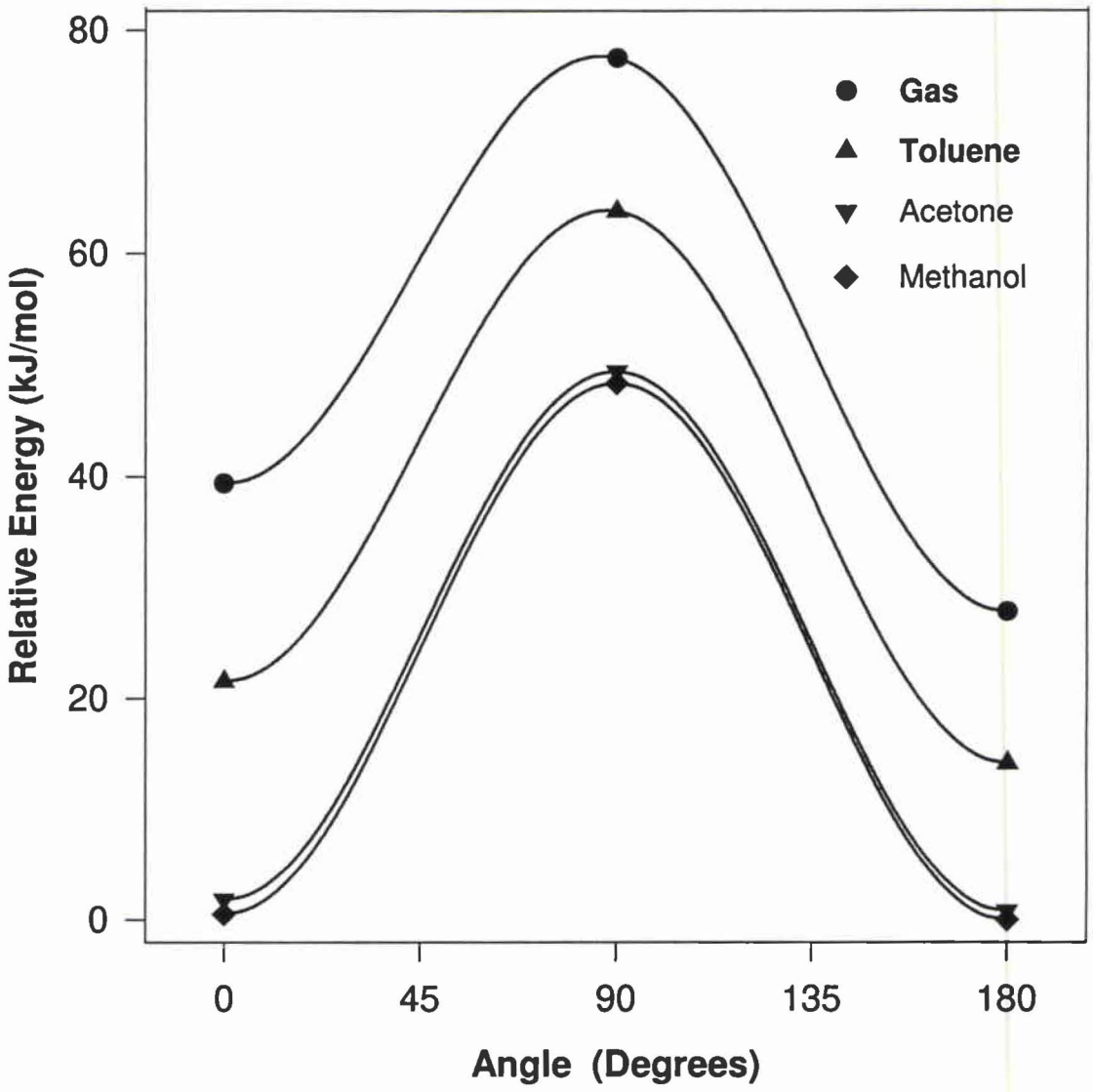

Figure 3.6 The barrier in three solvents and gas phase compared on an absolute scale. This depicts the stabilisation due to the solvent field with respect to gas phase, given by SCIPC HF/6-31g calculations.(see table 3.6) Notice differential stabilisation of the cis form with respect to the trans form. The gas phase energies are from HF/6-31g calculations. The energy of the cis conformer in methanol is set to zero. The lines are meant to guide the eye.

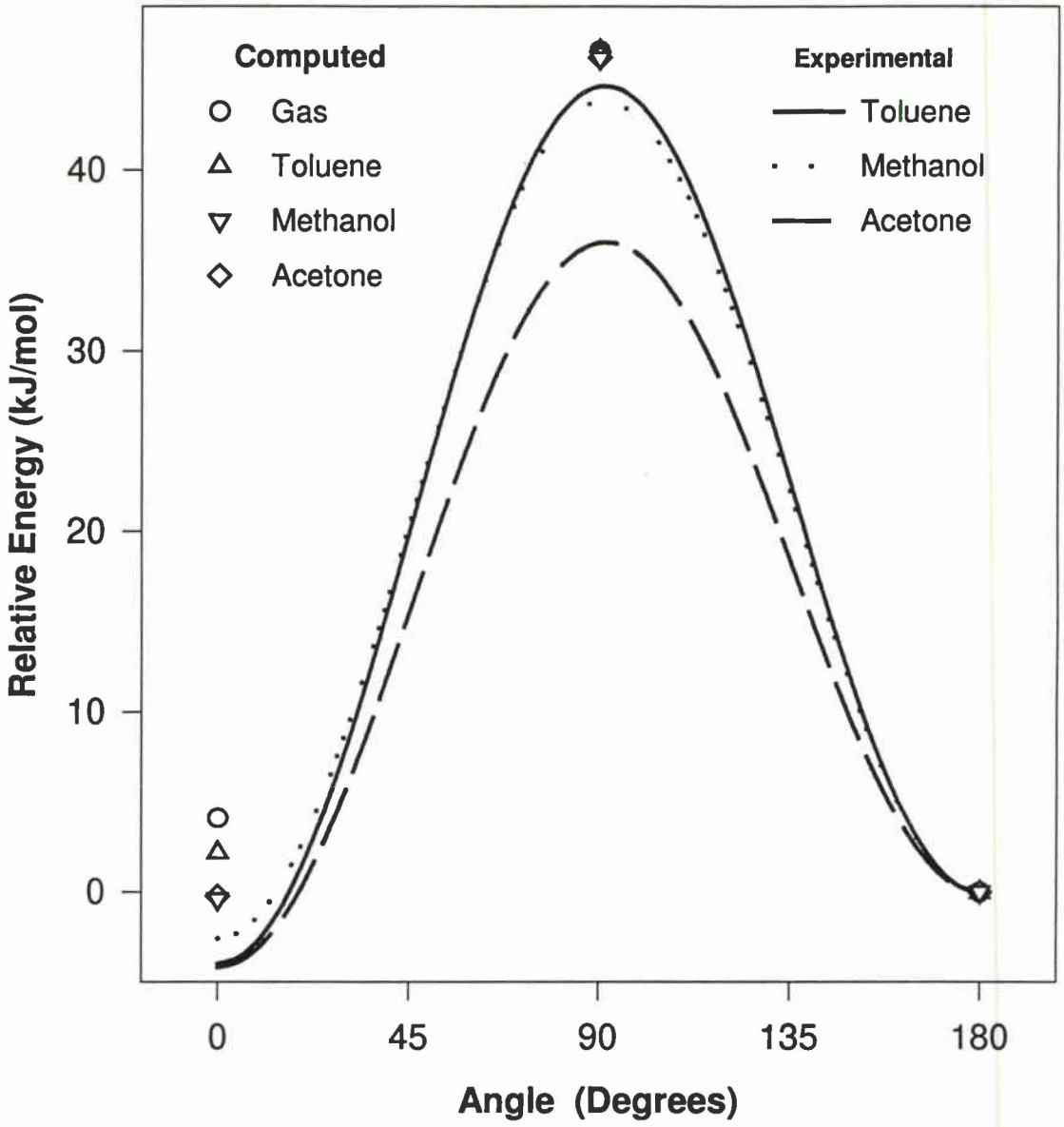

Figure 3.7 A schematic comparison between the experimental barriers and those determined by single point SCIPC mp2/6-31g** calculations. The experimental barriers are given in table 3.2 and the computed barriers are from table 3.8. The experimental barriers are shown as curves while the computational results are given as symbols. The lines are meant to guide the eye.

Table 3.9

The internal rotational barrier in furfural predicted by combining gas phase values from mp2/6-31g** computations and stabilisation energies from self-consistent IPC HF/6-31g calculations (table 3.6).

	$\Delta E^{t\dagger}$ [a]	$\Delta E^{c\dagger}$	ΔE^{tc}
Gas	46.51[b]	42.42	-4.09
Toluene	46.43	46.65	0.22
Acetone	45.48	52.02	6.54
MeOH	45.34	52.38	7.07

[a]The change in energy between the transition state (†) and the *trans* conformer (*t*)(*c* stands for the *cis* conformer). [b]Gas phase values from mp2/6-31g** calculations. All relative energies are reported in kJ/mol. [c]Stabilisation energies due to solvent taken from SCIPC HF/6-31g calculations.(see table 3.6)

Discussion

The assignment of the *cis* form as the major conformer in acetone was done previously by an nOe difference experiment.[30] This was an expected result since the *cis* form is known to predominate in polar solvents.[23,41,44,47,58,64] Based on the five-bond coupling constant from the aldehyde proton to the proton *ortho* to the ring oxygen, $^5J_{H8,H11}$, the *cis* conformer was found to prevail in toluene and methanol as well. These couplings were both 1.08 Hz which is in line with those measured by Dahlqvist and Forsen using the reverse assignment.[61,71]

The rate data were determined using three different sets of equilibrium constants based on different methods of extrapolation with the van't Hoff Isochore. The first method employs only the low temperature K_{eq}'s and makes no assumption about ΔS^o. The second method is similar to the first except that it assumes ΔS^o is zero. The last method uses room temperature K_{eq}'s from the literature,[58,64,72] based on NMR coupling constants, and those

measured at low temperature. The third method gave the best fitting Eyring plots where the data sets from all three NMR experiments fell perfectly along a straight line. (figure 3.3) In the other two methods the offset saturation data did not line up as well with the two remaining data sets. Lastly, the first two methods greatly over- and under- estimate the room temperature equilibrium constants. In the third approach $\Delta S^{\dagger}$'s and ΔS^{o}'s were the least extreme.

Having non-zero entropies is not unreasonable. The dipole moment and shape of the molecule change significantly throughout the rotational process, thus it is possible that changes occur in the steric and electrostatic interactions with local solvent molecules. These changes could affect the organisation of the local solvent giving rise to changes in entropy.

For all but the STO-3g level, the gas phase both the *cis-trans* and *trans-cis* barriers are over-estimated by the HF calculations. At 6-31g** and mp2/6-31g** level the *cis-trans* barrier is 40 kJ/mol which is 4 kJ/mol larger than the measured values. The energy difference between the two planar forms is 5 to 6 kJ/mol which is close to 6.28 kJ/mol reported previously.[59,60,64] The electronic dipole moments of the *trans* and *cis* conformers given in the literature are 3.23 D and 3.97 D, the transition state dipole moment was predicted to be 2.93 D.[42,64] Both 6-31g** and mp/6-31g** overestimate them, however their relative sizes are approximately correct.

It is better to follow the behaviour of the *cis-trans* barrier since it expected to be the most sensitive to solvent effects. Both theory and experiment have shown what is intuitively obvious, that the dipole moment of the *cis* form is much larger than the *trans*

form. Thus, in environments of high dielectric constant, the *cis* form should be the most stabilised. The *trans* dipole moment is approximately the same size as that of the transition state, thus the barrier from *trans* to *cis* is expected to be least sensitive to ε, as opposed to the *cis* to *trans* barrier which is expected to increase significantly.

The solvent calculations predict the same trend in relative conformer stabilities and barrier heights with respect to ε as previous investigators.[23,24,58,63,64] For the self consistent IPC method it was necessary to go to 6-31g** level to obtain the correct behaviour, and electron correlation was required for the Onsager SCRF approach. The self consistent IPC calculations with 6-31g basis did not recover the correct behaviour primarily because the gas phase energy difference between the *cis* and *trans* conformer, ΔE_{ct}, is greatly overestimated. When using the mp2/6-31g** for ΔE_{ct} the stabilisation of the *cis* with respect to the *trans* conformer is predicted for $\varepsilon > 5$ C^2/Nm^2. The self consistent IPC calculations at 6-31g** and mp2/6-31g** come closest to previous work, the barrier increases by 4 to 6 kJ/mol from gas to liquid phase ($\varepsilon = 32.63$ C^2/Nm^2), and in methanol and acetone it is predicted to be at least 3 kJ/mol larger than in toluene.

The behaviour of the enthalpies of activation for the *cis-trans* process with respect to ε deviates from previous observations[62,64] and predictions.[23,63-65] The value for toluene ($\varepsilon = 2.38$ C^2/Nm^2) is 8 kJ/mol larger than in acetone ($\varepsilon = 20.7$ C^2/Nm^2). No simple trend is observed with respect to ε, except that the barrier increases when going from gas to liquid phase. When considering the free energy of activation at 298 K, the relative order of toluene and acetone are reversed, which is in line with previous work. Thus the observed solvent effect is contrary to predictions made by current theoretical methods.[63-65] Since the

barriers do not obey a simple relationship with ε, it would seem that there is more at play than just the effect of a solvent field. Consequently the reaction field methods by themselves should not be expected to account for this behaviour.

The behaviour of $\Delta H^{\dagger}_{ct}$ and $\Delta S^{\dagger}_{ct}$ can be understood more clearly if direct interactions with the solvent are considered. These interactions can be steric, electrostatic or bonding in nature, giving rise to some type of preferred solute-solvent structure. In toluene the large entropy of activation of 20 J/molK indicates that the transition state is disordered with respect to the planar forms, which implies that there is some preferred orientation of the solvent with respect to the planar forms. Rotational processes could disrupt this solute solvent structure, possibly increasing the enthalpy of activation due to steric interactions between the solvent and the transition state. In acetone, the transition state is ordered when compared to the planar forms, as is indicated by an entropy of activation of -26 J/molK. Thus, there is some preferred assembly of solvent with the transition state which is disrupted when going to the planar forms. Steric interactions between the solvent and the ring could destabilise the planar forms, decreasing the barrier.

In methanol ($\varepsilon = 32.63\ C^2/Nm^2$) there is no significant entropy of activation indicating that there is no preferred interaction between the solute and any of the solute forms. This is not to say that there are no direct solute solvent interactions, because they are well known for furfural and primary alcohols.[73] The barrier in methanol is the most compatible with that determined in neat furfural,[64] and agrees reasonably to SCI-PCM calculations.

Conclusions

This study has served to illustrate that large entropies of activation exist for aprotic solvents like acetone and toluene. This means that entropies of activation can not be ignored for internal rotations and that measured enthalpies need to be reported in the literature. Approaches to modelling medium effects on these processes should allow for local interactions with the solvent.

Chapter 4

A reinterpretation of the substituent effect on the amide barrier. An experimental and theoretical study.

(Based on an article by A. D. Bain, P. Hazendonk and P. Couture published in the Canadian Journal of chemistry, volume 77 pages 1340-1348 in 1999.[74])

Introduction

Barriers to internal rotational in amides are commonly explained as a result of resonance structures between the oxygen and nitrogen.[2,9,11,75-84] One of the resonance structures has a double bond between the carbon and the nitrogen, and a negative charge on oxygen, as in Figure 4.1. Recent theoretical studies have proposed that this may not be appropriate.[81,82,85,86] Instead, they suggest that the barrier is dominated by energy differences in the carbon and nitrogen, and oxygen is hardly involved. However, this view is still controversial.[87-89] One way to test this hypothesis is to look at substituent effects on the barrier and see if they fit into this interpretation. What aspects of the substituent are important to the amide barrier?

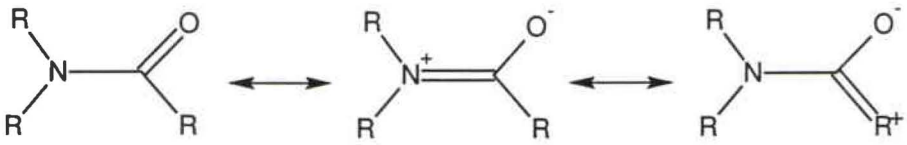

Figure 4.1 Resonance structures of an amide including interactions with a substituent on the carbon.

The concept of resonance predicts that, in the planar form of amides, there is interaction between the carbonyl π bond and the lone pair on the amide nitrogen.[75] This increases the C-N bond order, leading to a net stabilisation. In the transition state, this interaction is lost, since the orbitals are orthogonal. Substituents on the carbon capable of resonance interactions should reduce the interaction between oxygen and nitrogen (see Figure 4.1). As a result, the net stabilisation in the planar form is reduced, and the barrier decreases. Recently, the application of the resonance model to formamide has been brought into question.[81] These studies employ Atoms in Molecules (AIM)[90] analysis on electron density functions of formamide as the C-N bond is rotated. As the NH_2 group is rotated out of the plane, the main electron transfer is calculated to occur from the nitrogen to the carbon. The calculated atomic population of oxygen is virtually unchanged throughout this process. This disagrees with the resonance model, which requires significant participation of oxygen. As the molecule departs from the planar form, the calculations suggest that the nitrogen pyramidalises and the C-N bond lengthens. The C=O bond increases only marginally. The calculated energies of the nitrogen and carbon atoms in the molecule dominates the energy changes of the whole system. The energy of

oxygen changes insignificantly. Because of the central role of nitrogen, it is perhaps better to view this system as a particular case of an amine inversion rather than a hindered rotation.[81,91]

The AIM theory suggests that in amines, nitrogen is most stable in a planar form.[91] However, in this geometry the N-R bonds are shorter than in the pyramidal form, which increases the repulsive energies between the substituents. Since the planar nitrogen has higher *s* character in the N-R bonds, it requires a net transfer of electrons from its substituents, destabilising them.[81,82,85] Any consequent stabilisation of N in the planar form is overwhelmed by the loss of stability in the substituents, leaving the pyramidal form as most stable.[91] Thus the origin of the inversion barrier in amines depends on two factors:

1) The stability of nitrogen.
2) The stability of the substituents, especially with regard to changes in repulsive and attractive energies.

In this picture, amides are treated as amines - the carbonyl is just another substituent on the nitrogen. In the planar geometry, nitrogen stabilises more than the substituents destabilise. In the transition state, nitrogen is predicted to be somewhat pyramidal, where it is least stable. The analysis of the substituent effect on amide barriers should therefore attempt to answer the following questions:

1) Does the substituent alter the charge distribution between C and N, altering their atomic energies?
2) Does the substituent stability drive the changes in the barrier?

In this study, barriers of a series of spiro-fused oxazolidines (see Scheme 4.1) were measured using a suite of Nuclear Magnetic Resonance (NMR) spectroscopic techniques. The barriers of selected amides were computed and the electron densities were subjected to AIM analysis. The effect of substitution on the amide carbon was assessed by looking for changes in the atomic charges and energy contributions of the nitrogen, carbon and oxygen.

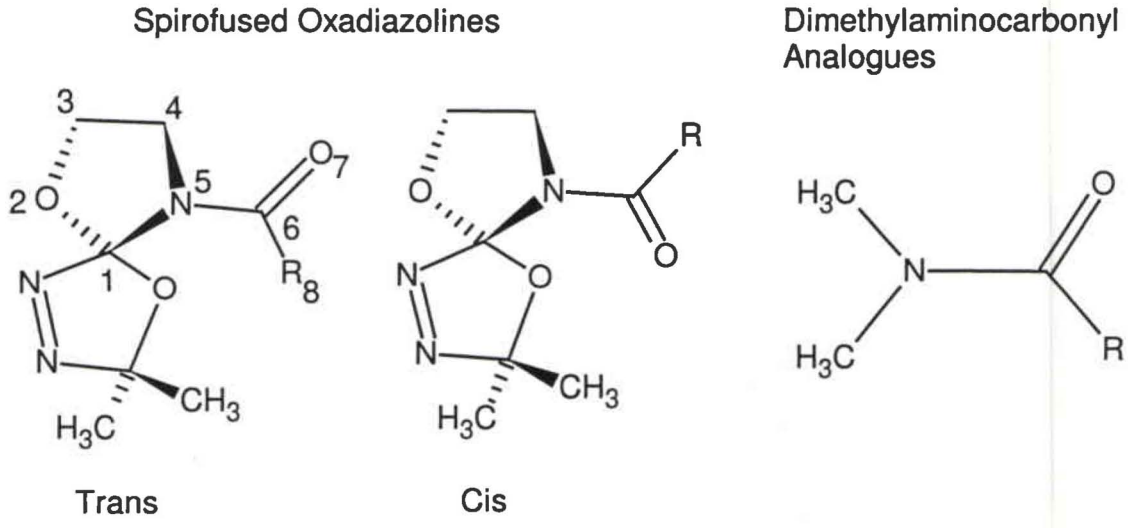

Scheme 4.1 Spiro-fused oxadiazoline derivatives and their dimethylaminocarbonyl analogues. The R groups are H, CH_3, OCH_3, $C(CH_3)=CH_2$, Ph, p-OCH_3 Ph and p-NO_2 Ph.

Methodology

NMR methods

Accurate activation parameters determined by NMR techniques require rate measurements over a wide temperature range.[29,30,92] Several methods can be employed to measure rates, each being optimal in different rate regimes.[6,8,29-33] Using selective inversion experiments during slow exchange (0.1 to 10 s^{-1})[32,37,38,93] and line shape fitting during medium and fast exchange,[2,4-10,94] it is possible to obtain $\Delta H^{\dagger}$ and $\Delta S^{\dagger}$ values to within 1 kJ mol^{-1} and 6 J $mol^{-1}K^{-1}$, respectively. [30]

The selective inversion experiments are best applied when the conformer lifetime is of the same order of magnitude as the spin-lattice relaxation time.[32,33,37] The line corresponding to one site, often the major site, is inverted selectively, and the relaxation of both lines is observed. The exchange rate is extracted by fitting the data to a set of differential equations, which describe the relaxation and exchange behaviour.

Lineshape methods are employed most effectively when the rates are comparable with the difference in the Larmor frequency between the two sites.[9,29,37] Experimental spectra are compared visually with sample spectra computed with varying exchange rates.

Theoretical methods

Initially, the electron densities (ρ) (this is the standard symbol for the electron density, it should not to be confused with the density matrix defined in chapter 2) of selected amides are obtained from the wave functions (Ψ) as in eqn. (4.1).

$$\rho = N\int \Psi^{*}\Psi d\tau \tag{4.1}$$

Using methods prescribed by the Atoms in Molecules theory[90,95-97] these densities were analysed for their topological properties, such as bond critical points (bcp) and bond paths. A critical point occurs where the gradient of ρ vanishes. These critical points are characterised by the properties of eigenvalues of the Hessian matrix at that location. The number of non-zero eigenvalues is its rank and the sum of their signs is its signature. A bond critical point is a (3,-1) critical point, and nuclear positions are (3,-3) critical points. The path of maximum density connecting two (3,-3) critical points and which passes through the BCP is known as the bond path.

Several properties of ρ at a bcp are commonly used in the analysis of ρ. The density at the bcp is related to the bond order, and the Laplacian at the bcp, $\nabla^2\rho$, indicates whether charge is locally concentrated or depleted.[95] A negative Laplacian indicates that charge is locally concentrated, while a positive value suggests that charge is locally depleted.

The next stage of analysis involves searching ρ for interatomic surfaces. These surfaces partition the molecule into atomic domains (Ω), which are used as integration boundaries to calculate atomic properties. Atomic populations, N(Ω), are calculated by

integrating the electron density up to these boundaries (eqn.(4.2)).

$$N(\Omega) = \int_{\Omega} \rho(r) d\tau \tag{4.2}$$

The atomic energies are computed by invoking an atomic virial theorem,[95] as in equation (4.3). For an equilibrium geometry, the total energy of subsystem, E(Ω), is given in eqn. (4.3).

$$E(\Omega) = \frac{V(\Omega)}{2} = -T(\Omega) \tag{4.3}$$

T(Ω) and V(Ω) are the kinetic and potential energies respectively. Thus E(Ω) and T(Ω) can be computed by integrating the potential energy within the relevant interatomic surface.

The potential energy of a system can be divided into contributions from repulsive V_{rp}) and attractive terms in the Hamiltonian. The attractive contribution, $V_{ne}(\Omega)$ (eqn. (4.4)), is the integral of the electron-nuclear potential, with all the nuclei of the system, over the atomic basin.

$$\langle V_{ne} \rangle = \sum_{\alpha} Z_{\alpha} e^2 \int_{\Omega} \frac{1}{r} \rho(r)\, d\tau \tag{4.4}$$

If only the nucleus within the basin is considered, V_{neo} is the basin attractive potential energy, as in eqn. (4.5).

$$\langle V_{neo} \rangle = Z_{\Omega} e^2 \int_{\Omega} \frac{1}{r} \rho(r)\, d\tau \tag{4.5}$$

The contribution from repulsive interactions is computed by integrating the electron-

electron potential between electrons within the same basin, $V_{ee}(\Omega,\Omega)$, or a given basin (Ω) and remainder of the electron density (Ω'), $V_{ee}(\Omega,\Omega')$. The repulsion energy is given in eqn. (4.6).

$$V_{rp} = V_{ee}(\Omega,\Omega) + \frac{1}{2}V_{ee}(\Omega,\Omega') \tag{4.6}$$

Experimental

Sample preparation

Oxazolidines were prepared by Dr P. Couture according to standard methods.[98-100]

NMR measurements

All 1-D ^{1}H NMR measurements were performed on a Bruker AC-300 spectrometer using a 5 mm four-nucleus probe. Temperature control was maintained to within ±0.5 °C using a BVT 2000 temperature controller, and was monitored periodically by inserting a copper/constantan thermocouple in a 5 mm NMR tube into the probe. The two readings always agreed to within 0.5 °C, and the BVT 2000 reading was used.

The selective inversion experiments were carried out employing the RD - $\pi/2$ - τ - $\pi/2$ - VD -- $\pi/2$ - Acq. pulse sequence. The carrier frequency was set to the line to be inverted, typically corresponding to the major site. The delay, τ, was set to $1/(2\Delta\nu_{cis\text{-}trans})$, where $\Delta\nu_{cis\text{-}trans}$ is the frequency difference (in Hz) between the *cis* and *trans* signals, which varied with substituent from 100 to 489 Hz. The variable delays, VD, were chosen from a range of 10 ms to 5 s, and the relaxation delay (RD) was typically 30 seconds. Data were transferred over a parallel interface to an SGI INDY workstation for

processing. Line intensity measurements of these data were obtained via the XWINNMR package, and were analysed with CIFIT.[33]

The assignment of the major and minor to *cis* and *trans* conformation was achieved with a gradient NOESY experiment, at 254 K, where the exchange rate is effectively zero (see figure 4.2). The exchange mechanism for the methyl resonances was determined with an gradient EXSY experiment in the slow-exchange regime at 270 K (see figure 4.3).

Lineshape analysis was performed with the MEXICO and MEX program.[6,8] MEXICO and MEX simulate lineshapes of exchanging systems with and without scalar coupling, respectively see figure 4.4 and 4.5). The simulated spectra are directly imported into the Bruker XWINNMR program on a Silicon Graphics Indy computer and compared with experiment using the dual display mode. The chemical shifts and coupling constants were obtained by simulating the static spectra (see figure 4.6) using XSIM available from K. Marat (University of Manitoba).

Molecular orbital calculations and atoms in molecules analysis

Restricted Hartree-Fock calculations were performed using Gaussian 94[69] with an IBM RS 6000 470 series computer. Calculations were performed only on the five-membered ring including the amide group and substituents, the second five-membered ring was not included (see Figure 4.9). Optimum geometries of both the *cis* and *trans* conformers (see Figure 4.9) were calculated with the 6-31G** basis set. Only the H, CH_3, OCH_3 and $C(CH_3)=CH_2$ derivatives were investigated, due to restricted cpu time. The transition state calculations were performed on the H, CH_3 and $C(CH_3)=CH_2$ derivatives using the QST3 method of searching for saddle-points in the energy surface, available in Gaussian 94. For the OCH_3 derivative, all attempts at finding the transition state failed.

Topological features of the electron densities were analysed with EXTREME, which is a program developed in Dr R.F.W. Bader's laboratory. The parameters $\rho(r)$ and $\nabla^2\rho(r)$ were determined at the bond critical points. The atomic populations and energies were computed using PROAIMV,[92] developed by the same group. This software package finds the interatomic surfaces, and uses them for integration boundaries. All integrations were carried out to $L < 0.001$ au. Atomic energies were also divided into their contributions from repulsion and attractive potential energy terms.

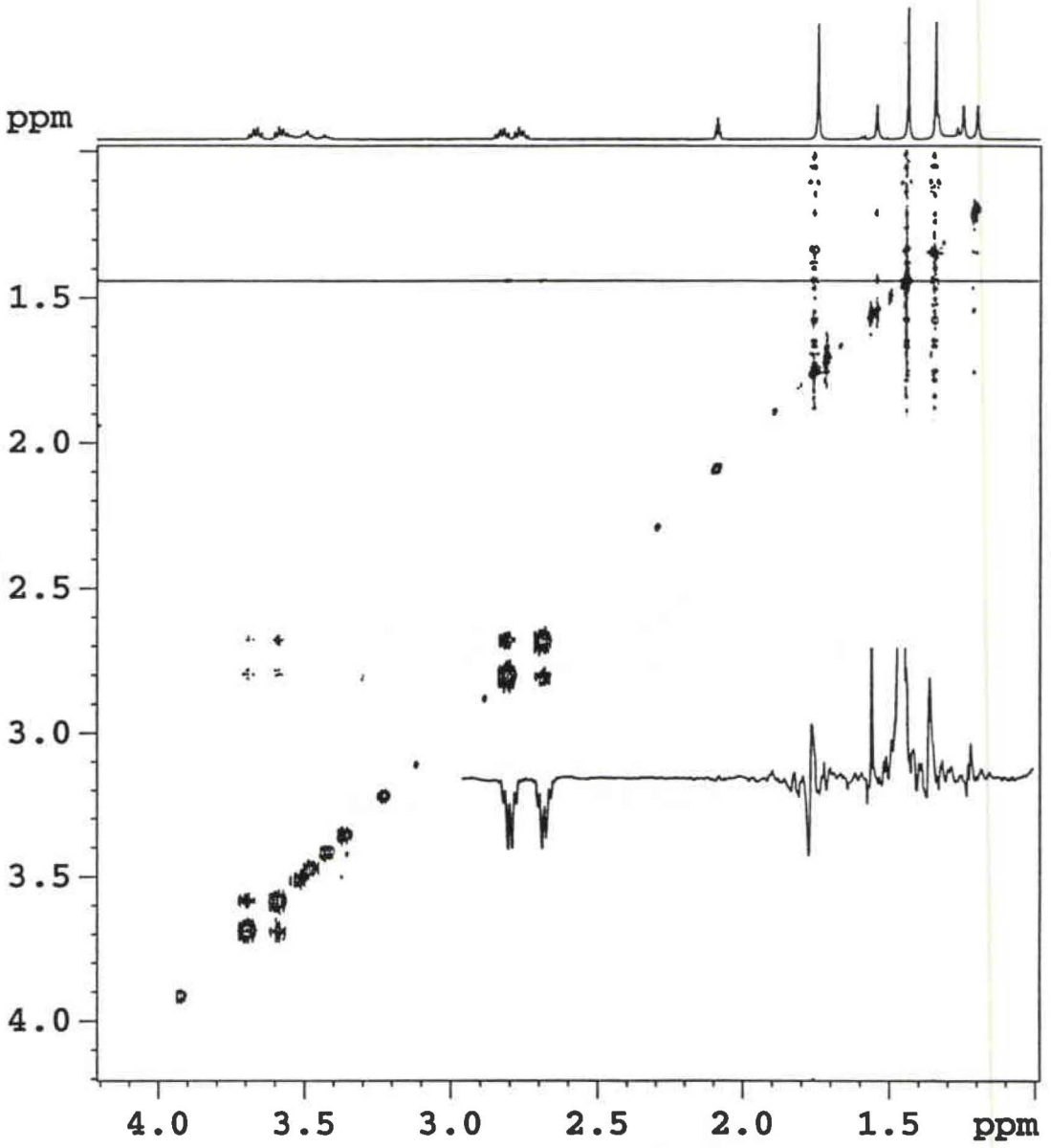

Figure 4.2 Gradient NOESY spectrum of the methyl derivative in acetone at 254 K. The insert is a slice indicated by the line. The cross-peaks at 2.7×1.45 ppm and 2.8×1.45 ppm show that the major conformation has the *cis* geometry.

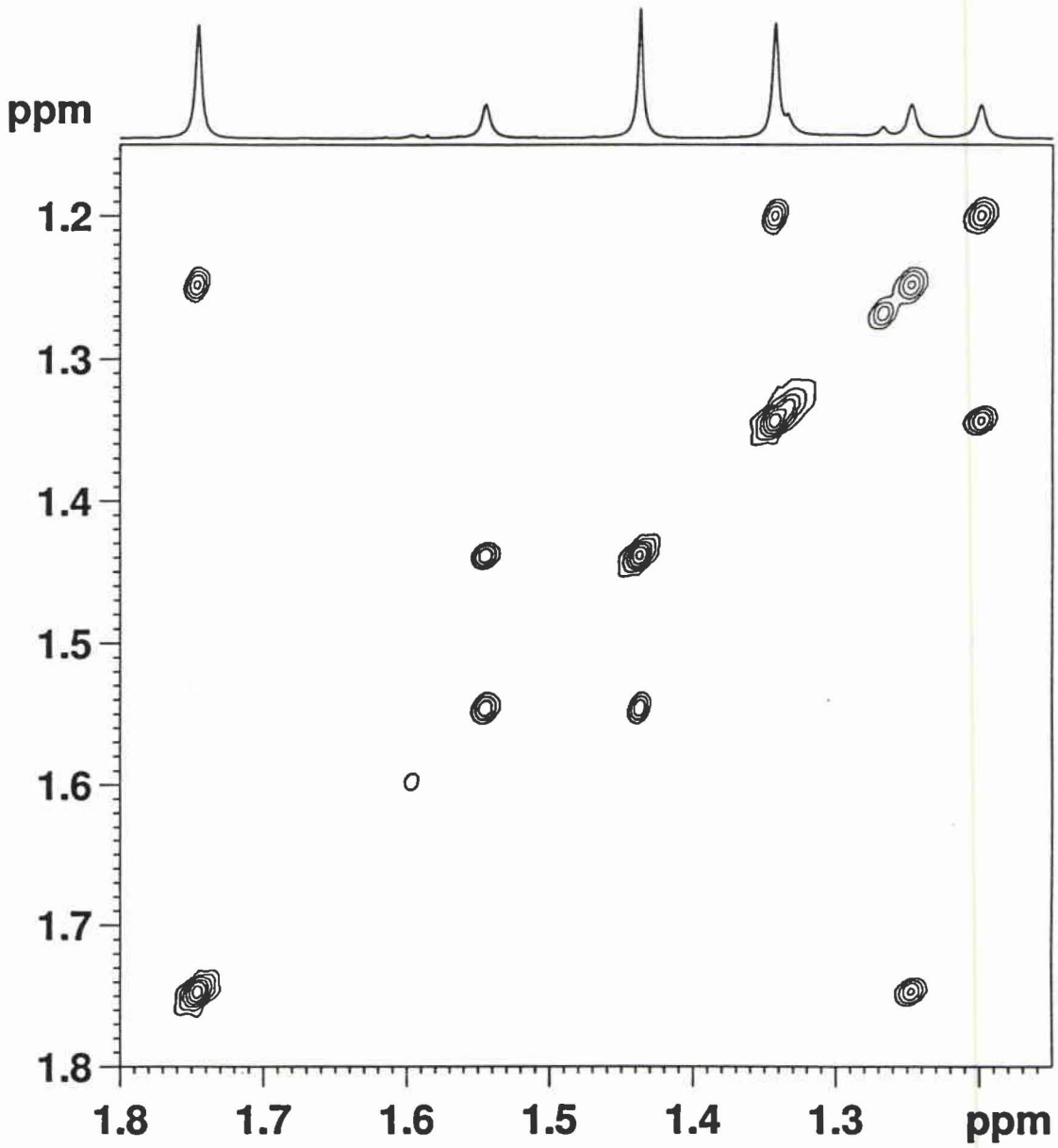

Figure 4.3 Gradient EXSY spectrum of the methyl region of the methyl derivative in acetone-d_6 at 270 K. The cross-peaks indicate which minor methyl resonance exchanges with a given major methyl resonance.

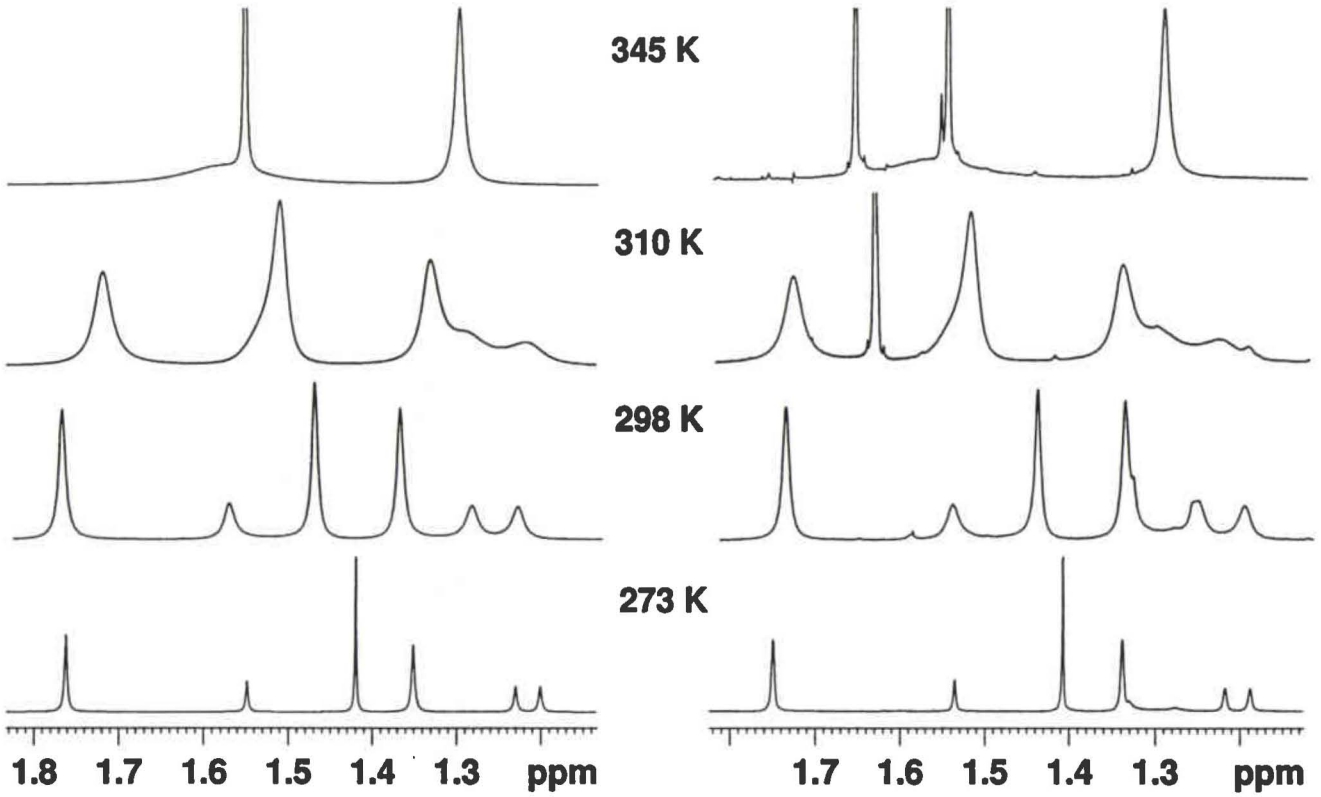

Figure 4.4 Line shape analysis of the methyl region of the methyl derivative in toluene-d_8 from 273 to 345 K. Simulated spectra are on the left, and were computed with MEX.

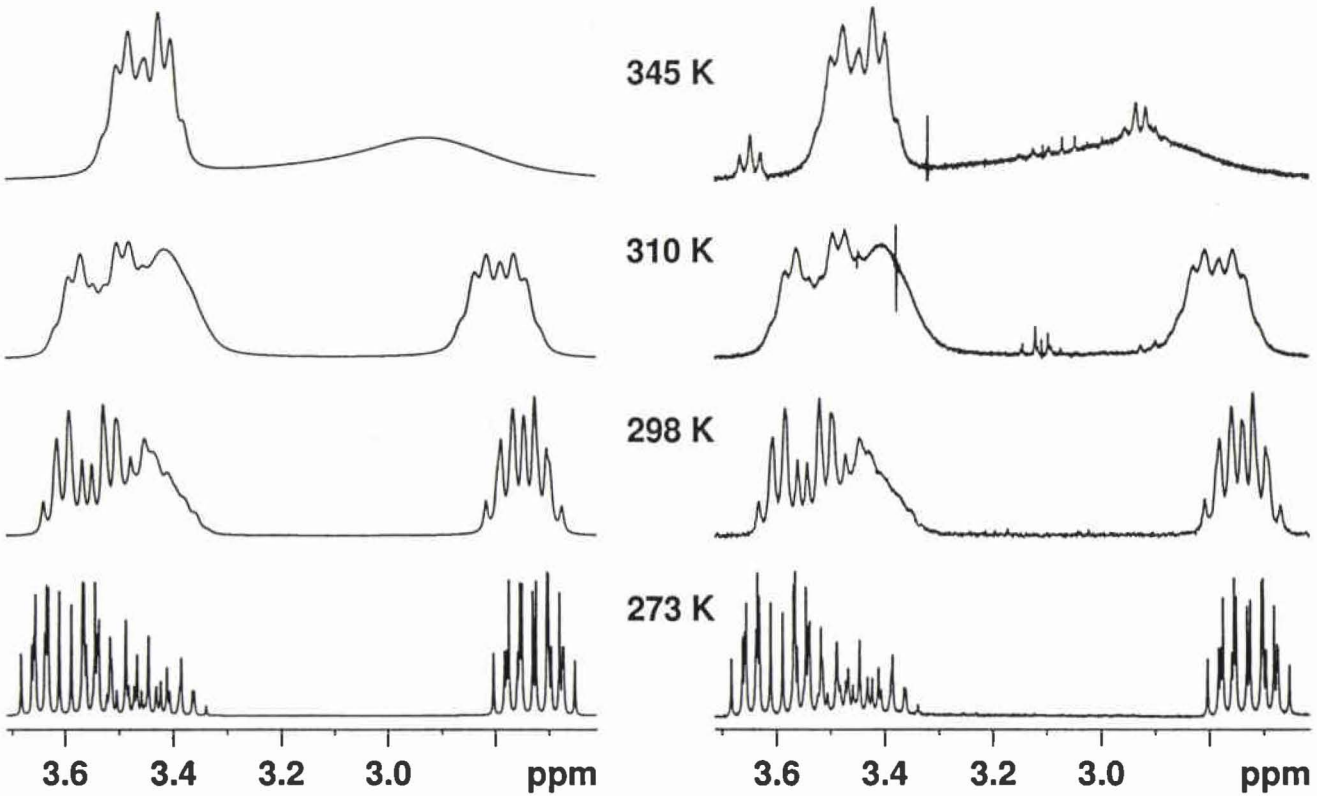

Figure 4.5 Lineshape analysis of the ring protons of the methyl derivative in toluene-d_8 from 273 to 345 K. Simulated spectra are on the left and were computed using MEXICO.

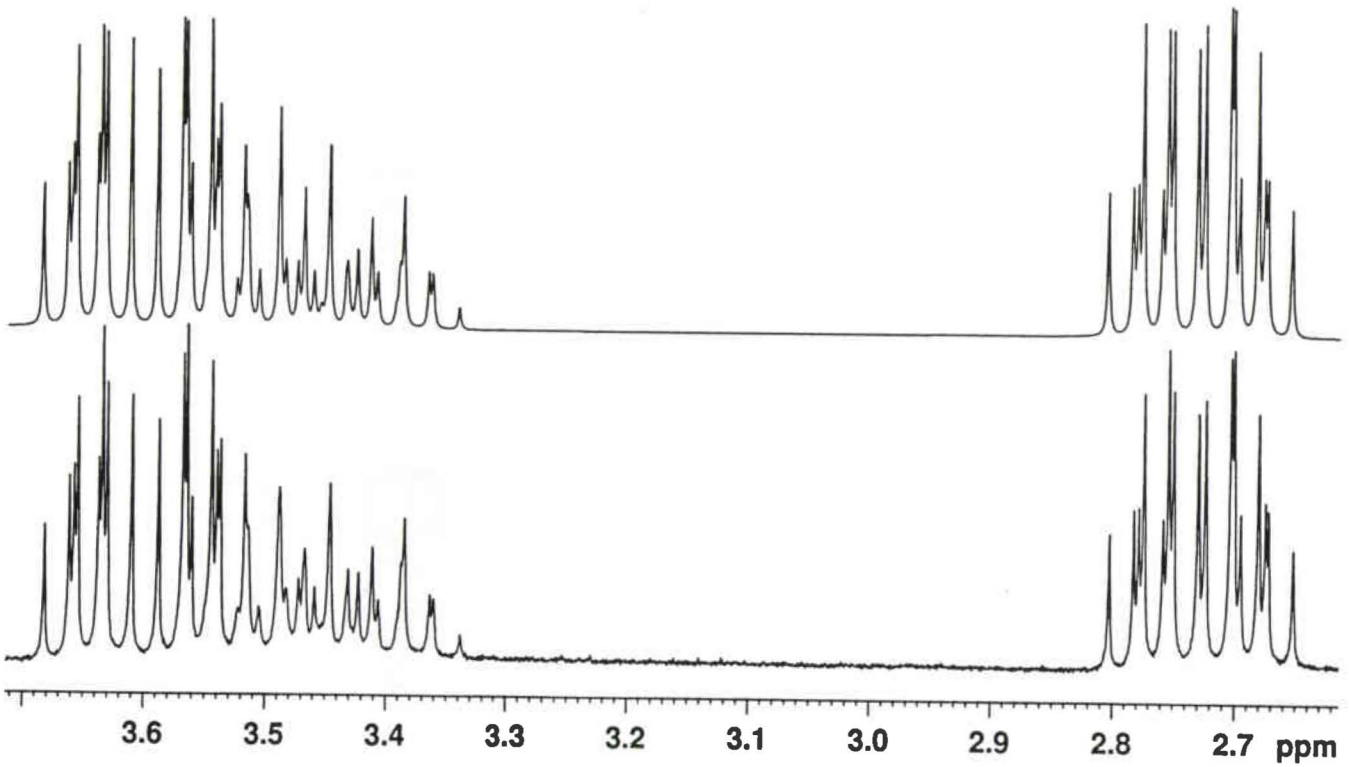

Figure 4.6 Experimental and simulated spectrum of the ring protons in the methyl derivative in acetone-d_6. Simulation was done with XSIM.

Table 4.1

Gibbs' Free Energies of spiro-fused oxazolidine derivatives and N,N' dimethylaminocarbonyl analogs

R	$\Delta G^{\dagger}$			ΔG^{0}	
	Toluene	Acetone	Analog	Toluene	Acetone
H	75	74	87	6	4
CH_3	68		72	2	
OCH_3	64		74	1	
$C(CH_3)=CH_2$	52	53	59	1	3
Ph	54	55	65	2	4
p-OCH_3 Ph		52	61		7
p-NO_2 Ph		59	69		4

All values in kJ mol^{-1} and have errors of approximately ± 1 kJ mol^{-1}. Data for the analogues is taken from reference(101). Gas-phase data for the analogues can be obtained from reference (102).

Results

The Eyring plots of the H, CH_3, OCH_3, $C(CH_3)=CH_2$ and phenyl derivatives in toluene are shown in Figure 4.7. Those of the H, $C(CH_3)=CH_2$, phenyl, *p*-methoxyphenyl, and *p*-nitrophenyl compounds in acetone are shown in Figure 4.8. Note that the graphs include the intercept at 1/T = 0, to aid in judging the error in the entropy of activation. The equilibrium constants for unequally-populated systems were measured at low temperature by integrating the methyl resonances of the major and minor conformers. Due to the large chemical shift differences, it was possible to obtain equilibrium constants at several temperatures. This allowed prediction at high temperature by extrapolation using the van't Hoff isochore. Rate measurements were

made over a wide temperature range, *ca.* 100°C. The activation parameters are shown in Tables 4.1, 4.2 and 4.3. Uncertainties in $\Delta H^{\dagger}$ and $\Delta S^{\dagger}$ are estimated to be in the range of 1 kJ/mol and 10 J/mol K, respectively.

To determine whether the ring changes geometry between *cis* and *trans* forms, the vicinal coupling constants between the methylene protons of the ring were measured for the methyl derivative. This was achieved with XSIM (available from K. Marat, University of Manitoba), a program that simulates static NMR spectra. The iterated spectral parameters are given in Table 4.4. The simulated spectrum is seen in Figure 4.6.

The barriers of the H, CH_3, and $C(CH_3)=CH_2$ derivatives, from MO calculations at the HF/6-31g** level are shown in Table 4.1. These are to be compared with the measured enthalpies of activation, $\Delta H^{\dagger}$. Throughout this analysis, the lowest energy transition states were used where the carbonyl group was gauche to both ring carbons. The electron density and the Laplacian are shown in Tables 4.5 and 4.6 (Δ denotes the change in value going from *trans* to the transition state). Table 4.7 contains atomic populations, and the atomic energies of N, C and O. These energies are divided into V_{ne}, V_{neo} and V_{rp}. The values in the parentheses represent changes when going to the transition state.

Table 4.2

Enthalpies of the barrier and the equilibrium constants in spiro-fused oxazolidine derivatives

R group	$\Delta H^{\dagger}$			ΔH^{0}		
	Toluene	Acetone	Calc'd	Toluene	Acetone	Calc'd
H	80	79	77.1	5.3	3.8	2.9
CH_3	70		66.1	2.3		2.4
OCH_3	63			2.4		
$C(CH_3)=CH_2$	55	57	48.0	1.4	5.2	0.1
Ph	57	58		3.5	7.0	
p-OCH_3 Ph		54			2.9	
p-NO_2 Ph		60			7.4	

All values in kJ mol^{-1} and have errors of approximately ± 2 kJ mol^{-1}

Table 4.3

Entropies of the barrier and the equilibrium constants in spiro-fused oxazolidine derivatives

R	$\Delta S^{\dagger}$		ΔS^{0}	
	Toluene	Acetone	Toluene	Acetone
H	18	4	0	0
CH_3	4		0	
OCH_3	0		4	
$C(CH_3)=CH_2$	11	5	0	8
Ph	12	7	4	12
p-OCH_3 Ph		3		-13
p-NO_2 Ph		7		10

All values in J K^{-1} mol^{-1} have statistical errors of approximately ± 10 J K^{-1} mol^{-1}

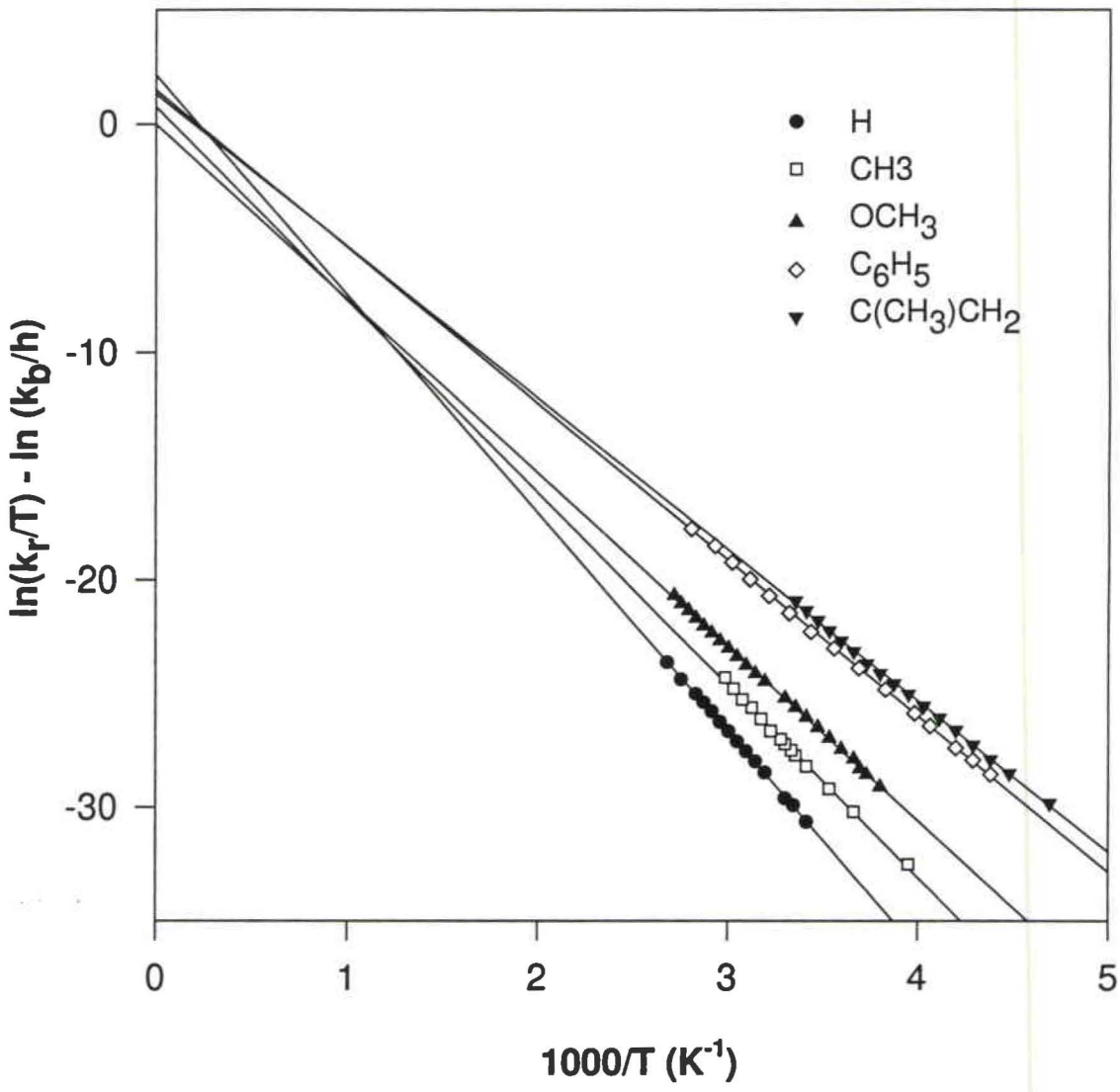

Figure 4.7 Eyring plot for the H, CH_3, OCH_3, $C(CH_3)=CH_2$ and C_6H_5 derivatives in toluene-d_8 using rate data obtained from NMR chemical exchange measurements.

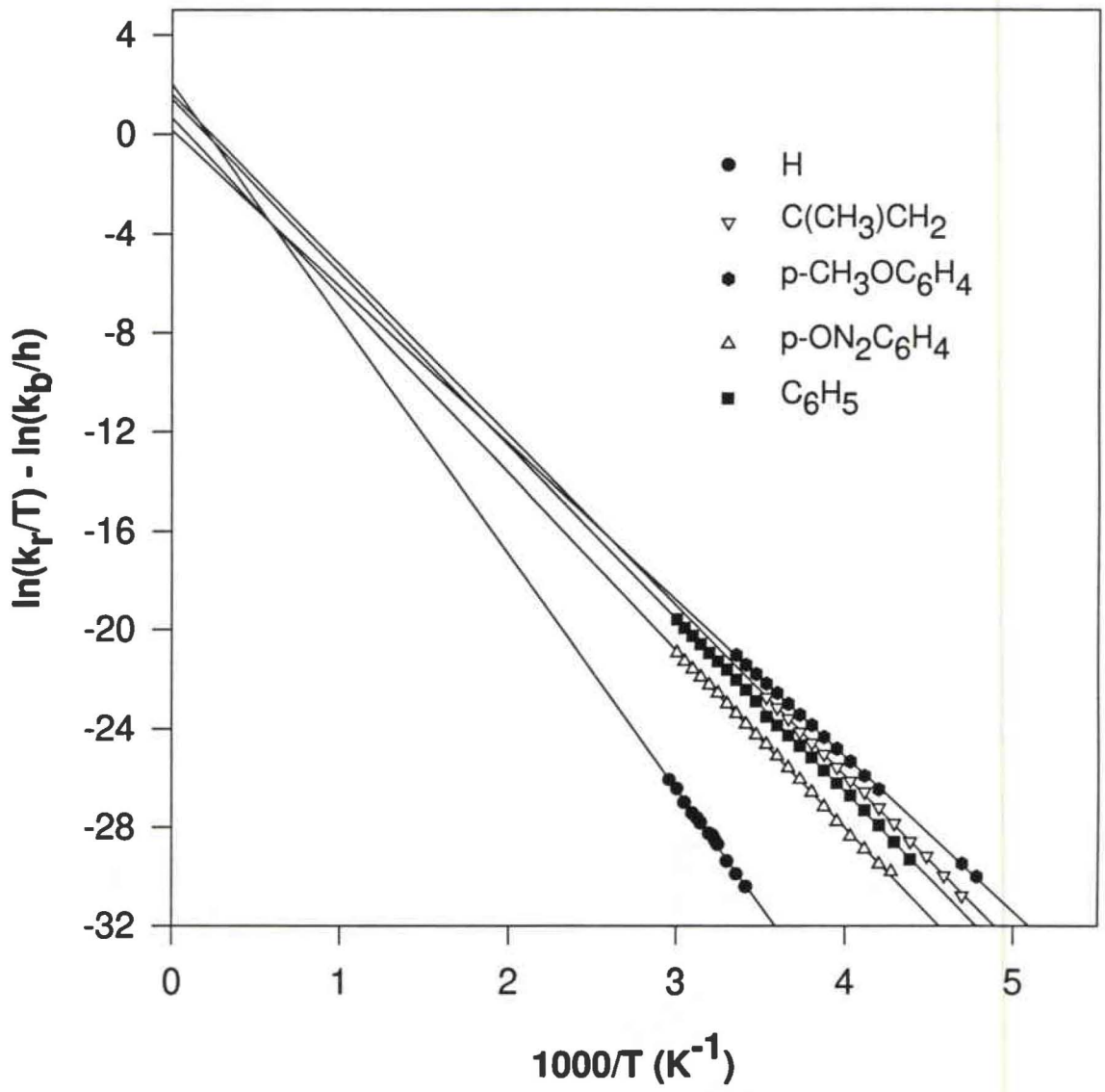

Figure 4.8 Eyring plot for the H, $C(CH_3)=CH_2$, C_6H_5, *p*-$NO_2C_6H_4$ and *p*-$OCH_3C_6H_4$ derivatives in acetone-d_6 using rate data obtained from NMR chemical exchange measurements.

Table 4.4

^{1}H NMR spectral parameters for the methyl derivative in toluene at 240 K at 300.13 MHz.

	Major	Minor		Major	Minor
ν_A(C3)	1097.2	1011.3	$^2J_{A,B}$	-8.25	-8.26
	(3.656)	(3.370)	$^3J_{A,C}$	7.34	5.41
ν_B(C3)	1065.5	993.9	$^3J_{A,D}$	5.96	7.46
	(3.550)	(3.312)	$^3J_{B,C}$	6.14	6.96
ν_C(C8)	822.7	1034.3	$^3J_{B,D}$	6.95	7.07
	(2.741)	(3.446)	$^2J_{C,D}$	-8.67	-10.70
ν_D(C8)	786.1	1047.1	$^5J_{C,CH3}$	0.12	0.28
	(2.619)	(3.489)	$^5J_{D,CH3}$	0.14	0.28

All chemical shift and coupling constants are given in Hz, at a spectrometer frequency of 300.13 MHz. Chemical shifts in parentheses are in ppm with respect to TMS.

Discussion

Rotational barriers of amides have been studied extensively using NMR methods.[2,9,11,13,14,25,29,76,77,83,84,103-107] The effects of substituent[9,11,14,106,107] and solvent[14,35,78,103,108,109] have received considerable attention. However, many barrier determinations were performed with few rate measurements. These often covered a narrow temperature range and employed only one experimental technique. As a result most barriers were reported as free energies, without a separation of enthalpy and entropy. Using a combination of selective inversion and lineshape methods, rate measurements can be made over a large temperature range, allowing the enthalpies of the barriers to be reported, which are more compatible with calculations.

In this work, the effects of the substituents on the carbonyl carbon corresponded to previous investigations.[9,11,14,35,79,101,103,106] Replacing H with CH_3 caused the activation enthalpy to decrease by 10 kJ mol^{-1}, which is in line with values between 10 and 13.5 kJ mol^{-1} in the literature.[9,79,103,110] The barriers were typically lower than in dimethylaminocarbonyl analogs (Table 4.1 and Scheme 4.1), which can be attributed to ring strain forcing the nitrogen to take on greater sp^3 character in the low energy geometries. This is consistent with studies done by Pinto,[106] who observed significant variation in amide barriers with changes in ring size. In the current study, the activation enthalpy for the OCH_3 substituent was 16 kJ/mol smaller than that of the H derivative, which is quite different from the literature.[9] Rather than this molecule being considered as a methoxyl derivative of an amide, it can be regarded as a carbamate ester. Carbamates are known to be similar to amides,[102,111] but they do not behave identically. The $C(CH_3)=CH_2$ substituent lowered the barrier by 24 kJ mol^{-1}, similar to values for analogous systems.[112] The phenyl substituents decreased the barrier by as much as 25 kJ mol^{-1}, where the effect of the substituents in the *para* position of the ring were as expected. The *p*-nitrophenyl substituent had a barrier 4 kJ mol^{-1} larger than the phenyl substituent and the *p*-methoxyphenyl was 3 kJ mol^{-1} smaller.

The computed barriers correspond reasonably well to experiment, in both trend and absolute value (Table 4.2). The computed barriers are consistently smaller, by as much as 7 kJ mol^{-1} for the $C(CH_3)=CH_2$ derivative. This may be due to the fact that solvation almost always increases barriers, relative to gas-phase values.[101]

The methyl groups in the major conformer are all deshielded with respect to those in the minor site, which suggest that the *cis* form predominates. This was confirmed by one- and two-dimensional NOE experiments, which showed interactions between the N-methyl of the major conformer and the two low-frequency ring protons at 2.62 and 2.74 ppm.(see figure 4.2) Changes in the vicinal couplings in the ring between the major and minor conformers indicate small changes in the average conformation of the ring between amide conformations (Table 4.4). All four vicinal couplings fall within 5 to 7.5 Hz, which are typical values for five-membered rings.[113] These are larger than normal *gauche* couplings and smaller than regular *trans* couplings suggested by Karplus type relationships,[114-117] which implies that the torsional angles are closer to 30° for a *gauche*-like and 150° for *trans*-like couplings. In both these ranges of dihedral angles, vicinal couplings are similar, thus it is not possible to quantify the change in the ring pucker.

The computed behaviour of the amide portion of the oxazolidines was similar to that of formamide. MO calculations suggest that the nitrogen is planar in the *trans* geometry and pyramidal in the transition state (see figure 4.9). The C-N bond length increases much more than the C-O bond decreases when going to the transition state from the *trans* form. X-ray crystallographic data of a series of 3,4-dihydro-2-oxo-1,4-propanoquinolines,[80,118,119] which contain severely distorted amide fragments, indicated similar behaviour.

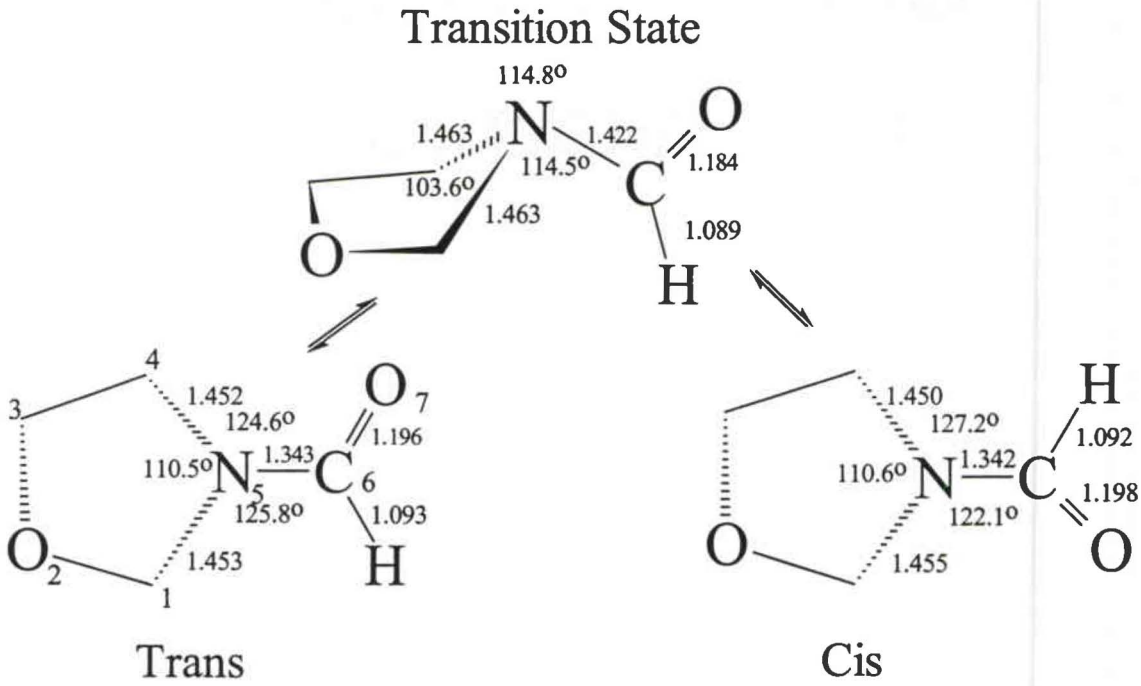

Figure 4.9 Some geometrical changes in the H derivative during the rotational process predicted by MO calculations.

Further similarity between formamide and these oxazolidines are seen in the electron density at the bond critical point, ρ(bcp), and the Laplacian, $\nabla^2\rho$(bcp). Values of these are given in Tables 4.5 and 4.6 for the C-N and C-O bonds. Table 4.7 gives values of the calculated atomic properties, E(Ω), N(Ω), $V_{neo}(\Omega)$, $V_{ne}(\Omega)$ and $V_{rp}(\Omega)$ of C, N and O in the amide group. The electron density at the bcp of the C-N bond diminishes by about 7% in the transition state with respect to the *cis* form for all derivatives (Table 4.5). The electron density at the bcp of the C-O bond is left virtually unchanged. The Laplacian at the C-N bcp (Table 4.6) is nearly identical to formamide in both the *trans*

and transition forms. In all three derivatives, when going to the transition states there is a net transfer of charge from N to C of *ca.* 0.2 a.u., and the charge on O changes much less. Nitrogen is destabilised by the loss of charge, which is seen as an increase $V_{neo}(N)$. Carbon, on the other hand, is stabilised by the gain in charge, thus $V_{neo}(C)$ decreases. As in formamide, the increase in attractive energies of N on going to the transition state, ΔV_{ne}, is greater than the corresponding decrease in the repulsive energies, ΔV_{rp}. In carbon, the attractive energies decrease more than the repulsive energies increase, causing the carbon to be stabilised greatly.

The Laplacian seems to be the most sensitive to changes in substituent. In C-N bond of the *trans* conformer, it decreases in the order H, CH_3, $C(CH_3)=CH_2$, but OCH_3 is anomalous (Table 4.6). The absolute value of the change in the Laplacian from *trans* to the saddle-point geometry decreases in the same order. Unfortunately, the search for the saddle point for the OCH_3 derivative failed, so data are not available for it. In all three derivatives available, the Laplacian in the transition state approaches the same value (*ca.* -1.2 a.u.).

Similarly, the trends in the atomic properties (Table 4.7) follow the barriers, but the methoxyl derivative is the exception. In general, there is no single dominant atomic contribution to the energy. The carbon and the nitrogen give the major contribution, but the combination of their energies does not duplicate the trend in the experimental barriers. This may be due to inaccuracies in the atomic integrations, which are good to roughly one part in 1000. For a relatively large system such as this, the energies are determined by a balancing of the energies of all the atoms.

Table 4.5

Electron density at bond critical points of interest in the amide portion of the molecules.

ρ	H		CH_3		OCH_3		$C(CH_3)=CH_2$	
	trans	Δ	*trans*	Δ	*trans*	Δ	*trans*	Δ
N_5-C_6	0.335	-0.024	0.329	-0.025	0.345	N/A	0.329	-0.023
N_5-C_4	0.266	0.001	0.268	-0.002	0.266	N/A	0.265	0.004
C_6-O_7	0.430	0.004	0.426	0.007	0.437	N/A	0.426	0.003
C_6-R_8	0.299	0.004	0.271	0.005	0.316	N/A	0.277	0.006

Values are reported for the *trans* conformers along with their change when going to the transition state. Attempts to find the transition state for the methoxyl derivative failed. The columns are ordered according to the measured barrier to rotation. All values are in atomic units.

Table 4.6

The Laplacian of the electron density at bond critical points of interest in the amide portion of the molecules.

$\nabla^2\rho$	H		CH_3		OCH_3		$C(CH_3)=CH_2$	
	trans	Δ	*trans*	Δ	*trans*	Δ	*trans*	Δ
N_5-C_6	-0.726	-0.503	-0.750	-0.415	-1.005	N/A	-0.847	-0.342
N_5-C_4	-0.666	-0.165	-0.713	-0.129	-0.627	N/A	-0.699	-0.142
C_6-O_7	0.368	0.421	0.297	0.400	0.180	N/A	0.319	0.334
C_6-R_8	-1.196	-0.043	-0.779	-0.026	-0.218	N/A	-0.815	-0.023

The values in the *trans* conformer are reported along with its corresponding change when going to the transition state. The columns are ordered according to the measured barrier to rotation. All values for the Laplacian are given in atomic units.

Table 4.7

The atomic populations (N) and energy contributions of N_5, C_6 and O_7 for the *trans* conformers of the H, CH_3, OCH_3, and $C(CH_3)=CH_2$ derivatives.

Nitrogen	H	CH_3	OCH_3	$C(CH_3)=CH_2$
N	8.63 (-0.26)	8.63 (-0.27)	8.64	8.60 (-0.23)
E[a]	-55.48 (0.27)	-55.46 (0.30)	-55.50	-55.40 (0.22)
V_{neo}[b]	-136.56 (1.17)	-136.52 (1.24)	-136.63	-136.34 (0.97)
V_{ne}[c]	-252.79 (6.78)	-266.48 (8.33)	-278.79	-283.35 (6.34)
V_{rp}[d]	141.79 (-6.21)	155.52 (-7.73)	167.77	172.50 (-5.89)
Carbon				
N	4.04 (0.20)	4.15 (0.21)	3.38	4.16 (0.21)
E	-36.55 (-0.16)	-36.61 (-0.17)	-36.09	-36.63 (-0.15)
V_{neo}	-81.61 (-0.93)	-82.07 (-0.96)	-78.84	-82.15 (-0.92)
V_{ne}	-130.24 (-3.21)	-142.02 (-5.29)	-136.00	-153.94 (-4.32)
V_{rp}	57.13 (2.89)	68.77 (4.94)	63.8	80.66 (4.02)
Oxygen				
N	9.39 (-0.05)	9.41 (-0.04)	9.44	9.40 (-0.08)
E	-75.60 (-0.02)	-75.60 (-0.02)	-75.66	-75.60 (-0.01)
V_{neo}	-185.59 (0.25)	-185.67 (0.18)	-185.90	-185.63 (0.19)
V_{ne}	-272.41 (-2.07)	-289.02 (-7.11)	-305.27	-310.38 (-1.69)
V_{rp}	121.17 (2.04)	137.780(7.06)	153.91	159.15 (1.67)

[a]E is the total energy of the basin (in a.u.). [b]V_{neo} is the basin attractive energy (in a.u.), to its own nucleus only as given in eqn 4.5. [c]V_{ne} is the total attractive energy (in a.u.) of the basin as in eqn 4.4. [d]V_{rp} is the total basin repulsion energy (in a.u.). The values in the parenthesis indicate the change in the respective value upon going to the transition state.

Conclusions

This study's main goal was to look into the effect of substituents on amide rotational barriers to test recent models. The experimental results on the spiro-fused oxazolidines follow the trends in simpler substituted amides. Calculations on the system, combined with an Atoms in Molecules (AIM) analysis, show similarities to calculations on formamide. However, the trends with substituent are not accurately reflected in the calculated results. For molecules of this size, the AIM analysis is helpful in interpreting the data, but it does not improve on the more traditional resonance model of the barrier.

References

1) Bain, A.D.; Hazendonk, P. *J.Phys.Chem.* **1997**, *101 A*, 7182-7188.

2) Gutowsky, H.S.; Holm, C.H. *J.Chem.Phys.* **1956**, *25*, 1228-1234.

3) Szymanski, S.; Witanowski, M.; Gryff-Keller, A.M.In *Annual reports on NMR spectroscopy*; Webb, G.A., Ed.; Academic Press: London, 1978; pp 227-289.

4) Piette, L.H.; Anderson, W.A. *J.Chem.Phys.* **1959**, *30*, 899-908.

5) Orrell, K.G.; Sik, V. *Annu.Rep.NMR Spectrosc.* **1987**, *19*, 79-173.

6) Bain, A.D.; Duns, G.J. *J.Magn.Reson.* **1995**, *112 A*, 258-260.

7) Binsch, G. *J.Am.Chem.Soc.* **1969**, *91*, 1304-1309.

8) Bain, A.D.; Duns, G.J. *Can.J.Chem.* **1996**, *74*, 819-824.

9) Kessler, H. *Angew.Chem.Int.Ed.Engl.* **1970**, *9*, 219-235.

10) Inglefield, P.T.; Krakower, E.; Reeves, L.W.; Stewart, R. *Mol.Phys.* **1968**, *15*, 65-86.

11) Stewart, W.E.; Siddall, T.H. *Chem.Rev.* **1970**, *70*, 517-551.

12) Friedl, Z.; Bohm, S.; Goljer, I.; Piklerova, A.; Poorova, D.; Rickova, A.; Kovac, J. *Coll.Czech.Chem.Commun.* **1987**, *52*, 409-424.

13) Haushalter, K.A.; Lau, J.; Roberts, J.D. *J.Am.Chem.Soc.* **1996**, *118* , 8891-8896.

14) Turnbull, M.M.; Nelson, D.J.; Lekouses, W.; Sarnov, M.L.; Tartarini, K.A.; Huang, T. *Tetrahedron* **1990**, *46*, 6613-6622.

15) Saurez, C.; LeMaster, C.B.; LeMaster, C.L.; Tafazzoli, M.; True, N.S. *J.Phys.Chem.* **1990**, *94*, 6679-6683.

16) Laidler, K.J.*Chemical Kinetics*; McGraw Hill: New York, 1965.

17) Berg, U.; Sjostrand, U. *Org.Magn.Reson.* **1978**, *11*, 555-560.

18) Tyson, R.L.; Weil, J.A. *J.Phys.Chem.* **1990**, *94*, 3951-3958.

19) Onsager, L. *J.Am.Chem.Soc.* **1936**, *58*, 1486-1493.

20) Tomasi, J.; Persico, M. *Chem.Rev.* **1994**, *94*, 2027-2094.

21) Miertus, S.; Tomasi, J. *Chem.Phys.* **1982**, *65*, 239-245.

22) Miertus, S.; Scrocco, E.; Tomasi, J. *Chem.Phys.* **1981**, *55*, 117-129.

23) Birnstock, F.; Hofman, H.J.; Kohler, H.J. *Theoret.Chim.Acta (Berl.)* **1997**, *42*, 311-323.

24) Wong, M.W.; Frisch, M.J.; Wiberg, K.B. *J.Am.Chem.Soc.* **1991**, *113*, 4776-4782.

25) Wong, M.W.; Wiberg, K.B.; Frisch, M.J. *J.Am.Chem.Soc.* **1992**, *114*, 1645-1652.

26) Wiberg, K.B.; Wong, M.W. *J.Am.Chem.Soc.* **1993**, *115*, 1078-1084.

27) Wong, M.W.; Wiberg, K.B.; Frisch, M.J. *J.Chem.Phys.* **1991**, *95*, 8991-8998.

28) Dillet, V.; Rinaldi, D.; Bertran, J.; Rivail, J.L. *J.Chem.Phys.* **1996**, *23*, 9437-9444.

29) Bain, A.D.; Duns, G.J.; Ternieden, S.; Ma, J.; Werstiuk, N.H. *J.Phys.Chem.* **1994**, *98*, 7458-7463.

30) Bain, A.D.; Duns, G.J.; Rathgeb, F.; Vanderkloet, J. *J.Phys.Chem.* **1995**, *99*, 17338-17343.

31) Bain, A.D.; Duns, G.J. *J.Magn.Reson.* **1994**, *109 A*, 56-64.

32) Bain, A.D.; Cramer, J.A. *J.Phys.Chem.* **1993**, *97*, 2884-2887.

33) Bain, A.D.; Cramer, J.A. *J.Magn.Reson.* **1993**, *103 A*, 217-222.

34) Wiberg, K.B.; Keith, T.A.; Frisch, M.J.; Murko, M. *J.Phys.Chem.* **1995**, *99*, 9072-9079.

35) Wiberg, K.B.; Rablen, P.R.; Rush, D.J.; Keith, T.A. *J.Am.Chem.Soc.* **1995**, *117*, 4261-4270.

36) Drakenberg, T.; Carter, R.E. *Org.Magn.Reson.* **1975**, *7*, 307-308.

37) Forsen, S.; Hoffman, R.A. *J.Chem.Phys.* **1963**, *39*, 2892-2901.

38) Hoffman, R.E.; Forsen, S. *Prog.Nucl.Magn.Reson.Spectrosc.* **1966**, *1* , 15-204.

39) Tomlinson, G. *J.Magn.Reson.* **1983**, *52*, 374-385.

40) Alagona, G.; Ghio, C.; Igual, J.; Tomasi, J. *J.Molec.Struct.(Theochem)* **1990**, *204*, 253-283.

41) Benassi, R.; Folli, U.; Schenetti, L.; Taddei, F. *Advances in Heterocyclic Chemistry* **1997**, *41*, 75-186.

42) Liegeous, C.; Barker, J.M.; Lumbroso, H. *Bull.Soc.Chim.Fr.* **1978**, *7-8*, I-329-I-332

43) Benassi, R.; Folli, U.; Mucci, A.; Schenetti, L.; Taddei, F. *Magn.Reson.Chem.* **1987**, *25*, 804-810.

44) Benassi, R.; Folli, U.; Schenetti, L.; Taddei, F. *J.Chem.Soc.Perkin Trans.2* **1988**, 1501-1507.

45) Bertran, J.F.; Rodriguez, M. *Org.Magn.Reson.* **1974**, *6*, 525-527.

46) Roques, B.; Combrisson, S.; Riche, C.; Pascard-Billy, C. *Tetrahedron* **1970**, *26*, 3555-3567.

47) Chadwick, D.J. *J.Chem.Soc.Perkin Trans.2* **1976**, 451-452.

48) Martin, M.L.; Roze, J.-C.; Martin, G.J.; Fournari, P. *Tetrahedron Lett.* **1970**, *39*, 3407-3410.

49) Abraham, R.J.; Chadwick, D.J.; Sancassan, F. *Tetrahedron* **1982**, *38*, 3245-3254.

50) Roques, B.; Combrisson, S.; Wehrli, F. *Tetrahedron Lett.* **1975**, *12* , 1047-1050.

51) Roques, B.; Fournie-Zaluski, M.C. *Org.Magn.Reson.* **1971**, *3*, 305-312.

52) Chadwick, D.J.; Meakins, G.D.; Richards, E.E. *Tetrahedron Lett.* **1974**, *36*, 3183-3184.

53) Caccamese, S.; Montaudo, G.; Recca, A.; Fringuelli, F.; Taticchi, A. *Tetrahedron* **1974**, *30*, 4129-4135.

54) Chadwick, D.J.; Chambers, J.M.; Meakins, G.D.; Snowden, R.L. *J.Chem.Soc.,Chem.Commun.* **1971**, 624-625.

55) Abraham, R.J.; Chadwick, D.J.; Sancassan, F. *Tetrahedron* **1982**, *38*, 1485-1491.

56) Barili, P.L.; Lunazzi, L.; Veracini, C.A. *Mol.Phys.* **1972**, *24*, 673-677.

57) Montaudo, G.; Caccamese, S.; Librando, V.; Maravigna, P. *Tetrahedron* **1973**, *29*, 3915-3923.

58) Petrongolo, C. *Chem.Phys.Lett.* **1976**, *42*, 512-516.

59) Miller, F.A.; Fateley, W.G.; Witkowski, R.E. *Spectrochimica Acta* **1967**, *23A*, 891-908.

60) Allen, G.; Bernstein, H.J. *Can.J.Chem.* **1955**, *33*, 1055-1061.

61) Dahlqvist, K.-I.; Forsen, S. *J.Phys.Chem.* **1965**, *69*, 4062-4071.

62) Casarini, D.; Lunazzi, L.; Macciantelli, D. *J.Chem.Soc.Perkin Trans.2* **1985**, 1839-1844.

63) Benassi, R.; Folli, U.; Schenetti, L.; Taddei, F. *J.Chem.Soc.Perkin Trans.2* **1987**, 961-968.

64) Abraham, R.J.; Siverns, T.M. *Tetrahedron* **1972**, *28*, 3015-3023.

65) Han, I.; Kim, C.K.; Jung, H.J.; Lee, I. *Theor.Chim.Acta* **1996**, *93*, 199-210.

66) Hore, P.J. *J.Magn.Reson.* **1983**, *55*, 283-300.

67) Muhandiram, D.R.; McClung, R.E.D. *J.Magn.Reson.* **1987**, *71*, 187-192.

68) Bain, A.D.; Fletcher, D.A. *Mol.Phys.* **1998**, *95*, 1091-1098.

69) Frisch, M.J.; Truck, G.W.; Schlegel, H.B.; Gill, P.M.W.; Johnson, B.G.; Robb, M.A.; Cheeseman, J.R.; Keith, T.A.; Petersen, G.; Montgomery, J.A.; Raghavachari, K.; Al-Laham, M.A.; Zakrzewski, V.G.; Ortiz, J.V.; Forseman, J.B.; Cioslowski, J.; Stefanov, B.; Nanayakkara, A.; Challacombe, M.; Peng, C.Y.; Ayala, P.Y.; Chen, W.; Wong, M.W.; Andres, J.L.; Replogle, E.S.; Gomperts, R.; Martin, R.L.; Fox, D.J.; Binkley, J.S.; Defrees, D.J.; Baker, J.; Stewart, J.P.; Head-Gordon, M.W.; Gonzalez, C.; Pople, J.A. *Gaussian,Inc.,Pittsburgh Pa* **1995**,

70) *CRC Handbook of Chemistry and Physics*; The Chemical Rubber Co.: Cleveland, 1968; pp E-58-E-61

71) Dahlqvist, K.-I.; Forsen, S. *J.Phys.Chem.* **1965**, *69*, 1760-1761.

72) Kotzian, M.; Kreiter, C.G.; Michael, G.; Ozkar, S. *Chem.Ber.* **1983**, *116*, 3637-3658.

73) Naorem, H.; Kishore, N.; Suri, S.K. *Can.J.Chem.* **1989**, *67*, 648-650.

74) Bain, A.D.; Hazendonk, P.; Couture, P. *Can.J.Chem.* **1999**, *77*, 1340-1348.

75) Streitweiser, A.; Heathcock, C.H.; Kosower, E.M.*Introduction to Organic Chemistry*; MacMillan: New York, 1992;

76) Dahlqvist, K.-I.; Forsen, S. *J.Phys.Chem.* **1969**, *73*, 4124-4129.

77) Rogers, M.T.; Woodbrey, J.C. *J.Phys.Chem.* **1962**, *66*, 540-546.

78) Gillespie, R.J.; Birchall, T. *Can.J.Chem.* **1963**, *41*, 148-155.

79) Graham, L.L.; Diel, R.E. *J.Phys.Chem.* **1969**, *73*, 2696-2699.

80) Bennet, A.J.; Wang, Q.P.; Slebocka-Tilk, H.; Somayaji, V.; Brown, R.S.; Santarsiero, B.D. *J.Am.Chem.Soc.* **1990**, *112*, 6383-6385.

81) Laidig, K.E.; Cameron, L.M. *Can.J.Chem.* **1993**, *71*, 872-879.

82) Laidig, K.E.; Cameron, L.M. *J.Am.Chem.Soc.* **1996**, *118*, 1737-1742.

83) Orrell, K.G.; Sik, V.; Stephenson, D. *Prog.Nucl.Magn.Reson.Spectrosc.* **1990**, *22*, 141-208.

84) Sutherland, I.O. *Annu.Rep.NMR Spectrosc.* **1971**, *4*, 71-235.

85) Wiberg, K.B.; Breneman, C. *J.Am.Chem.Soc.* **1992**, *114*, 831-840.

86) Wiberg, K.B.; Laidig, K.E. *J.Am.Chem.Soc.* **1987**, *109*, 5935-5943.

87) Perrin, C.L. *J.Am.Chem.Soc.* **1991**, *113*, 2865-2868.

88) Lauvergnat, D.; Hiberty, P.C. *J.Am.Chem.Soc.* **1997**, *119*, 9478-9482.

89) Fogarasi, G.; Szalay, P.G. *J.Phys.Chem.* **1997**, *101 A*, 1400-1408.

90) Bader, R.F.W.*Atoms in Molecules: A Quantum Theory*; Clarendon Press: Oxford, 1994;

91) Bader, R.F.W.; Cheeseman, J.R.; Laidig, K.E.; Wiberg, K.B.; Breneman, C. *J.Am.Chem.Soc.* **1990**, *112*, 6530-6536.

92) Biegler-Konig, F.W.; Bader, R.F.W.; Tang, T. *J.Comp.Chem.* **1982**, *3*, 317-328.

93) Bain, A.D.; Duns, G.J. *Bull.Magn.Reson.* **1993**, *15*, 64-69.

94) Szymanski, S.; Witanowski, M.; Gryff-Keller, A.M. *Annu.Rep.NMR Spectrosc.* **1978**, *8*, 227-286.

95) Bader, R.F.W. *Acc.Chem.Res.* **1985**, *18*, 9-15.

96) Bader, R.F.W. *Int.J.Quantum Chem.* **1994**, *49*, 299-308.

97) Bader, R.F.W. *Chem.Rev.* **1991**, *91*, 893-928.

98) Couture, P.; Terlouw, J.K.; Warkentin, J. *J.Am.Chem.Soc.* **1996**, *118*, 4214-4215.

99) Couture, P.; Warkentin, J. *Can.J.Chem.* **1997**, *75*, 1264-1280.

100) Couture, P.; Warkentin, J. *Can.J.Chem.* **1997**, *75*, 1281-1294.

101) LeMaster, C.B. *Prog.Nucl.Magn.Reson.Spectrosc.* **1997**, *31*, 119-154.

102) Martin, M.L.; Mabon, F.; Trierweiler, M. *J.Phys.Chem.* **1981**, *85*, 76-78.

103) Siddall, T.H.; Stewart, W.E.; Knight, F.D. *J.Phys.Chem.* **1970**, *74* , 3580-3583.

104) Neuman, R.C.; Jonas, V. *J.Am.Chem.Soc.* **1968**, *90*, 1970-1975.

105) Drakenberg, T.; Forsen, S. *J.Phys.Chem.* **1970**, *74*, 1-7.

106) Pinto, B.M.; Grindley, T.B.; Szarek, W.A. *Magn.Reson.Chem.* **1986**, *24*, 323-331.

107) Bonacorso, H.G.; Caro, M.S.B.; Zanatta, N.; Martins, M.A.P. *Magn.Reson.Chem.* **1993**, *31*, 451-454.

108) Ou, M.C.; Chu, S.Y. *J.Phys.Chem.* **1995**, *99*, 556-562.

109) Maia, H.L.; Orrell, K.G.; Rydon, H.N. *J.Chem.Soc.,Chem.Commun.* **1971**, 1209-1210.

110) Mayne, C.L.; Alderman, D.W.; Grant, D.M. *J.Chem.Phys.* **1975**, *63*, 2514-2523.

111) Remko, M.; Scheiner, S. *J.Molec.Struct.(Theochem)* **1988**, *180*, 175-188.

112) Jackman, L.M.In *Dynamic Nuclear Magnetic Resonance Spectroscopy*; Jackman, L.M., Cotton, F.A., Eds.; Academic Press: New York, 1975; pp 203-252.

113) Silverstein, R.M.; Bassler, G.C.; Morril, T.C.*Spectrometric Identification of Organic Compounds*; John Wiley & Sons, Inc.: Toronto, 1991; pp 165-225.

114) Karplus, M. *J.Chem.Phys.* **1959**, *30*, 11-15.

115) Haasnoot, C.A.G.; De Leeuw, F.A.A.M.; Altona, C. *Tetrahedron* **1980**, *36*, 2783-2792.

116) Imai, K.; Osawa, E. *Magn.Reson.Chem.* **1990**, *28*, 668-674.

117) Osawa, E.; Imai, K.; Fuijiyoshi-Yonda, T.; Jaime, C.; Ma, P.; Masamune, S. *Tetrahedron* **1991**, *47*, 4579-4590.

118) Wang, Q.P.; Bennet, A.J.; Brown, R.S. *Can.J.Chem.* **1990**, *68*, 1732-1739.

119) Wang, Q.P.; Bennet, A.J.; Brown, R.S.; Santarsiero, B.D. *J.Am.Chem.Soc.* **1991**, *113*, 5757-5765.

Part II

Application of 1D NMR Methods to the Measurement of Exchange Rates of Large Spin System.

Overview

Measuring exchange rates of large spin systems, or systems with many sites, is difficult at best. For slow-exchange measurements only two-dimensional (2D) NMR experiments can be used, which are time consuming and less accurate than their one-dimensional (1D) counterparts. The main difficulty with using 1D techniques with larger spin systems is spectral overlap. In the medium exchange regime complete lineshape analysis is possible if an assignment of the spin system can be made, where the chemical shift and couplings are measured. For slow exchange, selective inversion techniques are used, which require signals of different conformers to be adequately separated such that each can be inverted, or at least perturbed, separately and measured independently. Thus 1D experiments are not always practical, and in pathological cases EXSY measurements are the only alternative.

The objective of this work is to make accurate rate measurements on large spin systems using 1D experiments. These measurements are to be performed over as large a temperature range as possible, in order to obtain accurate enthalpies and entropies of activation for each process. Complete spectral assignment will be achieved with use of

1D techniques such as HSQC, HMBC, COSY, NOESY and selective TOCSY. The complete spectra, or subspectra available by selective TOCSY techniques, are simulated to obtain the spectral parameters, which in turn are used in complete lineshape analysis. EXSY methods are used to determine the exchange mechanism.

In the following two chapters detailed dynamic NMR studies were performed on large biologically relevant systems, each exemplifying a particular challenge. DADS, N,N'-[Dimethyl-(2,2'-dithiobisacetyl)]ethylenediamine (shown in figure 5.1), is a ten-membered ring which exchanges amoung 5 observable conformations. In this case a separate spectral assignment is required for each conformation, and the exchange mechanism has to be determined. Rate measurements were made over a large temperature range using selective inversion methods, and complete lineshape analysis. It was possible to obtain separate barriers for each observable process. Thyrotropin-releasing hormone (TRH), is a small tripeptide with the sequence L-pyroglutamyl-L-histidyl-L-prolineamide (figure 6.1). It contains a proline residue, which interconverts between the *cis* and *trans* geometry of the peptide bond. In this case, the spin systems are large, and full lineshape analysis was performed on the signal of the neighbouring histidine residue, which is sensitive to the proline exchange. With use of selective TOCSY methods, the subspectra of both *cis* and *trans* proline were measured and fully analysed giving information about the ring pucker in both conformations. The histidine catalysis of the proline barrier is discussed in terms of the activation and spectral parameters.

The studies on TRH and DADS emphasize the utility of 1D NMR methods for large spin systems undergoing complex exchange processes. 2D methods are most helpful in obtaining spectral assignments. However, rates are best measured using lineshape and selective inversion techniques. These methods give more accurate rates and over a larger temperature range than EXSY methods, consequently the activation parameters are more reliable.

Chapter 5

NMR Studies of Chemical Exchange Amongst Five Conformers of a Ten-membered Ring Compound Containing Two Amide Bonds and a Disulfide.

(Based on an article published in the Journal of the Chemical Society, Perkin Transactions, 2, 1999, pages 1447 to 1454.[1])

Introduction

The understanding of barriers to rotation about chemical bonds is crucial to many fields of chemistry. Particularly in biochemistry, the conformation of a molecule is as important as its composition. Many proteins will retain their function if some amino acids are substituted, but if the 3D structure is changed, activity is completely lost. These changes in conformation usually do not break classical chemical bonds; rather, they involve a complex interaction amongst electronic, electrostatic and steric effects. The more data that we can collect on how these effects balance, the better we can understand molecular conformation.

The compound, N,N'-[Dimethyl-(2,2'-dithiobisacetyl)]ethylenediamine (DADS)[2] (figure 1) provides an excellent test case. It is a ten-membered ring containing two amide bonds and a disulfide bond, and in solution there is one stable conformation and four different metastable conformations with significant populations. These arise because there is restricted rotation around both the amide and the disulfide bonds, as well as a ring-flip process. In this chapter, the geometry of each of these conformations is

assigned, and the barriers to four of the exchange processes reported. A combination of selective-inversion and lineshape NMR experiments over a range of temperatures has permitted the separation of the barrier, $\Delta G^{\dagger}$, into enthalpy and entropy of activation. The energies of these different conformations, plus the heights of the barriers to interconversion amongst them, give an extraordinarily detailed picture of the potential energy surface of this molecule.

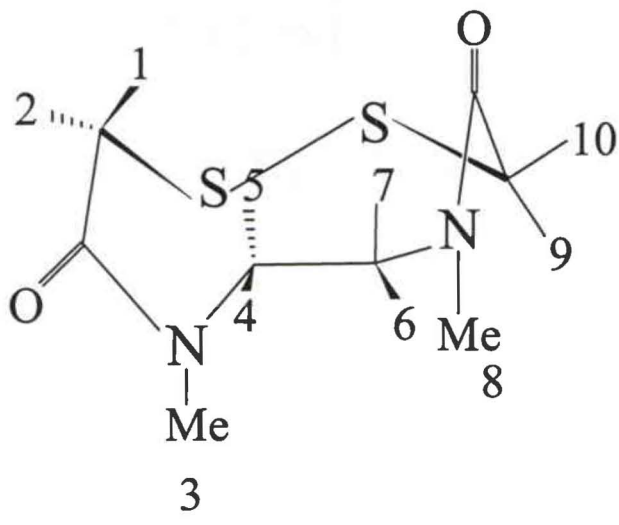

Figure 5.1 Structure of the C conformer of N,N'-[Dimethyl-(2,2'-dithiobisacetyl)]ethylenediamine (DADS).

DADS is an important molecule in itself. Certain chelates which contain two nitrogen and two sulfur atoms form stable complexes with ^{99m}Tc, the most widely used agent (at the tracer level) in diagnostic nuclear medicine.[3] The diamino-disulfide (DADS) chelate forms an anionic Tc(V) species which is stable *in vivo*.[4-6] Because of this stability, the DADS-type chelates are popular as a basis for the development of site-specific bifunctional

radiopharmaceuticals.[7,8]

Although not a peptide, DADS provides a useful analogy for the study of small, cyclic peptides.[9] The dynamic nature of peptides is well established experimentally, both when only a single, average conformation is observed,[10-13] and when multiple conformations can be seen in an NMR spectrum.[11,14-18] The amide bond[19] and the disulfide[20] both show significant barriers to rotation, and rings define a whole class of dynamic processes. When dynamic effects have been observed in the NMR spectra of peptides, a proline residue is often (but not always[11,16]) involved, since the amide bond in this case is known to adopt both the *cis* and the *trans* conformation.[21] In peptides, a disulfide bond can close a ring, even if two cysteines are next to each other in the sequence.[22,23] Restricted rotation has been observed in both acyclic and cyclic disulfides.[20,24-26] Finally, the exchange among conformations of rings is one of the classic studies in NMR.[27] Cyclohexane[28] is the standard example, and the work continues with recent careful studies of eight-membered[9,29] and ten-membered[30] rings.

Nuclear magnetic resonance (NMR) provides an excellent way of measuring the barriers to all these processes.[27,31] When the exchange rates are comparable to chemical shift differences, characteristic line broadening and coalescence occur in the spectrum. These can be simulated with classic methods,[32,33] or newer approaches[34] in order to estimate the exchange rate. At slower exchange rates, the exchange process competes with spin-lattice relaxation. In this regime, selective-inversion-recovery experiments provide an excellent way of measuring the exchange rate.[35-40] In combination, these methods permit measurement of rates over a wide range of temperatures,[41] so that the thermodynamics of the transition state can be investigated.

Quoting the Gibbs' free energy of activation, $\Delta G^{\dagger}$, is equivalent to quoting the rate, since transition state theory says that the rate constant, r, is given by equation (5.1), in which k_b is Boltzmann's constant and h is Planck's constant.

$$r = \frac{k_b T}{h} e^{\left(\frac{-\Delta G^{\dagger}}{RT}\right)} = \frac{k_b T}{h} e^{\left(\frac{\Delta S^{\dagger}}{R}\right)} e^{\left(\frac{-\Delta H^{\dagger}}{RT}\right)} \qquad (5.1)$$

In order to separate the enthalpy and the entropy of activation, the rate is measured as a function of temperature, and an Eyring plot of log(rate/T) *vs.* (1/T) is constructed. This is important, since a measured rate may have a significant entropy contribution, but a calculated potential energy surface[42] involves only enthalpy. It is therefore important to measure the rates over as wide a range of temperatures as possible, to get reliable thermodynamic data.

This work is divided into two parts. The first is qualitative: the assignment of the spectra of each conformation and elucidation of the mechanism of the exchange. The second is quantitative: the measurement of the exchange rates as a function of temperature. For the first part, 2D NMR was used extensively, although the precise values of chemical shifts and couplings were determined from a simulation of the static spectrum. For the quantitative work, 1D experiments were used exclusively. Although 2D experiments can be used quantitatively to extract rate data,[43-45] we believe that 1D experiments are more reliable and more efficient.[35-40,46-49]

Experimental

Preparation of DADS (Scheme)

The Synthesis of DADS was performed by Dr. J. Valliant, and is described in detail in the paper.[1]

NMR Spectroscopy

Approximately 30 mg of DADS was dissolved in dimethylformamide-d_7 (DMF-d_7, 99.5% D from ISOTEC), which had been dried over activated molecular sieves. The solution was filtered through glass wool when transferring to a 5mm medium-walled NMR tube.

High resolution ^{1}H spectra were recorded at 253, 273 and 303 K at 500.13 MHz, using between 512 and 1024 scans for each spectrum. Spectral widths were typically 1300 Hz with 3 s acquisition times for 32 K data points. Most spectra were zero filled twice, and were apodised with a Gaussian broadening of between 0.3 to 0.5, and a Lorentzian broadening ranging between -1 to -2 Hz. All spectra were referenced to the central line of the low-frequency methyl pentet of DMF-d_7 at 2.74 ppm. A ^{13}C spectrum was obtained at 253 K at 125.76 MHz; 20000 scans were collected over a spectral range of 3125 Hz. The FID was exponentially multiplied with a function corresponding to 1 Hz broadening. The spectrum was referenced to the central line of low-frequency septet of DMF-d_7 at 30.1 ppm.

All 2D experiments were performed on a Bruker DRX 500 spectrometer with a 5mm inverse triple axis gradient probe. The proton and carbon 90° pulse widths were 6.6 and 11.60 μs, respectively. All phase-sensitive methods used time proportional phase incrementation

(TPPI). Most spectra were apodised with either sine or cosine bell.

A high resolution HMBC spectrum optimised for long-range couplings was obtained, using 100 scans per increment, with 256 increments, without carbon decoupling during acquisition. Linear prediction was employed in the carbon dimension to 512 data points using 100 coefficients. The spectral range was 3600 Hz in ^{1}H and 3125 Hz in ^{13}C. Both dimensions used sinebell multiplication. A phase-sensitive gradient NOESY spectrum was acquired at 253 K using a spectral width of 1300 Hz in both dimensions, 128 increments and 32 scans per increment. At a mixing time of 0.8 s no EXSY cross peaks were observed. The first proton dimension was linear predicted to 256 points using 50 coefficients, and was zero filled to 1K, giving 1.3 Hz/point digital resolution.

A gradient COSY-45 was obtained at 253 K using most of the above mentioned parameters. Four scans were acquired for each of the 256 increments. The indirect proton dimension was linear predicted to 512 points using 100 coefficients and was zero filled to 1 K, giving 1.2 Hz/point.

A series of COSY and NOESY spectra was recorded for 275, 295 and 303 K to measure the temperature dependence of the chemical shifts and to determine the exchange mechanism. For the COSY spectra 256 increments with 8 scans were acquired, over a sweep width of 1570 Hz. These spectra were acquired and processed as magnitude-calculation experiments and apodised with sine bells in both dimensions. Each dimension has 1K data points giving 1.5 Hz/point digital resolution. The phase-sensitive gradient NOESY spectra were acquired under much the same conditions except that 512 increments were recorded with 16 scans each. In this case the first dimension was linear predicted up to 1 K data points using

50 coefficients and was zero filled to 2 K giving 0.8 Hz/point. Sinebell apodisation was used in both dimensions. At 275 K, a mixing time of 0.8 s was used; at 295 K, 0.4 s was used; and at 303 K, NOESY spectra were acquired using mixing times of 0.1, 0.4 and 0.8 s.

A series of spectra was obtained at 300.13 MHz as a function of temperature for lineshape analysis. The spectra were acquired with a Bruker AC 300 spectrometer using a 5mm four-nucleus probe. Temperature control was maintained to within ±0.5 °C using a BVT 2000 temperature controller, and was monitored periodically by inserting a copper/constantan thermocouple in a 5mm NMR tube into the probe. Temperatures ranged from 253 to 383 K where spectra were collected at 5 to 10 degree intervals. Between 512 and 2K scans were recorded over a 4200 Hz sweep width. For each FID 32 K data points were collected giving 0.13 Hz/pt. No apodisation was employed when processing these spectra. Some spectra were baseline corrected.

Selective-inversion and inversion-recovery experiments were carried out at 500 MHz between 253 and 303 K to measure rates in the slow exchange regime. The selective-inversion sequence used was a modification of the standard inversion-recovery sequence where a Gaussian-shaped 180° pulse was used, tuned to the resonance of interest to be inverted. The variable delays (VD) for both experiments varied from 0.01 to 15 s, and the relaxation delays (RD) were typically 15s. Experiments were performed on the N-methyl resonances of the C (*ca.* 3.01 and 3.26 ppm), A (*ca.*3.02 and 3.16 ppm) and E (*ca.* 2.91 and 3.32 ppm) conformers and the N-methylene resonance of the B (*ca.* 5.53 ppm) conformer. In order to obtain rate measurements of both processes of the mechanism C <-> A <-> E processes, inversion had to be carried out on C and E independently. Line intensity

measurements were made with Bruker's XWINNMR software package. Along with data from the inversion recovery experiments, the selective-inversion data were fit to the differential equations reflecting the exchange and relaxation behaviour of this system using CIFIT. This is a program which uses non-linear least squares optimisation methods to model the relaxation of a non-equilibrium uncoupled spin system, exchanging between multiple sites.

Once an assignment was obtained of all five conformations and the exchange mechanism was determined, a complete lineshape analysis was performed. This was done on an SGI Indy computer with MEXICO, a lineshape simulation program developed in this laboratory, which is capable of simulating at least a 5-spin system undergoing unequally populated exchange among up to 5 sites.

The rates obtained from 253 to 363 K for all four processes were plotted according to the Eyring equation giving values for both activation enthalpies and entropies. The standard deviation in the intercept was extrapolated to the y-axis including the contribution from the standard deviation in the slope.[50]

Results

The 1D ^{1}H spectra as a function of temperature (figures 5.18(a) and 5.19(a)) clearly showed that there were multiple conformations exchanging with each other. Quantitative ^{13}C spectra (figure 2) at 253 K identified five species: two of which showed only three carbon peaks, and three species had six peaks. The first two, conformers B and D in figure 5.17, were assigned to symmetrical conformations in which both amides adopted a *Z* arrangement. The three non-symmetric species, A, C and E in figure 5.17, had one amide *Z* and the other *E*. At 253 K the relative population of each species (relative to C, the most populated) are A : B : C : D : E = 0.24 : 0.71 : 1.0 : 0.12 : 0.29. The proton spectrum of each species was assigned using a 2D HMBC experiment (figure 5.4). In this molecule, the amide carbonyl shows long-range coupling to the protons of both the sulfur methylenes and the nitrogen methylenes, so comparison of the carbonyl carbon rows from the HMBC with the proton spectrum (figure 5.5) allowed estimation of the proton chemical shifts. Connectivities of the spectra were confirmed using a gradient COSY. The assignment for each conformer is shown in figures 5.6, 5.8, 5.10, 5.12, and 5.14, for conformers A, B, C, D, and E, respectively. Important NOESY cross peaks are shown for each conformer in figures 5.7, 5.9, 5.11, 5.13 and 5.15 respectively. From these data, a full analysis of each spectrum was performed using the XSIM program (available from Kirk Marat, University of Manitoba). Complete lists of chemical shifts and coupling constants are given in table 5.1.

Molecular modelling, using the AM1 method in SPARTAN and previous results,[2] gave a selection of candidate conformations for the molecule. This included both symmetrical *Z,Z* conformations as well as the non-symmetric *Z,E*. The spectra were assigned to individual conformations using a phase-sensitive NOESY experiment (figures 5.7, 5.9, 5.11, 5.13 and

5.15) at a temperature (253 K) at which chemical exchange is very slow. In dimethylformamide solution, the lowest-energy conformer matches the *Z,E* conformation seen in the crystal structure.[2]

The exchange mechanism was confirmed by doing an EXSY experiment at 275 K, when the processes with low barriers are in slow exchange. Figure 5.16 shows a portion of the spectrum illustrating the exchange amongst conformations A, C and E in figure 5.17. Note that this spectrum was run with a long mixing time (0.8 s), so that cross peaks appear between C and E even though the final analysis shows little direct exchange.

Exchange rates were measured by 1D methods. In the intermediate exchange region, lineshapes were simulated (figures 5.18(b) and 5.19(b)) using the MEXICO program, and compared visually with the experimental spectra (figures 5.18(a) and 5.19(a)) using the dual display features of the spectrometer software. Slower exchange rates were measured by performing selective-inversion experiments on the methyl signals.[35-38] Note that the selective-inversion experiments fit the whole of the exchange process, not just the initial linear part. Figure 5.20 illustrates this. If the magnetisation of C is inverted, then E should show no change at time zero if there is no direct exchange between the two sites. In figure 5.20, the initial slope of the E magnetisation is considerably smaller than that of A. At later times there is an indirect change, as was observed in the EXSY experiment in figure 5.16. The full observed relaxation, under the combined influence of spin-lattice relaxation and chemical exchange, was analysed using the CIFIT program.[39] Figure 5.20 shows the quality of the fit of these data.

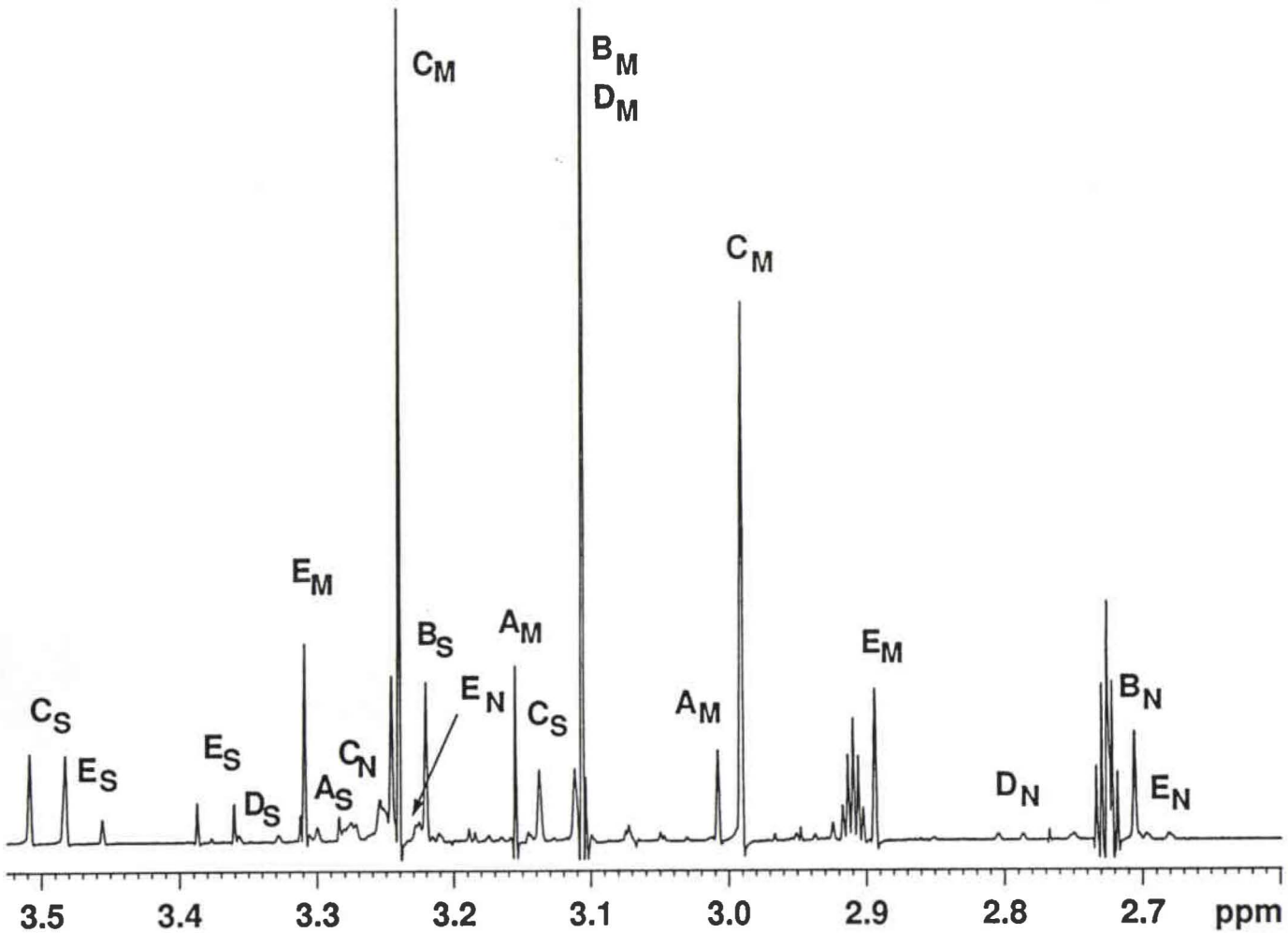

Figure 5.2 500 MHz ^{1}H NMR spectrum of DADS in DMF at 253 K. Region from 2.6 to 3.5 ppm is shown. Signal are assigned to the conformers and protons type, subscripts M, S, and N refer to proton in a methyl group, a methylene group near sulfur, and a methylene group near nitrogen, protons.

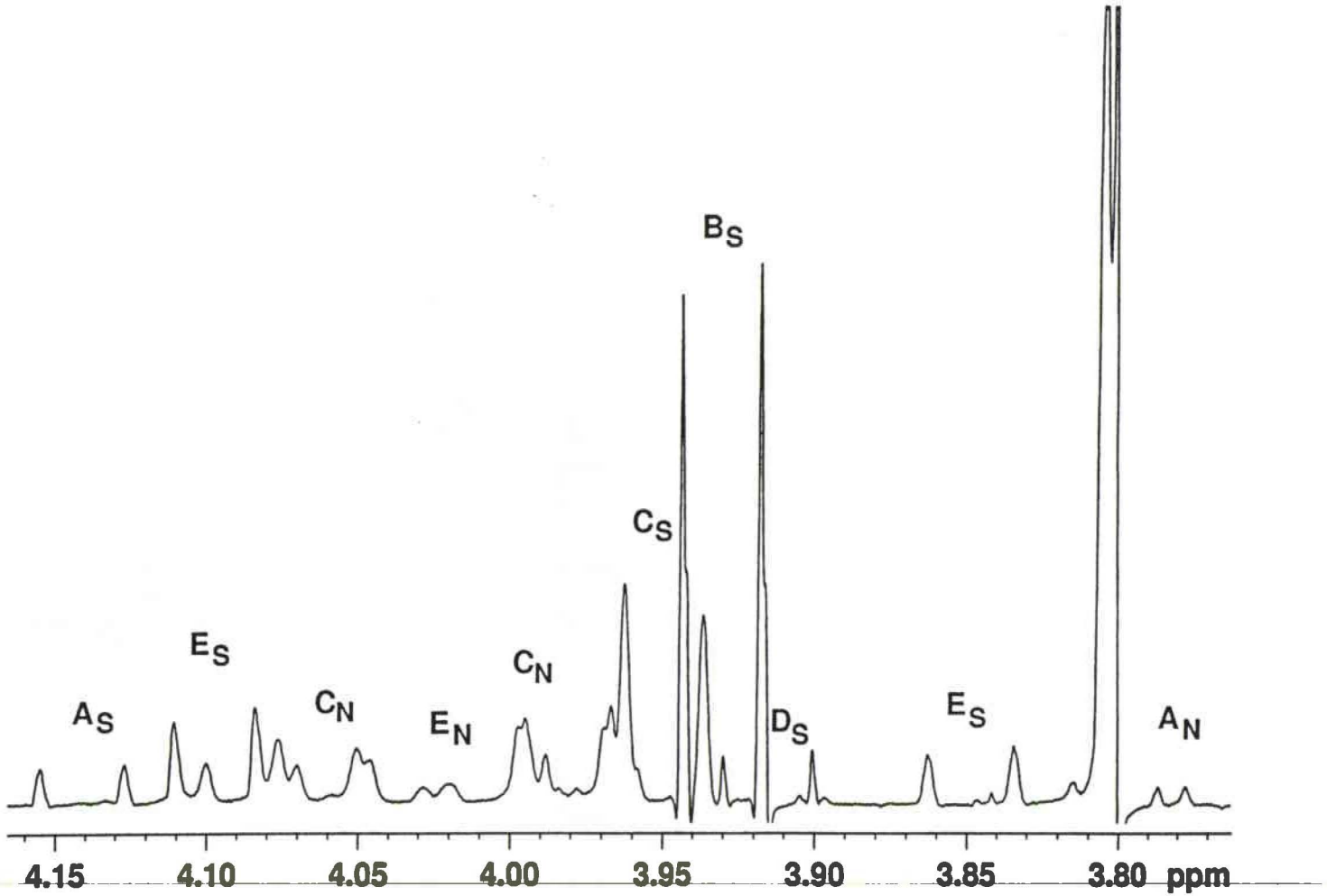

Figure 5.2 (continued) 500 MHz ^{1}H NMR spectrum of DADS in DMF at 253 K. Region from 3.7 to 4.2 ppm is shown.

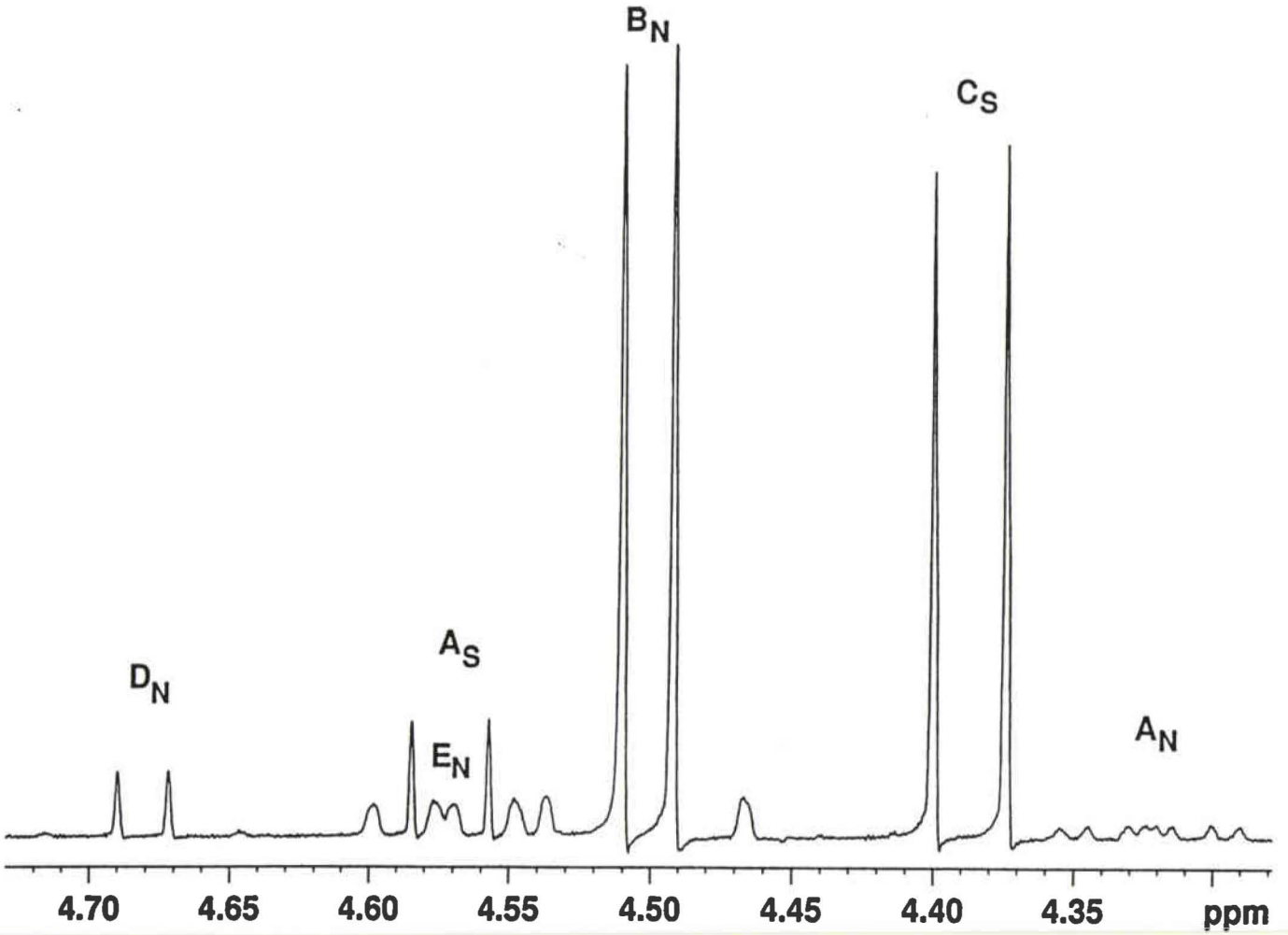

Figure 5.2 (continued) 500 MHz ^{1}H NMR spectrum of DADS in DMF at 253 K. Region from 4.3 to 4.75 ppm is shown.

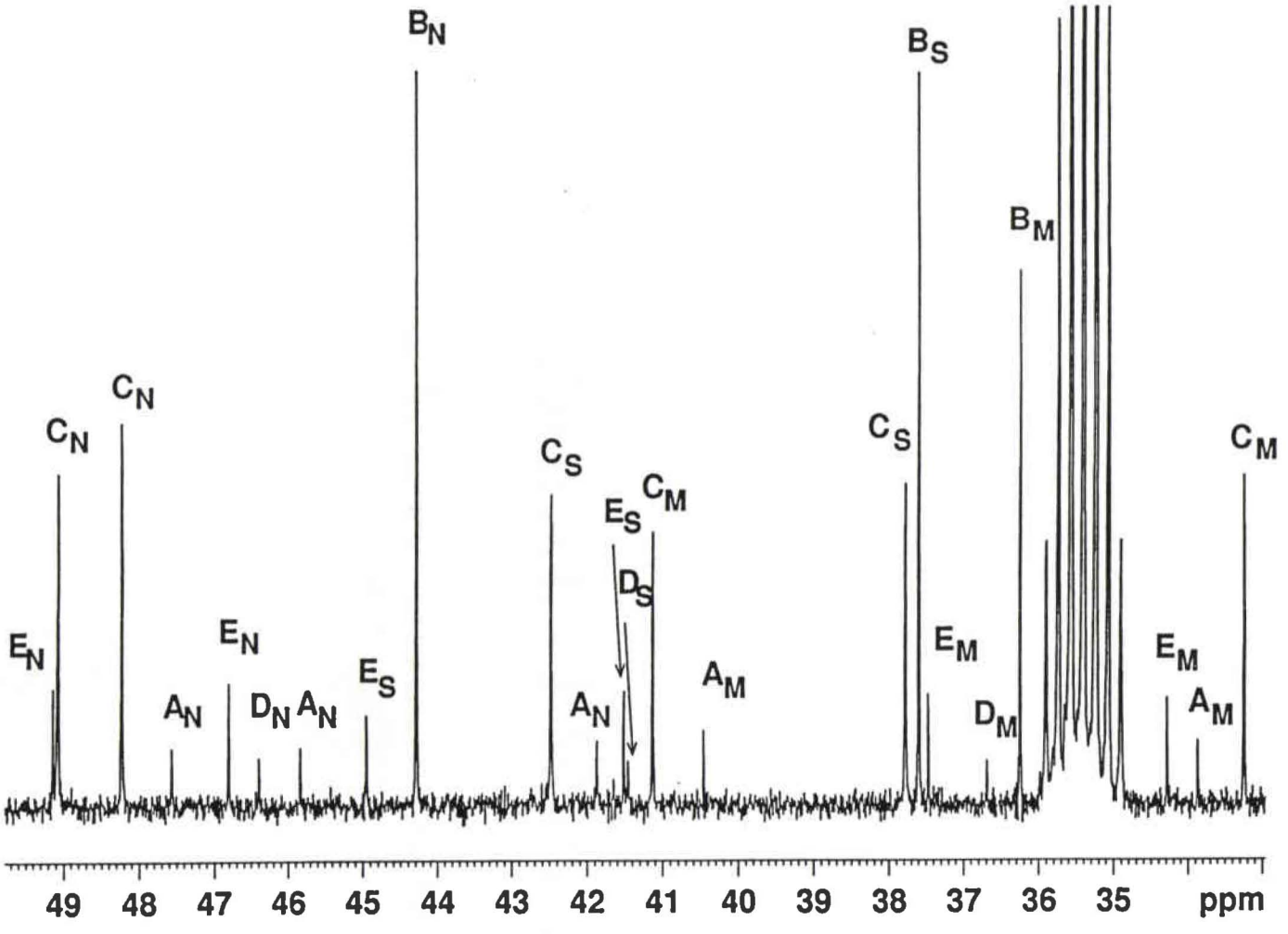

Figure 5.3 Aliphatic region of the 125 MHz ^{13}C NMR spectrum of DADS in DMF at 253 K. Signals are assigned to the conformers and the type of carbon. Subscripts M, S and N refer to carbon in a methyl group, methylene group near a sulfur, and methylene groups near a nitrogen.

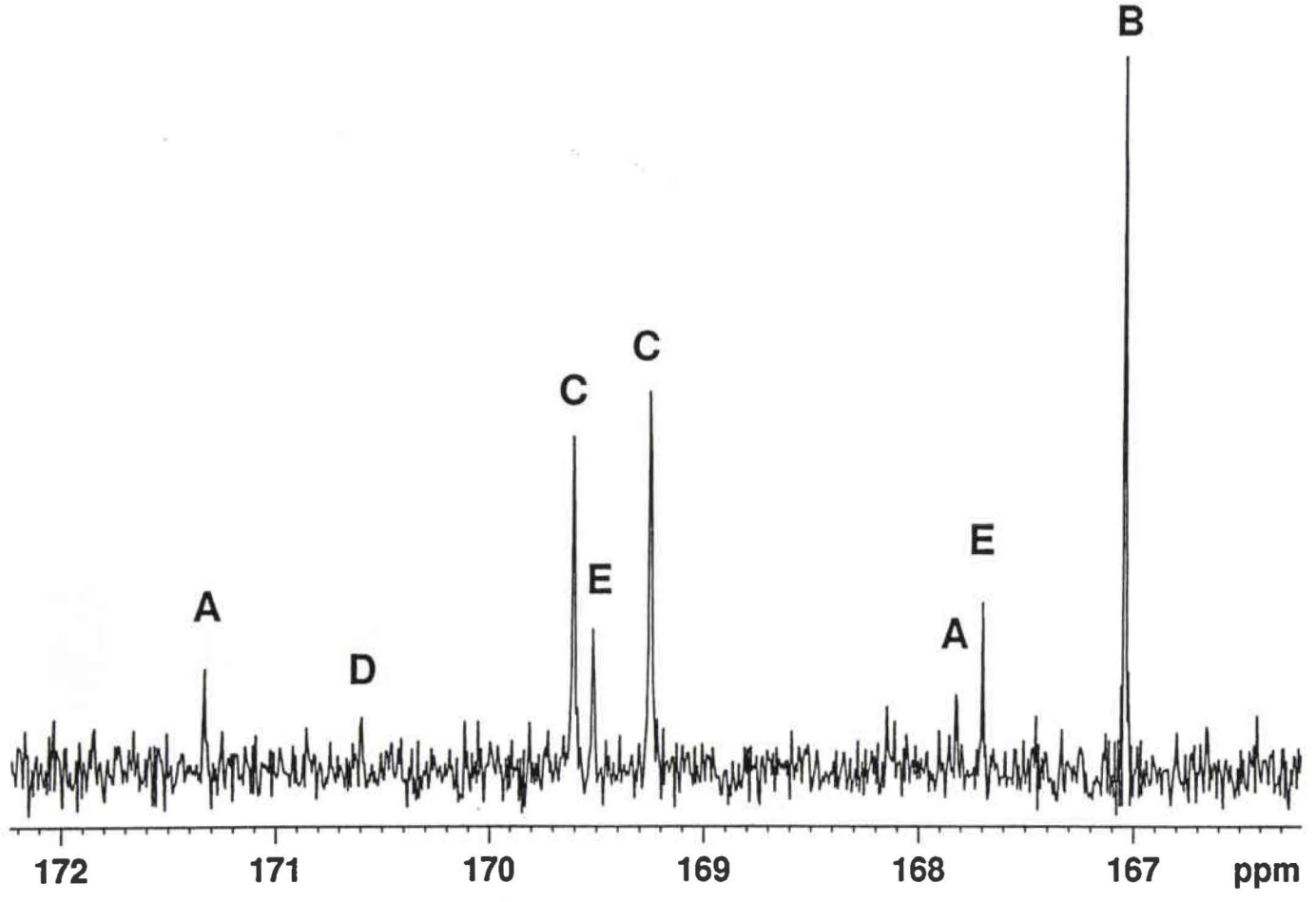

Figure 5.3 (continued) Carbonyl region of the 125 MHz ^{13}C NMR spectrum of DADS in DMF at 253 K. Signals are assigned to the conformers.

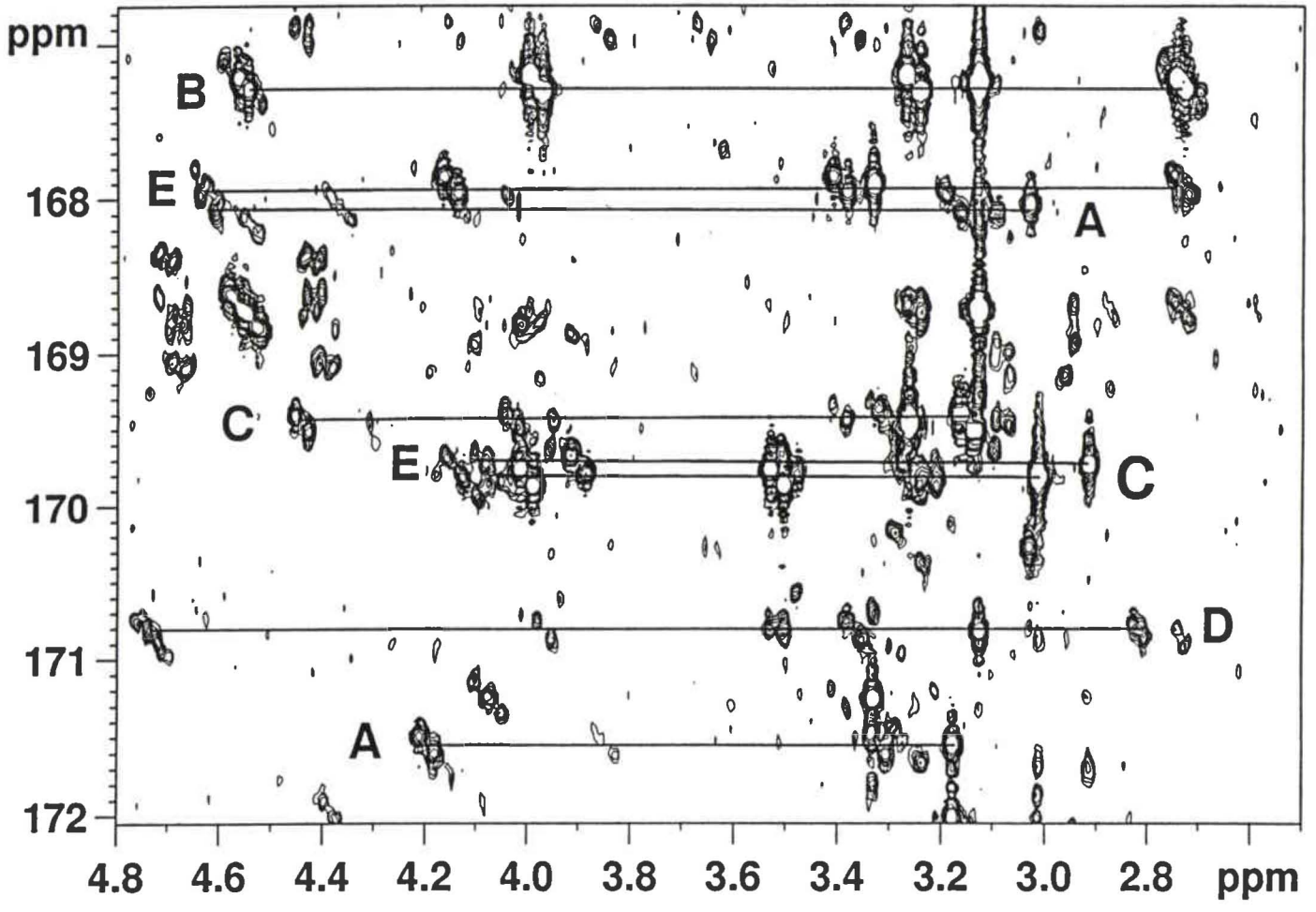

Figure 5.4 Contour plot of part of the HMBC spectrum of DADS in dimethylformamide-d_7 at 253 K. The aliphatic region was acquired in the carbon dimension (f1), but carbonyl signals are folded in and the scale represents the chemical shifts of the carbonyls. The labelled lines highlight the carbonyl signals of each conformation.

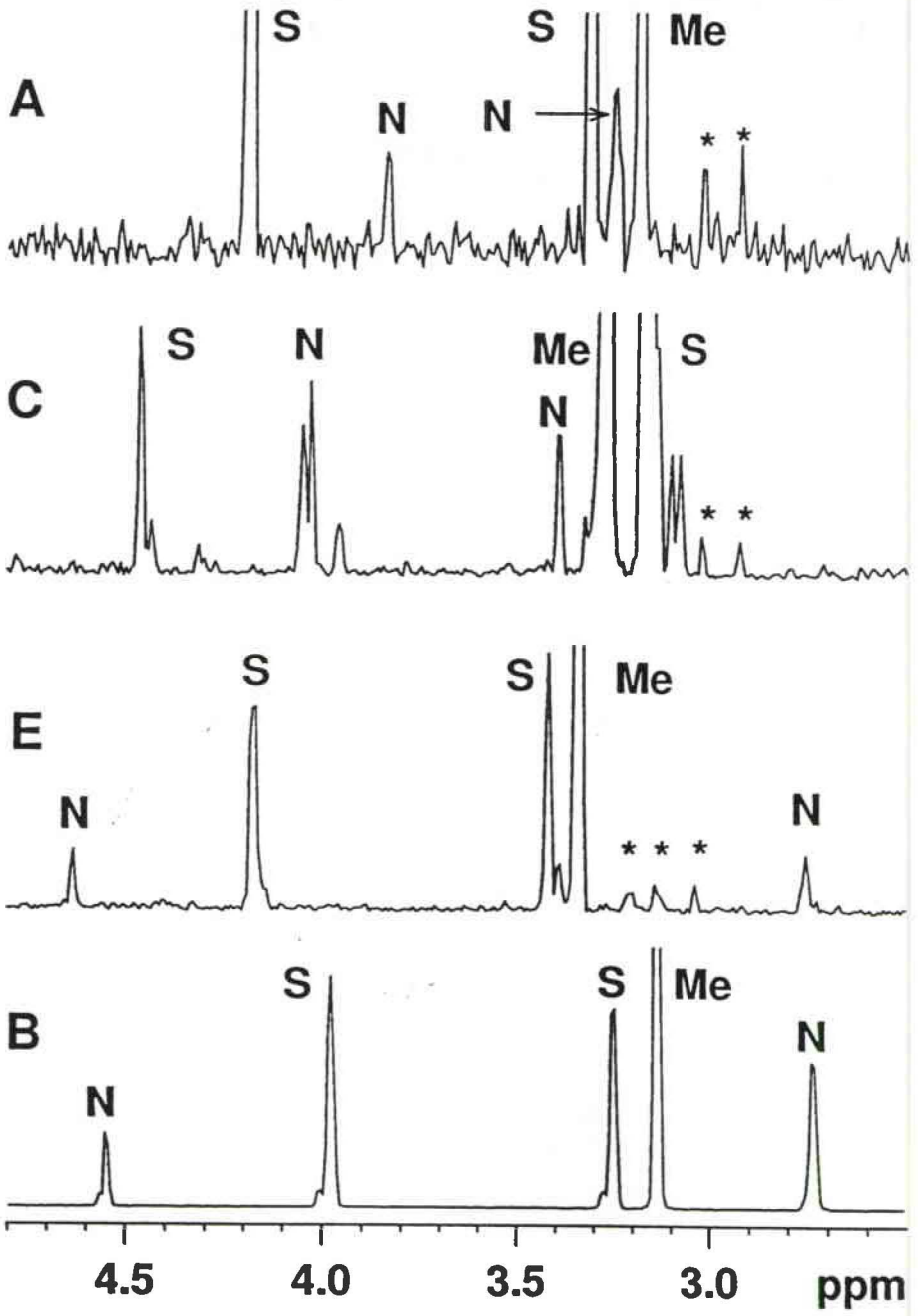

Figure 5.5 Proton slices from the HMBC spectrum of DADS in dimethylformamide-d_7 at 253 K corresponding to each carbonyl carbon. Assignments for each proton are given. Conformers B and D are symmetrical and thus have only one carbonyl signal. These slices were used to confirm which sets of proton signal belong to a given side of the ring.

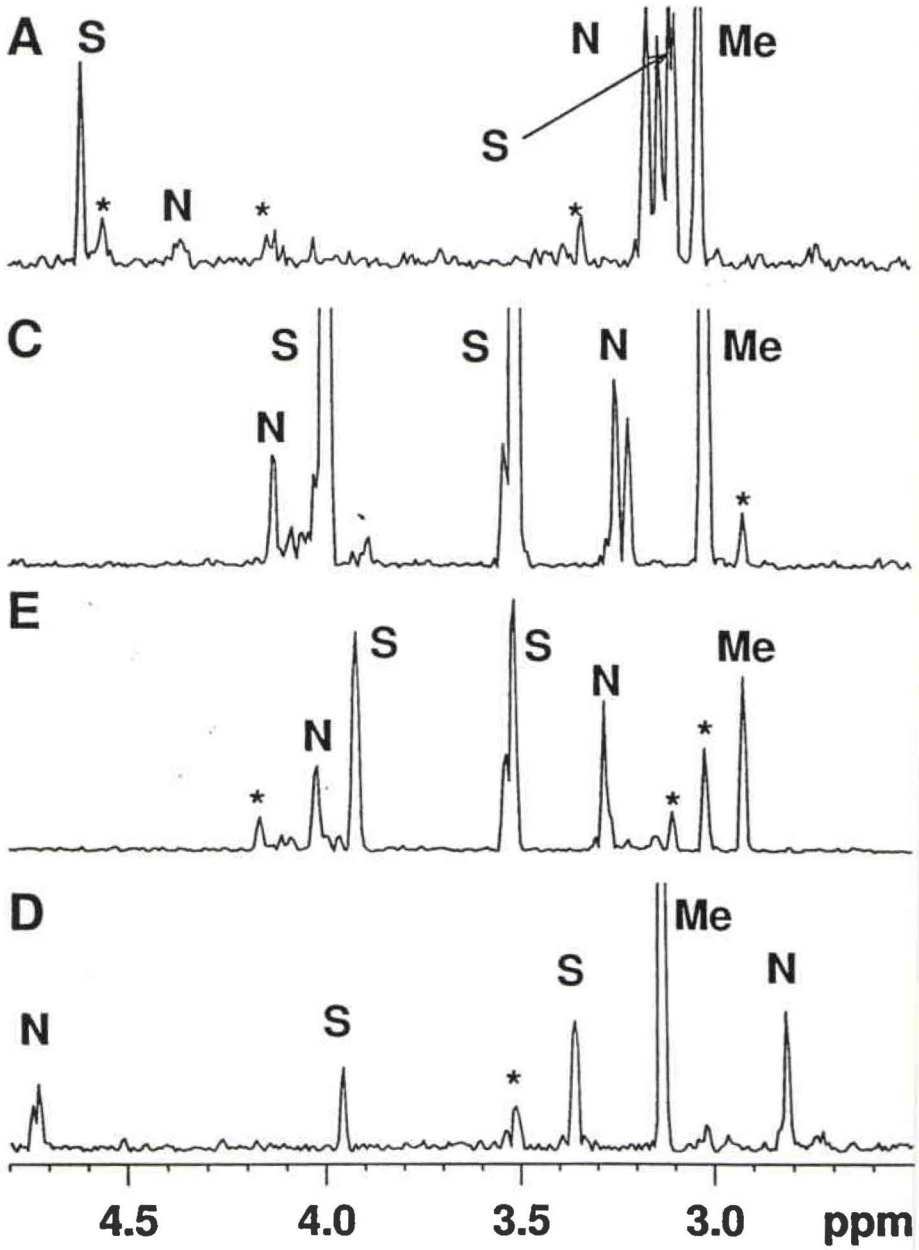

Figure 5.5 (continued) Proton slices from the HMBC spectrum of DADS in dimethylformamide-d_7 at 253 K corresponding to each carbonyl carbon.

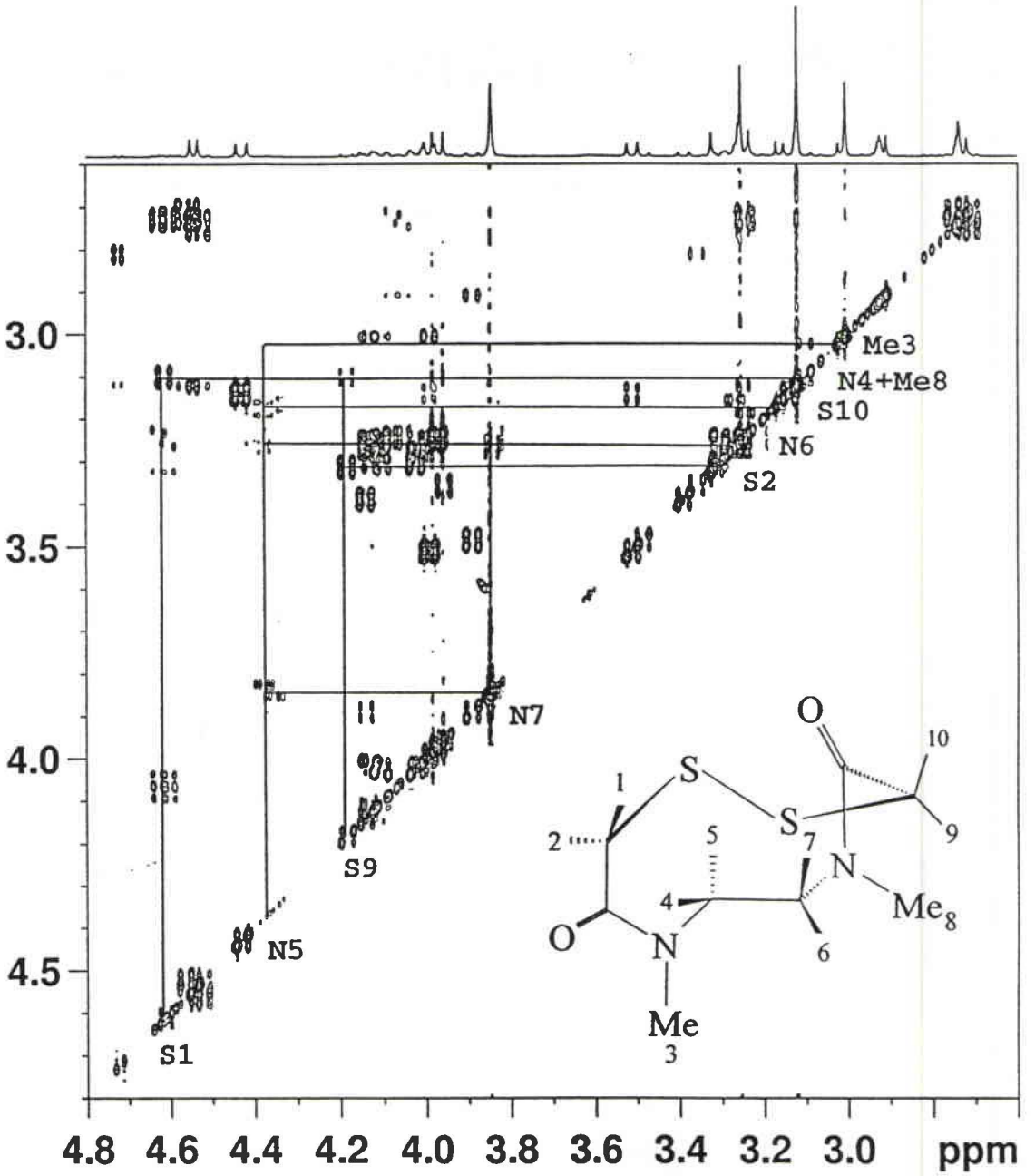

Figure 5.6 Gradient COSY spectrum of DADS spectrum at 500 MHz, taken at 253 K - a temperature at which the chemical exchange in negligible. The correlations drawn in correspond to conformer A, shown in the insert.

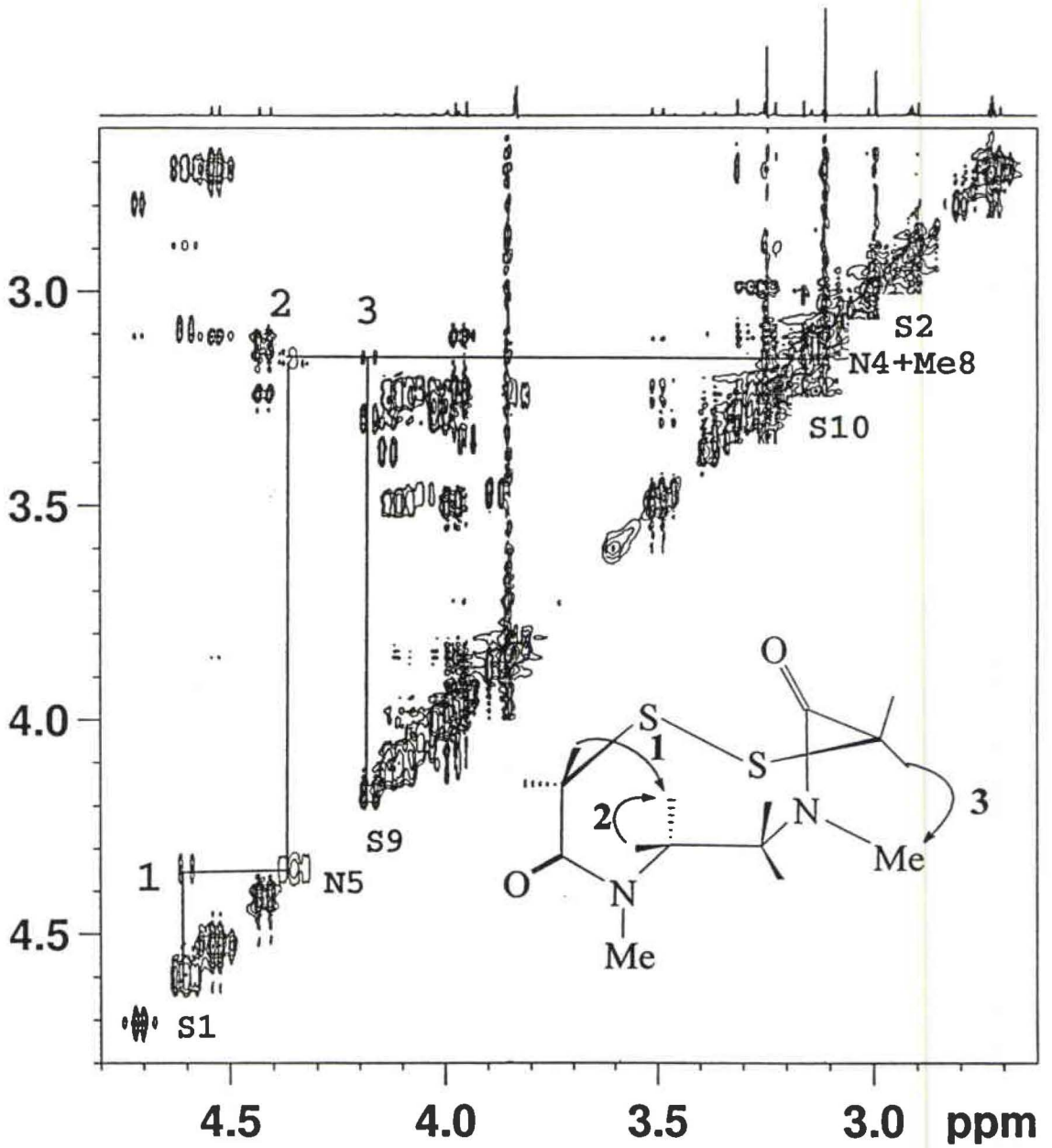

Figure 5.7 500 MHz phase-sensitive NOESY spectrum of DADS at a temperature of 253 K. The cross peaks indicated correspond important nOe contacts for conformer, A shown in the insert.

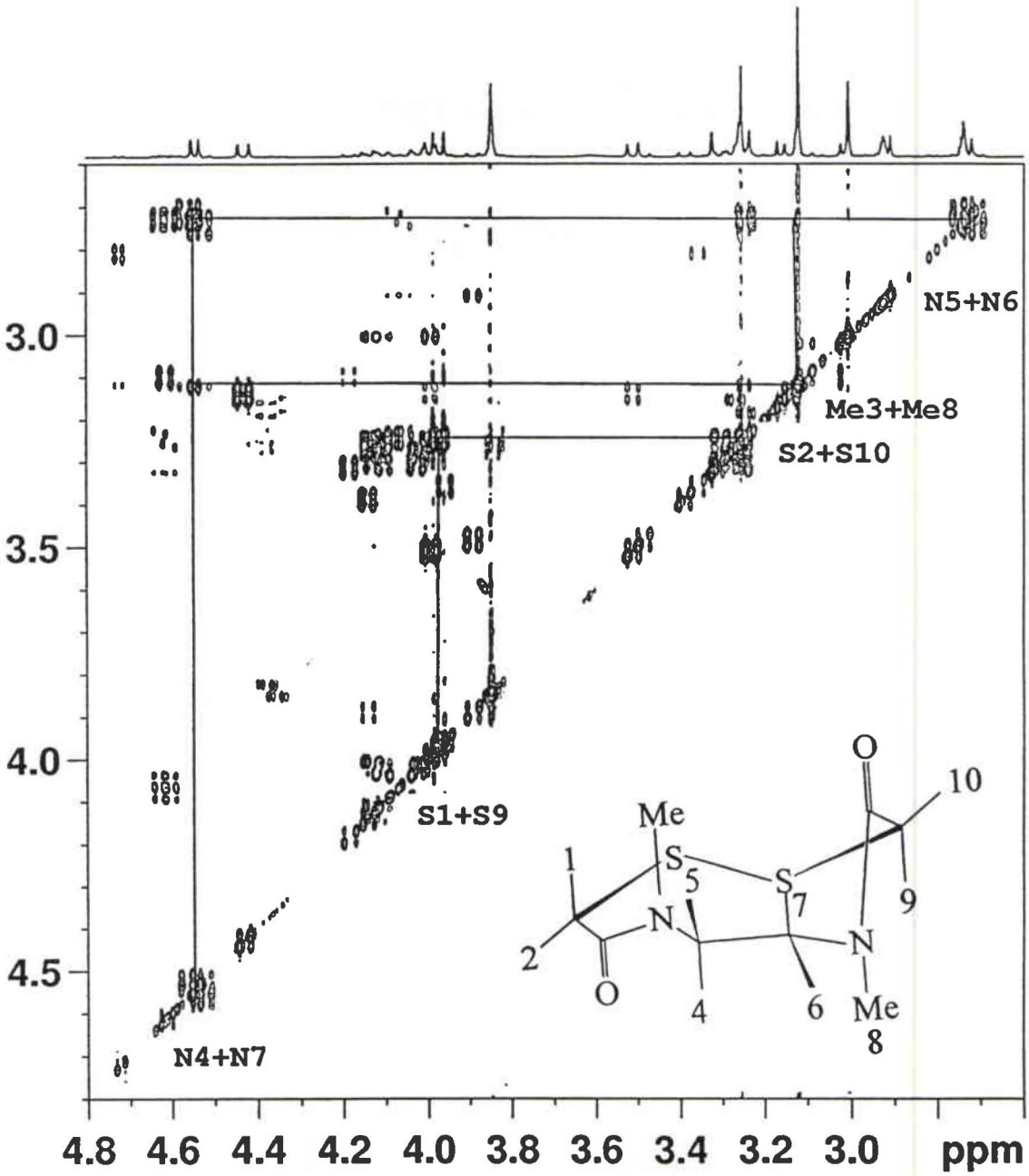

Figure 5.8 Gradient COSY spectrum of DADS spectrum at 500 MHz, taken at 253 K - a temperature at which the chemical exchange in negligible. The correlations drawn in correspond to conformer B, shown in the insert.

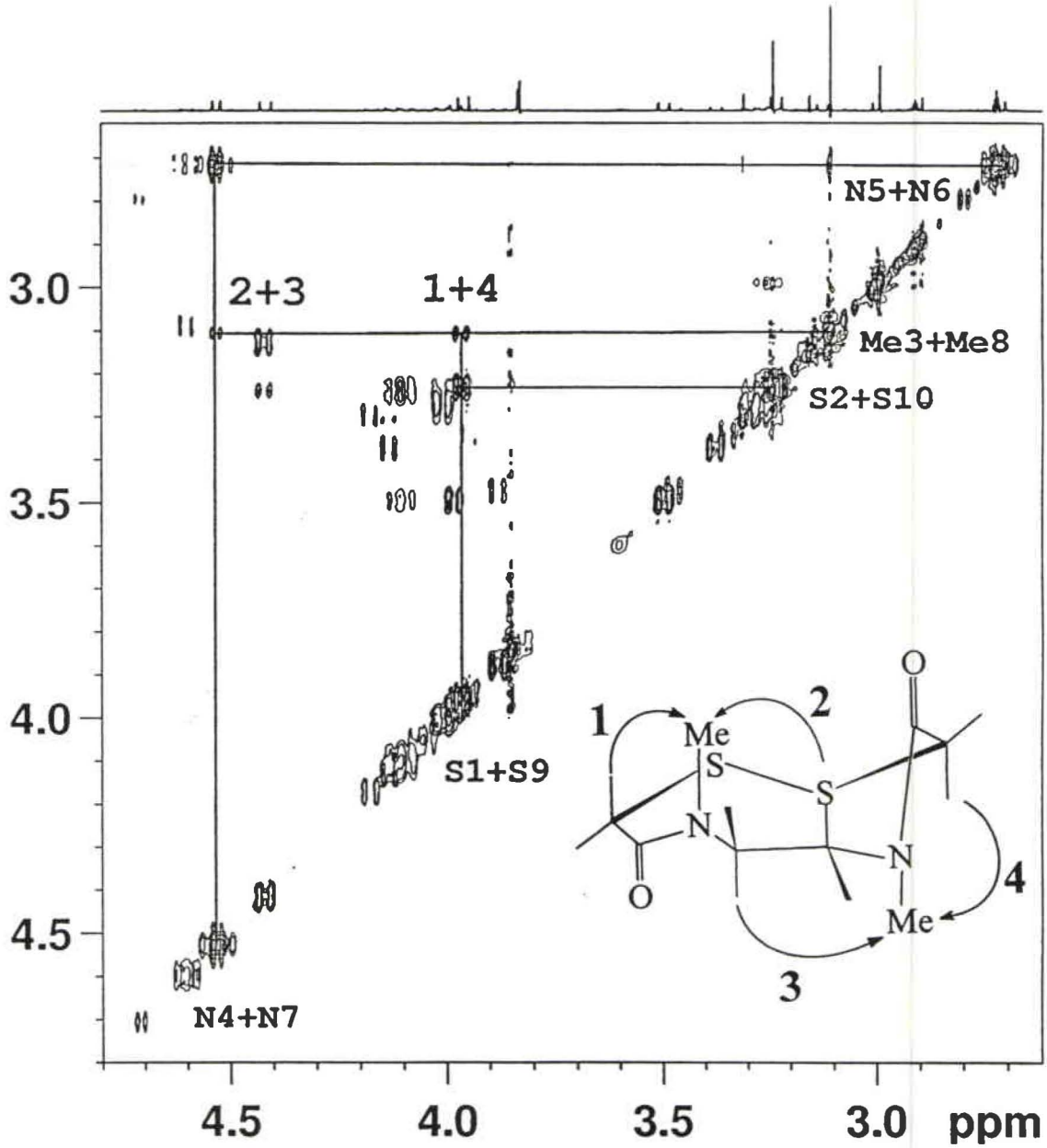

Figure 5.9 500 MHz phase-sensitive NOESY spectrum of DADS at a temperature of 253 K. The cross peaks indicated correspond important nOe contacts for conformer B, shown in the insert.

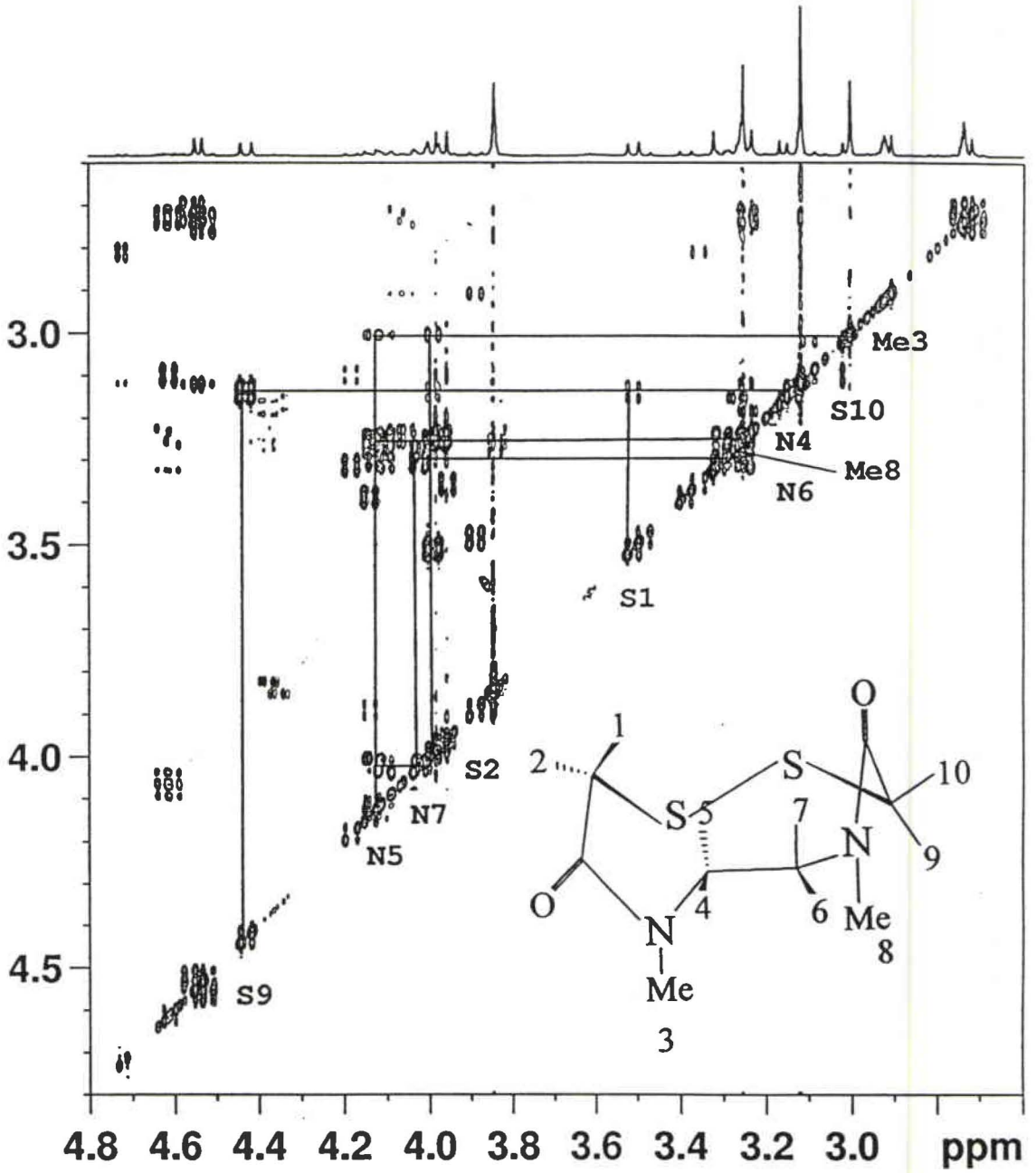

Figure 5.10 Gradient COSY spectrum of DADS spectrum at 500 MHz, taken at 253 K - a temperature at which the chemical exchange in negligible. The correlations drawn in correspond to conformer C, shown in the insert.

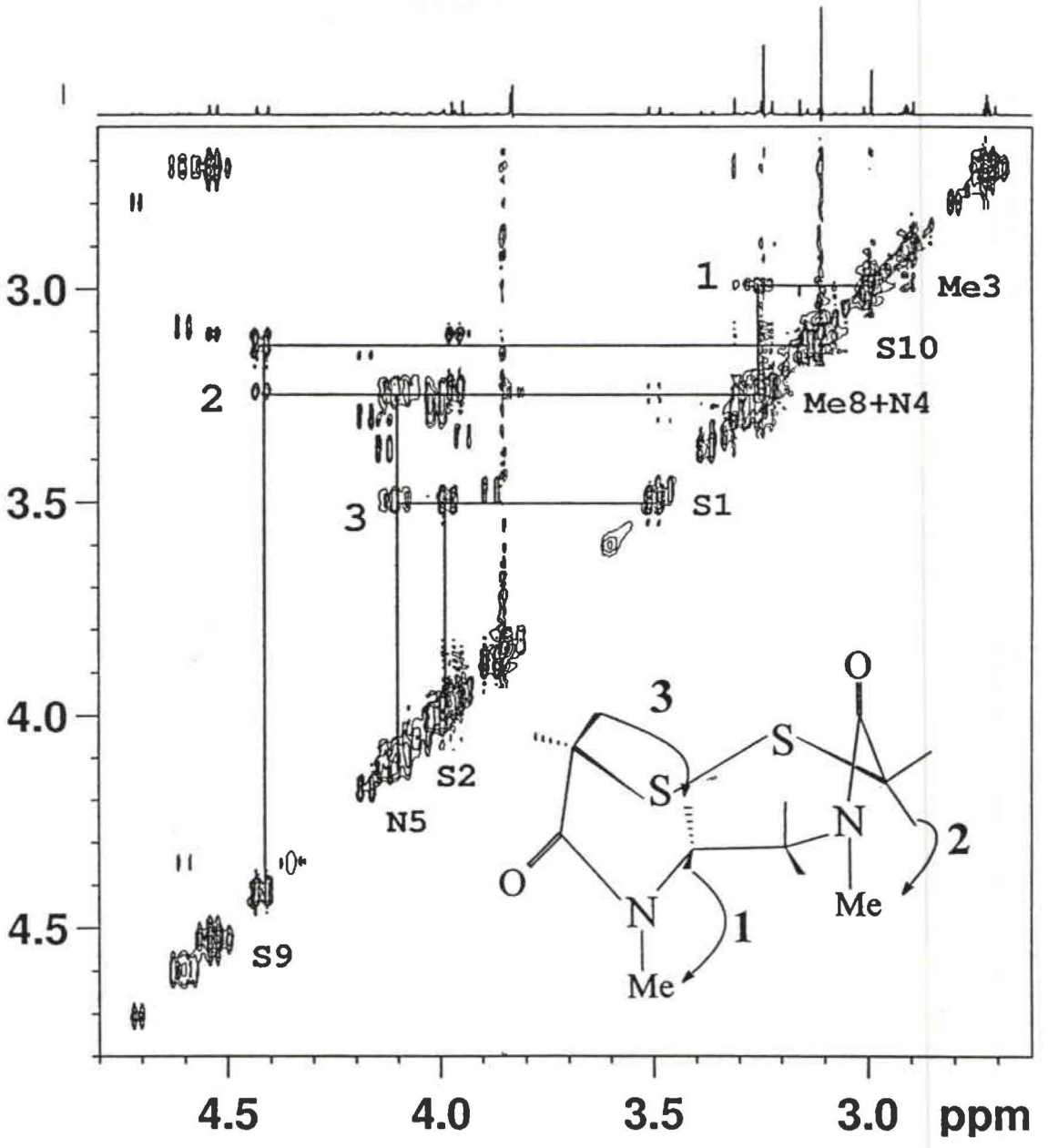

Figure 5.11 500 MHz phase-sensitive NOESY spectrum of DADS at a temperature of 253 K. The cross peaks indicated correspond important nOe contacts for conformer C, shown in the insert.

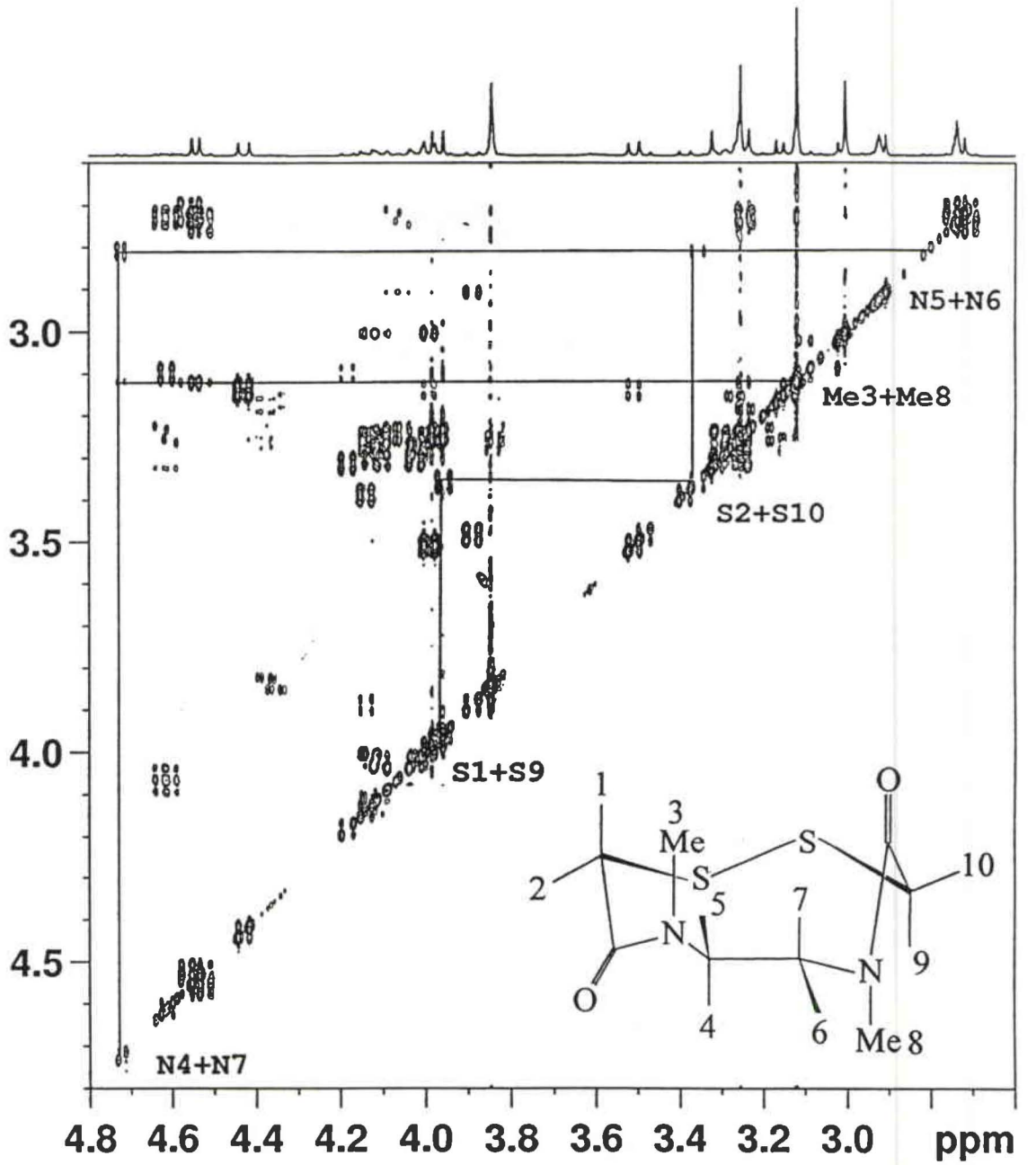

Figure 5.12 Gradient COSY spectrum of DADS spectrum at 500 MHz, taken at 253 K - a temperature at which the chemical exchange in negligible. The correlations drawn in correspond to conformer D, shown in the insert.

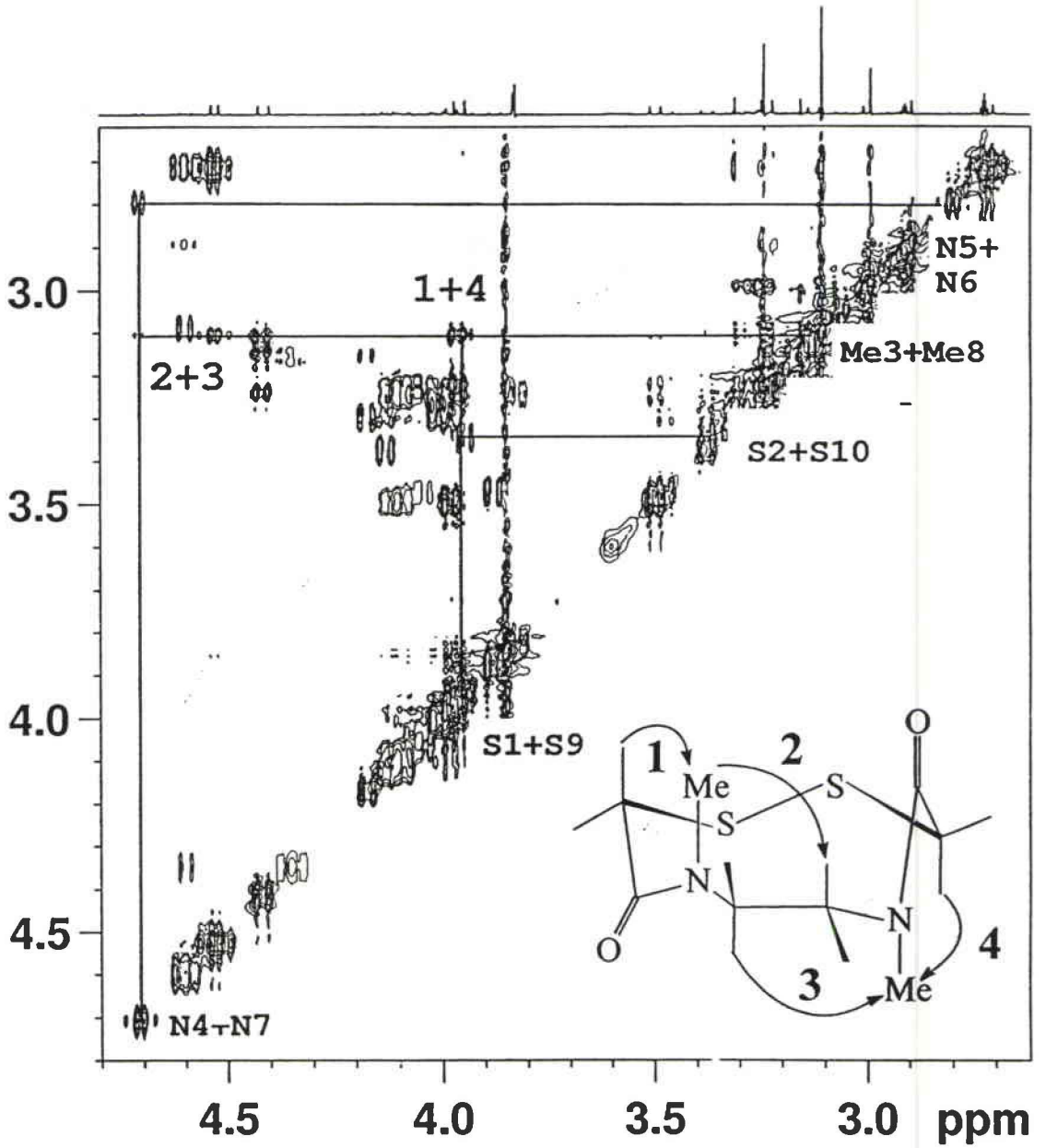

Figure 5.13 500 MHz phase-sensitive NOESY spectrum of DADS at a temperature of 253 K. The cross peaks indicated correspond important nOe contacts for conformer D, shown in the insert.

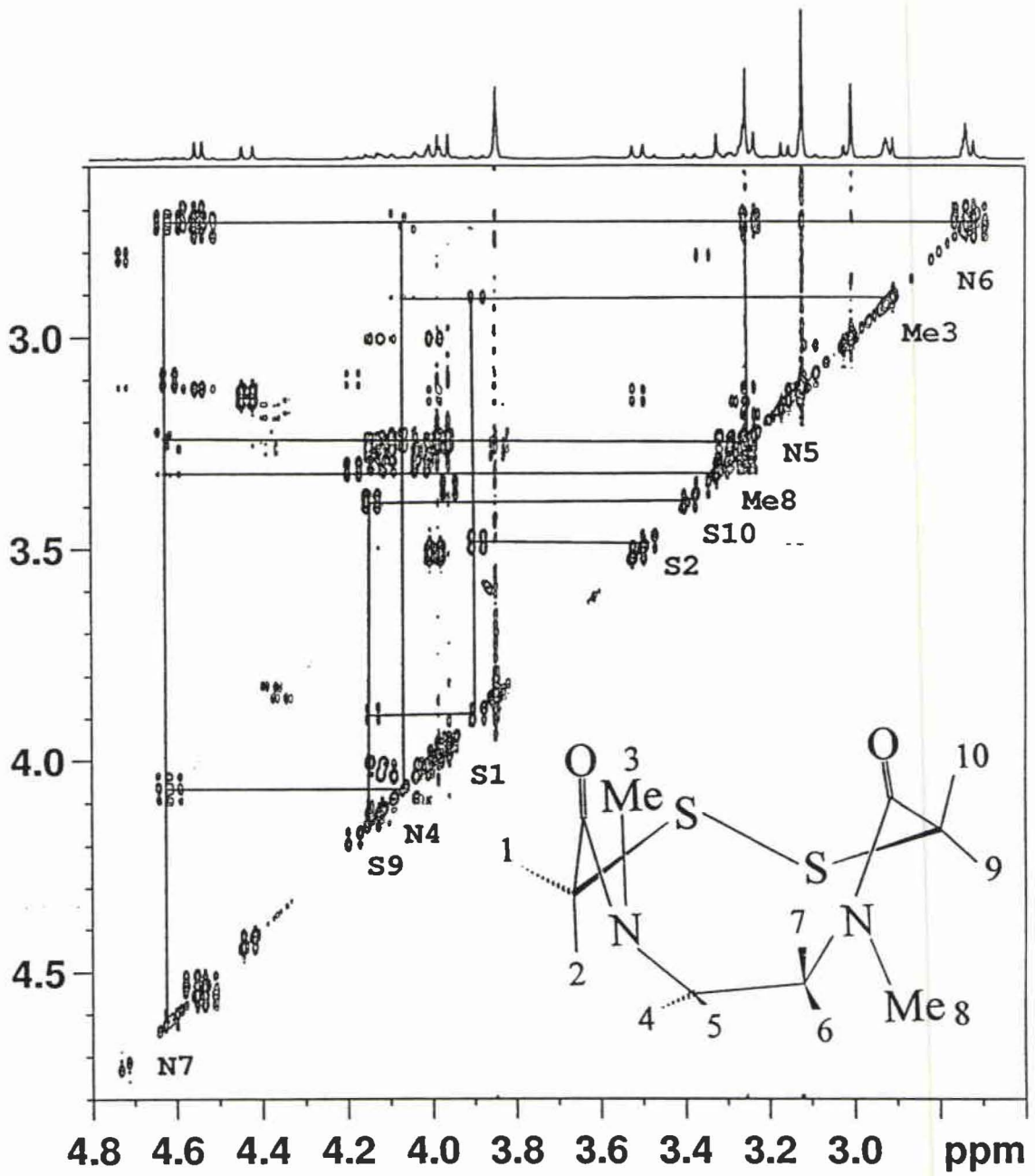

Figure 5.14 Gradient COSY spectrum of DADS spectrum at 500 MHz, taken at 253 K - a temperature at which the chemical exchange in negligible. The correlations drawn in correspond to conformer E, shown in the insert.

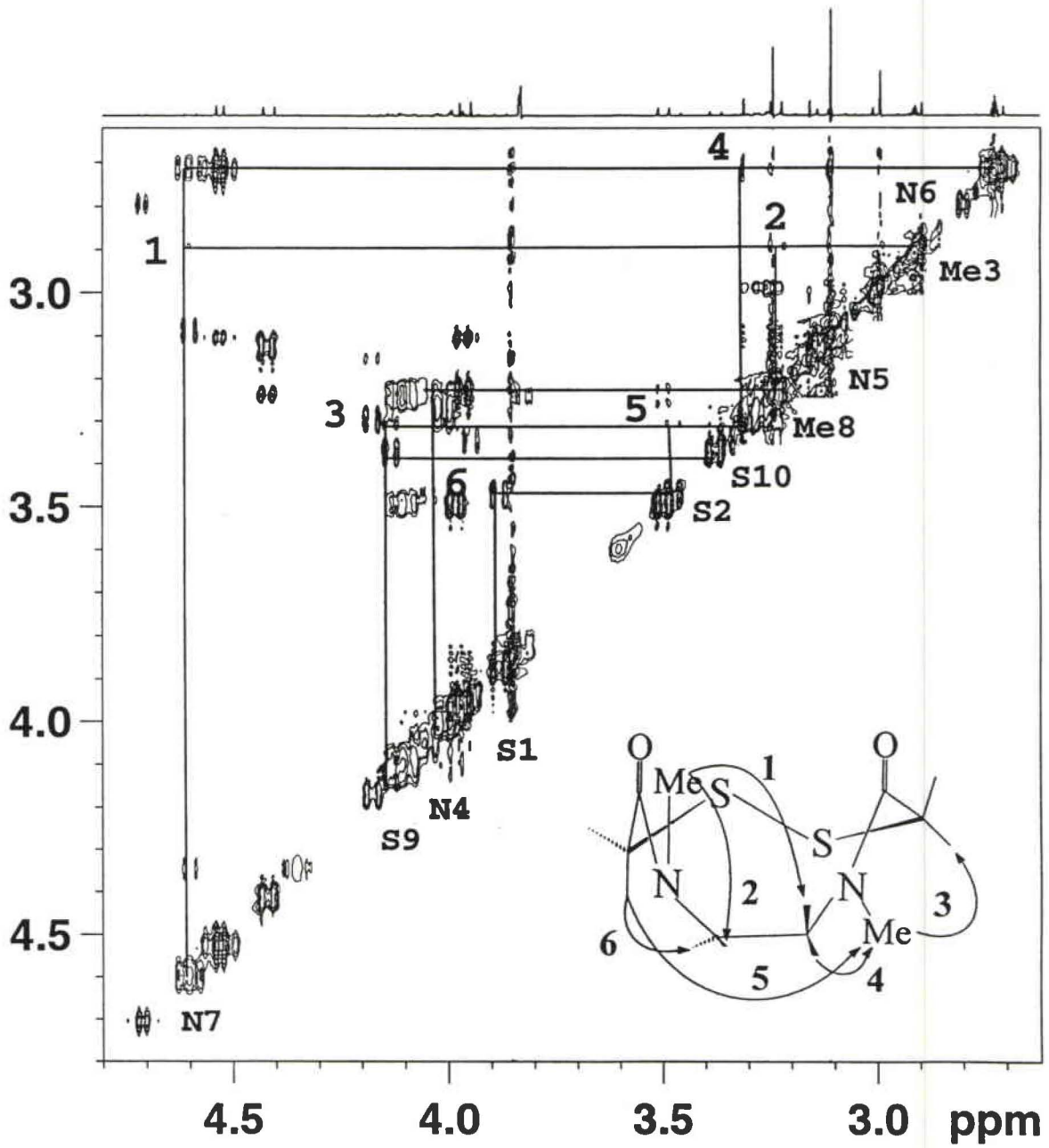

Figure 5.15
500 MHz phase-sensitive NOESY spectrum of DADS at a temperature of 253 K. The cross peaks indicated correspond important nOe contacts for conformer E, are shown in the insert.

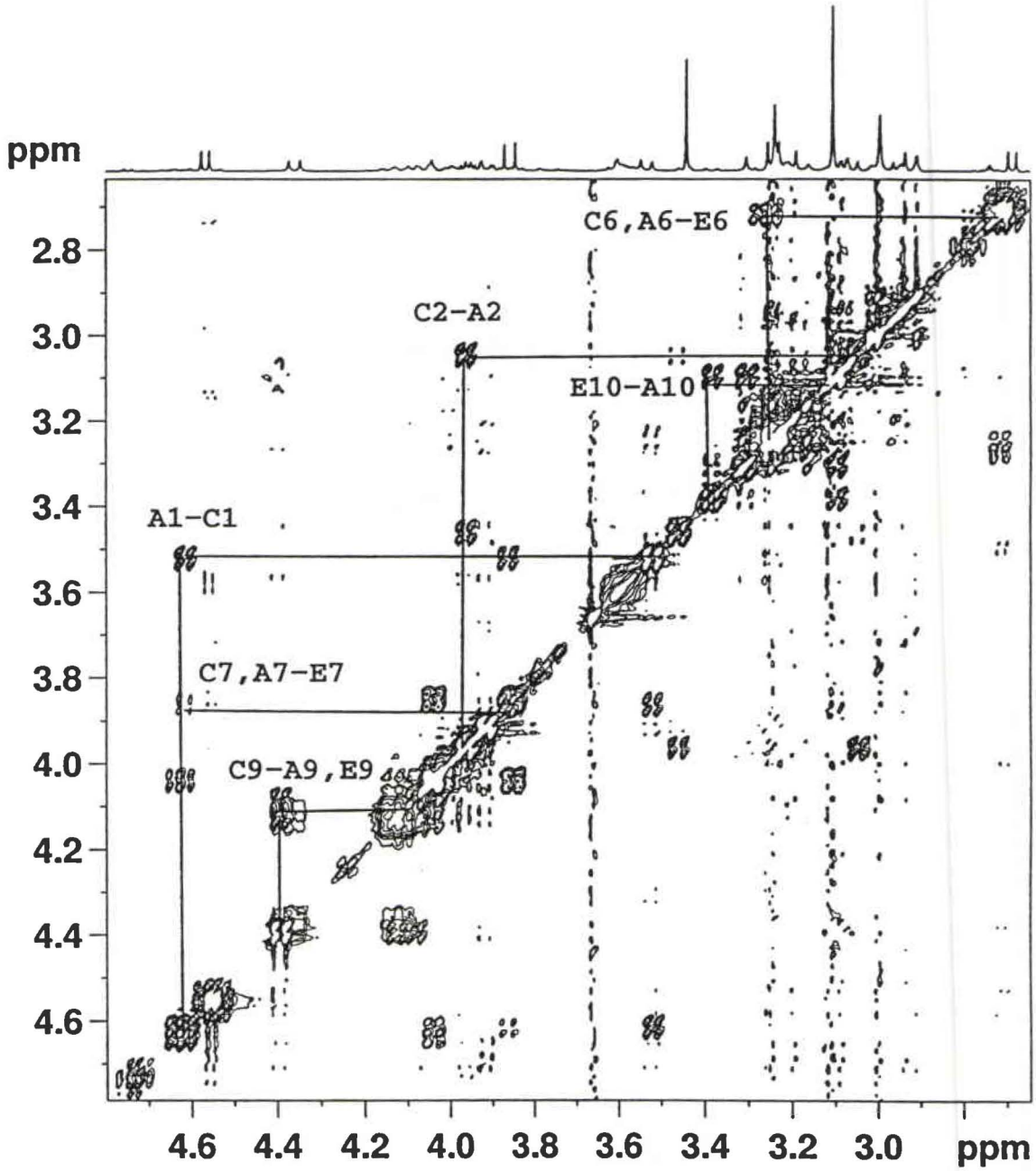

Figure 5.16 500 MHz phase-sensitive EXSY spectrum of DADS taken at a temperature of 295 K. At this temperature, processes with the lower barriers (involving conformers A, C and E) are in slow, but observable, exchange. The spectra were taken with long mixing times in order to map the whole exchange mechanism. The lines show the correlations for six of the protons in the molecule.

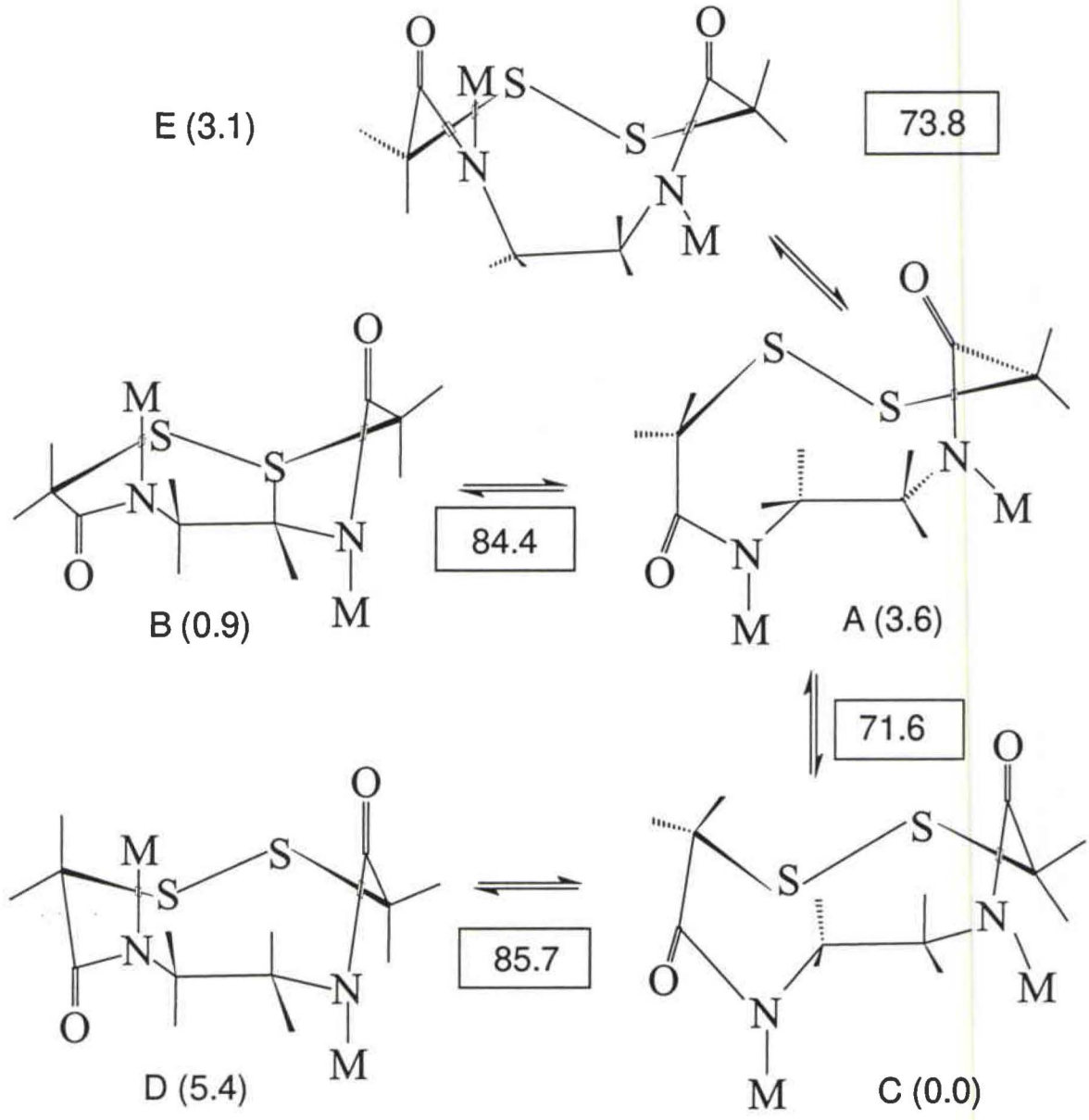

Figure 5.17 Structures and exchange mechanism of the five observable conformations of N,N'-[Dimethyl-(2,2'-dithiobisacetyl)]ethylenediamine (DADS), labelled A to E. Two are symmetrical (B and D), in which both amides are *Z*, and the others non-symmetrical with one amide as *E* and the other *Z*. The number in the parenthesis are ΔH^{o} value with respect to C. The numbers in the boxes are the $\Delta H^{\ddagger}$ of the process. All values are in kJ/mol.

Table 5.1 DADS ^{1}H NMR Spectral Parameters in DMF-d_7 at 273 K

N-methylenes

N-CH_2	A	B	C	D	E
ν_4	3.17	4.56	3.25	4.74	4.03
ν_5	4.38	2.72	4.13	2.80	3.24
ν_6	3.24	2.72	3.27	2.80	2.73
ν_7	3.86	4.56	4.05	4.74	4.64
$^2J_{4,5}$	-15.18	-13.49	-15.29	-13.38	-15.36
$^3J_{4,6}$	4.87	4.46	3.38	4.51	0.09
$^3J_{4,7}$	12.38	0.49	12.24	0.54	3.44
$^2J_{5,6}$	0.52	12.97	1.42	12.80	11.26
$^2J_{5,7}$	4.46	4.46	2.95	4.51	1.13
$^2J_{6,7}$	-14.13	-13.49	-14.02	-13.38	-14.95

S-methylenes

S-CH_2	A	B	C	D	E
ν_1	4.63	3.93	3.53	3.96	3.87
ν_2	3.18	3.25	3.97	3.33	3.47
$^2J_{1,2}$	-13.56	-12.94	-13.07	-14.52	-14.33
ν_9	4.14	3.93	4.43	3.96	4.095
ν_{10}	3.06	3.25	3.11	3.33	3.394
$^2J_{9,10}$	-13.80	-12.94	-12.98	-14.52	-13.42

Methyls

CH_3	A	B	C	D	E
ν_3	3.02	3.12	2.99	3.10	2.91
ν_8	3.17	3.12	3.25	3.10	3.31

All chemical shifts are in ppm and coupling constants are in Hz. Chemical shifts were measured with respect to TMS at 300.13 MHz. The numbering system refers to figure 5.1.

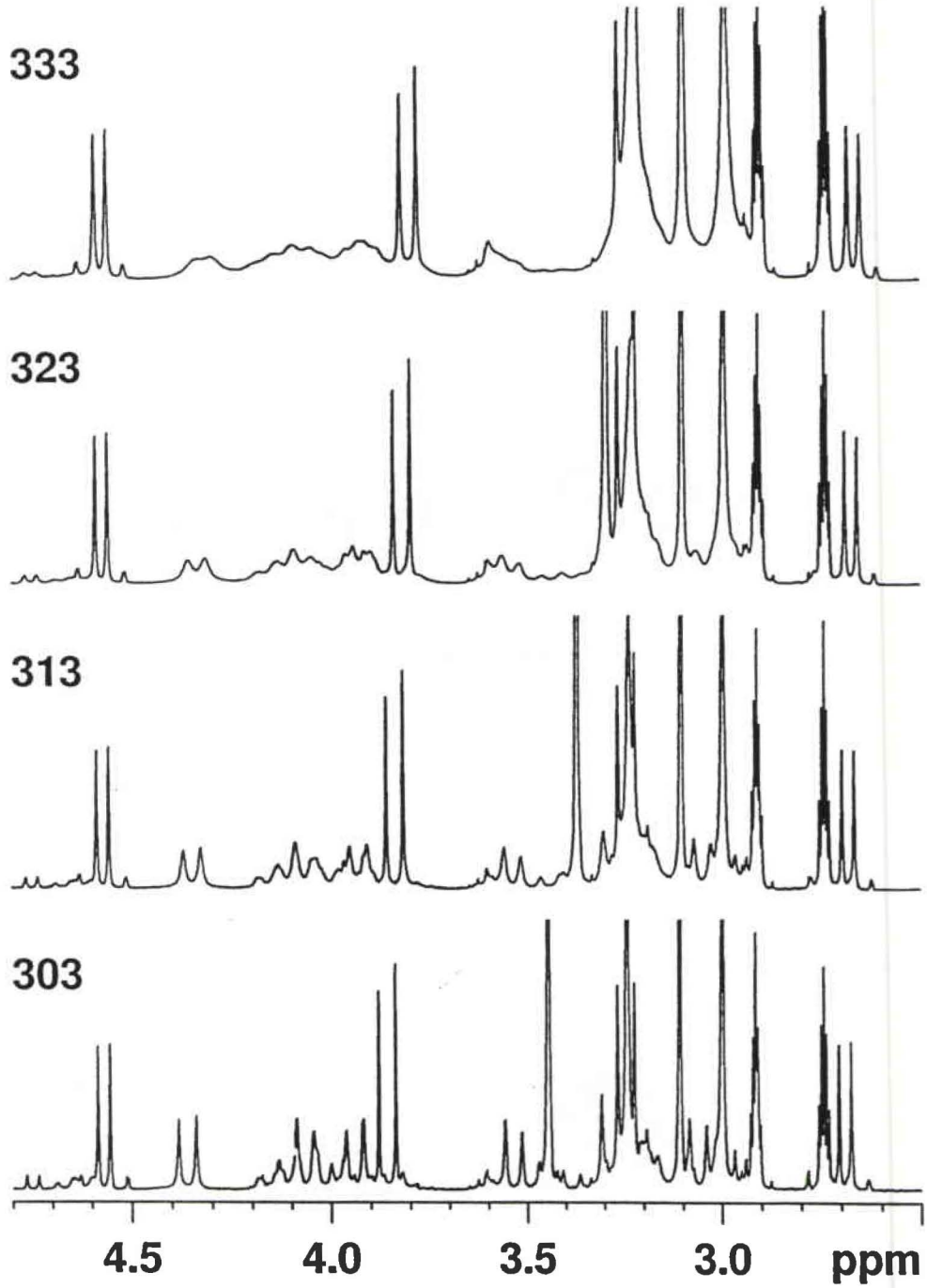

Figure 5.18(a) Experimental 300 MHz proton NMR spectra of DADS at 303, 313, 323, and 333 K.

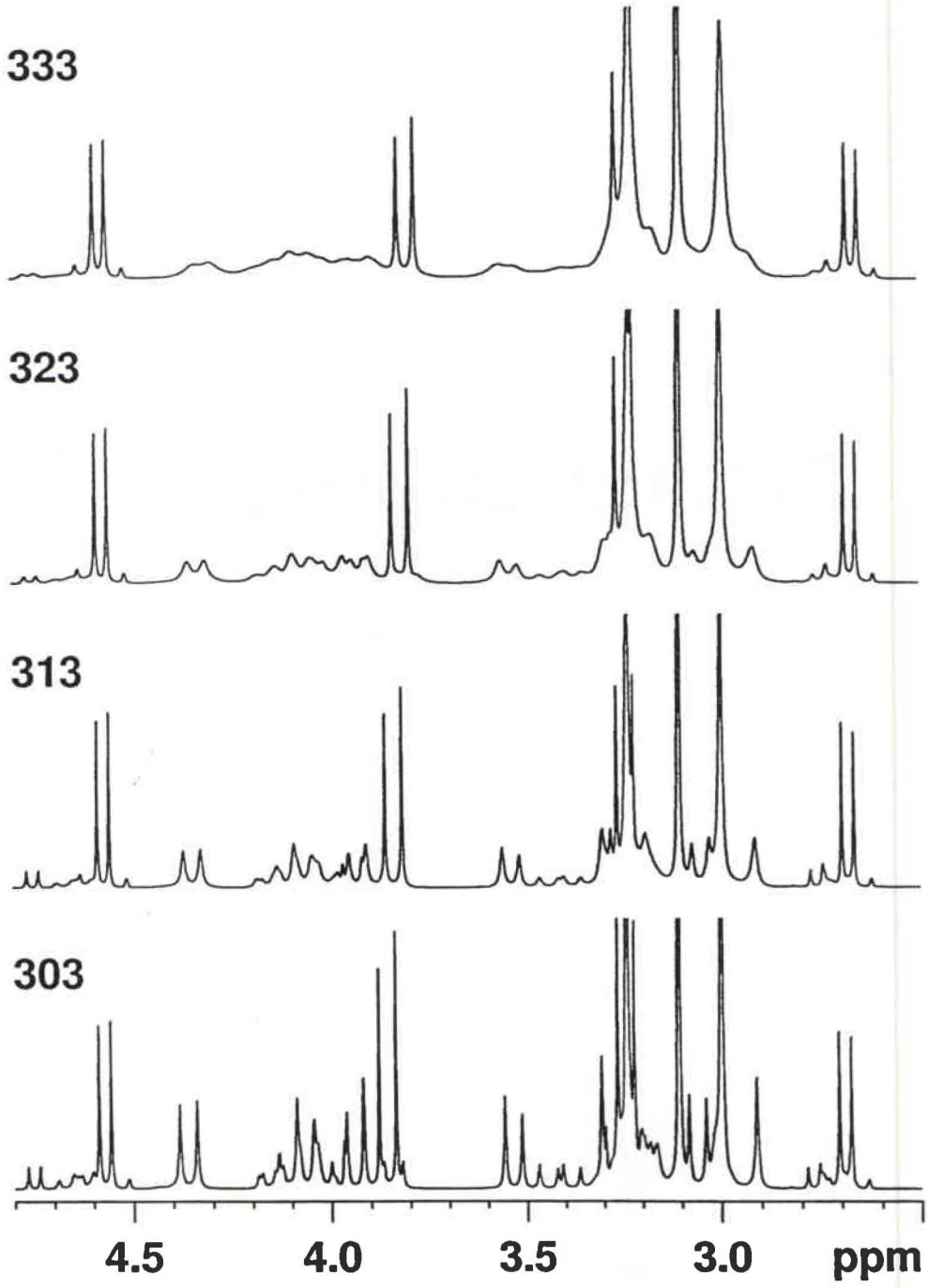

Figure 5.18(b) Simulated 300 MHz proton NMR spectra of DADS at 303, 313, 323 and 333 K. The spectra were simulated using the program MEXICO.

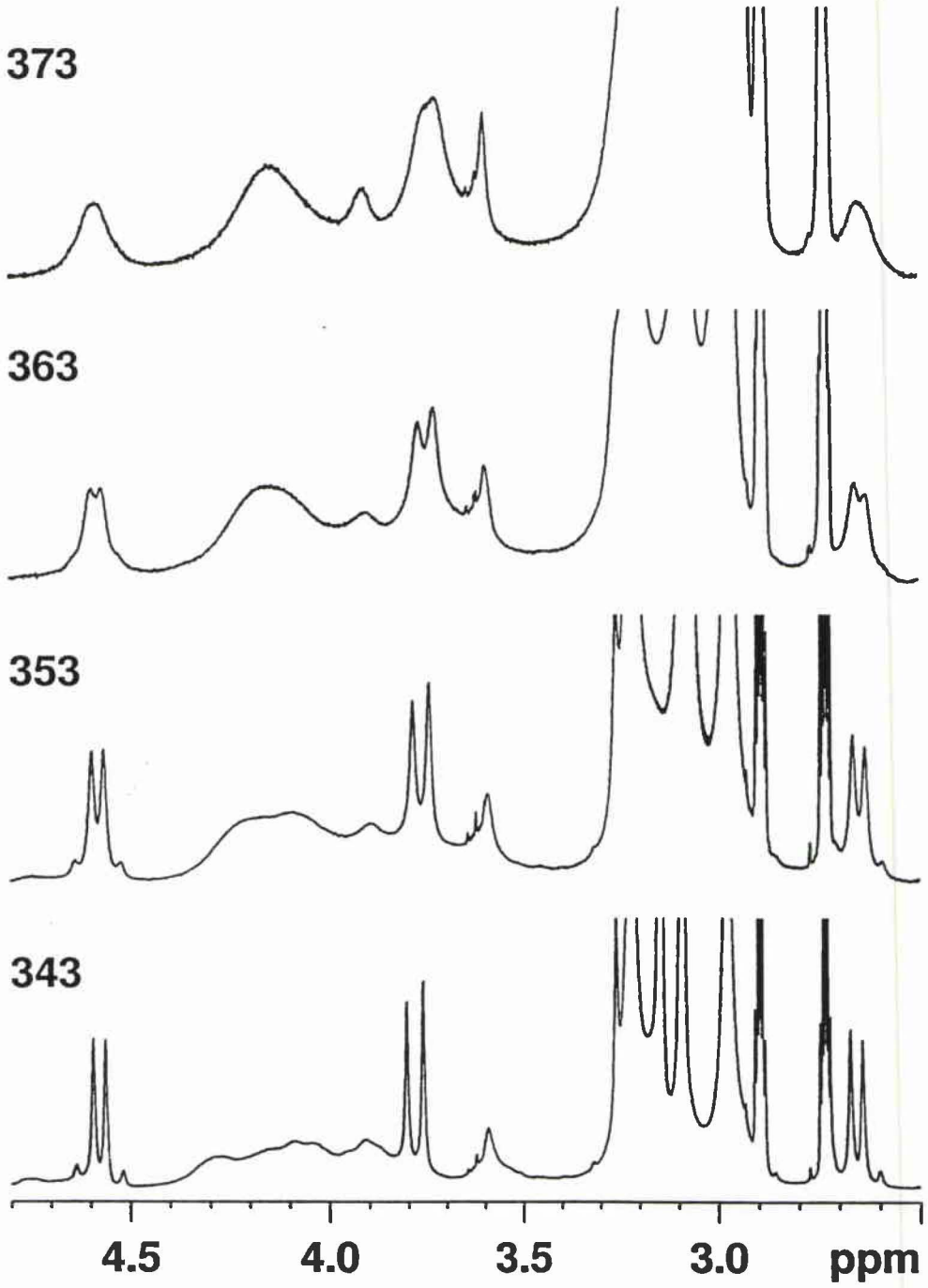

Figure 5.19(a) Experimental 300 MHz proton NMR spectra of DADS at 343, 353, 363, and 373 K.

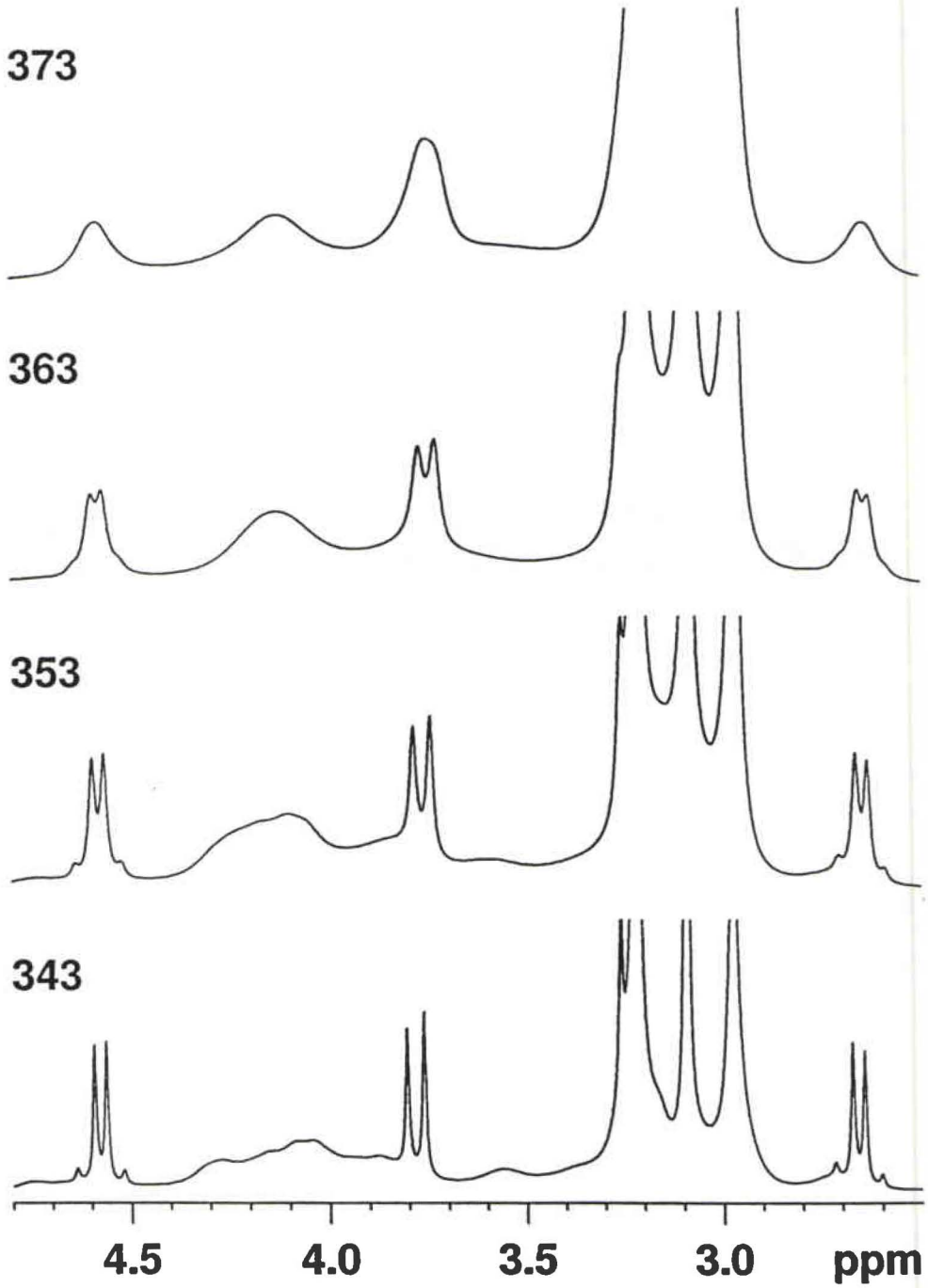

Figure 5.19(b) Simulated 300 MHz proton NMR spectra of DADS at 343, 353, 363 and 373 K. The spectra were simulated using the program MEXICO.

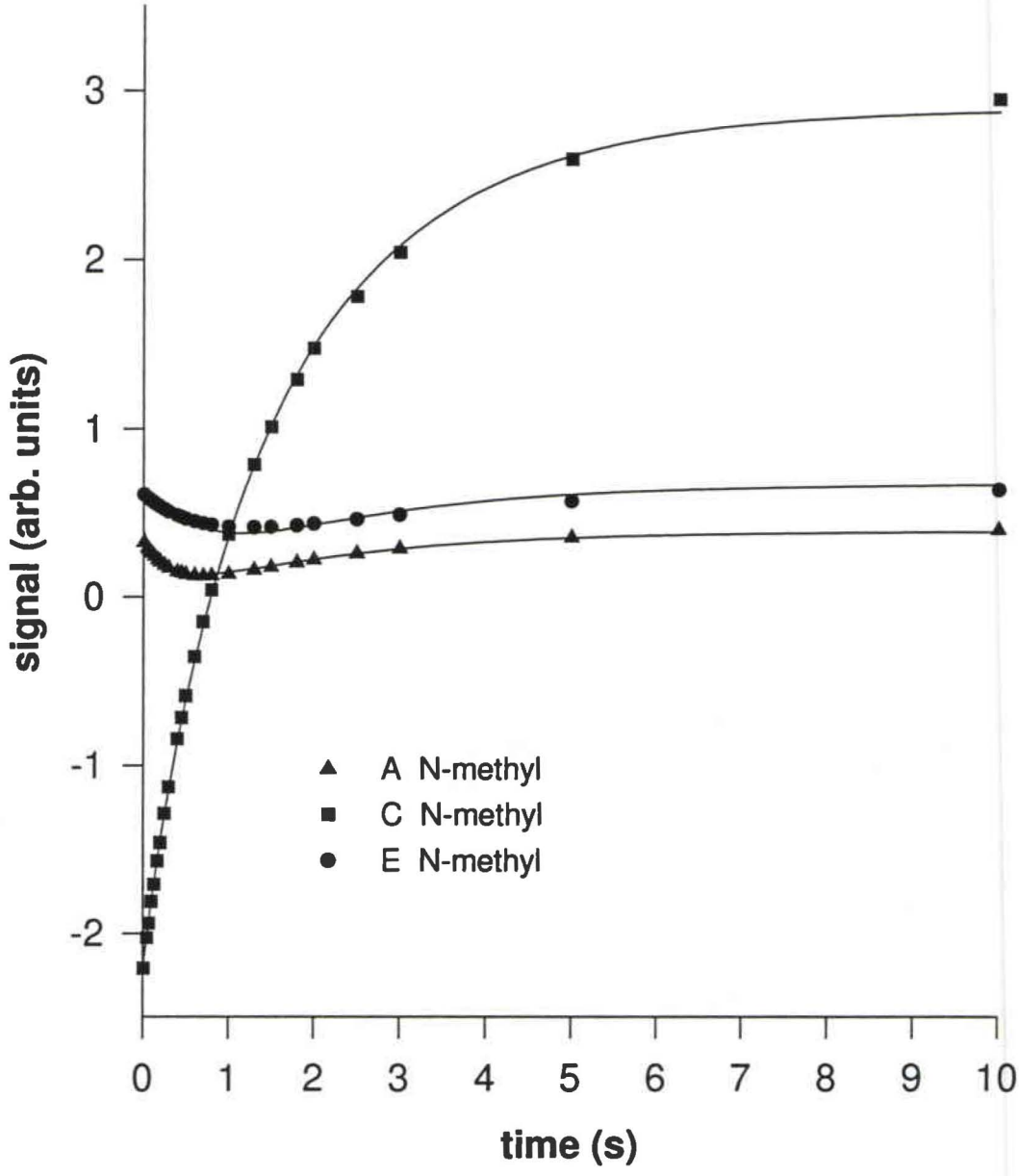

Figure 5.20 Results of a selective-inversion experiment. One of the N-methyl signals of conformer C was inverted. The points represent measured values and the lines are the best fit to the data. Note the small slope at time zero of the signal E. This shows there is little direct exchange between conformers C and E.

Discussion

The exchange rates are summarised in the Eyring plot in figure 5.21. The disulfide inversion and the ring flip process have the lowest barriers: $\Delta H^{\dagger} = 69.1 \pm 1$ kJ mol^{-1} and $\Delta H^{\dagger} = 73.8 \pm 1$ kJ mol^{-1}, respectively. The entropies of activation are small or close to zero: $\Delta S^{\dagger} = 0$ within experimental error for the disulfide process and $\Delta S^{\dagger} = 11 \pm 3$ J K^{-1} for the ring flip. The sizes of amide barriers[51] are typical: for the C to D process, $\Delta H^{\dagger} = 85.7 \pm 1.5$ kJ mol^{-1} and for the A to B process, $\Delta H^{\dagger} = 84.4 \pm 1.2$ kJ mol^{-1}. However, both barriers have significant positive entropies of activation: $\Delta S^{\dagger} = 19 \pm 4$ J K^{-1} and $\Delta S^{\dagger} = 22 \pm 4$ J K^{-1}, respectively. This means that the barrier estimated from a single rate measurement and equation 5.1, $\Delta G^{\dagger}$, would be different from a calculated barrier, $\Delta H^{\dagger}$, by approximately 6 kJ mol^{-1} at ambient temperature.

It appears that the disulfide can invert only if one of the amides is *E* - no firm evidence of direct interconversion of conformers B and D was observed. This seems to be a steric effect. The *Z,Z* form has a more crowded ring, since there is a methyl group and an amide oxygen on each side of the ring (figure 5.17). The modelling studies suggest that these groups are only 3.14 Å apart in conformer B, and 3.26 A in conformer D. In the *Z,E* form (conformers C and A), there is only one amide oxygen on one side of the ring. Furthermore, the two methyl groups on the other side are 3.8 - 3.9 Å apart in both conformers. The distance from the methyl groups to the oxygen atom on the same side of the ring is even larger. This appears to give the ring sufficient flexibility so that conformer C can convert to conformer A without significant steric hindrance.

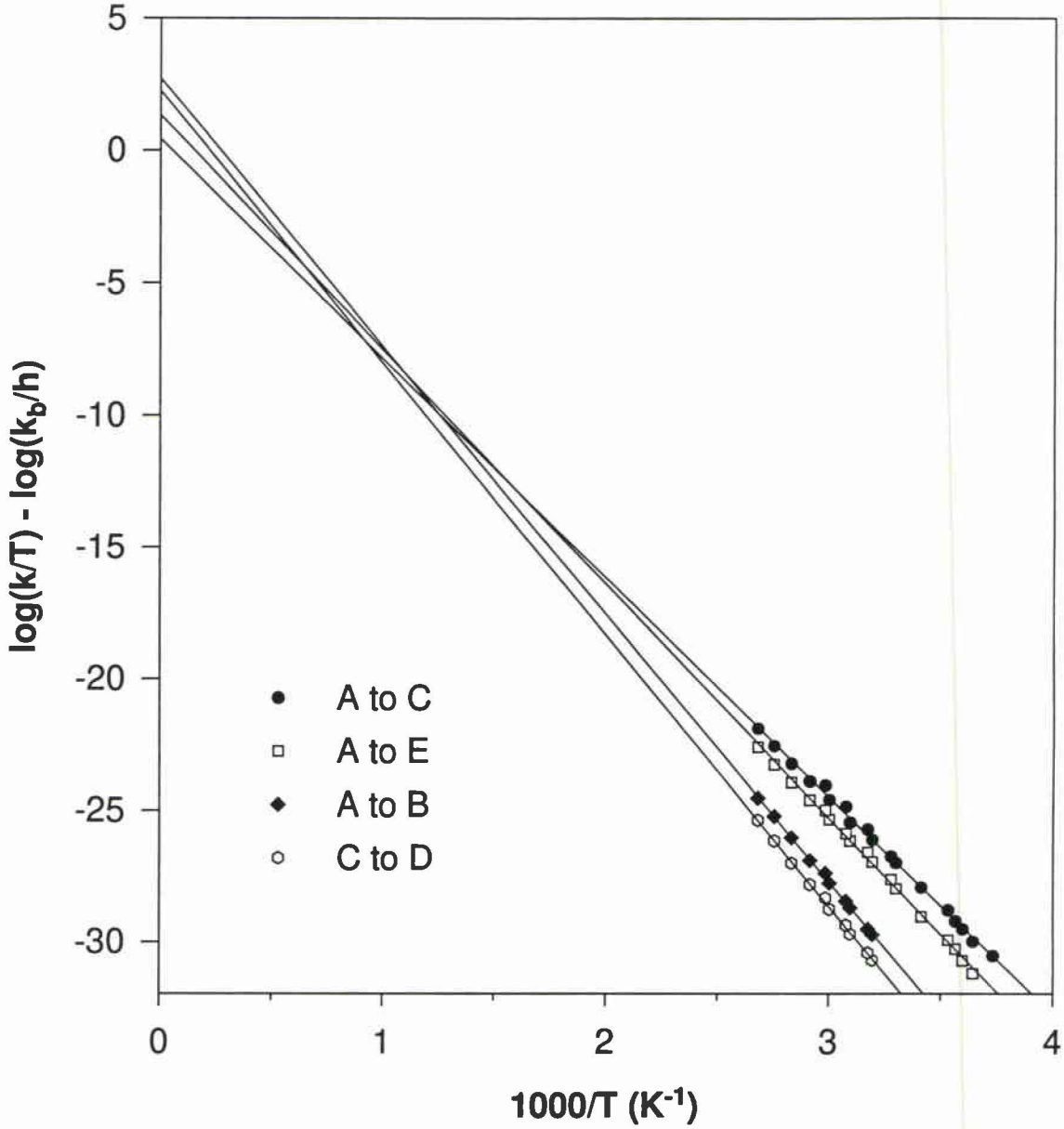

Figure 5.21 Eyring plot of the rate data for the four observed exchange processes in DADS. The lowest set of experimental data (octagons) represent the C to D process, the next highest set (diamonds) represent A to B, the next set (squares) represent A to E, and finally the highest set (circles), the A to C process.

Table 5.2

The activation parameters of all four exchange processes of DADS.

Process	$\Delta H^{\dagger}$ (kJ mol^{-1})	$\Delta S^{\dagger}$ (J K^{-1})	$\Delta G^{\dagger}_{300}$ (kJ mol^{-1})
C to A	71.6 ± 1	3 ± 3	71.6
C to D	85.7 ± 1.5	19 ± 4	80.0
A to B	84.4 ± 1.2	22 ± 4	77.8
A to E	73.8 ± 1	11 ± 3	70.5

Conclusions

This work is an example of how much detailed information is available through the application of modern 1D and 2D NMR methods. Measurement of the equilibrium constants and the exchange rates has provided nine points on the potential energy surface. For the exchange rate determinations, a combination of slow and intermediate exchange techniques provides data over a wider range temperature range. In particular, the 1D selective-inversion experiments provide excellent rate data in the slow exchange regime. This means that the free energy of activation can be separated into enthalpy and entropy effects. The disulfide inversion and the ring flip process are dominated by enthalpy effects, but the two amide inversions show significant positive entropy contributions to the barriers. Figure 5.17 summarises the measured energies of the five local minima, and four of the transition states joining them. This system is by no means the limit of the methods used here, so systems that are larger and more complicated are still tractable.

Chapter 6

A Complete NMR Analysis of the Proline Proton Spin System, and the Proline *cis-trans* Exchange Rate in Thyrotropin-Releasing Hormone (TRH), a Tripeptide.

(Based on a manuscript by Alex. D. Bain, P. Hazendonk and Zhe Zhou submitted to Biopolymers.[52])

Introduction

Thyrotropin-releasing hormone (TRH), L-pyroglutamyl-L-histidyl-L-prolineamide (figure 6.1), has a wide variety of biomedical effects.[53,54] Because of its own importance, and because of a general interest in proline-containing peptides, TRH has been widely studied[53-65] by NMR methods. Proline is unique among the common amino acids, in that the sidechain is bonded back onto the nitrogen of the backbone, creating a 5-membered ring. Furthermore, the peptide bond to proline is often observed in both *cis* and *trans* conformations (figure 1),[15,21,66-72] with slow interconversion under typical biological conditions.[14,17,73-76] Many biological systems have enzymes to catalyse the process, since it is a potential bottleneck in the folding of proteins from their denatured state.[77-79] Because of all these factors, it is important to understand the energetics and dynamics of TRH in solution.

Recently, it has been observed that the *cis-trans* isomerisation rates in histidine-proline moieties depend on the pH of the solution.[55] For TRH, the rate decreased by approximately a factor of 2 on going from pH 4.5 to pH 8.7. These rates were measured for a variety of peptides by pH-jump experiments (for rates of less than 5×10^{-3} s^{-1}) and by 2D NMR experiments (EXSY) (for rates of about 0.5 s^{-1}). It was suggested that protonation of the histidine generated some internal catalysis for the isomerisation.

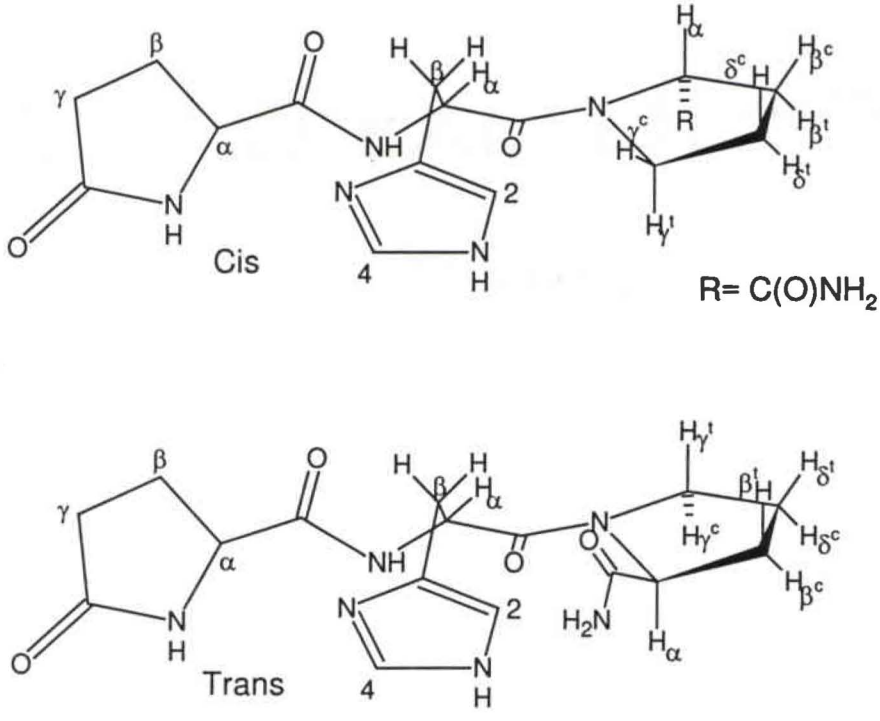

Figure 6.1 Schematic drawing of TRH, thyrotropin-releasing hormone, L-pyroglutamyl-L-histidyl-L-prolineamide, in the *cis* (upper) and *trans* (lower) conformation.

This postulate can now be examined more deeply, given new NMR techniques for the analysis of spectra, and for the measurements of exchange rates. The selective TOCSY experiment allows the isolation of individual spin systems from a complex spectrum. These subspectra can then be analysed, using classical spectral analysis, to yield chemical shifts and couplings for all of the protons. Karplus relations can then be used to help identify the structures.[80,81] For exchange rates, it is important to measure them over a wide range of temperatures, in order to separate the free energy of activation into enthalpy and entropy effects. Both enthalpy and entropy can affect the reaction rate (through the Eyring equation, which relates the free energy of activation to the rate constant). Enthalpy effects are relatively easy to visualise and model, but entropy is more difficult to rationalise.

Experimental

TRH (thyrotropin-releasing hormone, L-pyroglutamyl-L-histidyl-L-prolineamide free base) (98% purity) was obtained from Sigma Chemical and used without further purification. Approximately 40 mg of material was dissolved in a 50 mM phosphate buffer prepared with 99.9% D_2O (Cambridge Isotopes). The samples also contained 100 mM NaCl. The pH of the samples was adjusted using NaOD and DCl. The pH readings were from a glass electrode, and were not corrected for the deuterium isotope effect.

Samples were put into 5mm thin-wall NMR tubes. NMR spectra were obtained on a Bruker DRX500 NMR spectrometer operating at 500.13 MHz for protons, using a 5 mm triple-axis-gradient inverse probe and on a Bruker AC300 NMR spectrometer operating at 300.13 MHz for protons, using a 5 mm four-nucleus probe. Temperatures in the probe were controlled by a BVT2000 controller on both spectrometers, and were checked using a thermocouple in a 5 mm NMR tube. Temperatures were considered accurate to within $\pm$ 0.5 K.

The samples were characterised by the standard suite of 2D NMR experiments: gradient COSY(figure 6.2), phase-sensitive NOESY (figure 6.3), HSQC (figure 6.4) and HMBC.

Spin parameters (chemical shifts and coupling constants) were obtained by analysing selective TOCSY spectra (figures 6.5 and 6.6). Protons from each spin system were excited using a Gaussian selective pulse, and then the system was spin-locked using an MLEV-17 pulse sequence. The resulting spectra were simulated with the XSIM

program (available from Kirk Marat, University of Manitoba). All spin systems were analysed, with the exception of the pyroglutamate ring in the minor conformation.

Chemical exchange rates were measured at high temperature by simulating [32,34] the changes in NMR lineshape of the histidine ring protons, caused by chemical exchange. The program MEXICO was used for these simulations. At lower temperatures (and slower exchange rates), rates were measured using a selective-inversion recovery experiment, sometimes called the Hoffman-Forsen technique. The spins corresponding to the histidine H_4 ring protons in the major site were inverted selectively, using a Gaussian shaped pulse. The recovery of this site, and the transient in the minor site, were measured by taking spectra at a series of times after the inversion.[35-39,82] Data from this coupled recovery was analysed, and rates extracted, using a program called CIFIT.

Activation parameters, and their errors were obtained by doing a linear least-squares fit of log(rate/T) vs. (1/T) (Eyring plot), where T is the absolute temperature.

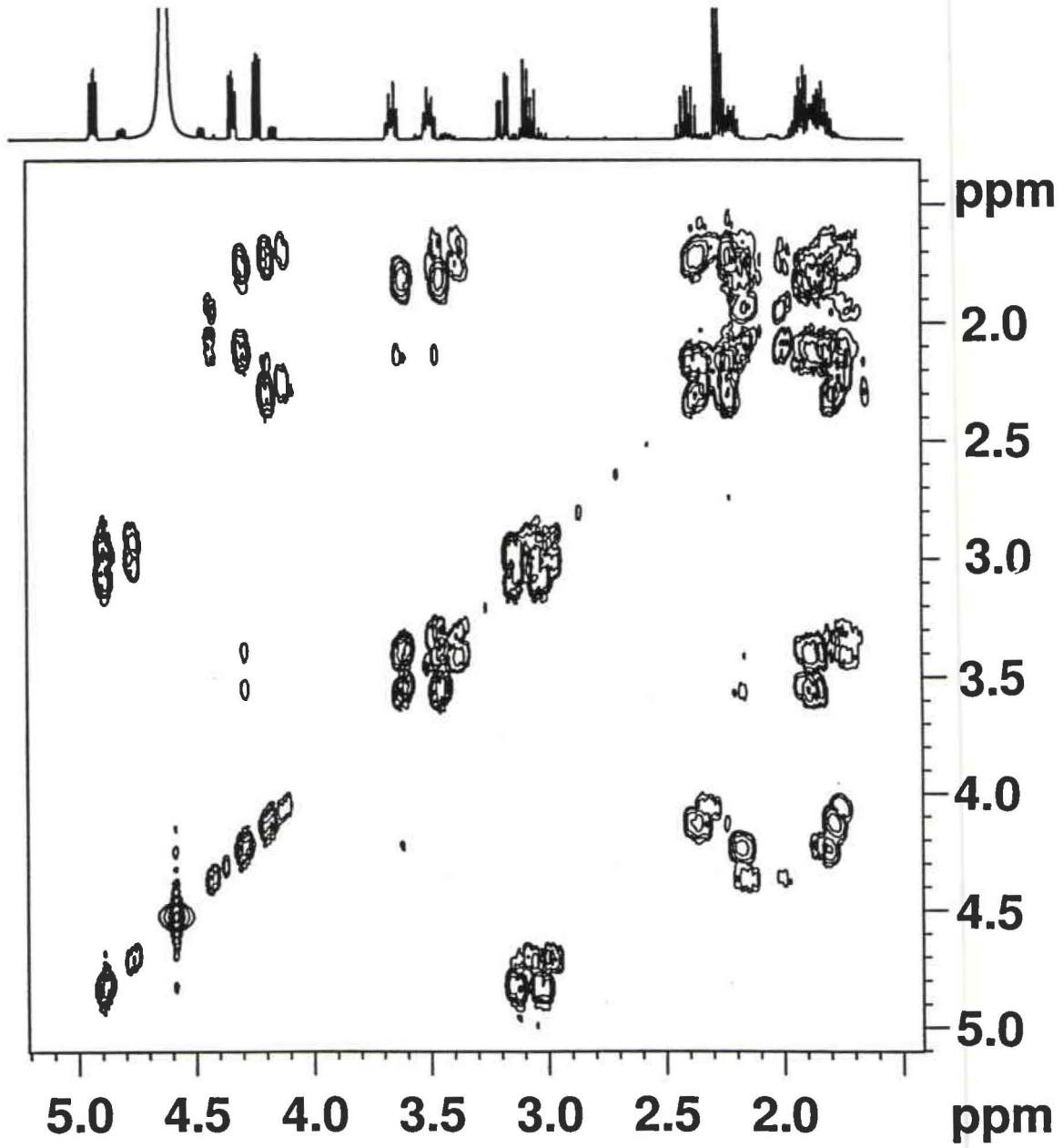

Figure 6.2 Gradient COSY-45 of TRH at pH= 3.3 at 303k. Expansion of the region 1.5 to 5.0 ppm.

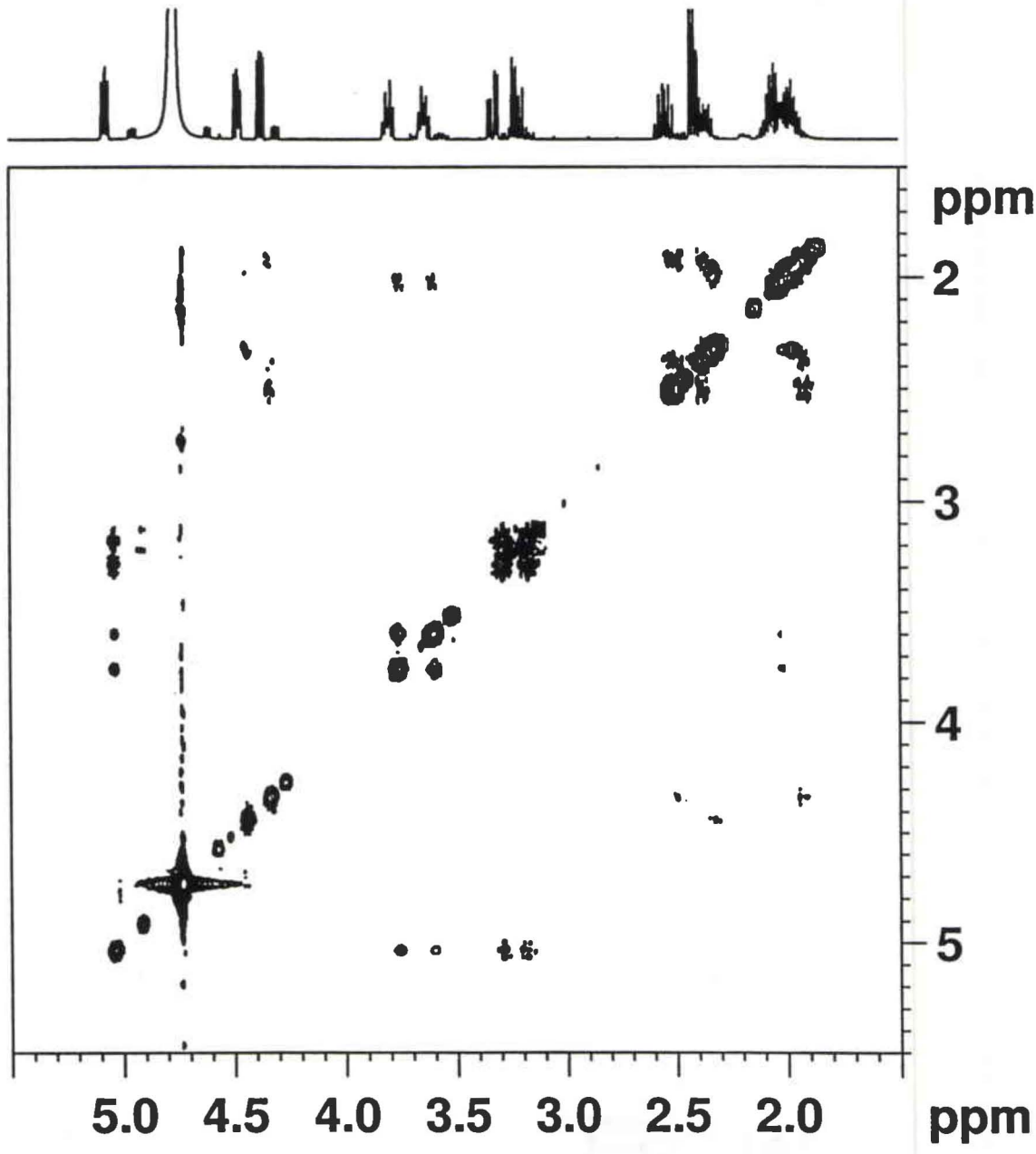

Figure 6.3 Gradient NOESY of TRH at pH=3.3 at 303 K. Expansion of the region 1.5 to 5.5 ppm.

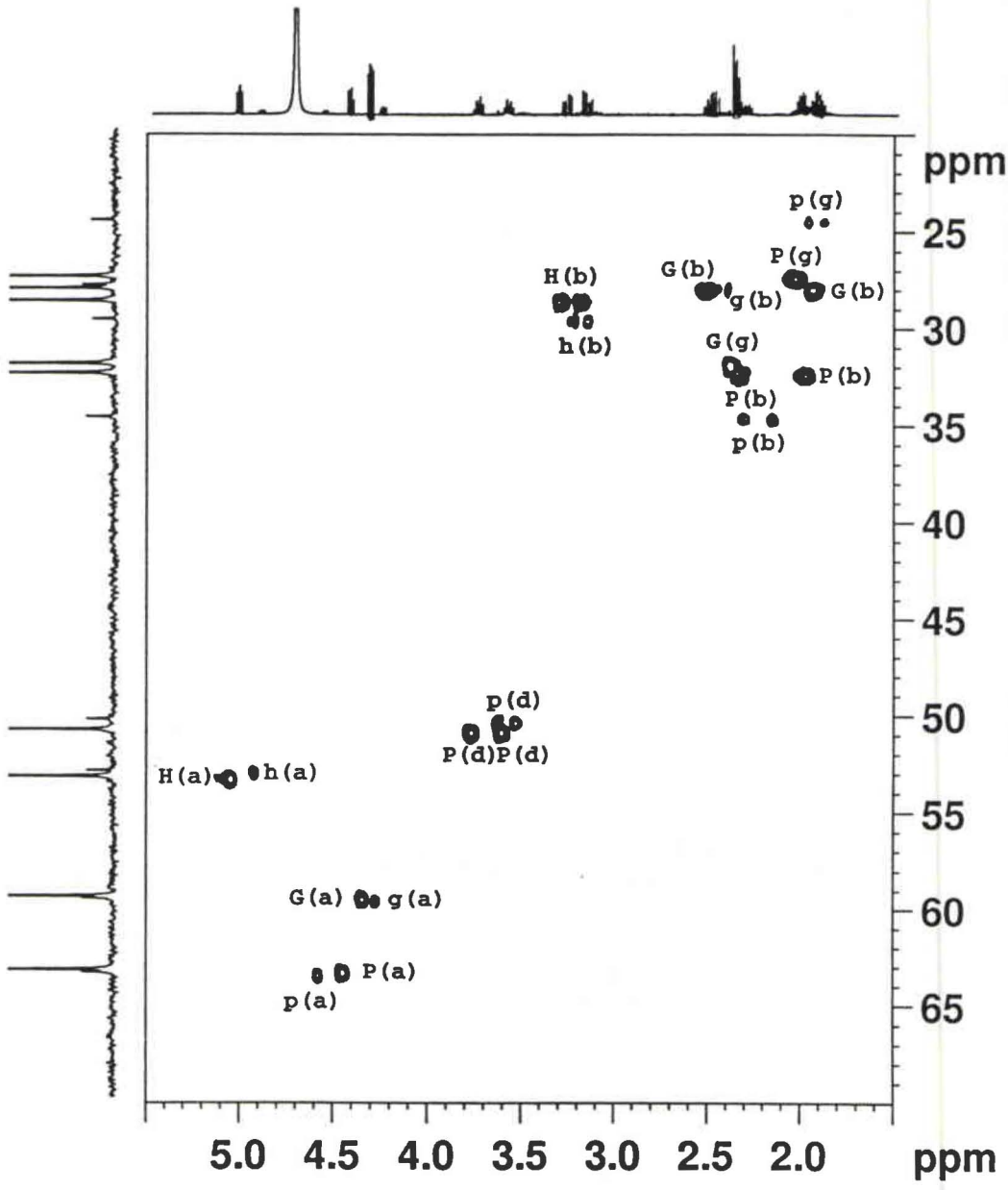

Figure 6.4 ^{13}C - ^{1}H 2DNMR chemical shift correlation spectrum of TRH at pH 3.3 and 303 K. The spectrum was obtained using a gradient version of the HSQC (homonuclear single quantum coherence) pulse sequence.

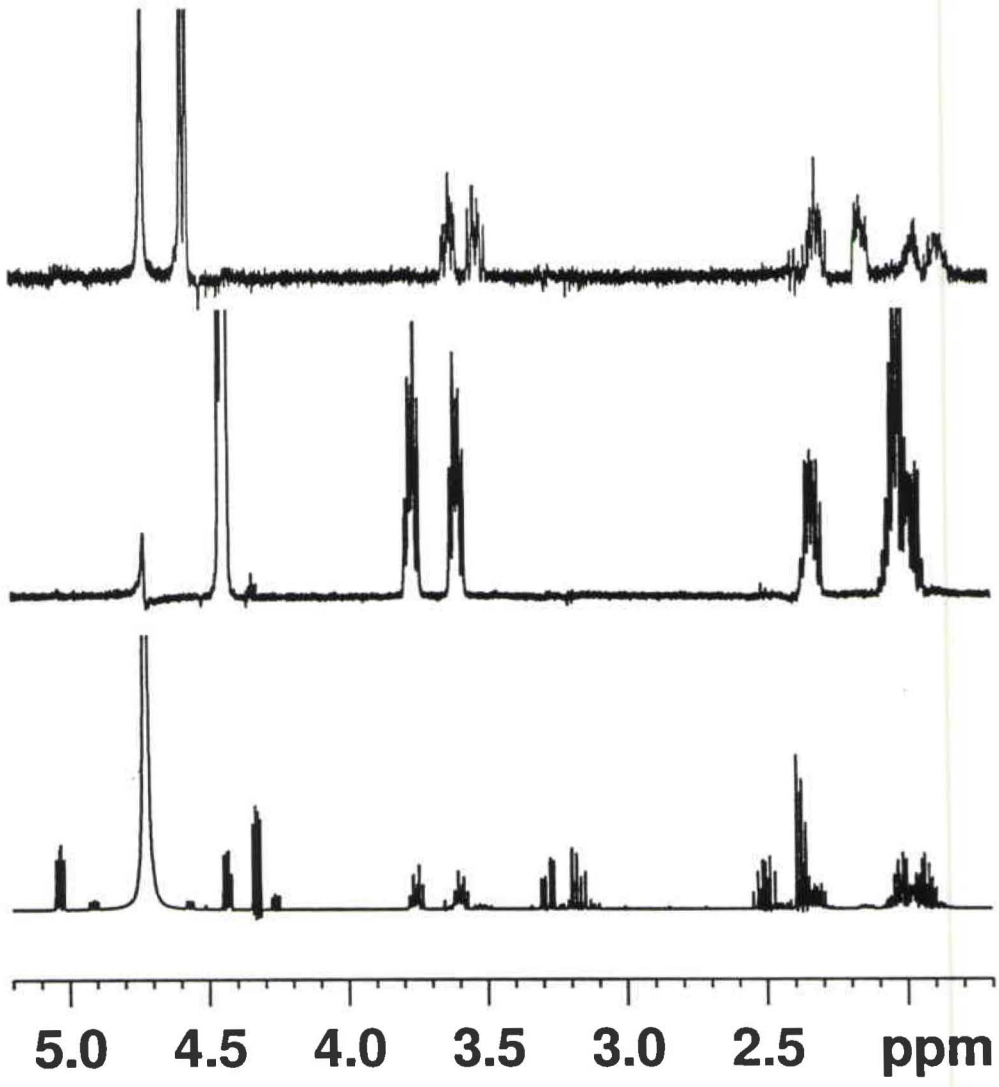

Figure 6.5 Results of selective TOCSY (total correlation spectroscopy) on TRH at pH 3.3 and 303 K. The bottom trace shows the full proton spectrum; the middle trace the results of irradiation of the α proton of proline in the *trans* conformation; and the upper trace, the results of irradiation of the α proton of proline in the *cis* conformation. The TOCSY spectrum shows only the protons that are connected to the irradiated proton by some direct or indirect scalar coupling. In this case, the subspectra of proline are clearly separated from the other overlapping in the normal spectrum.

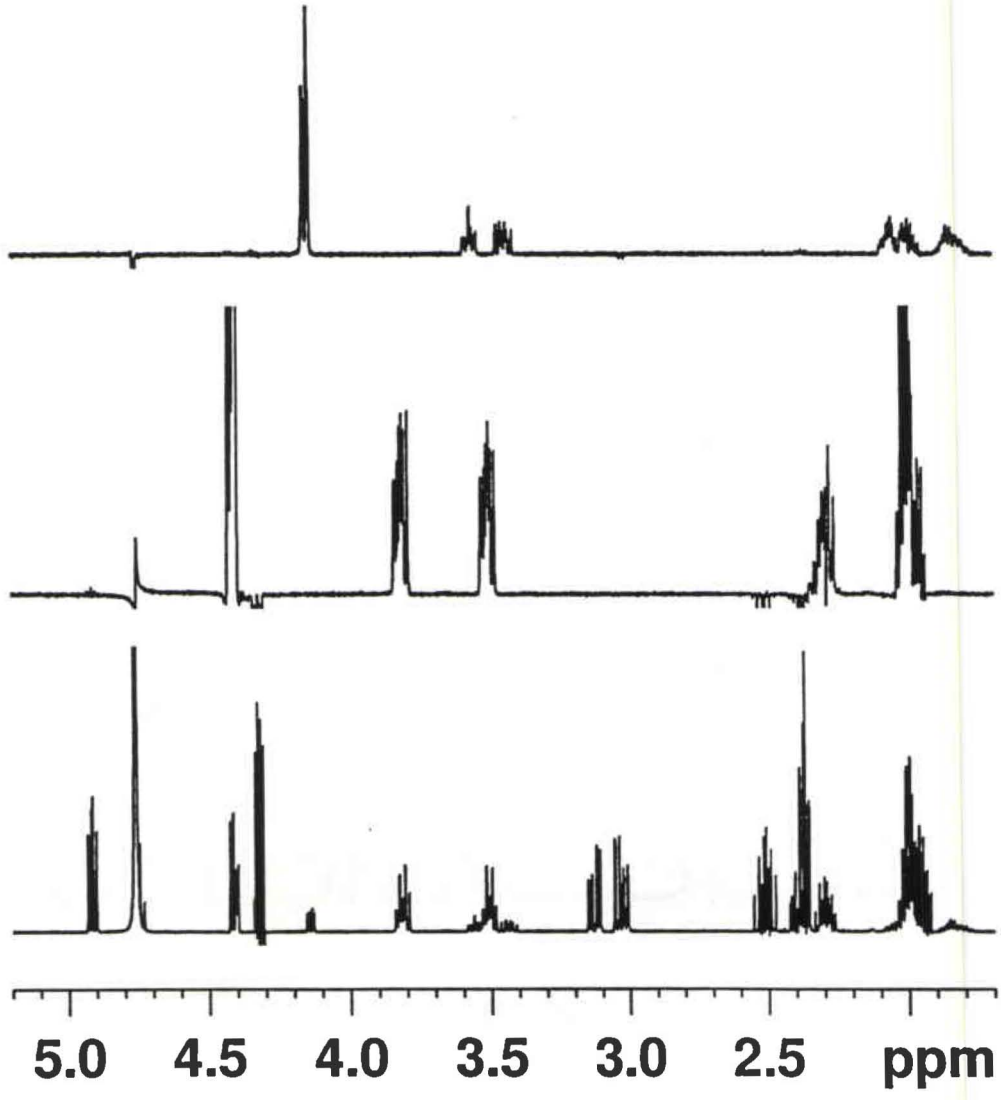

Figure 6.6 Results of selective TOCSY (total correlation spectroscopy) on TRH at pH 8.3 and 303 K. The bottom trace shows the full proton spectrum; the middle trace the results of irradiation of the α proton of proline in the *trans* conformation; and the upper trace, the results of irradiation of the α proton of proline in the *cis* conformation.

Results and Discussion

The chemical shifts and coupling constants for all the protons in the system, except for the pyroglutamate ring in the minor (*cis* proline) site, are given in tables 6.1, 6.3, 6.5 through 6.8. Tables 6.1 and 6.3 give the shifts and couplings for proline and tables 6.2 and 6.4 give values from the literature for comparison. Tables 6.5 and 6.6 give the histidine parameters, and tables 6.7 and 6.8 give the parameters for pyroglutamate in the major site (*trans* proline). The parameters are typical, and agree with published values.[56,60-62,83-87] Table 6.7 gives all the assignments of the ^{13}C NMR spectra, which agree with, and extend, previous work.[56,57,63]

The protons in the proline ring have been fully analysed,[60,81,85-92] however complicated methods such as selective deuteration,[93] shift reagents,[90,94] and 2D NMR experiments,[55,84,88,89,95,96] were required. This is because the seven spins in the system are strongly coupled, and the resolution of typical spectra just provides broad bands. For small peptides, the signal from other amino acids overlap obscuring part of the proline spectrum. This makes a full assignment difficult if not impossible, especially before the days of 2D techniques, when most of this work was done. Often the spectral parameters of only the major conformer is reported. Also many studies restricted themselves to ^{13}C NMR methods.[67,97-99] Seven coupled spins, however, present no problem for modern NMR spectral analysis programs, provided the signals of the spin systems are readily identified. In this case, the selective TOCSY spectra provided excellent spectra (figures 6.5 and 6.6), allowing a full analysis (figure 6.7 and 6.8) of the proline spectra in both the

cis and *trans* conformations of the peptide bond.

The spin parameters indicate that the pucker of the proline ring is different in the two proline conformations, and that the ring is rapidly interconverting between the *endo* and *exo* forms.[100-105] In particular, many of the coupling constants (table 6.3) are significantly different in the two conformations suggesting a difference in the populations between the two ring puckers. The five-membered proline ring is shaped like an envelope, where C_δ-N-C_α-C_β are roughly coplanar, and C_γ is either on the same (*endo*) or opposite (*exo*) side of the plane to the carboxyl carbon.

Table 6.4 contains the vicinal coupling of various proline derivatives. The couplings in Gly-Pro-Cha, where Cha is cyclohexylalanine, for both *cis* and *trans* conformations are similar to those of *cis* and *trans* proline in TRH.[85] The same can be said about the couplings in the *trans* form of propionylalanylprolineethylamide, PAPE,[87] which closely resemble those in the *cis* conformer of the proline in TRH at both pH 3 and 8. Proline-N-methylthiohydantoin[106] exists predominately as the endo pucker. This is indicated by the large 11.73 Hz coupling between the β^c and γ^t, where superscript *c* and *t* denote that the proton is on the same or opposite side of the ring to the α proton. The last two columns of table 6.4 contains vicinal couplings for the pure *endo* and *exo* forms of proline, predicted by a Karplus equation calibrated with the vicinal couplings in the proline ring.[81] These predict the same large coupling between β^c and γ^t for the *endo* pucker. The *exo* pucker is characterised by a similarly large vicinal coupling between β^t and γ^c, which in both TRH conformations are smaller. This leads to the conclusion that

the *trans* conformer does not significantly favour any of the *endo* or *exo* puckers, while the *cis* conformation favors the *endo* pucker, over the *exo*. There is still significant *exo* contribution for the *cis* form since the β^t and γ^c coupling is 2.68 for pH 3.3 and 3.25 for pH 8.3, which are significantly larger than 0.26 Hz predicted for the pure *endo* form.

The rates of exchange (table 6.8) tell us about the barrier between the *cis* and *trans* forms of proline in this molecule. Reaction rates are governed by the Gibbs' free energy of activation ($\Delta G^{\dagger}$) which includes both enthalpy and entropy effects. Enthalpy effects ($\Delta H^{\dagger}$) are usually assumed to be intramolecular, and to correspond to values obtained from molecular modelling. Entropy effects ($\Delta S^{\dagger}$) are much more difficult to measure and to interpret.[107] For the process of *cis* to *trans* isomerisation of proline in TRH, the barrier enthalpy ($\Delta H^{\dagger}$) is 85 kJ mol^{-1} at pH 3.3 and 88 kJ mol^{-1} at pH 8.3, which fall within the typical range of amide-type barriers.[108-110] The entropy ($\Delta S^{\dagger}$) for the same process is small and positive at both pH's: 10 J K^{-1} at pH 3.3 and 17 J K^{-1} at pH 8.3. Errors in these numbers are estimated to be ± 1-2 kJ mol^{-1} for ΔH and ± 3-5 J K^{-1} for ΔS.

These numbers are difficult to interpret with certainty. Note that at 323 K the rates are significantly different, but they are almost equal at 370 K. This is further illustrated in the Eyring plot (figure 6.9), in which the slopes and intercepts of the two lines are slightly different. The slope gives us the enthalpy, and the intercept at 1000/T = 0 gives us the entropy. It seems that the transition state is stabilised in enthalpy at low pH relative to pH 8.3. However, the transition state is always more disordered than the *cis* ground state, since the entropy of activation is positive. This disordering appears to be

less at pH 3.3 (when histidine is protonated) than at high pH. These effects are small, but they support the hypothesis of the acceleration of the rate by the protonated histidine. The proton stabilises the transition state, but it also restricts the geometry somewhat and lowers the entropy of activation. These two contributions counteract each other in the total free energy, so we get the observed change in relative rates as a function of temperature. The effects are quite small, but they are consistent, and so we believe them to be genuine.

It has been proposed that the *trans* form is stabilised by a hydrogen bonding interaction between a hydrogen on the imidazole ring of the histidine and the carbonyl oxygen of the proline.[57] This interaction is lost upon an increase in pH leading to an increase in the *cis/trans* ratio. This would imply that the *trans* to *cis* barrier decreased with increased pH, which is not observed. One would also expect a decrease in the entropy of activation from the *trans* form to the transition state between pH 3 and pH 8, which is also not observed. In fact the opposite is seen for both. In addition, if the imidazole ring were to be in close proximity to the proline, one would expect the nearby proton to be significantly deshielded in the *trans* form with respect to the *cis* form at low pH. This effect would be lost at higher pH. The trends of the chemical shifts of the proline protons on the same side of the ring as the carbonyl carbon remain roughly the same between pH 3.3 and 8.8. In addition, a hydrogen bond would restrict the motion of the histidine side chain, thus significant changes would be expected in the vicinal couplings, in the side chain, between the *cis* and *trans* forms at low pH. This is not

observed. These data do not support the existence of this hydrogen-bonding interaction, however some catalytic effect is still apparent. The mechanism with which this catalysis takes place is still unclear, however pH titration studies do indicate that histidine is involved in some way.[55,57,63] Other experimental and theoretical studies have suggested that a hydrogen bond to the proline nitrogen or carbonyl oxygen significantly decrease barriers of this type.[111-113]

Conclusions

Accurate measurements of the rate constant as a function of temperature for the process of *cis* to *trans* isomerisation of proline peptide bond in TRH have supported the hypothesis that the protonated histidine catalyses the process. However, the process is more complicated than it might appear: both entropy and enthalpy effects are important, and the pucker of the proline ring changes at the same time. This study shows the importance of detailed and accurate rate measurements in the analysis of these kinetic processes. It also exemplifies the utility of using 1D NMR techniques in these rate measurements.

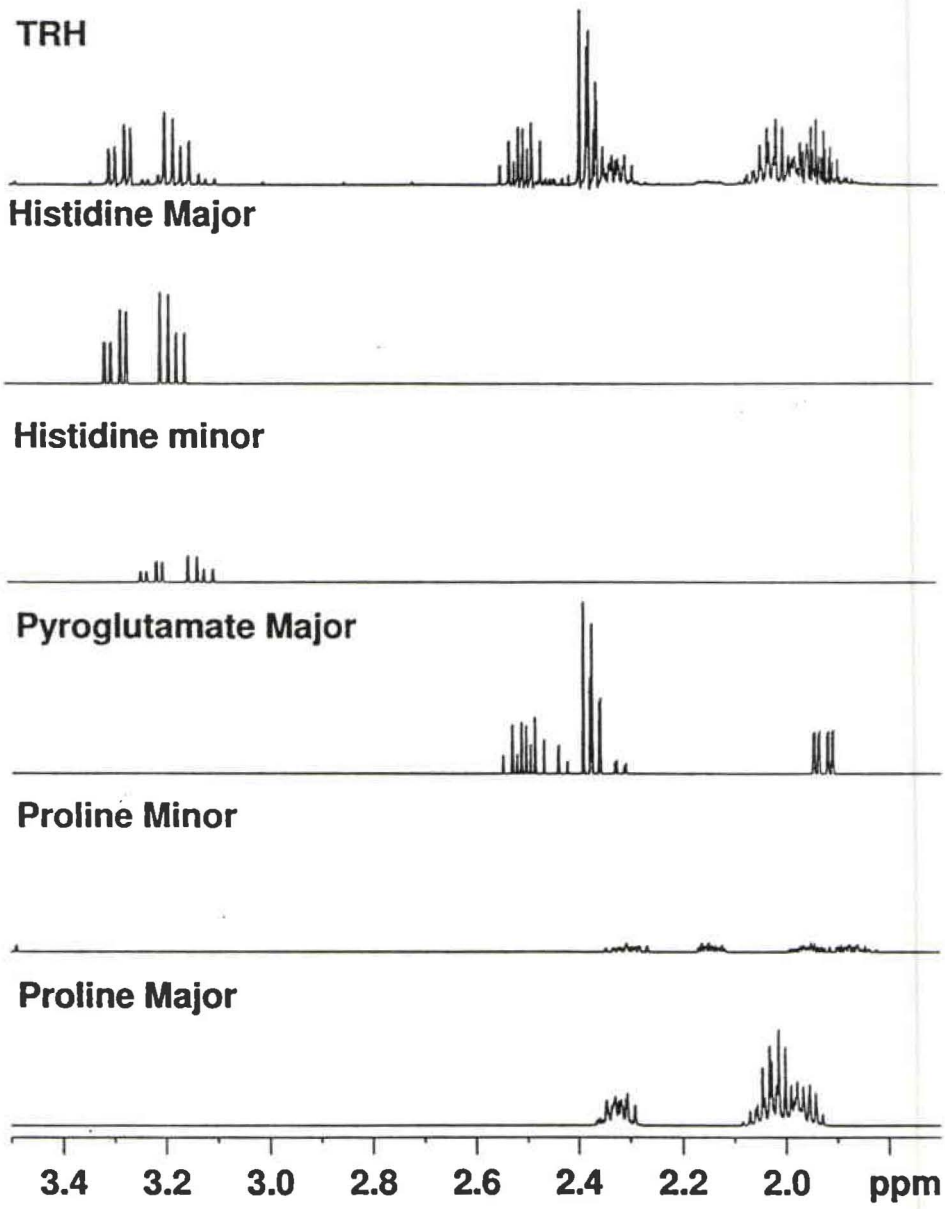

Figure 6.7 Simulated spectra of each of the amino acids individually, compared to the experimental proton spectrum of TRH at pH 3.3 and 303 K, 1.7 to3.5 ppm region. (top spectrum, number 6). The parameters used in the simulations are given in tables 6.1, 6.3, 6.5-6.8. The bottom spectrum (number 1) is that of proline in the *trans* conformation and the next (number 2) is that of proline in the *cis* conformation. Spectrum 3 corresponds to the spectrum of pyroglutamate in the *trans* conformation, and spectra 4 and 5 correspond to histidine, which has no peaks in this region in either conformation of TRH.

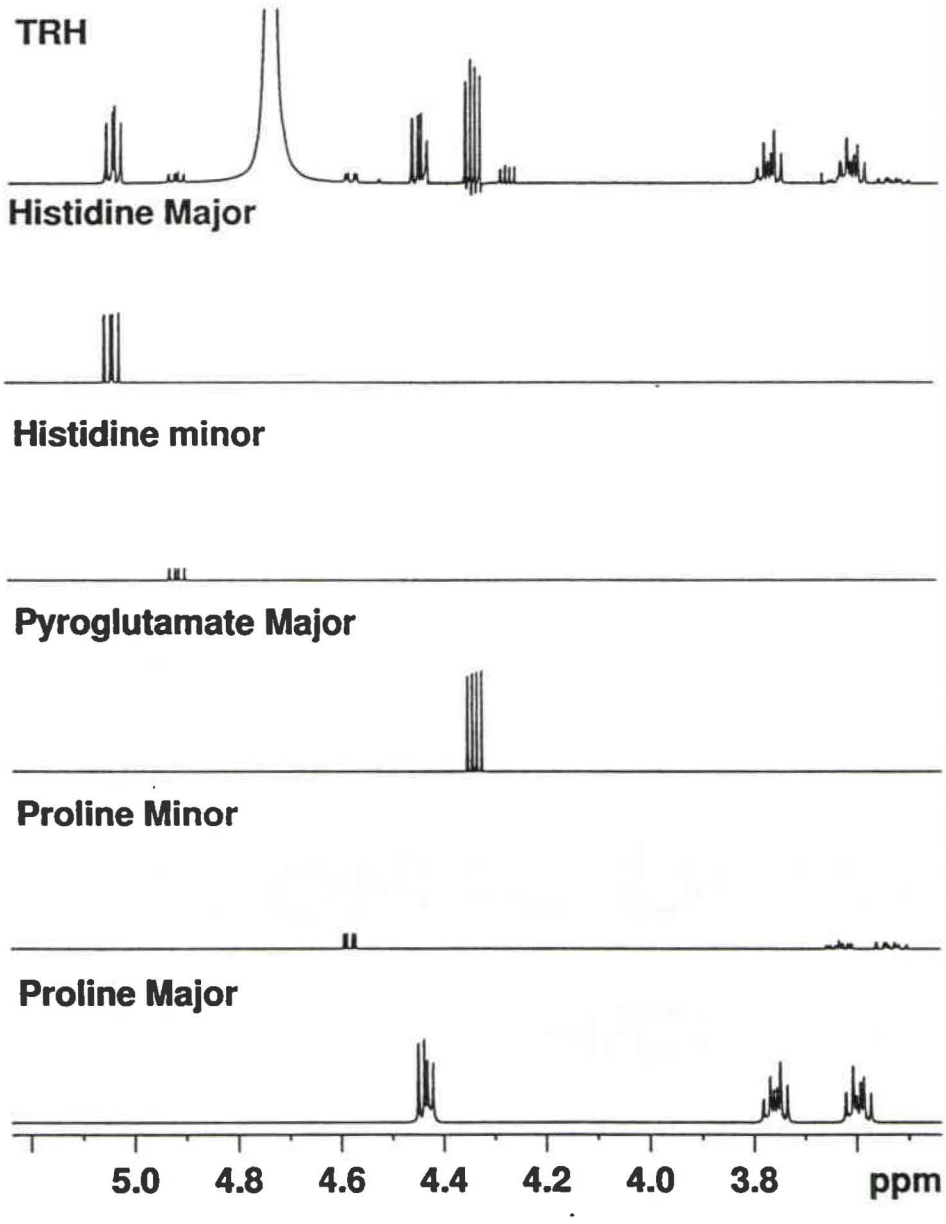

Figure 6.8 The 3.5 to 5.3 region of the simulated spectra of TRH.(see caption for 6.7)

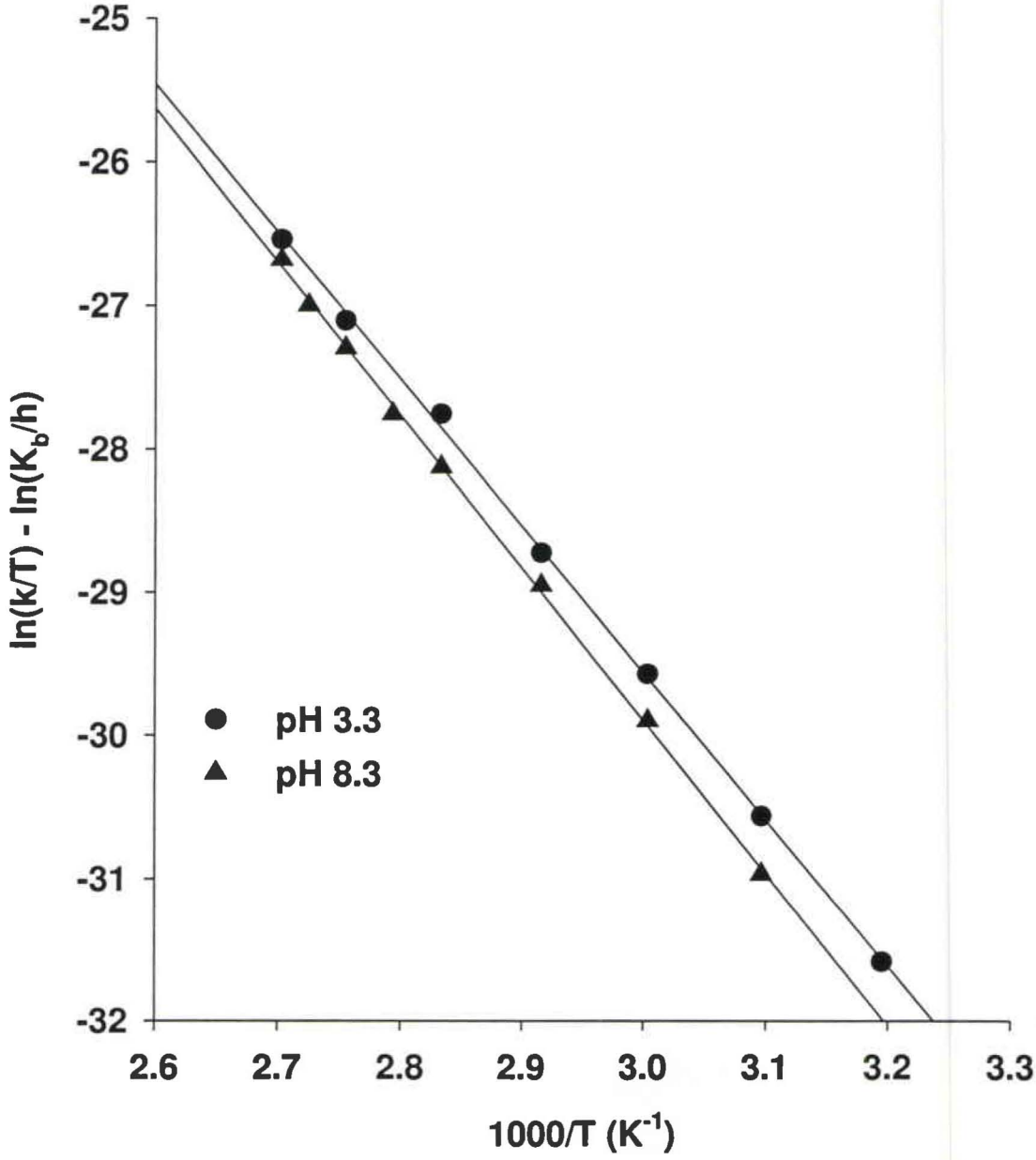

Figure 6.9 Eyring plot of log(rate/T) *vs* 1/T, where T is the absolute temperature. The slope of the line is related to the enthalpy of activation, and the intercept at 1/T=0 is related to the entropy of activation.

Table 6.1

Chemical shifts (in ppm) of the seven protons in the proline ring in the proline *cis* and *trans* conformations at 303K in D_2O at pH 3.3 and pH 8.3.

	pH 3.3		pH 8.3	
Proton	*trans*	*cis*	*trans*	*cis*
α	4.441	4.575	4.413	4.145
β^c	2.331	2.311	2.295	1.991
β^t	1.969	2.149	1.971	2.059
γ^c	2.045	1.963	2.011	1.808
γ^t	2.011	1.878	2.005	1.854
δ^c	3.763	3.623	3.817	3.561
δ^t	3.603	3.525	3.509	3.441

Table 6.2

Chemical shifts (in ppm) of the seven protons in the proline ring in the proline *cis* and *trans* conformations selected from literature.

	Gly-Pro-Cha[85] pH. 6		Acetyl-proline-amide[60] pH 5		Proline[86] pH 2	TRH[60] pH 1	TRH[60] pH 9	PAPE[87] $CDCl_3$
Proton	*trans*	*cis*	*trans*	*cis*		trans	trans	trans
α	4.49	4.50	4.84	4.99	4.328	4.77	4.88	4.53
β^c	2.31	2.40	2.80	2.80	2.420	2.81	2.86	1.89
β^t	2.02	2.00	2.50	2.50	2.143	2.38	2.45	2.38
γ^c	2.04	2.20	2.50	2.50	2.064	2.38	2.45	2.01
γ^t	2.04	1.9	2.50	2.50	2.040	2.38	2.45	2.16
δ^c	3.57	3.48	4.10	3.97	3.450	4.26	4.20	3.67
δ^t	3.63	3.55	4.10	3.97	3.393	3.95	4.20	3.55

Table 6.3

Geminal and vicinal proton-proton coupling constants (in Hz) for the seven protons in the proline ring in the proline *cis* and *trans* conformations at 303K in D_2O at pH 3.3 and pH 8.3. Some small, long-range couplings (<0.3 Hz were also observed). The vicinal (3-bond) coupling constants are accurate to ± 0.1 Hz, but the geminal couplings are considerably less well determined.

	pH 3.3		pH 8.3	
Coupling	*trans*	*cis*	*trans*	*cis*
$\alpha\beta^c$	8.55	8.40	8.61	8.60
$\alpha\beta^t$	5.76	2.68	5.02	2.61
$\beta^c\beta^t$	-12.68	-12.98	-12.97	-12.86
$\beta^c\gamma^c$	7.24	6.97	6.13	7.01
$\beta^c\gamma^t$	7.08	11.33	8.44	11.23
$\beta^t\gamma^c$	6.67	2.68	5.45	3.25
$\beta^t\gamma^t$	7.09	6.73	8.01	6.64
$\gamma^c\gamma^t$	-12.33	-1105	-12.26	-12.56
$\gamma^c\delta^c$	6.54	8.76	5.97	8.76
$\gamma^c\delta^t$	6.99	3.31	7.77	3.36
$\gamma^t\delta^c$	7.29	9.67	7.12	9.07
$\gamma^t\delta^t$	6.60	7.49	6.25	7.48
$\gamma^c\gamma^t$	-10.20	-11.78	-10.11	-11.86

Table 6.4

Geminal and vicinal proton-proton coupling constants (in Hz) for the seven protons in the proline ring in the proline *cis* and *trans* conformations taken from literature for various proline derivatives.

	Gly-Pro-Cha[85] pH 6		PAPE[87] $CDCl_3$	Acetyl-proline-amide[81] pH 6.9		Proline-N-methyl-thio-hydantion[106]		Proline predicted[81]
J	*trans*	*cis*	*trans*	*trans*	*cis*	*endo* (87%)	*endo*	*exo*
$\alpha\beta^c$	8.88	8.90	8.18	8.5	9.0	10.64	9.13	7.32
$\alpha\beta^t$	4.50	2.85	2.79	4.0	3.0	6.86	2.19	9.91
$\beta^c\beta^t$	-13.1	-13.35	-12.63	--	--	--	--	--
$\beta^c\gamma^c$	7.6	7.0	7.19	7.50	7.50	7.74	8.46	7.37
$\beta^c\gamma^t$	5.1	10.8	10.12	9.5	9.5	11.73	11.27	0.32
$\beta^t\gamma^c$	8.4	2.9	3.99	1.5	1.5	1.86	0.26	11.93
$\beta^t\gamma^t$	7.8	8.7	6.87	7.5	7.5	6.86	8.21	7.63
$\gamma^c\gamma^t$	-13.0	-13.2	-12.54	--	--	--	--	--
$\gamma^c\delta^c$	7.70	7.0	7.18	7.5	7.5	7.88	7.16	8.07
$\gamma^c\delta^t$	7.60	3.10	3.87	5.5	1.5	2.57	0.46	10.65
$\gamma^t\delta^c$	5.00	9.2	8.64	5.5	9.5	9.25	10.93	0.50
$\gamma^t\delta^t$	7.00	8.5	8.23	5.0	7.5	9.12	7.72	7.50
$\gamma^c\gamma^t$	-10.1	-11.00	-9.83	--	--	--	--	--

Table 6.5

Chemical shifts (in ppm) of the histidine protons in the proline *cis* and *trans* conformations at 303K in D_2O at pH 3.3 and pH 8.3. Protons labelled 2 and 4 are on the imidazole ring of the histidine.

	pH 3.3		pH 8.3	
Proton	*trans*	*cis*	*trans*	*cis*
α	5.033	4.911	4.913	4.749
β	3.179	3.129	3.033	3.011
β'	3.285	3.219	3.129	3.017
2	7.362	7.328	7.040	6.980
4	8.646	8.636	7.734	7.736

Table 6.6

Proton-proton coupling constants (in Hz) for histidine in the proline *cis* and *trans* conformations at 303K in D_2O at pH 3.3 and pH 8.3.

	pH 3.3		pH 8.3	
Coupling	*trans*	*cis*	*trans*	*cis*
αβ	8.11	8.91	8.05	7.6
αβ′	5.95	5.60	6.50	7.9
ββ′	-15.53	-15.27	-14.76	-18.39
β2	0.56	0.75	0.59	0.5
β′2	0.81	0.84	0.82	0.7
2-4	1.43	1.38	1.18	1.13

Table 6.7

Chemical shifts (in ppm) of the protons of the pyroglutamate residue in the proline *trans* conformation only at 303K in D_2O at pH 3.3 and pH 8.3.

	pH 3.3		pH 8.3	
Proton	*trans*	*cis*	*trans*	*cis*
α	4.333	-	4.323	-
β	2.509	-	2.509	-
β'	1.931	-	1.955	-
γ	2.359	-	2.351	-
γ'	2.399	-	2.387	-

Table 6.8

Proton-proton couplings (in Hz) of the protons of the pyroglutamate residue in the proline *trans* conformation only at 303K in D_2O at pH 3.3 and pH 8.3.

	pH 3.3		pH 8.3	
Coupling	*trans*	*cis*	*trans*	*cis*
αβ	9.23	-	9.19	-
αβ′	4.78	-	4.59	-
ββ′	-13.46	-	-13.31	-
βγ	8.22	-	7.82	-
βγ′	9.16	-	9.54	-
β′γ	1.73	-	2.21	-
β′γ′	0.07	-	0.19	-
γγ′	-24.56	-	-17.33	-

Table 6.9

^{13}C NMR assignments for TRH at 303K in D_2O at pH of 7.0.

Carbon	*trans* shift (ppm)	*cis* shift (ppm)
pro α	63.4	63.2
pro β	32.4	34.4
pro γ	27.4	24.6
pro δ	50.8	50.1
pro carbonyl	179.6	179.1
his α	54.2	54.2
his β	30.2	31.8
his 1 (ring junction)	134.0	134.4
his 2	120.2	119.9
his 4	138.2	138.4
his carbonyl	173.7	173.9
p-glu α	59.5	59.6
p-glu β	27.9	27.9
p-glu γ	31.9	32.0
p-glu ring carbonyl	185.1	185.3
p-glu carbonyl	177.3	177.6

Table 6.10

Rates of *cis* to *trans* conversion, and the equilibrium constant (*cis/trans*) for TRH as a function of pH and temperature. The slower rates (at temperatures of 343 and below) were measured by selective inversion experiments, the faster rates by lineshape methods.

	pH 3.3		pH 8.3	
T (K)	rate[a] (*cis/trans*)	K (*cis/trans*)	rate (*cis/trans*)	K (*cis/trans*)
313	0.125	0.148	-	-
323	0.36	0.153	0.24	0.217
333	1.0	0.158	0.72	0.223
343	2.4	0.163	1.91	0.229
353	6.5	0.168	4.5	0.235
358	-	-	6.6	0.238
363	12.8	0.172	10.6	0.241
367	-	-	14.4	0.243
370	23	0.175	20	0.245

[a]All rates are in s^{-1} and are accurate to within 10%.

References

1) Bain, A.D.; Bell, R.A.; Fletcher, D.A.; Hazendonk, P.; Maharajh, R.B.; Rigby, S.; Valliant, J.F. *J.Chem.Soc.Perkin Trans.2* **1999**, 1447-1454.

2) Maharajh, R.B.; Synder, J.P.; Britten, J.F.; Bell, R.A. *Can.J.Chem.* **1997**, *75*, 140-161.

3) Schwochau, K. *Angew.Chem.Int.Ed.Engl.* **1994**, *33*, 2258-2267.

4) Brenner, D.; Davison, A.; Jones, A.G.; Lister-James, J. *Inorg.Chem.* **1984**, *23*, 3793-3797.

5) Stepniak-Biniakiewicz, D.; Chen, B.H.; Deutsch, E. *J.Med.Chem.* **1992**, *35*, 274-279.

6) Klingensmith, W.C.; Fritzberg, A.R.; Spitzer, V.M.; Johnson, D.L.; Kuni, C.C.; Williamson, M.R.; Washer, G.; Weil, R. *J.Nucl.Med.* **1984**, *25*, 42-48.

7) Hom, R.K.; Katzenellenbogen, J.A. *Nucl.Med.Biol.* **1997**, *24*, 485-498.

8) Capretta, A.; Maharajh, R.B.; Bell, R.A. *Carbohydrate Research* **1995**, *267*, 49-63.

9) Avizonis, D.Z.; Farr-Jones, S.; Kosen, P.A.; Basus, V.J. *J.Am.Chem.Soc.* **1996**, *118*, 13031-13039.

10) Kopple, K.D.; Bhandary, K.K.; Kartha, G.; Wang, Y.S.; Parameswaran, K.N. *J.Am.Chem.Soc.* **1986**, *108*, 4637-4642.

11) Kopple, K.D.; Bean, J.W.; Bhandary, K.K.; Briand, J.; D'Ambrosio, C.A.; Peishoff, C.E. *Biopolymers* **1993**, *33*, 1093-1099.

12) Blackledge, M.J.; Bruschweiler, R.; Griesinger, C.; Schmidt, J.M.; Ernst, R.R. *Biochemistry* **1993**, *32*, 10960-10974.

13) Shimizu, T.; Tanaka, Y.; Tsuda, K. *Int.J.Peptide Protein Res.* **1983**, *22*, 194-203.

14) Carpenter, K.A.; Schiller, P.W.; Schmidt, R.; Wilkes, B.C. *Int.J.Peptide Protein Res.* **1996**, *48*, 102-111.

15) Kern, D.; Kern, G.; Scherer, G.; Fischer, G.; Drakenberg, T. *Biochemistry* **1995**, *34*, 13594-13602.

16) Pinet, E.; Neumann, J.M.; Dahse, I.; Girault, G.; Andre, F. *Biopolymers* **1995**, *36*, 135-152.

17) Viles, J.H.; Mitchell, J.B.; Gough, S.L.; Doyle, P.M.; Harris, C.J.; Sadler, P.J.; Thornton, J.M. *Eur.J.Biochem.* **1996**, *242*, 352-362.

18) Lombardi, A.; Saviano, M.; Nastri, F.; Maglio, O.; Mazzeo, M.; Isernia, C.; Paolillo, L.; Pavone, V. *Biopolymers* **1996**, *38*, 693-703.

19) Stewart, W.E.; Siddall, T.H. *Chem.Rev.* **1970**, *70*, 517-551.

20) Fraser, R.R.; Boussard, G.; Saunders, J.K.; Lambert, J.B.; Mixan, C.E. *J.Am.Chem.Soc.* **1971**, *93*, 3822-3823.

21) Deber, C.M.; Bovey, F.A.; Carver, J.E.; Blout, E.R. *J.Am.Chem.Soc.* **1970**, *92*, 6191-6198.

22) Ptak, M. *Biopolymers* **1973**, *12*, 1575-1589.

23) Kim, K.W.; Sugawara, F.; Yoshida, S.; Murofushi, N.; Takahashi, N.; Curtis, R.W. *Biosci.Biotechnol.Biochem.* **1993**, *57*, 787-791.

24) Jiao, D.; Barfield, M.; Combariza, J.E.; Hrubny, V.J. *J.Am.Chem.Soc.* **1992**, *114*, 3639-3643.

25) Renugopalakrishnan, V.; Walter, R. *Z.Naturforsch.* **1984**, *39(a)*, 495-498.

26) Lidert, Z. *Tetrahedron* **1981**, *37*, 967-969.

27) Jackman, L.M.; Cotton, F.A.*Dynamic Nuclear Magnetic Resonance Spectroscopy*; Academic Press: New York, 1975;

28) Anet, F.A.L.; Bourn, A.J.R. *J.Am.Chem.Soc.* **1967**, *89*, 760-768.

29) Cepas, S.C.; North, M. *Tetrahedron* **1997**, *53*, 16859-16866.

30) Pawar, D.M.; Noe, E.A. *J.Am.Chem.Soc.* **1996**, *118*, 12821-12825.

31) Sandstrom, J.*Dynamic NMR spectroscopy*; Academic Press: London, 1982;

32) Binsch, G. *J.Am.Chem.Soc.* **1969**, *91*, 1304-1309.

33) Kleier, D.A.; Binsch, G. *J.Magn.Reson.* **1970**, *3*, 146-160.

34) Bain, A.D.; Duns, G.J. *Can.J.Chem.* **1996**, *74*, 819-824.

35) Grassi, M.; Mann, B.E.; Pickup, B.T.; Spencer, C.M. *J.Magn.Reson.* **1986**, *69*, 92-99.

36) Led, J.J.; Gesmar, H. *J.Magn.Reson.* **1982**, *49*, 444-463.

37) Muhandiram, D.R.; McClung, R.E.D. *J.Magn.Reson.* **1987**, *71*, 187-192.

38) Bain, A.D.; Cramer, J.A. *J.Magn.Reson.* **1993**, *103 A*, 217-222.

39) Bain, A.D.; Cramer, J.A. *J.Magn.Reson.* **1996**, *118 A*, 21-27.

40) McClung, R.E.D.; Aarts, G.H.M. *J.Magn.Reson.* **1995**, *115 A*, 145-154.

41) Bain, A.D.; Duns, G.J.; Rathgeb, F.; Vanderkloet, J. *J.Phys.Chem.* **1995**, *99*, 17338-17343.

42) Vasques, M.; Nemethyl, G.; Scheraga, H.A. *Chem.Rev.* **1994**, *94*, 2183-2239.

43) Jeener, J.; Meier, B.H.; Bachmann, P.; Ernst, R.R. *J.Chem.Phys.* **1979**, *71*, 4546-4553.

44) Perrin, C.L.; Dwyer, T. *Chem.Rev.* **1990**, *90*, 935-967.

45) Orrell, K.G.; Sik, V.; Stephenson, D. *Prog.Nucl.Magn.Reson.Spectrosc.* **1990**, *22*, 141-208.

46) Perrin, C.L.; Engler, R.E. *J.Magn.Reson.* **1990**, *90*, 363-369.

47) Perrin, C.L.; Engler, R.E. *J.Magn.Reson.* **1996**, *123 A*, 188-195.

48) Engler, R.E.; Johnston, E.R.; Wade, C.G. *J.Magn.Reson.* **1988**, *77*, 377-381.

49) Bellon, S.F.; Chen, D.; Johnston, E.R. *J.Magn.Reson.* **1987**, *73*, 168-173.

50) Bain, A.D.; Duns, G.J.; Ternieden, S.; Ma, J.; Werstiuk, N.H. *J.Phys.Chem.* **1994**, *98*, 7458-7463.

51) Taha, A.N.; Neugebauer Crawford, S.M.; True, N.S. *J.Am.Chem.Soc.* **1998**, *120*, 1934-1935.

52) Bain, A.D.; Hazendonk, P.; Zhou, Z. *Biopolymers* **1999**,

53) Metcalf, G.; Jackson, I.M.D. *Ann.N.Y.Acad.Sci.* **1989**, *553*, 1-631.

54) Mordier, E.; Fermandjian, S.; Lhoste, J.-M.; Rips, R. *Biochimie* **1981**, *63*, 495-505.

55) Reimer, U.; ElMokdad, N.; Schutkowski, M.; Fischer, G. *Biochemistry* **1997**, *36*, 13802-13808.

56) Aksnes, D.W.; Athanassopoulos, C.; Magafa, V.; Aaberg, A.; Francis, G.W.; Papaioannou, D. *Acta Chem.Scand.* **1996**, *50*, 411-416.

57) Unrath, W.; Walker, R.D.; London, R.E. *Int.J.Peptide Protein Res.* **1983**, *22*, 582-589.

58) Vicar, J.; Abillon, E.; Toma, F.; Piriou, F.; Lintner, K.; Blaha, K.; Fromageot, P.; Fermandjian, S. *FEBS Letters* **1979**, *97*, 275-278.

59) Bellocq, A.M.; Dubien, M.; Dupart, E. *Biochemical and Biophysical Research Communications* **1975**, *65*, 1393-1399.

60) Montagut, M.; LeManceau, B.; Bellocq, A.M. *Biopolymers* **1974**, *13*, 2615-2629.

61) Donzel, B.; Rivier, J.; Goodman, M. *Biopolymers* **1974**, *13*, 2631-2647.

62) Feeney, J.; Bedford, G.R.; Wessels, P.L. *FEBS Letters* **1974**, *42*, 347-351.

63) Deslauriers, R.; McGregor, W.H.; Sarantakis, D.; Smith, I.C.P. *Biochemistry* **1974**, *13*, 3343-3348.

64) Nutt, R.F.; Holly, F.W.; Homnick, C.; Hirschmann, R.; Veber, D.F. *J.Med.Chem.* **1981**, *24*, 692-698.

65) Papaioannou, D.; Athanassopoulos, C.; Magafa, V.; Karigiannis, G.; Karamanos, N.; Stavropoulos, G.; Napoli, A.; Sindona, G.; Aksnes, D.W.; Francis, G.W.; Aaberg, A. *Acta Chem.Scand.* **1995**, *49*, 103-114.

66) Maia, H.L.; Orrell, K.G.; Rydon, H.N. *J.Chem.Soc.,Chem.Commun.* **1971**, 1209-1210.

67) London, R.E.; Matwiyoff, N.A.; Stewart, J.M.; Cann, J.R. *Biochemistry* **1978**, *17*, 2277-2283.

68) Ramachandran, G.N.; Mitra, A.K. *J.Mol.Biol.* **1976**, *107*, 85-92.

69) Stewart, D.E.; Sarkar, A.; Wampler, J.E. *J.Mol.Biol.* **1990**, *214*, 253-260.

70) Grathwohl, C.; Wuthrich, K. *Biopolymers* **1976**, *15*, 2025-2041.

71) Toma, F.; Fermandjian, S.; Low, M.; Kisfaludy, L. *Biochim.Biophys.Acta* **1978**, *534*, 112-122.

72) MacArthur, M.W.; Thornton, J.M. *J.Mol.Biol.* **1991**, *218*, 397-412.

73) John, I.G.; Radom, L. *J.Am.Chem.Soc.* **1978**, *100*, 3981-3991.

74) Weisshoff, H.; Wieprecht, T.; Henklein, P.; Frommel, C.; Antz, C.; Mugge, C. *FEBS Letters* **1996**, *387*, 201-207.

75) Maruta, S.; Saeki, N.; Banno, K.; Gagne, S.M.; Ikebe, M.; Sykes, B.D. *Biophys.J.* **1996**, *70*, TUP19-TUP19

76) Odefey, C.; Mayr, L.M.; Schmid, F.X. *J.Mol.Biol.* **1995**, *245*, 69-78.

77) Dobson, C.M.; Ptitsyn, O. *Current Opinion in Structural Biology* **1997**, *7*, 1-72.

78) Mirny, L.A.; Shaknovich, E.I. *J.Mol.Biol.* **1996**, *264*, 1164-1179.

79) Dyson, H.J.; Wright, P.E. *Annu.Rev.Phys.Chem.* **1996**, *47*, 369-395.

80) Haasnoot, C.A.G.; De Leeuw, F.A.A.M.; Altona, C. *Tetrahedron* **1980**, *36*, 2783-2792.

81) Haasnoot, C.A.G.; De Leeuw, F.A.A.M.; De Leeuw, H.P.M. *Biopolymers* **1981**, *20*, 1211-1245.

82) Forsen, S.; Hoffman, R.A. *J.Chem.Phys.* **1964**, *40*, 1189-1196.

83) Gorbitz, C.H.; Krane, J. *Acta Chem.Scand.* **1993**, *47*, 979-984.

84) Zhou, N.; Moore, G.J.; Vogel, H.J. *J.Protein Chem.* **1991**, *10*, 333-343.

85) Anteunis, M.J.O.; Borremans, F.A.M.; Stewart, J.M.; London, R.E. *J.Am.Chem.Soc.* **1981**, *103*, 2187-2191.

86) Pogliani, L.; Ellenberger, M.; Valat, J. *Org.Magn.Reson.* **1975**, *7*, 61-71.

87) Abraham, R.J.; Hudson, B.D.; Thomas, W.A. *Magn.Reson.Chem.* **1986**, *24*, 812-815.

88) Kessler, H.; Bermel, W.; Friedrich, A.; Krack, G.; Hull, W.E. *J.Am.Chem.Soc.* **1992**, *104*, 6297-6304.

89) Madi, Z.L.; Griesinger, C.; Ernst, R.R. *J.Am.Chem.Soc.* **1990**, *112*, 2908-2914.

90) Kessler, H.; Friedrich, A.; Hull, W.E. *J.Org.Chem.* **1981**, *46*, 3892-3895.

91) De Leeuw, F.A.A.M.; Altona, C.; Kessler, H.; Bermel, W.; Friedrich, A.; Krack, G.; Hull, W.E. *J.Am.Chem.Soc.* **1983**, *105*, 2237-2246.

92) Ellenberger, M.; Pogliani, L. *Biochemical and Biophysical Research Communications* **1974**, *58*, 613-623.

93) Anteunis, M.J.O.; Borremans, F.A.M.; Becu, C.; Sleeckx, J. *Int.J.Peptide Protein Res.* **1979**, *14*, 445-450.

94) DeTar, D.F.; Luthra, N.P. *J.Org.Chem.* **1979**, *44*, 3299-3305.

95) Bremer, J.; Mendz, G.L. *Aust.J.Chem.* **1989**, *42*, 1011-1028.

96) Xu, Y.; Sugar, I.P. *J.Magn.Reson.B* **1993**, *101*, 145-157.

97) Haar, W.; Fermandjian, S.; Vicar, J.; Blaha, K.; Fromageot, P. *Proc.Natl.Acad.Sci.U.S A* **1975**, *72*, 4948-4952.

98) Fermandjian, S.; Tran-Dinh, S.; Savrda, J.; Sala, E.; Mermet-Bouvier, R.; Bricas, E.; Fromageot, P. *Biochemical and Biophysical Research Communications* **1975**, *399*, 313-338.

99) Nagaraj, R.; Venkatachalapathi, Y.V.; Balaram, P. *Int.J.Peptide Protein Res.* **1980**, *16*, 291-298.

100) Sarkar, S.K.; Young, P.E.; Torchia, D.A. *J.Am.Chem.Soc.* **1986**, *108*, 6459-6464.

101) Sone, M.; Yoshimizu, H.; Kurosu, H.; Ando, I. *J.Molec.Struct.* **1993**, *301*, 227-230.

102) DeTar, D.F.; Luthra, N.P. *J.Am.Chem.Soc.* **1977**, *99*, 1232-1244.

103) Panasik, N.; Eberhardt, E.S.; Edison, A.S.; Powell, D.R.; Raines, R.T. *Int.J.Peptide Protein Res.* **1994**, *44*, 262-269.

104) Milner-White, E.J.; Bell, L.H.; Maccallum, P.H. *J.Mol.Biol.* **1992**, *228*, 725-734.

105) Deslauriers, R.; Smith, I.C.P.; Walter, R. *J.Biol.Chem.* **1974**, *249*, 7006-7010.

106) Sleeckx, J.J.M.; Anteunis, M.J.O.; Borremans, F.A.M. *Coll.Czech.Chem.Commun.* **1988**, *53*, 2503-2510.

107) Bain, A.D.; Hazendonk, P. *J.Phys.Chem.* **1997**, *101 A*, 7182-7188.

108) Scherer, G.; Kramer, M.L.; Schutkowski, M.; Reimer, U.; Fischer, G. *J.Am.Chem.Soc.* **1998**, *120*, 5568-5574.

109) Fischer, S.; Dunbrack, R.L.Jr.; Karplus, M. *J.Am.Chem.Soc.* **1994**, *116*, 11931-11937.

110) Cheng, H.N.; Bovey, F.A. *Biopolymers* **1977**, *16*, 1465-1472.

111) Grathwohl, C.; Wuthrich, K. *Biopolymers* **1981**, *20*, 2623-2633.

112) Cox, C.; Lectka, T. *J.Am.Chem.Soc.* **1998**, *120*, 10660-10668.

113) Tonelli, A.E. *J.Am.Chem.Soc.* **1973**, *95*, 5946-5948.

Part III

Simulation of Coupled Spin Systems in Rotating Solids Undergoing Chemical Exchange by Application of Sparse Matrix Methods to Floquet Theory

Overview

A powerful aspect of solid-state NMR is its application to the study of dynamic processes in crystalline and amorphous solids. The tensorial nature of the terms in the solid state Hamiltonian permits detection of molecular motions not observable with liquid phase NMR.[1] Such motions include methyl rotation,[2,3] five-fold ring rotation in permethylferrocene,[4] in-plane rotation of hexamethylbenzene,[3,5] rotational jumps of tetrahedral symmetry by hexamethylenetetramine,[6,7] or 180° flips of dimethylsulfone.[8-10]

NMR in the solid state is much more complex than liquids, since additional interactions, and their orientational dependence, need to be considered.[11-13] Simulation of dynamic spectra in the solid state is especially involved. The chemical shielding term in the Hamiltonian depends on the orientation of the molecule with respect to the applied field. The traceless dipole-dipole internuclear coupling is observed in solid state spectra.[14] It depends on the orientation of the internuclear vector between the interacting nuclei. Further interactions include quadrupolar coupling, where the nuclear electric quadrupole moment is coupled to the electric field gradient, which has orientational dependence.[15]

Experiments are frequently performed on powders.[11-13] Because of the orientational dependence of the Hamiltonian, an average over all possible orientations is necessary. The resulting powder patterns are broad and featureless, often making slow-exchange processes nearly invisible.[7,16] Rotating the sample at the magic angle with respect to the magnetic field averages to zero the leading terms of the orientational dependence of these tensors.[17-19] However, the averaging effect is not always complete and the spectrum is transformed into a set of equally spaced narrow lines, which have intensity distributions that are dependent on the tensor parameters.[20,21] MAS greatly improves the signal to noise ratio, while still allowing for measurement of the tensor components. On the other hand MAS renders the Hamiltonian time-dependent. A theoretical treatment is consequently more complicated.[5]

Not much can be done about the orientational dependence of the Hamiltonian, nor the need to compute powder averages. However, the way in which the time-dependent Hamiltonian is treated can be significantly improved. This is especially important for the multiple-spin system and for chemical exchange, where computational performance issues become important. In this situation, the matrices have the potential of becoming extremely large.

In the past, complete spectral simulation of multispin systems under MAS was beyond the reach of computational power. As a result, experiments focussed mainly on isolated spins and heteronuclear coupled spin pairs.[5] They were thus limited to secular terms in the Hamiltonian.[3,5,21] The Hamiltonian remains self-commuting at all times, and

is thus easily propagated through time by direct integration methods. Sometimes analytical expressions can be derived, significantly decreasing computational demand.

With modern computer speed and memory capacity, problems involving large matrices, such as simulation of MAS spectra of exchanging multispin systems, are within reach. There are currently two major schools of thought in simulating MAS spectra. One either computes the signal in the time domain using very small time steps,[22] or expands the propagator as a Fourier-like series, as in Floquet theory.[23] In the Floquet-spin space, the problem is solved using time-independent methods. Therefore, one either performs many small calculations or one large one. Remember in both cases, powder averaging has to be performed - the time for each orientation should be kept to a minimum. The time propagation technique can be implemented in three ways either by direct integration, average Hamiltonian theory, or the COMPUTE algorithm.[22] Floquet theory provides a time-independent Hamiltonian, which we employ in this work.

Of the other three time propagation methods, the COMPUTE algorithm is most competitive in performance with Floquet, since it exploits the periodicity of the time dependence.[22] In fact, it can be thought of as a combination of a multistep method and Floquet theory.[24] The average Hamiltonian method is suited only to stroboscopic observation since it averages the Hamiltonian over an entire rotor period. Direct integration is most commonly used, yet it is least efficient. It does not exploit the periodic nature of the time dependence of the Hamiltonian, and thus requires a larger number of time steps to calculate an FID.

To date, the COMPUTE method has not been used to simulate chemical exchange MAS spectra. There are implementations using Floquet theory, by S. Vega et al.[25,26] However chemical exchange has generally been performed by direct integration, as seen in work by D. Kuwahara,[27] J. R. Long et al.,[28] and N. J. Heaton,[29,30] to name some of the more recent works. Kuwahara limited himself to a single homonuclear-spin-1/2 pair exchanging between two sites, using only the isotropic chemical shifts, and the dipole-dipole coupling term in the Hamiltonian. His calculations took 4 hours on an IBM RS6000 workstation cluster system. Heaton's work was limited to only one term, either CSA or quadrupolar. He achieved spectacular computational performance using sparse matrix methods. Calculations took less than 4 minutes on a Power Macintosh 6100/60 personal computer. Linear scaling was achieved with respect to the number of sites. Unfortunately, his approach is not extendible to larger spin system with multiple interactions. The most thorough simulation of chemical exchange under MAS conditions was done by Long et al.[28] He utilised direct integration with a Hamiltonian including CSA, homonuclear and heteronuclear coupling terms, of a IS_3 spin system, were the S spins were being decoupled. His objective was to illustrate how molecular motion interfered with decoupling efficiency. He makes no mention of the time required for simulation, however his results should be in line with those of Kuwahara.

Floquet theory has long been recognised for its elegance, but has also been criticised for its inefficiency for multispin systems. This is largely due to the fact that most methods rely on diagonalizing the Floquet Hamiltonian, which is of the order $N_S N_F$, where N_S is the order of the spin space and N_F is the size of the Floquet space. Matrix

diagonalisation is generally performed using Householder routines,[31] which scale as the cube of the order of the matrix. Roughly speaking, the Floquet approach requires N_F^3 more operations than a single time step in direct methods. For typical systems, N_F is taken to be twice the number of sidebands, which could range anywhere between one to several hundred, depending on the rotor speed and the frequency range of the interactions considered. Direct methods scale in an opposite fashion, as the rotor speed is increased the number of time steps required increases. Thus, for slow rotor speeds with large interactions such as quadrupolar terms, Floquet methods would be impractical requiring as many as 10^6 more operations, than direct methods. However, for weaker interactions under fast spinning speeds only 1000 more operations are required than a single time step, which in some cases is more efficient than direct methods, that would require many time steps. However, propagation methods, which exploit the periodicity of the time dependence of the Hamiltonian, are more efficient than Floquet implementations. With such methods, the propagator is computed only for one rotor period – it is reused for subsequent rotor periods. With a perturbation treatment, Ding and McDowell[24] found conditions for which propagation methods and Floquet methods require the same computational effort. However, perturbation treatments are not generally applicable, and they tend to diverge under rotary resonance conditions at small spinning speeds.[32,33] We do not consider a perturbation approach here.

If a method were available to simulate spectra using the Floquet formalism that scaled more favourably than the cube of the matrix order, Floquet methods would look more attractive for MAS spectral simulations. The matrices in the Floquet formalism,

applied to MAS, are inherently sparse, since they have block pentadiagonal structure. In other words the number of nonzero entries in the matrix scale as the matrix order, O. Using sparse matrix algorithms, the matrix-vector multiplication scales as O. The Lanczos algorithm is a recursion formula, based solely of sparse matrix-vector multiplications, which is used to convert the Liouvillian to a tridiagonal representation. This conversion to the Lanczos representation requires N_L iterations and thus the complete transformation scales as $N_L \times O$. With the tridiagonal representation, it is possible to compute the spectrum directly in the frequency domain - a tridiagonal system of equations is solved for each frequency. This computation scales as the order of the matrix and the number of frequencies, N_v,, *i.e.* $O \times N_v$. For small spin systems, the spectrum calculation dominates the computation time since $N_v > O$ and N_L. For very large systems, where $O > N_v$ and $N_L < O$, the number of operations required is less then O^2. Therefore, with the Lanczos method for larger spin systems, a scaling of O^2 or better is expected.

In the following two chapters, a method is developed to compute MAS spectra of exchanging multispin systems. Initially, a numerical method is devised which has significantly improved performance over traditional approaches. This strategy employs the Lanczos method in such a way to compute the spectrum directly in the frequency domain. This study focuses on the convergence issues of the Lanczos method and makes a comparison between the Householder and Lanczos scaling behaviour. The next chapter sees the application of the Lanczos methodology to the simulation of chemical exchange MAS spectra. The Liouvillian included additional terms due to dipole-dipole and small

quadrupolar interactions. The Floquet theory is reformulated in Liouville space and modified for direct spectrum calculation. The performance of the Floquet-Lanczos method is compared with Householder using doubly ^{13}C labelled dimethylsulfone as a sample experimental system.

Improved performance of the Floquet approach through the use of sparse matrix methods makes it more practical to simulate larger spin systems undergoing chemical exchange among several sites. It also allows for more complete simulation of existing problems previously treated using simplifying assumptions.

Chapter 7

Dual Lanczos Simulation of Dynamic NMR Spectra for Systems with Many Spins or Sites

(Based on a manuscript prepared for Journal of Chemical Physics by R. Dumont, P. Hazendonk and A.D Bain.[34])

Introduction

This work is a continuation of previous attempts at applying sparse matrix methodologies to NMR spectral simulation. Dumont, Bain and Jain used a combination of Chebychev-based time propagation of the Hermitian part of the Liouvillian, with a split-operator approach to incorporate the non-Hermitian part of the Liouvillian.[35] The following introduces another approach using another sparse matrix method known as Lanczos tridiagonalisation.[36] In this Lanczos representation, the spectrum is computed directly in the frequency domain. This method scales with the square of the matrix order, O, or better, representing a considerable improvement over methods based on Householder tridiagonalisation, with O^3 scaling.[37]

The problem with large spin systems is the exponential growth of the number of possible states. For instance an n spin-1/2 systems has 2^n states, and thus 2^{2n} density matrix elements. Traditional methods, such as Householder tridiagonalisation, scale as O^3 and thus require a 64-fold increase in the number of operations with each added spin-

1/2. This places a practical limitation on the size of the spin system that can be simulated. In our experience 6 to 7 spins-1/2 is the limit, with present computational power. Even when blocking, based on sum of all I_z components, F_z, is implemented, this computational "brick wall" is pushed up by only one spin-1/2. In the end, to be able to solve large systems, a method which scales more favourable than Householder must be developed. Since NMR Liouvillians are typically very sparse, Lanczos methods are obvious candidates.

Sparse matrix methods, such as Lanczos, have been previously applied to simulating magnetic resonance spectra. Moro and Freed[38-40] used this approach to compute electron spin resonance lineshapes of a system undergoing a dynamic process. In this case, the system was described in terms of a complex symmetric matrix and established Lanczos methods could be applied directly. More generally, when the spin dynamics is described by a non-Hermitian Liouvillian, the Lanczos iterations must be applied in a bi-directional fashion with both the Liouvillian and its Hermitian conjugate. This is known as the dual Lanczos method. Implementation of general dual Lanczos methods has had tremendous difficulty with "breakdown",[41-45] where the left and right Lanczos vectors become nearly orthogonal. However, with the formulation described by Wassam,[36] this problem does not arise - the "breakdown" condition coincides with the convergence criterion. This formulation of the dual Lanczos algorithm, together with a direct method for computing dynamic NMR spectra in the frequency domain, as proposed below, provides the computational scaling desired. The Chebychev method, combined with the split-operator procedure, exhibited similar scaling. However, it had

large memory requirements. The dual Lanczos method requires only a few Lanczos vectors in memory at any given time, and thus does not have large memory requirements. This permits studies on larger systems.

The following presents a method for simulating dynamic NMR spectra in liquids using a dual Lanczos methodology. The dual Lanczos algorithm is used to tridiagonalise the Liouvillian. The spectrum is then computed directly in the frequency domain, avoiding the expensive diagonalisation step,[46] common to standard methods of spectral simulation.[42-44] This strategy provides significant improvement in performance and minimises memory requirements. The theory of dual Lanczos is presented, along with the direct frequency method. This is followed by a description of the convergence behaviour of the dual Lanczos method. Calibration of a prediction algorithm for the number of Lanczos iterations required for convergence is also discussed.

Theory

Spin dynamics and blocking

The state of a spin system described by the density matrix, ρ, evolves according to the Liouville-von Neumann equation:

$$i\hbar\frac{\partial}{\partial t}\rho = \mathbf{L}\rho = [\mathbf{H}, \rho] \tag{7.1}$$

Where **H** is the spin Hamiltonian and **L** is the Liouvillian. The density matrix can be expressed in terms of product basis states,

$$\rho = \left|m_1' \, m_2' \ldots m_n'\right\rangle\left\langle m_1 m_2 \ldots m_n\right| \tag{7.2}$$

where m_j and m_j' are the $\mathbf{I}_{jz}$ quantum numbers and j is the spin index. To implement blocking, the basis is divided into groups of density matrix elements, according to the total $\mathbf{I}_z$ for each spin type (Two groups of spins are treated as different types if all couplings between the constituent spins are weak- *i.e.* small compared with the associated chemical shift difference).[47] A basis state is assigned to a group by separately summing the m_j's and m_j''s for each spin type. This makes it possible to keep track of the sum z-components of the angular momentum of each state. Division into groups, in this manner, makes it possible to exploit the block structure of the Liouvillian by considering only transitions between states differing by

$$\Delta F_z = \sum_j m_j - \sum_{j'} m_j' = +1.$$

This allows the total calculation to be done in parts, saving significant CPU time and reducing total memory requirements.

To include the effect of chemical exchange, an anti-Hermitian term is added to the Liouvillian. The resulting effective Liouvillian is consequently non-Hermitian. In the case of multiple sites, it is necessary to expand the spin-state to include a "site" label.[35,48-51] In other words, the state of the system is described by a direct product of the individual site spin states. This corresponds to a direct product space between spin and site spaces, which have sizes N and N_S respectively. The resulting Liouvillian, has order $N_T = N \times N_S$, and takes on the form

$$\begin{aligned}\tilde{\mathbf{L}} &= \mathbf{L} - i\mathbf{K} \\ &= \left[\begin{pmatrix} L_1 & 0 & \cdots & 0 \\ 0 & L_2 & \ddots & \vdots \\ \vdots & \ddots & \ddots & 0 \\ 0 & \cdots & 0 & L_{N_S} \end{pmatrix} - i \begin{pmatrix} K_{11}\mathbf{1} & -k_{12}\mathbf{1} & \cdots & -k_{1N_S}\mathbf{1} \\ -k_{21}\mathbf{1} & K_{22}\mathbf{1} & \cdots & -k_{2N_S}\mathbf{1} \\ \vdots & \vdots & \ddots & \vdots \\ -k_{N_S1}\mathbf{1} & -k_{N_S2}\mathbf{1} & \cdots & K_{N_SN_S}\mathbf{1} \end{pmatrix}\right],\end{aligned} \tag{7.3}$$

where $\mathbf{L}_j$ is spin dynamics Liouvillian of the jth site, $\mathbf{1}$ is the identity matrix of order N, and K_{ii} is the iith element of the rate matrix defined by $K_{ii} = \sum_{j \neq i} k_{ji}$, where

$$A_i \underset{k_{ij}}{\overset{k_{ji}}{\rightleftharpoons}} A_j \tag{7.4}$$

is the corresponding unimolecular reaction. One should note that since $\mathbf{K}$ is diagonal with respect to spin state indices, the F_z blocking of $\mathbf{L}_j$ is preserved between sites. As a result calculations can be performed blockwise for multiple site systems.

The solution to the Liouville-von Neumann equation, Eq. (7.5) is expressed in terms of the propagator matrix and the initial state, $\rho(0)$, which is the equilibrium density matrix subsequent to a $90^0{}_x$ pulse

$$\rho(t) = \exp(-i\tilde{\mathbf{L}}t)\rho(0)\,. \tag{7.5}$$

The NMR signal is the inner product between a detector $\mathbf{d}$, which in general is $\sum_j \mathbf{I}_+^j$, and the evolved density matrix $\rho(t)$.

$$FID(t) = \mathbf{d}^\dagger \cdot \rho(t)\,, \tag{7.6}$$

where $\mathbf{d}^\dagger$ is the Hermitian conjugate of $\mathbf{d}$. To obtain the signal in the frequency domain a Fourier transform is performed on the FID as

$$\begin{aligned} S(\omega) &= \int_0^\infty dt \exp(i\omega t)\mathbf{d}^\dagger \rho(t) \\ &= \mathbf{d}^\dagger \frac{1}{i(\omega\mathbf{1} - \tilde{\mathbf{L}})}\rho(0). \end{aligned} \tag{7.7}$$

The dual Lanczos method

The effective Liouvillian, $\tilde{\mathbf{L}}$, is sparse.[35] It has order of magnitude of N_T non-zero elements, out of N^2_T total elements, where N_T is the order of the Liouvillian. The matrix-vector multiplication can be reformulated such that it only works with the non-zero elements of the sparse matrix. Looping over only the non-zero elements of the vector allows for further improvement. For the sparse Liouvillian, the matrix-vector multiply can be implemented in order N_T operations. Herein lies the advantage of a numerical method based solely on repeated matrix-vector multiplications. The dual Lanczos method works in this fashion. It generates a sequence of **v** and **w** states (Lanczos vectors) by successive applications of $\tilde{\mathbf{L}}$ and its Hermitian conjugate $\tilde{\mathbf{L}}^\dagger$, starting with an initial density matrix $\mathbf{v}_1 = \rho(0)$. The successive applications of $\tilde{\mathbf{L}}$ and $\tilde{\mathbf{L}}^\dagger$ are done in such a way that $\tilde{\mathbf{L}}$ is converted to a tridiagonal form, **T**, in the representation made by the Lanczos vectors, **v** and **w**.[41] The set of equations implied in Eq. (7.7) can be converted to this representation, allowing the spectrum to be computed directly in the frequency domain.

Direct spectral calculation in the frequency domain, as in Eq. (7.7), avoids the matrix diagonalisation step common in traditional methodologies. It also avoids the common problem with Lanczos methods, the appearance of spurious eigenvalues.[52] These eigenvalues always have insignificant transition moments and are consequently not seen in the spectrum.

The dual Lanczos method is described by the equations,[36]

$$\tilde{\mathbf{L}}\mathbf{V}_{N_L} = \mathbf{V}_{N_{L+1}}\mathbf{T}' \tag{7.8}$$

and $$\tilde{\mathbf{L}}^{\dagger}\mathbf{W}_{N_L} = \mathbf{W}_{N_{L+1}}(\mathbf{T}')^{*} \tag{7.9}$$

where $\mathbf{V}_{N_L}$ and $\mathbf{W}_{N_L}$ are the $N_T \times N_L$ columnwise arrays of dual Lanczos vectors. N_L is the number of Lanczos iterations taken. $\mathbf{V}_{N_L}$ and $\mathbf{W}_{N_L}$ are constructed such that, if $\mathbf{v}_{j'}$ is the j'th column of $\mathbf{V}_{N_L}$ and $\mathbf{w}_j$ is the jth column of $\mathbf{W}_{N_L}$, then $\mathbf{w}_j^{\dagger}\mathbf{v}_{j'} = \delta_{jj'}$; *i.e.* $\mathbf{W}_{N_L}^{\dagger}\mathbf{V}_{N_{N_L}} = 1_{N_L}$. $\mathbf{T}'$ is an $(N_L+1) \times N_L$ tridiagonal matrix,

$$\mathbf{T}' = \begin{pmatrix} \alpha_1 & \beta_2 & 0 & \cdots & 0 \\ \beta_2 & \alpha_2 & \beta_3 & \ddots & \vdots \\ 0 & \beta_3 & \ddots & \ddots & 0 \\ \vdots & \ddots & \ddots & \ddots & \beta_{N_L} \\ \vdots & \ddots & \ddots & \beta_{N_L} & \alpha_{N_L} \\ 0 & \cdots & \cdots & 0 & \beta_{N_{L+1}} \end{pmatrix}, \tag{7.10}$$

with complex α_j and real β_j, which are derived later. $\mathbf{T}'$ is complex symmetric without its bottom row.

Equations (7.8) and (7.9) imply an iteration wherein the columns of $\mathbf{V}_{N_L}$ and $\mathbf{W}_{N_L}$ are determined in sequence. Starting with a vector

$$\mathbf{v}_1 = \mathbf{w}_1 = \frac{\rho(0)}{\left[\rho^{\dagger}(0)\rho(0)\right]^{1/2}} . \tag{7.11}$$

the iteration proceeds

$$\mathbf{v}_{j+1} = \frac{\left[\tilde{\mathbf{L}}\mathbf{v}_j - \alpha_j\mathbf{v}_j - \beta_j\mathbf{v}_{j-1}\right]}{\beta_{j+1}} = \frac{\tilde{\mathbf{v}}_{j+1}}{\beta_{j+1}} \tag{7.12}$$

and

$$\mathbf{w}_{j+1} = \frac{\left[\tilde{\mathbf{L}}^{\dagger}\mathbf{w}_j - \alpha_j^{*}\mathbf{w}_j - \beta_j\mathbf{w}_{j-1}\right]}{\beta_{j+1}} = \frac{\tilde{\mathbf{w}}_{j+1}}{\beta_{j+1}}, \tag{7.13}$$

where j = 1, 2, ..., N_L. α_j is uniquely determined by requiring $\mathbf{v}_{j+1}$ to be orthogonal to $\mathbf{w}_j$ by $\alpha_j = \mathbf{w}_j^{\dagger}\tilde{\mathbf{L}}\mathbf{v}_j$. The $(j+1)^{th}$ basis vectors are determined by requiring $\mathbf{w}_{j+1}^{\dagger}\mathbf{v}_{j+1} = 1$, and consequently $\beta_{j+1} = \sqrt{\tilde{\mathbf{v}}_{j+1} \cdot \tilde{\mathbf{w}}_{j+1}}$.

The dual Lanczos iteration converges within N_L steps if $\beta_{N_L} \cong 0$, which is chosen to be 10^{-6} for this work. In this case, the bottom line of $\mathbf{T}'$ is dropped and Eqs. (7.8) and (7.9) imply an exact similarity transformations between $\tilde{\mathbf{L}}$ and $\mathbf{T}$.

With finite precision arithmetic the orthogonality between basis vectors is gradually lost. Despite this loss of orthogonality, Eqs. (7.8) and (7.9) are still valid, and the corresponding transformation is still useful. Loss of orthogonality is the cause of spurious eigenvalues. Methods have been developed to identify these spurious eigenvalues.[52] However, they are not required using the direct spectrum calculation approach.

A problem specific to dual Lanczos, known as "breakdown",[41-44] occurs when $\tilde{\mathbf{v}}_{j+1}$ and $\tilde{\mathbf{w}}_{j+1}$ are nearly orthogonal. This problem occurs for certain formulations of dual Lanczos. However, in the current formulation, the criterion for breakdown corresponds to that of convergence and thus does not pose a problem. In other words when $\tilde{\mathbf{v}}_{j+1}$ is orthogonal to $\tilde{\mathbf{w}}_{j+1}$, $\beta_{j+1} = \sqrt{\tilde{\mathbf{v}}_{j+1} \cdot \tilde{\mathbf{w}}_{j+1}} = 0$.

Direct spectrum evaluation

The value of an observable in Liouville space is given by the dot product between the vector representing the operator and the density matrix in vector form. In NMR, the signal in the frequency domain can be expressed as an inner product between a detector operator and the density matrix expressed as a function of frequency as in eqn.(7.14) .

$$S(\omega) = d \cdot \tilde{\rho}(\omega), \tag{7.14}$$

where $\tilde{\rho}(\omega)$ is the solution the system of equations,

$$i(\omega \mathbf{1} - \tilde{\mathbf{L}})\tilde{\rho}(\omega) = \rho(0). \tag{7.15}$$

Now, we expand $\rho(0)$ in terms of the Lanczos vectors $\mathbf{v}_j$ as $\rho(0) = \mathbf{V}_{N_L}\sigma(0)$, where $\sigma(0)$ is $\rho(0)$ in the Lanczos representation. Referring to Eq. (7.11), which is the expression for the starting Lanczos vector, this expansion is achieved with $\sigma(0)$ just the first unit vector - the Lanczos iteration is started with $\rho(0)$.

Consider the solution to be expanded in a similar manner as $\tilde{\rho}(\omega) = \mathbf{V}_{N_L}\tilde{\sigma}(\omega)$. $\tilde{\sigma}(\omega)$ is the solution to the system of equations, in the Lanczos representation. The proposed expansion is possible if $\mathbf{V}_{N_L}$ spans a space of sufficient size to include $\tilde{\rho}(\omega)$. Substitution of the expansion of $\rho(0)$ and $\tilde{\rho}(\omega)$ into Eq. (7.15) gives $i(\omega \mathbf{1} - \tilde{\mathbf{L}})V_{N_L}\tilde{\sigma}(\omega) = V_{N_L}\sigma(0)$. Equation (7.8), leads to

$$V_{N_L} i(\omega \mathbf{1}' - \mathbf{T}')\tilde{\sigma}(\omega) = V_{N_L}\sigma(0),$$

which is satisfied when

$$i(\omega \mathbf{1}' - \mathbf{T}')\tilde{\sigma}(\omega) = \sigma(0) \tag{7.16}$$

Here $\mathbf{1}'$ is the N_L^{th} order unit matrix with an additional row of zeros. Eq. (7.16) represents a system of N_{L+1} equations with N_L unknowns, where the last equation is $\beta_{N_{L+1}}\tilde{\sigma}_{N_L}(\omega) = 0$. In general, the dual Lanczos iteration does not converge such that $\beta_{N_{L+1}} = 0$. Consequently $\tilde{\sigma}_{N_L}(\omega) = 0$ is required. This condition signals convergence in practice. It is found that $\tilde{\sigma}_j(\omega)$ decays faster than exponentially in j for sufficiently large j. The Lanczos iteration effectively converges (with respect to frequency, ω) when $\tilde{\sigma}_{N_L}(\omega)$ becomes sufficiently small. The Lanczos iteration is stopped when the spectrum is converged at all desired frequencies. The $N_L \times N_L$ system of equations $i(\omega \mathbf{1} - \mathbf{T})\tilde{\sigma}(\omega) = \sigma(0)$, is uniquely solved at all such frequencies. (The primes are dropped since both **1** and **T** are now $N_L \times N_L$ matrices)

Convergence of the spectrum

The numerical method is implemented blockwise, with subspectra computed for each block. The subspectra are accumulated to give the total spectrum. A total of N_L dual Lanczos iterations are applied, starting with the block specific initial vector $\rho(0)$, which is the resultant state after a 90°_x pulse on the block equilibrium state. The number of iterations is an underestimate needed for convergence of each block. At this point, the yet-unconverged spectrum is computed via Eq (7.16) solved using an LU decomposition routine available in LINPACK.[53] Convergence is assessed by evaluating $\sigma(N_L)$ for each frequency, which is described below and in detail in the appendix of the paper by Dumont.[34] If the subspectrum is not converged, additional iterations are performed and

the spectrum is re-computed, after which convergence is reassessed. This procedure is continued until the subspectrum is converged for all frequencies. Accurate prediction of N_L and the subsequent number of additional iterations is subject to calibration, which is described later.

The LU decomposition of $i(\omega 1 - \mathbf{T})$ is achieved via Gaussian elimination with partial pivoting, followed by the solution of the L and U systems of equations.[41,54] The matrix is separated into a product of a lower triangular, L, and an upper triangular matrix, U, as

$$i\begin{pmatrix} \omega-\alpha_1 & -\beta_2 & 0 & \cdots & 0 \\ -\beta_2 & \omega-\alpha_2 & -\beta_3 & \ddots & \vdots \\ 0 & -\beta_3 & \omega-\alpha_3 & \ddots & 0 \\ \vdots & \ddots & \ddots & \ddots & -\beta_{N_L} \\ 0 & \cdots & 0 & -\beta_{N_L} & \omega-\alpha_{N_L} \end{pmatrix} = LU \tag{7.17}$$

$$= P_1 L_1 \ldots P_{N_L-1} L_{N_L-1} \begin{pmatrix} d_1 & u_2 & s_3 & \cdots & 0 \\ 0 & d_2 & u_3 & \ddots & \vdots \\ 0 & 0 & d_3 & \ddots & s_{N_L} \\ \vdots & \ddots & \ddots & \ddots & u_{N_L} \\ 0 & 0 & 0 & \cdots & d_{N_L} \end{pmatrix}$$

where L_j are identity matrices with an additional element l_j below the diagonal in the jth column, which are the elements of the L matrix. P_j's are either j to $j+1$ exchange matrices or identity matrices. Looking at the first two rows, the LU decomposition is started as

$$\begin{pmatrix} 1 & 0 \\ -l_1 & 1 \end{pmatrix} P_1 \begin{pmatrix} i(\omega-\alpha_1) & -i\beta_2 & 0 \\ -i\beta_2 & i(\omega-\alpha_2) & -i\beta_3 \end{pmatrix} = \begin{pmatrix} d_1 & u_2 & s_3 \\ 0 & d_2' & u_3' \end{pmatrix}$$

where d_2' and u_3' are intermediate values used in the next step of the algorithm.

If $|\omega - \alpha_1| \geq |\beta_2|$, P_1 is chosen to be the 2×2 identity matrix, otherwise it is the exchange matrix. In general P_j are chosen such that $|l_j| \leq 1$. The process continues as

$$\begin{pmatrix} 1 & 0 \\ -l_j & 1 \end{pmatrix} P_j \begin{pmatrix} d_j' & u_{j+1}' & 0 \\ -i\beta_{j+1} & i(\omega - \alpha_{j+1}) & -i\beta_{j+2} \end{pmatrix} = \begin{pmatrix} d_j & u_{j+1} & s_{j+2} \\ 0 & d_{j+1}' & u_{j+2}' \end{pmatrix} \tag{7.18}$$

With L and U constructed, the solution proceeds in two stages. First the set of equations is solved in terms of L as $L\sigma' = \sigma(0)$. Then the final solution is obtained via $\sigma' = U\tilde{\sigma}(\omega)$.

Convergence of the subspectrum is monitored via the components of σ', σ_j'. Solving $L\sigma' = \sigma(0)$ proceeds as

$$\begin{pmatrix} \sigma_j' \\ \sigma_{j+1}'' \end{pmatrix} = \begin{pmatrix} 1 & 0 \\ -l_j & 1 \end{pmatrix} P_j \begin{pmatrix} \sigma_j'' \\ \sigma_{j+1}(0) \end{pmatrix}, \tag{7.19}$$

for j=1,...N_L-1. σ_j'' is an intermediate value initialised by $\sigma_1'' = \sigma_1(0)$. Since the starting Lanczos vector is $\rho(0)$, $\sigma_{j+1}(0) = 0$, and the jth element of σ' is

$$\sigma_j' = \sigma_1(0) \prod_{j'} (-l_{j'}). \tag{7.20}$$

Since $|l_j| \leq 1$, σ_j' decays monotonically and exponentially, and eventually indicates convergence for the subspectrum when it drops below a prescribed threshold. This behaviour is illustrated in figure 7.1, which shows $\ln|\sigma_j'|$ as a function of j for the two largest blocks of the Liouvillian of a 6 spin-1/2 system undergoing mutual exchange. The frequencies chosen correspond to the slowest (left) and the fastest (right) decays

observed. The top panels correspond to an exchange rate of 1 s^{-1}, while the bottom correspond to 30 s^{-1}, with a natural broadening of 1 Hz is included. The convergence is faster than a simple exponential decay, as seen in the fit of $\ln|\sigma'_j|$ as a function of j, shown as the dashed lines, which has significant quadratic character. This behaviour allows the prediction of the number of iterations required to converge to a given accuracy, based on extrapolation of σ'_j's of the unconverged sub-spectrum.

Figure 7.2 shows the number of Lanczos iterations required to converge to $|\sigma'_j| \leq 10^{-6}$ as a function of frequency. This is done for the largest block of the previously described 6 spin-1/2 system with exchange rates of 1 and 30 s^{-1}. The corresponding subspectra are shown as the dashed lines. Notice that convergence is slower at, or near, resonance. This can be explained by looking into the expression for an upper bound for $|\sigma'_j|$, based on Eq. (7.20).

$$|\sigma'_j| \leq \frac{\sigma_1(0)\prod_{j'}^{j}|\beta_{j'}|}{\prod_{j'}^{j}|d_{j'}|} \tag{7.21}$$

The denominator is the absolute value of the determinant of **U**, which is the equal to the determinant of $i(\omega\mathbf{1} - \mathbf{T})$. Therefore, as ω approaches an eigenvalue of **T**, which is an eigenvalue of $\tilde{\mathbf{L}}$, the denominator becomes smaller, increasing $|\sigma'_j|$, thus requiring more iterations to achieve convergence. Intrinsic broadening or significant imaginary components of the eigenvalue of $\tilde{\mathbf{L}}$ impose a lower bound on the denominator, effectively decreasing the number of iterations required for convergence. This is

observed with the previously mentioned 6 spin-1/2 sample system, where the lines of the spectrum with 30 s^{-1} rate are broader than that for $1s^{-1}$. The number of iterations required for convergence is 230 and 550 respectively.

The number of Lanczos iterations required ranges from a small multiple of the block size, N_T, in the case of narrow lines, to some constant value that is a small fraction of N_T, for wide lines. This is an important for the numerical efficacy of the Lanczos method, since it ensures the N_T^2 scaling behaviour or better. This result is one of the main reasons why Lanczos outperforms Householder, when the Liouvillian is sparse.

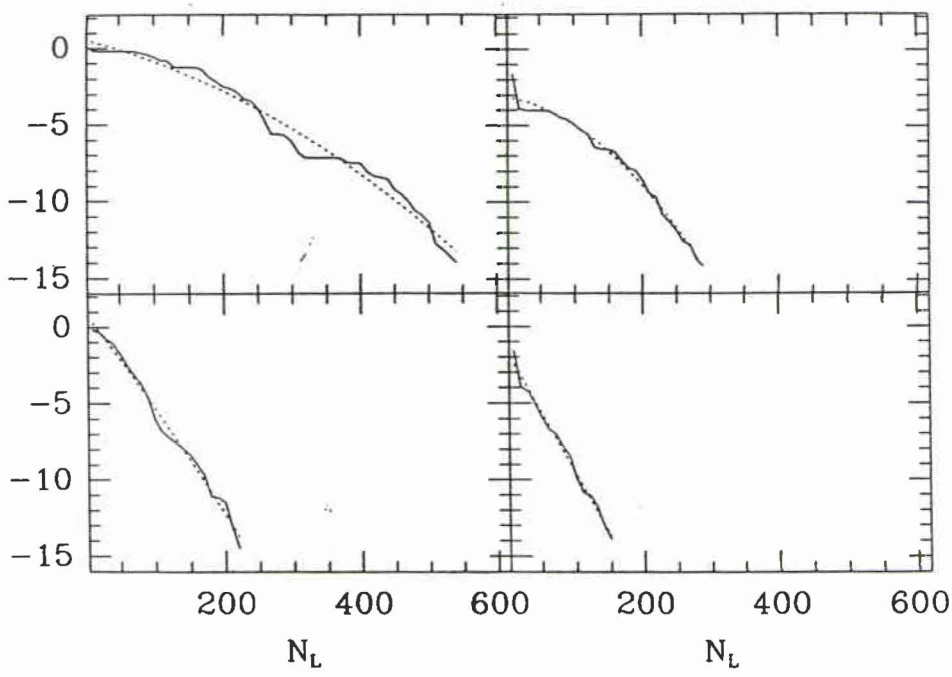

Figure 7.1 Convergence behaviour of the Lanczos iteration for a sample system. $\ln|\sigma_j'|$ as a function of N_L. This data is from the largest block of a 6-spin-1/2 system, undergoing a mutual exchange process at a rate of 1 s^{-1} for the top two panels and 30 s^{-1} for the bottom panels. The left and right panels are for the frequency giving the slowest and fastest decay. The dashed lines give the best fit to a quadratic function.

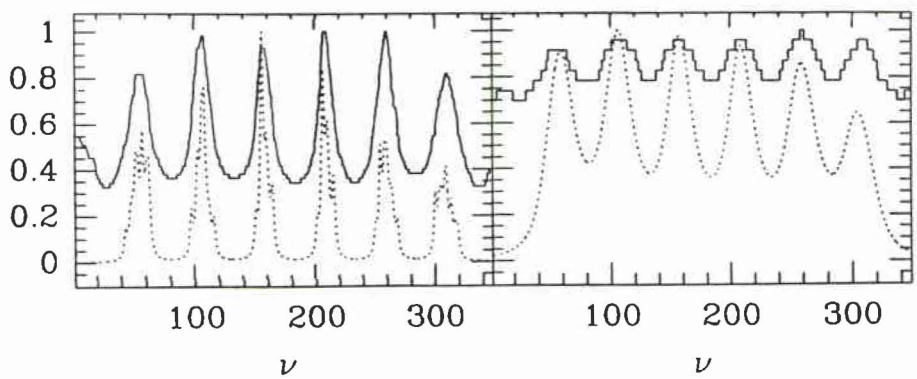

Figure 7.2 The number of Lanczos iterations required to converge $|\sigma_j'|=10^{-6}$ as a function of frequency for a sample system. As in figure 7.1 this data corresponds only to the largest block of the 6-spin-1/2 system. The left and right panels contain data corresponding to rates of 1 and 30 s^{-1}, respectively. Both data sets were normalised to the largest value. The subspectra are shown as dashed lines.

Calibration for optimal performance

To obtain optimum performance, it is necessary to obtain an accurate prediction of the number of iterations that are required to converge a block of a given size, and inherent linewidth of the corresponding subspectrum. Since convergence is assessed after an initial number of iterations, it is important to avoid overshooting convergence before convergence is assessed. Optimal performance of the method depends on a reliable underestimate of the number of iterations. After these iterations, subsequent convergence can be predicted from extrapolation as in figure 7.1. We know of no way to determine the required underestimate for general Liouvillians, based on first principles. It is necessary to do a calibration of the block size dependence and linewidth dependence of N_L.

A series of spectra were computed for spin systems varying in size from 4 to 10 spin-1/2 nuclei, with linewidth varied between 1 and 10 Hz. The spin systems were chosen to give greatest computational demand. In other words the spectra were highly second order and did not contain any high degree of symmetry. Chemical shifts were spaced 30 Hz apart. Nearest neighbour, next-to-nearest neighbour, and next-to-next-to-nearest neighbour coupling constants were 20 Hz, 12 Hz, and 5 Hz, respectively. The exchange rate was fixed at $1s^{-1}$, and the mutual exchange mechanism was a cyclic permutation of the sites. The number of Lanczos iterations, $N_L(max)$, required to converge a subspectrum corresponding to a given block was plotted as a function of block size, for the series of linewidths, as seen in figure 7.3. $N_L(max)$ exhibited saturation behaviour in the limit of large block size for all series. The saturation behaviour depends markedly on the inherent linewidth. For instance, for narrow lines

with $\Delta\nu_{1/2}$= 0.1 Hz, full saturation does not occur until the blocksize exceeds 45,000. Convergence requires more than 25000 iterations in such cases. For broader lines, where $\Delta\nu_{1/2}$= 10 Hz, complete saturation occurs at blocksizes of 5000, which require only 1500 iterations to converge. The observed behaviour determines a simple empirical curve modelled by:

$$N_L = \frac{A(\Delta\nu_{1/2})N_T}{B(\Delta\nu_{1/2}) + N_T}, \tag{7.22}$$

where N_T is the block size. N_T– independent, A and B, contain the dependence on $\Delta\nu_{1/2}$, as seen in figure 7.4. These parameters were fit including both linear and quadratic terms in $(\Delta\nu_{1/2})^{-1}$. Eq. (7.22) is implemented as an initial predictor of number of iterations to converge the spectrum. In practice, a fraction of the predicted value is used, typically 80%, to ensure underestimation of N_L.

A second series of spectra were computed where the exchange rate was varied between 1 and 10^5 s^{-1}. The results are shown in figure 7.5(b). In the slow exchange regime, as the rate increases, the effective broadening increases and the saturation behaviour is similar to that observed with the variation of the inherent broadening. In the intermediate exchange regime the lines are broad and saturation occurs early. In the fast exchange regime, the lines begin to narrow, and saturation occurs later. The predictor function was modified to include the contribution to the line width from exchange. In the slow exchange regime it works reasonably well, as seen in figure 7.5(a), for k= $1s^{-1}$. In the intermediate exchange regime, it fails, consistently overestimating the N_L. This is the result of spectrum convergence being dependent on the width of the narrowest feature.

This in general is not easily predicted for strongly-coupled multispin systems. The predictor estimates $\Delta\nu_{1/2}$ as the sum of intrinsic broadening and a simple approximation of exchange broadening which ignores strong coupling. The system is treated as a set of two spin exchanges, where $\Delta\nu_{1/2}$ is assessed for each exchange process. In practice the contributions from coupling are too large to ignore, and the effective broadening is always larger than predicted, consequently N_L is overestimated.

It is preferable to use a fraction of the predictor estimate. With some experience the user can probably make a better estimate. For large spin systems, such as 8 spins or larger, it is better to greatly underestimate the number of iterations required, and assess convergence many times, slowly stepping towards convergence, rather than grossly overestimate it. In this case, the overhead due to repeated spectrum evaluation represents only a small fraction of the total computation time. For smaller systems overestimating N_L is not a major inconvenience, since the amount of extra CPU time required is small.

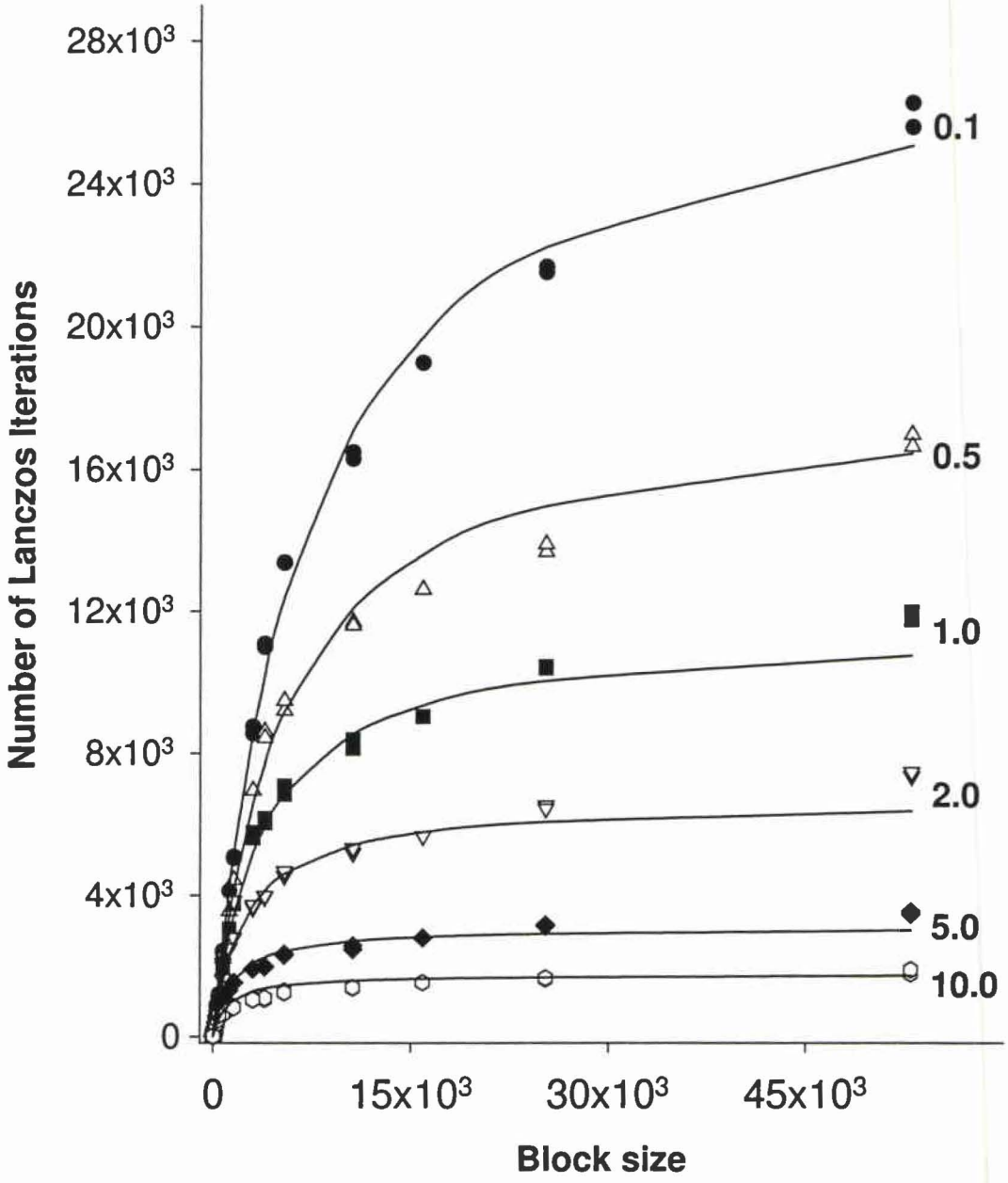

Figure 7.3 The number of Lanczos iterations required to converge sub-spectra as a function of blocksize, N_T, for all blocks of spin-1/2 systems ranging between 4 to 10 spins in size. All systems were set up as mutual exchange with a cyclic permutation mechanism. Each curve corresponds to different intrinsic broadenings, which were varied between 0.1 to 10 Hz. Details about the spin systems are given in the text. Lines indicate best-fit curves according to Eq. (7.22).

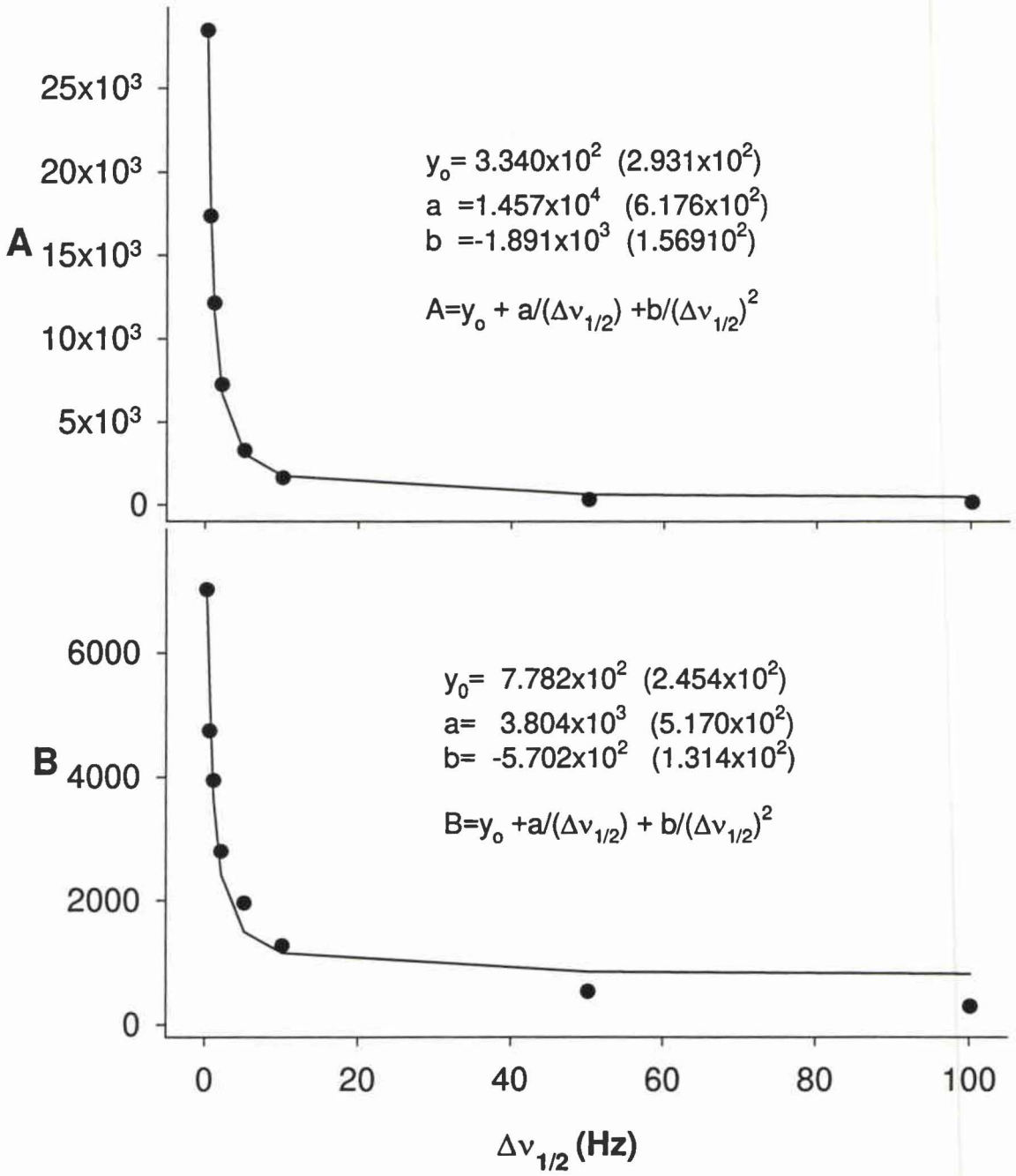

Figure 7.4 The linewidth, $\Delta\nu_{1/2}$, dependence of the parameters A and B in Eq. (7.22). The lines indicate the best-fit to a quadratic function in $(\Delta\nu_{1/2})^{-1}$indicated in the graph.

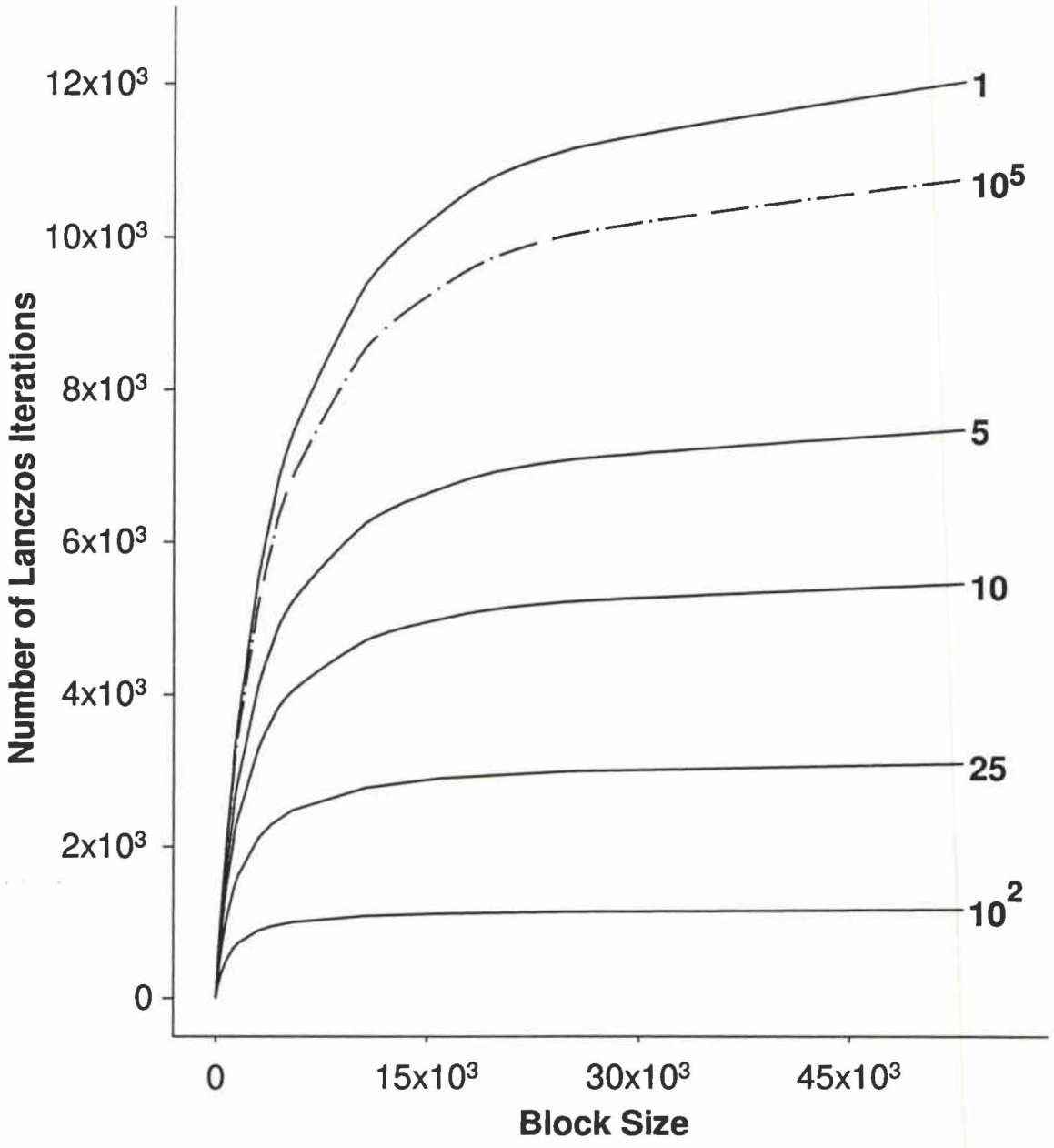

Figure 7.5(a) Predicted number of Lanczos iterations required to converge subspectra at a given exchange rate. The predictions were based on the calibration to $\Delta\nu_{1/2}$, and an estimator of $\Delta\nu_{1/2}$ from the exchange rate, described in the text. An intrinsic broadening of 1 Hz was assumed and the rate was varied between 1 to 10^5 s^{-1}.

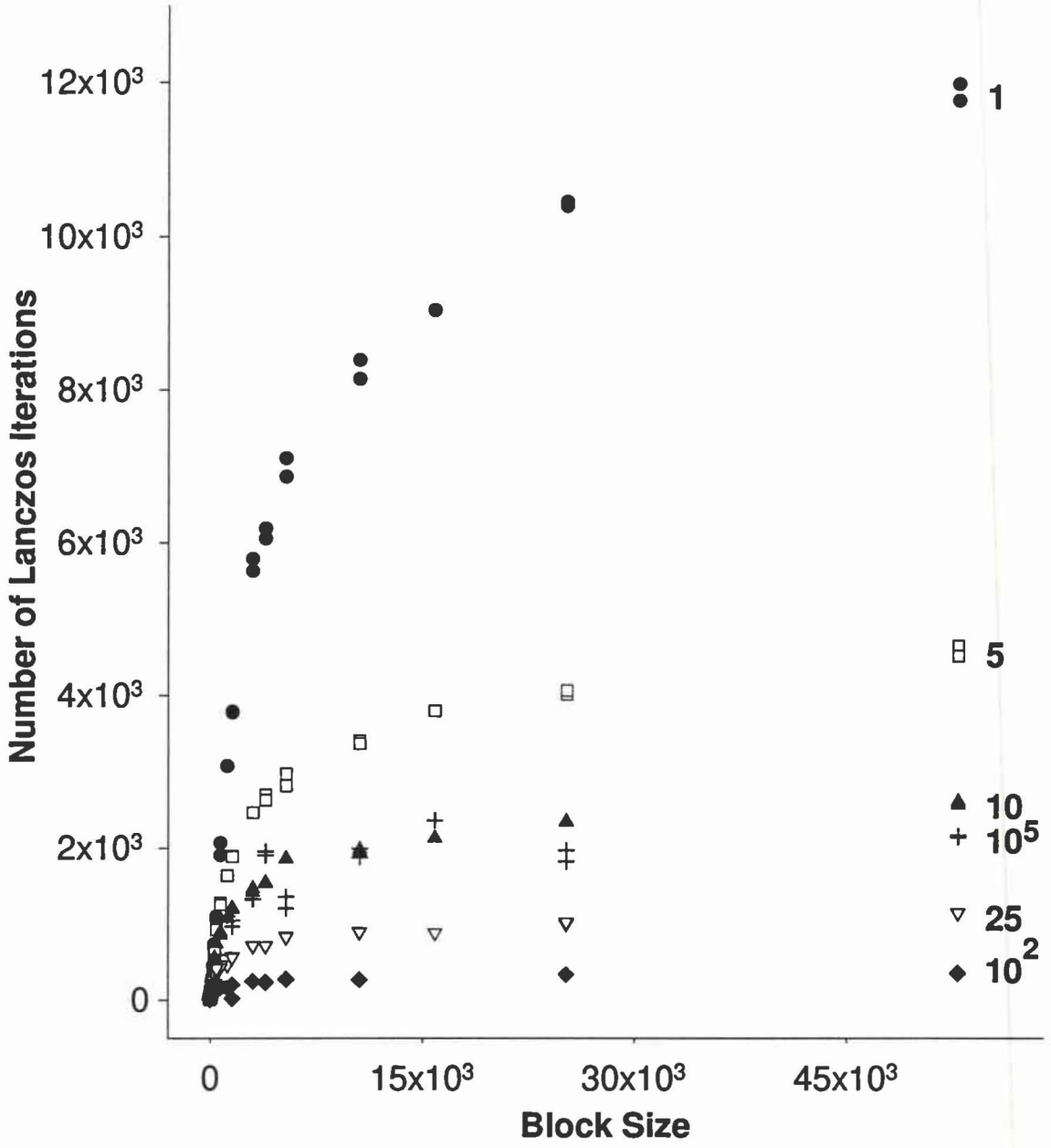

Figure 7.5(b) The number of Lanczos iterations required to converge subspectra as a function of blocksize for a series of exchange rates. Spins systems varied between 4 to 10 spins and rates ranged from 1 to 10^5 s^{-1}. Spins systems and exchange mechanism were identical to those in figure 7.3, which are described in the text.

Computational scaling

The scaling of the Lanczos method is compared with Householder as implemented in MEXICO, McMaster Exchange Program with Iteration and Coupling,[49] a spectral simulation program written by A. D. Bain. Both methods employ blocking. All calculations were performed using a Silicon Graphics Octane, with dual R10000 processors with a clock speed of 250 MHz and 2 GB RAM. The CPU time for each method is plotted as a function of the size of the spin system, as shown in figure 7.6. For the Lanczos method, different types of spin systems were used, illustrating the worst and best scaling behaviour expected. There are two types of spins systems: one which is simple, highly symmetric and first order, the other is strongly second order and exhibits less symmetry. The chemical shifts are spaced by 30 Hz and 150 Hz for the strong and weakly coupled systems respectively. The coupling constants of the strongly coupled system are the same as used previously. The weak coupling case used 20 Hz for all couplings. For each spin system, scaling studies were performed for both slow and intermediate exchange.

The Lanczos method outperforms the Householder method past 5 spins. For spin systems smaller than 5 spins, simulations take only a few seconds and therefore the Lanczos method is at no significant disadvantage. Similar behaviour was seen using the Chebychev/split-operator method, where both methods did not employ blocking. Both sparse matrix methods perform comparably. However, the Lanczos method imposes much smaller memory demands. Memory restricted the Chebychev/split-operator method to 9 spins.[35] The Chebychev/split-operator method required the whole

propagator to be stored in memory, in contrast to the few Lanczos vectors were stored at any given time using the Lanczos method.

Table 7.1 Table of the spectral parameters of the sample 6 spins systems.

A						B					
δ (ppm)	J (Hz)					δ (ppm)	J (Hz)				
0.1						0.1					
0.4	20					0.4	20				
0.7	20	20				0.7	12	20			
1.3	20	20	20			1.3	2	12	20		
1.3	20	20	20	20		1.3		2	12	20	
1.6	20	20	20	20	20	1.6			2	12	20

Spectrometer frequencies were 100 and 500 MHz for the strong and weakly coupled simulation respectively. A is the simple systems and B is the less symmetric system.

The computational performance is described in terms of the rate of exponential increase in CPU time with the number of spins. This is applicable to larger spin systems where the computational overhead from other parts of the program becomes insignificant. The Householder method exhibits $O(2^{5.8n})$ scaling, which is close to the theoretical asymptote of $O(2^{6n})$. The discrepancy is due to the non-uniform scaling of the maximum block size with the number of spins. The size of the spin systems was limited to 7, so the scaling is determined with few data points. Calculations of larger systems were not possible due to CPU time limitations.

The scaling of the Lanczos methods was far more efficient than using Householder techniques. For spectra in the slow exchange regime the scaling was $O(2^{2.8n})$ - during fast exchange it was $O(2^{2.2n})$. A difference between strong and weak

coupling was only observed in the intercepts of the linear fits. This corresponds only to a difference in overhead.

For very broad lines, the scaling approaches $O(2^{2n})$ resulting from complete saturation. In this case the spectrum converges in relatively few steps for all frequencies, independent of the number of spins. The scaling is linear in the size of the spin density matrix, which reflects the number of operations required for the matrix-vector multiplication of the Liouvillian with the density matrix, $\mathbf{L}\rho$.

Summary and conclusions

A new numerical method has been developed to simulate NMR spectra including exchange and relaxation. The method makes use of the sparsity of the Liouvillian, **L**, and exhibits significantly improved scaling over Householder methods. The method developed here is based on the stable formulation of the dual Lanczos tridiagonalisation algorithm proposed by Wassam. The spectrum is computed directly in the frequency domain using the tridiagonal form of L, thereby avoiding the expensive diagonalisation procedure. This method scales as $O \times N_\nu$ for small systems, and $O \times N_L$ for larger systems, typically larger than 6 spins, where N_ν is the number of frequencies, and N_L is the number of Lanczos iterations required for convergence. N_L ranges between a small multiple of O for narrow lines, or a small fraction of O, for wide lines. This implies that the Lanczos method has O^2 scaling or better, which represents a significant improvement over conventional methodologies.

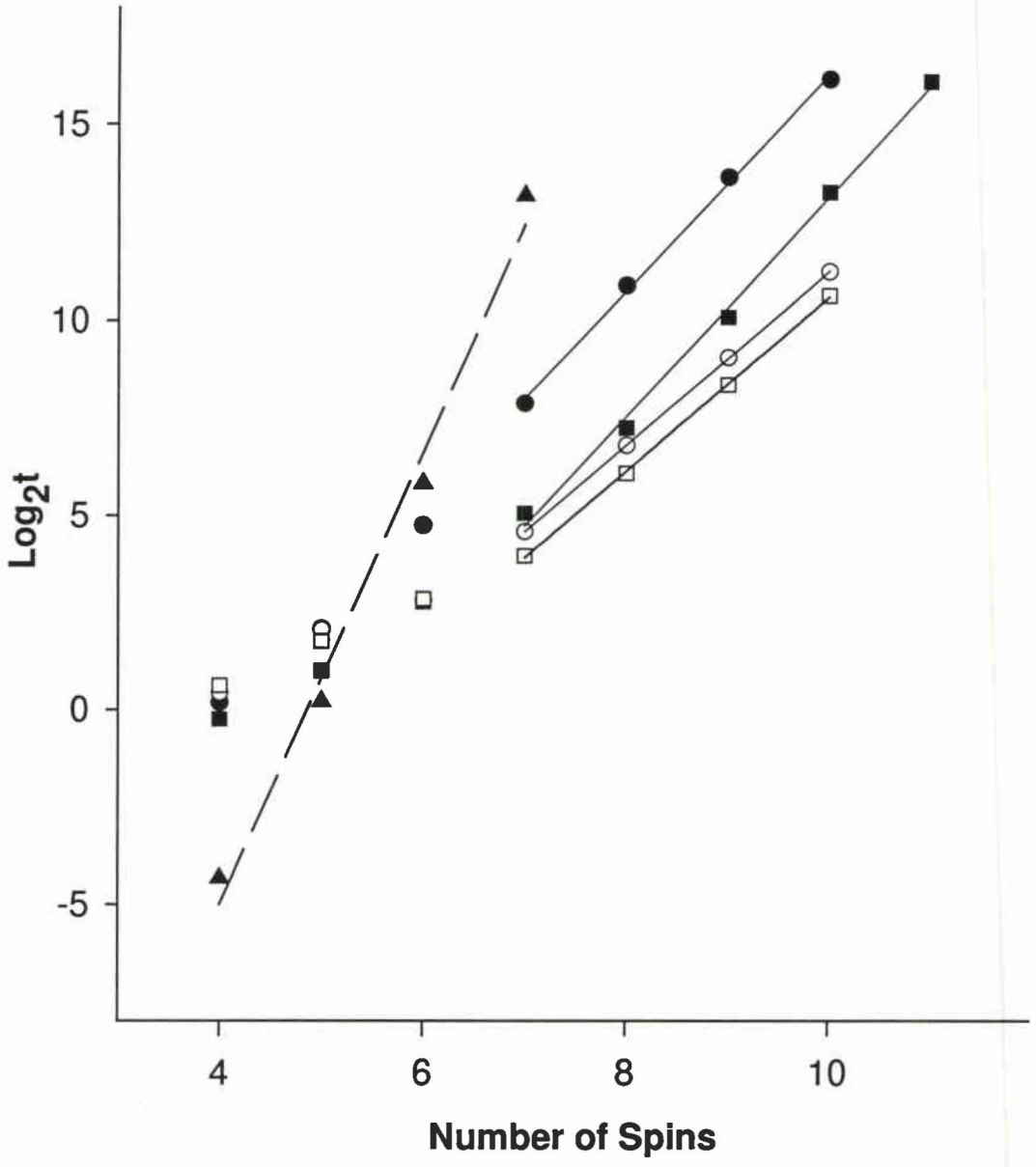

Figure 7.6 Scaling of CPU time with spin system size - a comparison between Lanczos and Householder methods. Log_2(CPU time (s)) as a function of the number of spin-1/2 nuclei. The solid triangles show the Householder results. The remaining data were obtained using Lanczos methods. A description of the spin systems is given in the text. Open and closed symbols correspond to fast and slow exchange, respectively. Circle and squares are for highly second order and first order spectra, respectively.

Chapter 8

Simulation of Chemical Exchange Lineshapes in CP/MAS Spectra Using Floquet Theory and Sparse Matrix Methods

(Based on a manuscript by P. Hazendonk, R. S. Dumont, H. Grondey, P. H. M. Harrison and A.D. Bain submitted to the Journal of Magnetic Resonance.[55])

Introduction

Floquet theory was introduced to spectroscopic problems by Shirley.[23] He applied this theory to compute the propagator corresponding to a time dependent non-self-commuting Hamiltonian (*i.e.* at two different times). When the time dependence is periodic, one can introduce a Fourier-spin space, for which the effective Hamiltonian is time independent, but infinite in dimension. Using a simple perturbation approach, Shirley was able to describe the Bloch-Siegert shift. Seventeen years later, using essentially the same methods, Shimon Vega described multiple quantum effects in double frequency pulsed NMR experiments on spin-1/2 and spin-1 systems.[56-58] Later Zax and Vega used Floquet methods to design broad band pulses.[59,60]

Vega applied Floquet theory to compute sideband patterns of rotating solids. For a single spin-1/2 system, analytic forms of the diagonalisation matrix were derived. This led to expressions for sideband intensities that were similar to those derived by Herzfeld and Berger,[20] and Maricq and Waugh.[61] For multispin systems numerical

methods are required. Based on a perturbation method proposed by Maricq,[62] spectra of coupled spin pairs were computed to model rotational resonance[32,33,63-65] and REDOR dephasing curves.[66,67]

Schmidt and Vega applied Floquet theory to uncoupled exchange in rotating solids using the Bloch-McConnell approach.[25,26,68] In this case, only numerical diagonalisation was possible for the general solution. However in both the slow and fast exchange regimes it was possible to derive eigenvalues and diagonalisation matrices using perturbation theory along with the solutions to the static single spin case.[25]

In this work, dynamic spectra of coupled spins in rotating solids are simulated by incorporating Floquet theory into chemical exchange methodologies demonstrated in solution NMR. This theory retains both secular and non-secular terms in the Hamiltonian, and places no limitation on rotor speeds and exchange rates. The spectra are computed directly in the frequency domain, using the sparse matrix methods developed in chapter 7. Powder averaging is achieved with implicit averaging with respect to the polar angles about the rotor axis.

Theory

Spin dynamics and chemical exchange

A general treatment of the theory of chemical exchange is provided in chapters 2 and 7. Spin and exchange dynamics are described by the master equation

$$\begin{aligned}\rho(t) &= \exp\left[-(i\,\mathbf{L}+\mathbf{K}+\mathbf{R})t\right]\rho(0)\\ &= \exp\left[-i\,\tilde{\mathbf{L}}t\right]\rho(0)\end{aligned}, \tag{8.1}$$

where $\mathbf{L}$ is the Liouville superoperator, $\mathbf{K}$ is the exchange superoperator and $\mathbf{R}$ is the relaxation superoperator. The state of the system, at any time, is given by the density matrix $\rho(t)$, treated as a vector in Liouville space. The density matrix resides in a composite spin-site space composed of basis states,

$$\prod_{i=1}^{N_s}\left[\left|\phi_1'\right\rangle\left|\phi_2'\right\rangle\ldots\left|\phi_N'\right\rangle\left\langle\phi_N\right|\ldots\left\langle\phi_2\right|\left\langle\phi_1\right|\right]_i .$$

The Liouville superoperator, defined by $\mathbf{L}\rho = [\mathbf{H},\rho]$, where $\mathbf{H}$ is the Hamiltonian, is block diagonal in the site manifold (*i.e* the Liouvillian is block diagonal with respect to the site index.). The exchange superoperator acts between sites and is diagonal in the spin dimension – it takes on the form $\mathbf{K} = \mathbf{1}\otimes\mathbf{K}$, where $\mathbf{1}$ is the $2^{2N}\times 2^{2N}$-identity matrix. The rate matrix $\mathbf{K}$ is as in Eq. (7.4) with mechanism in Eq. (7.5). The relaxation superoperator is assumed to be diagonal in both the site and spin manifolds, with $R_{ij,ij} = \left[1/T_{1,2}\right]_{ij,ij}$ for each spin i in site j.

Floquet Liouvillian

In the Floquet formalism, the time dependence of the Hamiltonian is described as a Fourier series in multiples of the rotor spinning frequency, ω_S, as in eqn (8.2). The time dependence enters through the CSA, dipole coupling and quadrupole tensors. The Fourier series of each of these terms is limited to 5 terms, owing to their quadratic form in the nuclear spin operators, $\mathbf{I}_j$ and linearity with respect to the tensors (see Chapter 2 for details).

$$\begin{aligned}\mathbf{H} = \mathbf{H}_0 + \mathbf{H}_1 \exp(i\omega_S) + \mathbf{H}_{-1} \exp(-i\omega_S) \\ + \mathbf{H}_2 \exp(2i\omega_S) + \mathbf{H}_{-2} \exp(-2i\omega_S)\end{aligned}, \tag{8.2}$$

This leads to a formulation wherein the propagator is an exponential of a block-pentadiagonal Floquet Hamiltonian.

Since the Liouvillian is linear in the Hamiltonian, it has the same simple periodic structure. One can develop a theory of the Floquet Liouvillian in a similar fashion to the Floquet Hamiltonian. To this end, suppose the Liouvillian is expanded as a Fourier series.

$$\tilde{\mathbf{L}}(t) = \sum_{j=-2}^{2} \tilde{\mathbf{L}}_j e^{ij\omega_S t} \tag{8.3}$$

Since only the spin dynamics is affected by sample rotation, the exchange and relaxation parts reside in $\tilde{\mathbf{L}}_0$. The components $\tilde{\mathbf{L}}_j$ are related to those of the Hamiltonian through $\tilde{\mathbf{L}}_j \rho = [\mathbf{H}_j, \rho]$.

Time evolution is described by a time-dependent propagator, corresponding to $\tilde{\mathbf{L}}(t)$. It is expressed as a Fourier-like series,

$$\mathbf{U}(t) = \sum_{j=-\infty}^{\infty} \mathbf{U}_j^F(t) e^{ij\omega_S t}. \tag{8.4}$$

Substituting Eq. (8.3) and (8.4) into the Liouville-von Neumann equation,

$$i\frac{\partial}{\partial t}\mathbf{U}(t) = \tilde{\mathbf{L}}(t)\mathbf{U}(t), \tag{8.5}$$

one obtains

$$\sum_{j=-\infty}^{\infty} i\frac{\partial}{\partial t}\mathbf{U}_j^F(t)\, e^{ij\omega_S t} = \sum_{j=-\infty}^{\infty}\sum_{j'=-2}^{2}\left[\tilde{L}_{j'} + (j)\omega_S\delta_{j',0}\right]\mathbf{U}_j^F(t)\, e^{i(j+j')\omega_S t}.$$

Changing the index from $j+j'$ to j the expression becomes

$$\sum_{j=-\infty}^{\infty} i\frac{\partial}{\partial t}\mathbf{U}_j^F(t)\, e^{ij\omega_S t} = \sum_{j=-\infty}^{\infty}\sum_{j'=-2}^{2}\left[\tilde{L}_{j'} + (j-j')\omega_S\delta_{j',0}\right]\mathbf{U}_{j-j'}^F(t)\, e^{ij\omega_S t}$$

which is valid for all time and thus is satisfied term by term; *i.e.*

$$i\frac{\partial}{\partial t}\mathbf{U}_j^F(t) = \sum_{j'=-2}^{2}\left[\tilde{L}_{j'} + (j-j')\omega_S\delta_{j',0}\right]\mathbf{U}_{j-j'}^F(t), \tag{8.6}$$

for $-\infty < j < \infty$. In block form, where each block is the size of the spin space (or more generally site-spin space), the equation appears as:

$$i\frac{\partial}{\partial t}\begin{pmatrix}\vdots\\ U_2^F\\ U_1^F\\ U_0^F\\ U_{-1}^F\\ U_{-2}^F\\ \vdots\end{pmatrix} = \begin{pmatrix}\ddots & \ddots & \ddots & \ddots & \ddots & \ddots & \ddots\\ \ddots & \tilde{L}_0 + 2\omega_S & \tilde{L}_1 & \tilde{L}_2 & 0 & 0 & \ddots\\ \ddots & \tilde{L}_{-1} & \tilde{L}_0 + \omega_S & \tilde{L}_1 & \tilde{L}_2 & 0 & \ddots\\ \ddots & \tilde{L}_{-2} & \tilde{L}_{-1} & \tilde{L}_0 & \tilde{L}_1 & \tilde{L}_2 & \ddots\\ \ddots & 0 & \tilde{L}_{-2} & \tilde{L}_{-1} & \tilde{L}_0 - \omega_S & \tilde{L}_1 & \ddots\\ \ddots & 0 & 0 & \tilde{L}_{-2} & \tilde{L}_{-1} & \tilde{L}_0 - 2\omega_S & \ddots\\ \ddots & \ddots & \ddots & \ddots & \ddots & \ddots & \ddots\end{pmatrix}\begin{pmatrix}\vdots\\ U_2^F\\ U_1^F\\ U_0^F\\ U_{-1}^F\\ U_{-2}^F\\ \vdots\end{pmatrix}$$

$$= \tilde{\mathbf{L}}^F\mathbf{U}^F.$$

This is the Liouville-von Neumann equation for the propagator $\mathbf{U}^F$, in the combined Floquet-spin space (or Floquet site-spin). Notice that the time-dependent Liouvillian of the spin space has been replaced by a time-independent Liouvillian of a Floquet-spin space. This equation has the solution, $\mathbf{U}^F(t) = \exp\left(-i\,\tilde{\mathbf{L}}^F t\right)\mathbf{U}^F(0)$, where $\mathbf{U}_j^F(0) = \delta_{j,0}$. The initial condition implies that the initial Floquet propagator is just the unit vector in the Floquet dimension. As a result, the j[th] component of the Floquet propagator becomes

$$\mathbf{U}_j^F(t) = \left[\exp\left(-i\,\tilde{\mathbf{L}}^F t\right)\right]_{j,0}, \tag{8.7}$$

the central block-column of the propagator matrix.

The NMR signal in the frequency domain is

$$S(\omega) \propto \int_0^\infty dt \exp(i\omega t)(d \mid U(t)\rho(0)), \tag{8.8}$$

where d is the detector operator, and $\rho(0)$ is the initial state of the density matrix. When measuring single quantum transitions after an initial $90^0{}_{x,y}$ observation pulse, both d and $\rho(0)$ are the same, except that $\rho(0)$ is weighted according to the relative populations of the sites. Substituting Eq. (8.4) and (8.7) into (8.8) gives

$$\begin{aligned} S(\omega) &\propto \left(d \mid \int_0^\infty dt \exp(i\omega t) \sum_{j=-\infty}^{\infty} U_j^F \exp(ij\omega_S t) \mid \rho(0)\right) \\ &= \left(d \mid \int_0^\infty dt \exp(i\omega t) \sum_{j=-\infty}^{\infty} \left[\exp\left(-i\,\mathbf{L}^F\right)\right]_{j,o} \exp(ij\omega_S t) \mid \rho(0)\right), \\ &= \sum_{j=-\infty}^{\infty} \left(\tilde{d}_j \mid \int_0^\infty dt \exp\left[i(\omega + j\omega_S - \mathbf{L}^F)t\right] \mid \tilde{\rho}_0(0)\right) \end{aligned} \tag{8.9}$$

where $\tilde{d}$ and $\tilde{\rho}_0(0)$ are the detector and initial density matrices represented in the full Floquet-spin space. The above expression, Eq. (8.9) can be further simplified to

$$S(\omega) \propto \sum_{j=-\infty}^{\infty} \left(d \mid \left[\frac{1}{i\left(\omega - j\omega_S - \mathbf{L}^F\right)} \right]_{j,0} \mid \rho(0) \right). \tag{8.10}$$

Powder averaging introduces further simplification of Eq. (8.10).

Powder averaging

In practice, these calculations are performed for each crystal orientation separately and accumulated to obtain a powder average. Thus, the Floquet Hamiltonian is evaluated for each crystal orientation and used to construct the Floquet Liouvillian of Eq. (8.10). It is important to note that crystal orientations related to another by a rotation α around the rotor axis have spectra which are related by a phase factor. When averaging around the rotation axis, the phase angle averages to 0, thus eliminating the Euler angle α from the powder average.[69] The following treatment, inspired by the work of Virlet and Charpentier,[70] proves this result.

In this case, it is necessary to work in a frame where the z-axis is the rotor axis. Euler angles (α,β,γ) are defined with respect to this frame. A final rotation of (0,β_M,0) transforms to laboratory frame, where β_M is the magic angle.

Rotation about the rotor axis can be seen as a phase shift in the periodic time dependence of all the terms in the Liouvillian. Thus the Liouvillian, $\tilde{\mathbf{L}}(\alpha, \beta, \gamma; t)$, at a given orientation (α,β,γ), is related to that at orientation (0,β,γ) with a shift in time, *i.e.*

$$\tilde{\mathbf{L}}(\alpha,\beta,\gamma;t) = \tilde{\mathbf{L}}(0,\beta,\gamma;t+\alpha/\omega_S)\text{, or}$$

$$\sum_{j=-2}^{2}\tilde{\mathbf{L}}_j(\alpha,\beta,\gamma)\exp(ij\omega_S t) = \sum_{j=-2}^{2}\tilde{\mathbf{L}}_j(0,\beta,\gamma)\exp(ij\omega_S(t+\alpha/\omega_S))$$

$$= \sum_{j=-2}^{2}\tilde{\mathbf{L}}_j(0,\beta,\gamma)\exp(ij\alpha)\exp(ij\omega_S t).$$

Consequently $\tilde{\mathbf{L}}_j(\alpha,\beta,\gamma) = \tilde{\mathbf{L}}_j(0,\beta,\gamma)\exp(ij\alpha)$. Using Eq. (8.6) the components of the Floquet Liouvillian can be expressed as

$$\tilde{\mathbf{L}}^F_{j,j'}(\alpha,\beta,\gamma) = \tilde{\mathbf{L}}^F_{j,j'}(0,\beta,\gamma)\exp(i(j-j')\alpha). \tag{8.11}$$

This is a unitary transformation of $\tilde{\mathbf{L}}^F$, represented by a diagonal matrix, $\mathbf{W}$. From the spectral theorem,[71] any function of $\tilde{\mathbf{L}}^F$, $f(\tilde{\mathbf{L}}^F)$, is transformed in a similar way as $f(\mathbf{W}^{-1}\tilde{\mathbf{L}}^F\mathbf{W}) = \mathbf{W}^{-1}f(\tilde{\mathbf{L}}^F)\mathbf{W}$. In other words, the (*j*,*0*)th block of Eq. (8.10) is multiplied by a factor $\exp(ij\alpha)$, as in Eq. (8.12). The signal for a single crystal orientation is thus given by

$$S(\omega) \propto \sum_{j=-\infty}^{\infty}\left(d \mid \left[\frac{1}{i\left(\omega - j\omega_S - \mathbf{L}^F(0,\beta,\gamma)\right)}\right]_{j,0}\exp(ij\alpha) \mid \rho(0)\right). \tag{8.12}$$

Integration over α from 0 to 2π, eliminates all terms in the infinite sum except for the j = 0 term. The α-averaged spectrum is given by

$$\begin{aligned}\int_0^{2\pi} d\alpha S(\alpha,\beta,\gamma;\omega) &\propto \left(d \mid \left[\frac{1}{i\left(\omega - \mathbf{L}^F(0,\beta,\gamma)\right)}\right]_{0,0} \mid \rho(0)\right) \\ &= \left(\tilde{d} \mid \left[\frac{1}{i\left(\omega - \mathbf{L}^F(0,\beta,\gamma)\right)}\right] \mid \tilde{\rho}(0)\right)\end{aligned} \tag{8.13}$$

where $\tilde{d}$ and $\tilde{\rho}(0)$ are vectors in the expanded Floquet-spin space which contain only non-zero elements in the j = 0 blocks. The desired powder average is the integral over the remaining Euler angles β and γ.

$$\int_0^{2\pi} d\gamma \int_0^{\pi} \sin\beta \, d\beta \left(\tilde{d} \mid \left[\frac{1}{i\left(\omega - \mathbf{L}^F(0,\beta,\gamma)\right)} \right] \mid \tilde{\rho}(0) \right).$$

This is evaluated numerically via a set of points which sample the unit-sphere uniformly.[72,73] Spectra are computed for the corresponding values of β and γ and accumulated, weighted by the corresponding solid angle. The spectrum calculation for each orientation proceeds just as described in chapter 7. First $\mathbf{L}^F(0,\beta,\gamma)$ is tridiagonalised using the dual Lanczos method. Then in the Lanczos representation, $\tilde{\sigma}(0) = \tilde{\sigma}'(0)\left(\omega - \mathbf{T}(0,\beta,\gamma)\right)$ is solved for each frequency, giving $\tilde{\sigma}'(0,\beta,\gamma,\omega)$, using LU decomposition. The spectrum is computed as the inner product, $\left(\tilde{d}' \mid \tilde{\sigma}'(0,\beta,\gamma,\omega)\right)$, where $\tilde{d}'$ is the vector of inner products of $\tilde{d}$ with the Lanczos basis vectors.

Experimental

Sample preparation

Unlabelled dimethylsulfone was purchased from Aldrich chemicals, and used without further purification. The doubly-^{13}C- labelled dimethylsulfone was prepared by Dr. P. Harrison. ^{13}C-iodomethane was combined with sodium sulphide using the procedure developed by Tarbel and Weaver.[4] The resulting dimethyldisulfide was distilled and subsequently oxidised by potassium permanganate without further purification using the method by Maleweski and Mitzinger.[74] Details of the preparation are given in ref. 55.

NMR spectroscopy

The ^1H NMR spectra of the doubly-^{13}C- labelled dimethylsulfone was obtained at 400 MHz in $CDCl_3$. The spectrum consisted of a doublet of multiplets centred at δ2.96. The ^{13}C spectrum was a singlet at δ42.67. The ^1H NMR spectrum was simulated using NUMMARIT with XSIM as a front end (see figure 8.1), available from K. Marat at the University of Manitoba. It was analysed as a $X_3AA'X_3'$ spin system with $^1J_{C\text{-}H} = +137.6$ Hz, $^3J_{C\text{-}H} = +0.8$ Hz, $^2J_{C\text{-}C} = \pm 9.5$ Hz and $^4J_{H\text{-}H} = +0.9$ Hz.

The ^{13}CPMAS spectra were obtained with a Bruker DSX-200 spectrometer equipped with a wide bore magnet with field strength of 4.7 T. This system was equipped with a standard Bruker 4 mm double-tuned MAS probe. The probe uses a 4 mm spinner which is a zirconia cylinder of 4 mm diameter and 18 mm length. The spinner is sealed at one end with a boron nitride cap, which is engraved with turbine-like grooves on the

outer rim. Magic angle spinning is achieved with a combination of two air streams. The bearing stream provides a cushion of air between the spinner and the probe wall reducing the friction. The drive stream is applied at an angle with the grooves on the cap, causing the sample to spin. With this set-up it is possible to attain stable spinning rates between 2 to 16 kHz, however spinning rates below 1 kHz were impractical. In order to achieve rates in this range the spinner caps were ground down to smoothness using a razor blade. This allowed for spinning speeds between 180 to 2000 Hz, stable to within 5 Hz.

Temperature control was achieved with a Bruker BVT-3000 unit, which regulates the current through a heater in the bearing gas. The temperature was monitored with a copper/constantan thermocouple, placed in close proximity to the sample in the bearing gas stream.

The proton 90^{o} pulse length was 5.5 μs, and the contact time was 2 ms. Transients were collected every 4 seconds. The number of transients collected varied for each spectrum ranging between 512 to 15000 depending on the signal to noise ratio.

Simulation of CPMAS spectra

The CPMAS spectra of DMS and 2^{13}CDMS were simulated using the EisXSS, and LanXSS programs. These were written in FORTRAN77, where EisXSS uses Householder, and LanXSS uses Lanczos tridiagonalisation. Computations were performed on a SGI Octane Dual R10000 at 250 MHz. Programs were compiled with the MIPS 7.21. FORTRAN compiler, with 64-bit word size, running in an Irix 6.5.2 environment.

All simulated spectra contained 4096 points, with an 8000 Hz spectral width. Powder averages were done over 952 points, assuming no symmetry. The sphere was divided into quadrants where one polar angle β ranged between 0 to 180° and the remaining polar angle γ varied from 0 to 90^0. The quadrant was divided into 2n equally spaced bands parallel to the equator. These bands are divided equally into squares such that the solid angle is roughly the same for squares from different bands. The band just above the equator splits into 2n+1 squares. The same pattern is repeated in reverse order for the bottom half of the quadrant. The actual angles used correspond to the centre of these squares. The weights for each orientation were equal to the solid angle of each square. The linewidths were set to 13 Hz, and 75 Hz for DMS and 2-^{13}CDMS respectively. Rotor speeds ranged between 540 to 580 Hz for DMS and 320 to 400 Hz for 2-^{13}CDMS and the 40 Floquet blocks were require for the simulations.

The DMS spectra were simulated as a one-spin two-site exchange, and the 2^{13}CDMS were simulated as two-spin two-site mutual exchange. The chemical shift tensors have principal values 18.6, 18.6 and –37.3 ppm for both sites, and Euler angles,

(0, 0, 0) and (0, 108°, 0). The carbon-carbon internuclear distance was set to 2.9Å. Exchange rates of 50, 800, 2000, and 5500 s^{-1} were matched to temperatures 295, 333, 343 and 348 K, respectively. Experimental and simulated spectra were compared visually. The EisXSS calculations took 7 minutes while the LanXSS calculations took 20 minutes.

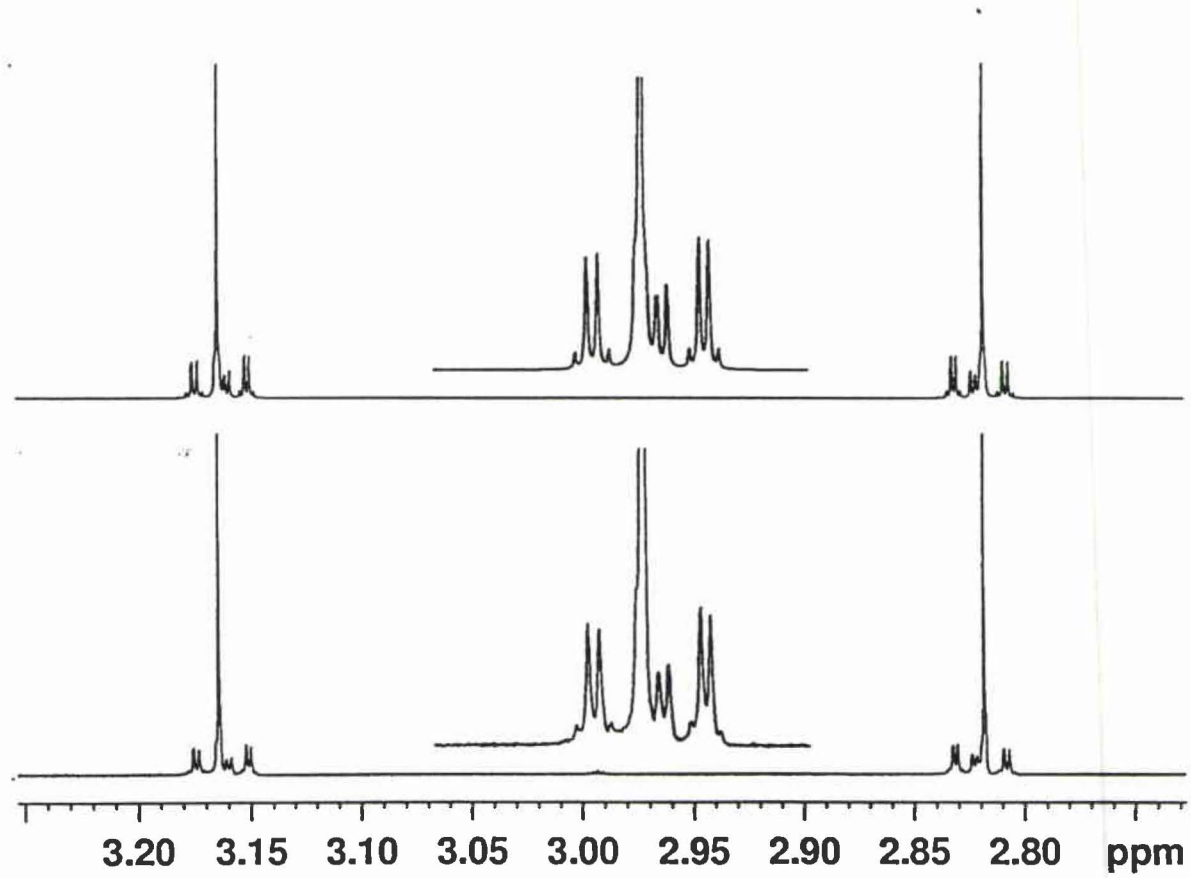

Figure 8.1 The ^{1}H NMR spectrum of doubly ^{13}C-labelled dimethylsulfone in $CDCl_3$ at 400 MHz. The simulated spectrum is seen on the top. The inlay in both the simulated and experimental spectra are expansions of the multiplet at 3.165 ppm.

Results and discussion

The CPMAS spectra of DMS are shown in figure 8.2. Corresponding simulations are seen in figure 8.3. The simulated spectra closely resembled the experimental spectra, and the corresponding spectral parameters agree with those of Veeman et. al.[75] and Vega et. al.[25,26] Spectra predicted for the larger rates considered by Vega were not reproduced with this method. However, experimental spectra in this study in the faster rate regime did agree with simulation. Rates determined by the simulations were precise to within 10 %. The entropy and enthalpy of activation were 35.5 J/molK and 73.0 kJ/mol, respectively. These values are in line with previous investigations. The corresponding Eyring plot is seen in figure 8.4.

The CPMAS spectra of the doubly ^{13}C-labeled-DMS are shown in figure 8.5 and the corresponding simulations in figure 8.6. The spectra parameters were identical to those of DMS. The carbon-carbon internuclear distance used was 2.9Å. The rates required for these spectra were within 10 % of those of the unlabelled compound. Since there were only a few milligrams of the doubly labelled DMS, the rotor had to be packed with a filling material. As a result the inherent linewidth was 75 Hz, much broader than that of the unlabelled material.

Doubly ^{13}C labelled DMS simulations, using Householder were again about 3 times faster than those with Lanczos. A systematic study was conducted of the scaling behaviour of both methods. A two-spin two-site system was simulated by increasing the number of Floquet blocks, from 15 to 2000, whereby matrix orders ranged between 30 to 4000. This series corresponds to a sequence of decreasing rotor speeds for a system with fixed spectral range. The observed scaling is compared in figure 8.7 where the logarithm

of the CPU time required is plotted as a function of the logarithm of the matrix order. In the asymptotic limit Householder methods are known to scale as the cube of the matrix order. A slope of 3 is therefore expected in a log-log plot. Observed data gives a slope of 3.2. The Lanczos method has a slope of 2.1, indicating a square dependence on matrix order. This is in line with studies of solution phase spectra (chapter 7).

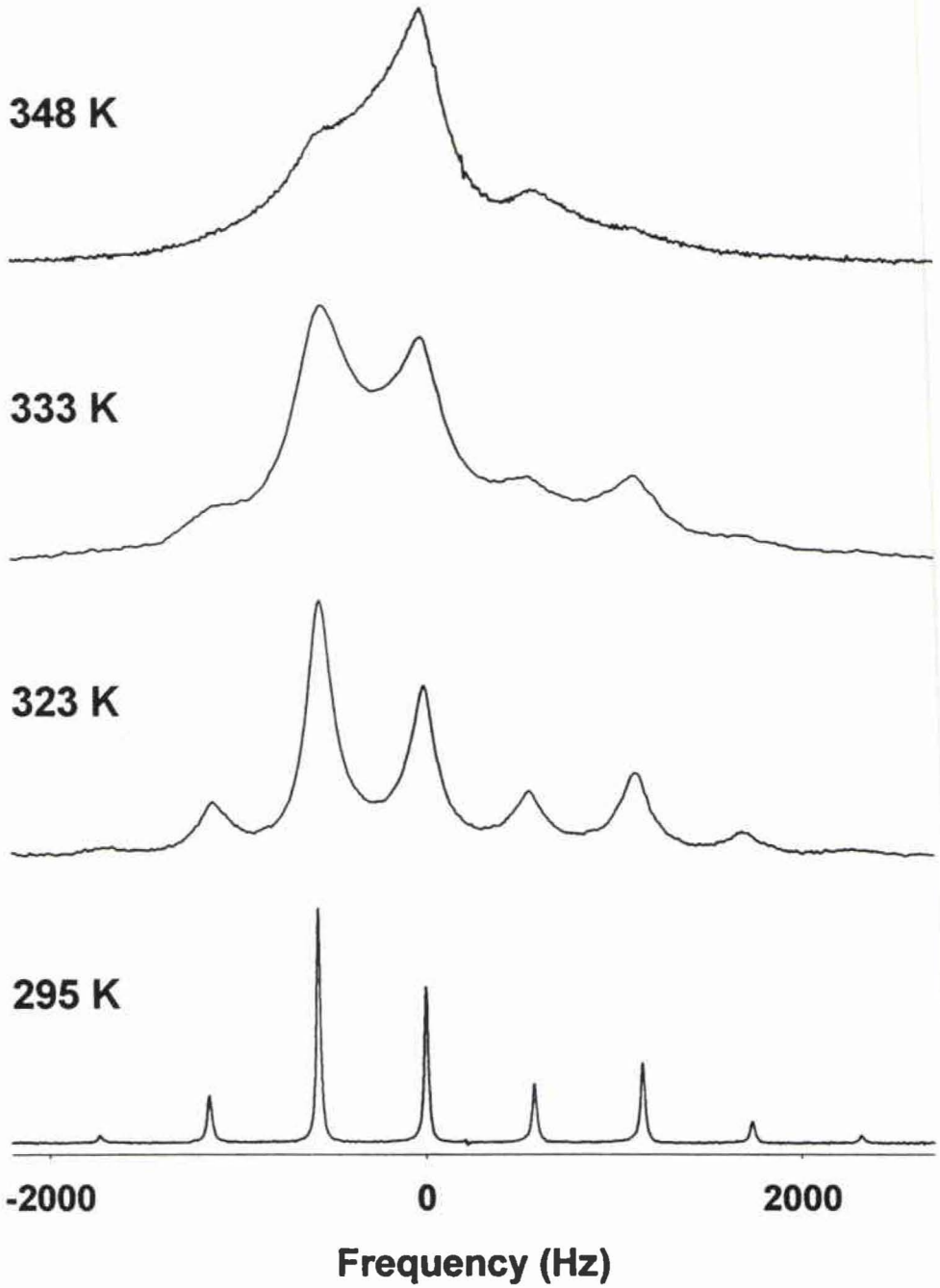

Figure 8.2 The ^{13}C CPMAS spectra of dimethylsulfone at 50 MHz, for a series of temperatures. A) 295 K (577 ± 2 Hz), B) 323 K (565 ± 2 Hz), C) 333 K (558 ± 2 Hz) and D) 348 K (568 ± Hz). The spinning speeds are given in the parentheses.

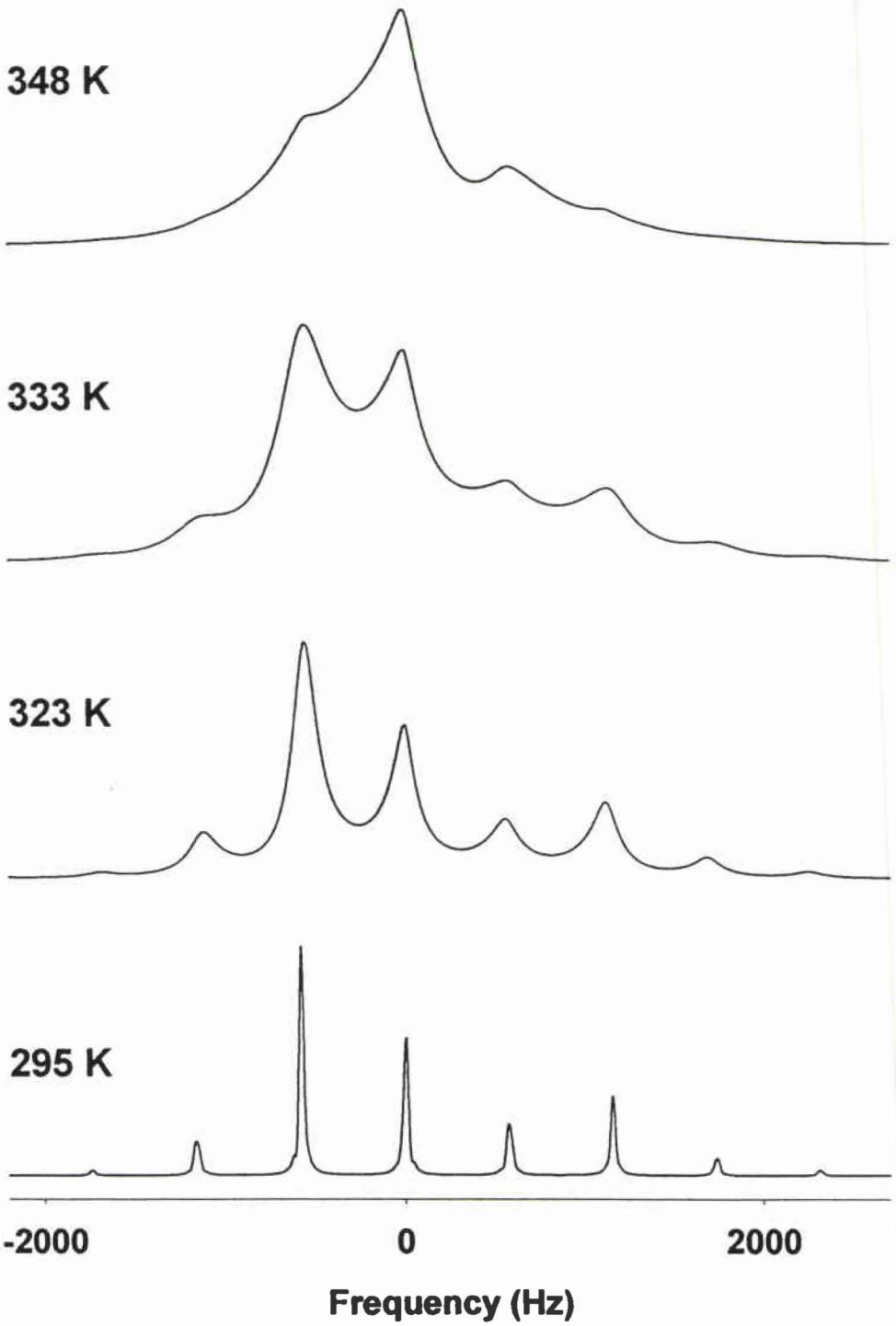

Figure 8.3 Simulations of the ^{13}C CPMAS spectra of dimethylsulfone at 50 MHz. A) 295 K (577 Hz), B) 323 K (565 Hz), C) 333 K (558 Hz) and D) 348 K (568 Hz). The spinning speeds are given in the parentheses.

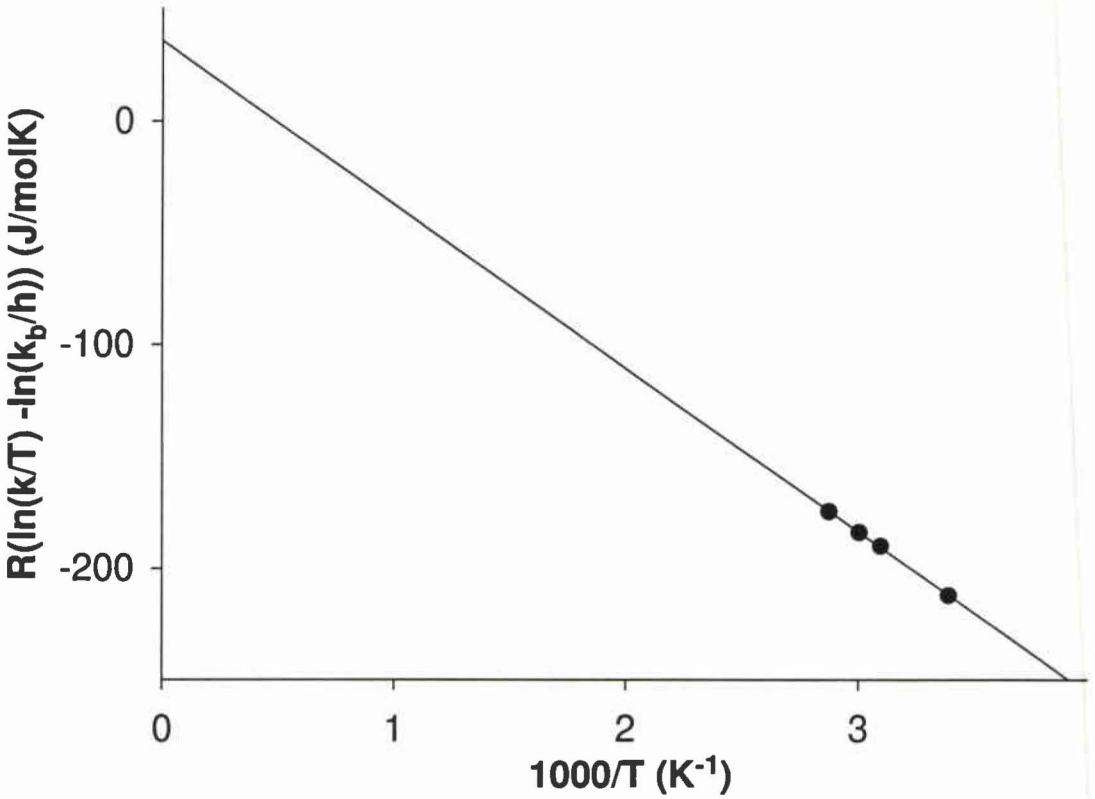

Figure 8.4 Eyring plot for dimethylsulfone

For the experimental system the Lanczos method did not outperform the Householder approach. However, according to the scaling study one does not have to go too much larger systems before Lanczos takes over. This takes place between matrix order 50 to 100. At matrix order 1000 the Lanczos method is almost 2 orders of magnitude faster. It is possible to encounter matrices of this size for larger spin systems. For example, the largest block of a three-spin two-site exchange using 20 Floquet blocks would be order 360, or as a mutual exchange problem it would still be order 180. The largest block of a five spin mutual exchange would be order 1000 when using 10 Floquet blocks, which by the dual Lanczos method would take about a day to compute and about 50 days with Householder.

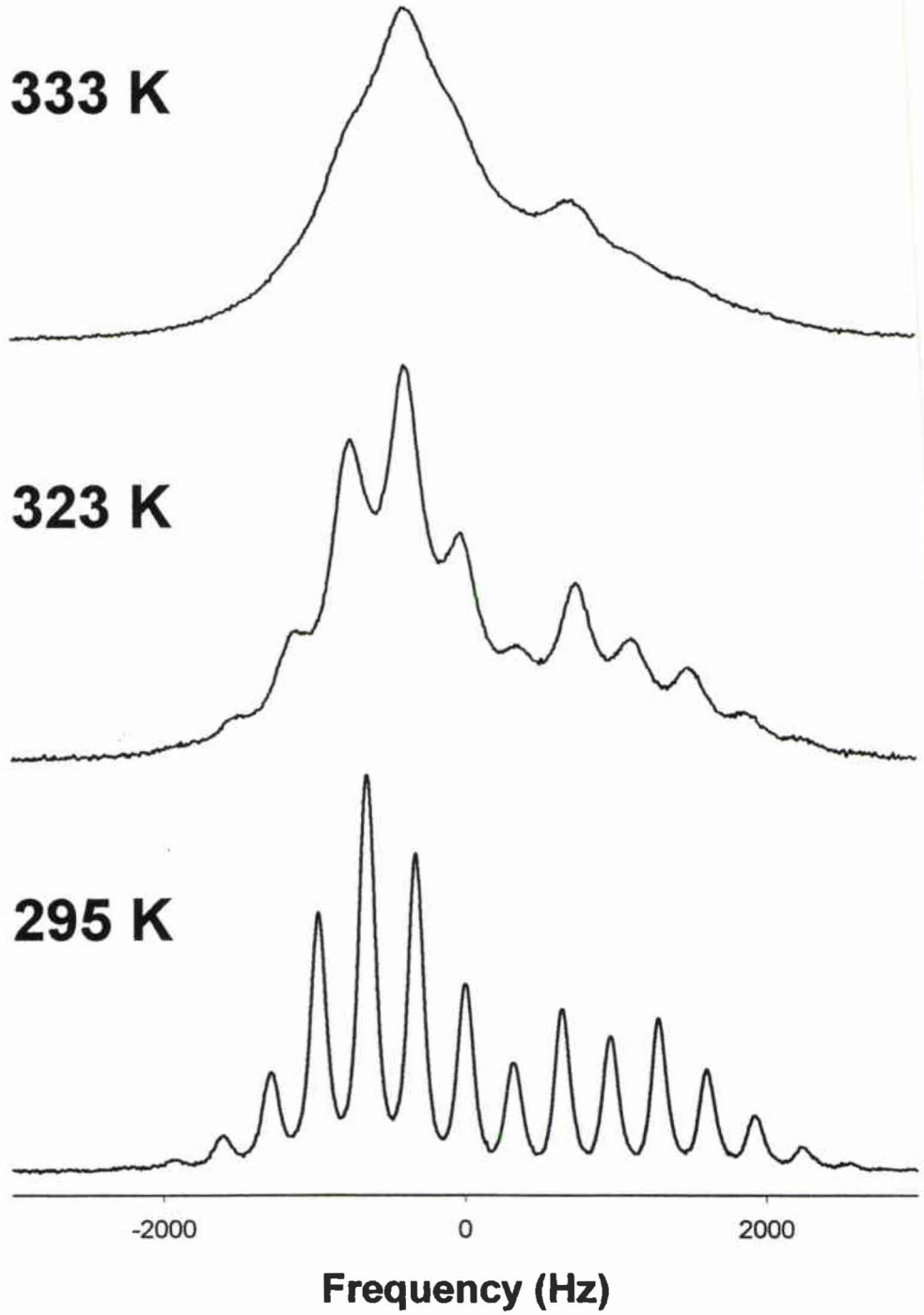

Figure 8.5 ^{13}C CPMAS spectra of doubly ^{13}C-labeled dimethylsulfone for a series of temperatures at 50 MHz. A) 295 K (320 ± 5 Hz), B) 323 K (375 ± 2 Hz) and C) 333 K (400 ± 2 Hz). The spinning speeds are given in the parentheses.

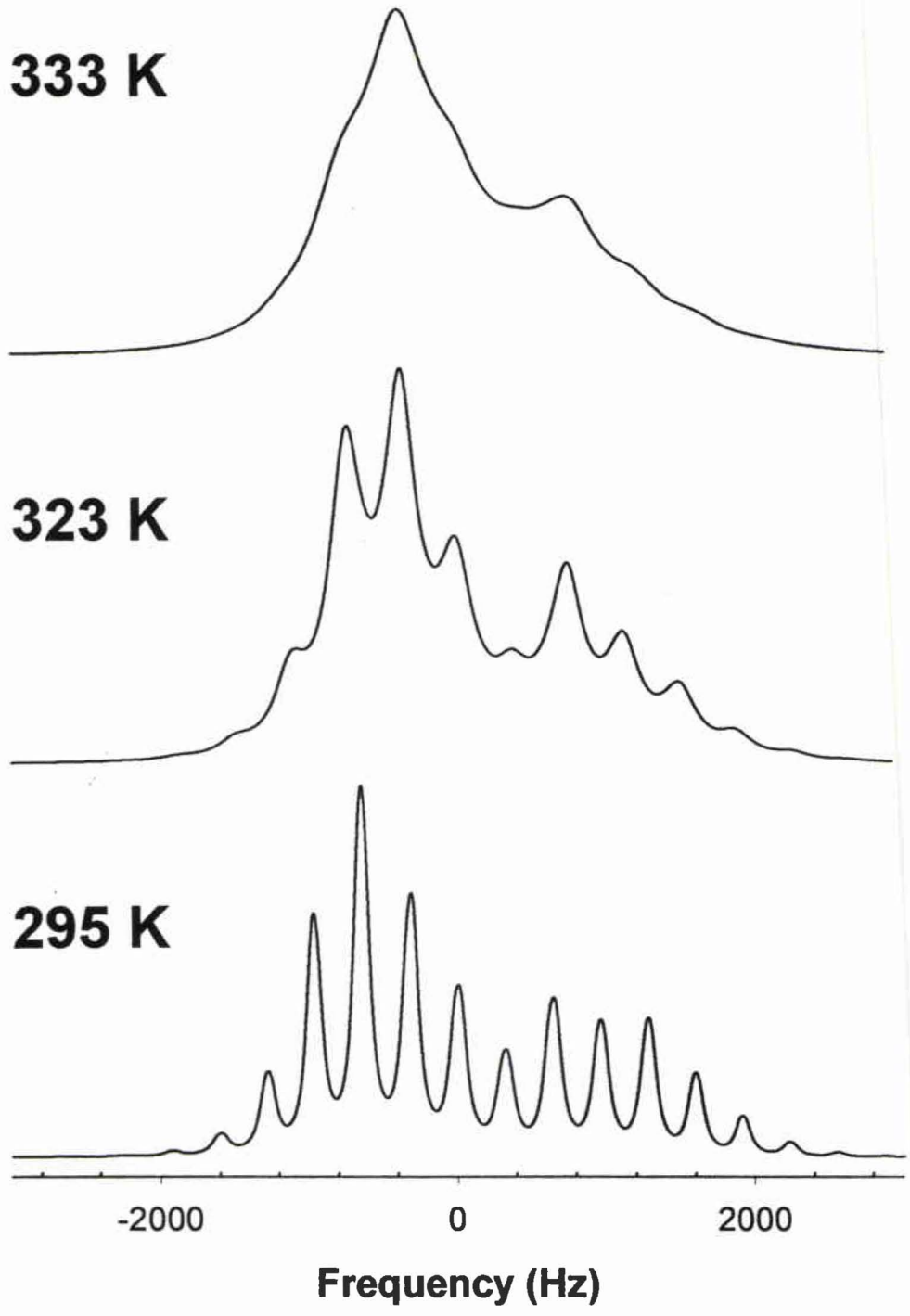

Figure 8.6 Simulation of the ^{13}C CPMAS spectra of doubly ^{13}C-labeled dimethylsulfone for a series of temperature at 50 MHz. A) 295 K (320 Hz), B) 323 K (375 Hz) and C) 333 K (400 Hz) . The spinning speeds are given in the parentheses.

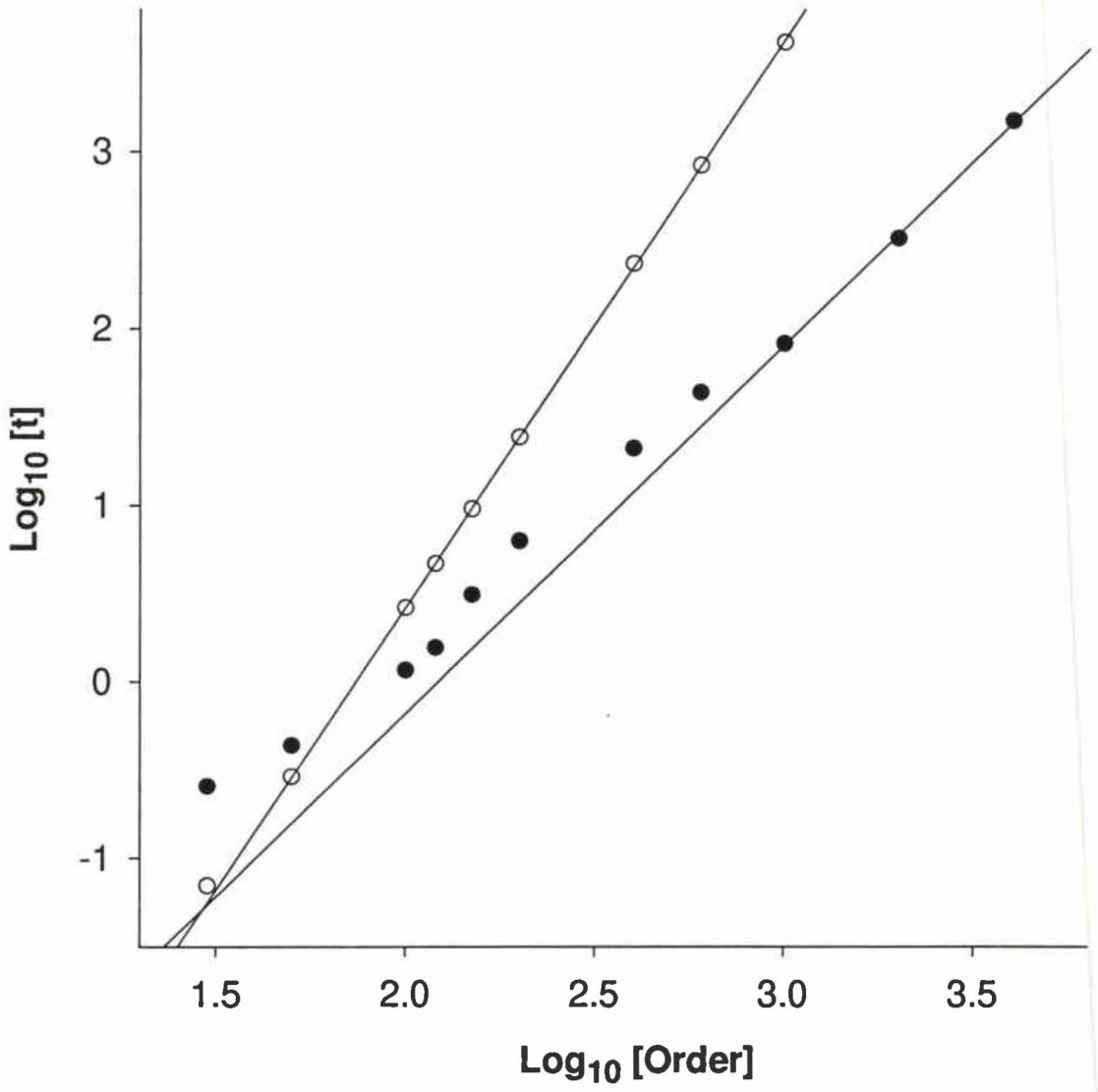

Figure 8.7 Comparison between Lanczos and Householder methods based on the scaling of the CPU time with the matrix order. Log_{10}(CPU time) as a function of Log_{10}(Order), for a two spin two site spin system with inherent broadening of 1 Hz. The spectral range was kept constant and the rotor frequency was scaled inversely with the number of Floquet Blocks. The CPU time reported is that for a single crystal orientation.

The linewidth dependence of the scaling was investigated in two ways. The first method preserved the spectral range. The spinning speed was decreased, inversely proportional to the increasing Floquet dimension (see figure 8.8). The second method scaled the tensor with the Floquet dimension while keeping the rotor speed constant (see figure 8.9). Using the first method, the broadened lines crowded the spectrum for large Floquet dimensions. The number of Lanczos iterations required for convergence consequently plateaus with increasing block size. The same behaviour was seen for liquid spectra and is described in chapter 7. The second method avoids the crowding phenomenon by keeping the rotor speed constant. In this case, there is no saturation and the maximum number of Lanczos iterations required decreases with increasing linewidth. This effect is also explained in the chapter 7. In fact there is a linear dependence between the number of iterations required and the block size, where the slope decreases as a function of linewidth. Figure 8.10 shows the dependence on the number of iterations required to converge the block of order 4000 as a function of linewidth. The best-fit line has biexponential behaviour. The same behaviour is seen in the first study, but is somewhat obscured by saturation.

Chemical exchange is a source of line broadening in the slow and intermediate exchange regimes. A study of the scaling behaviour with respect to exchange rate is similar to that with increasing the inherent linewidth, where saturation was observed. Figure 8.11 shows plots of number of Lanczos iterations with increasing blocksize for various exchange rates, which remain in the slow and intermediate-exchange regimes.

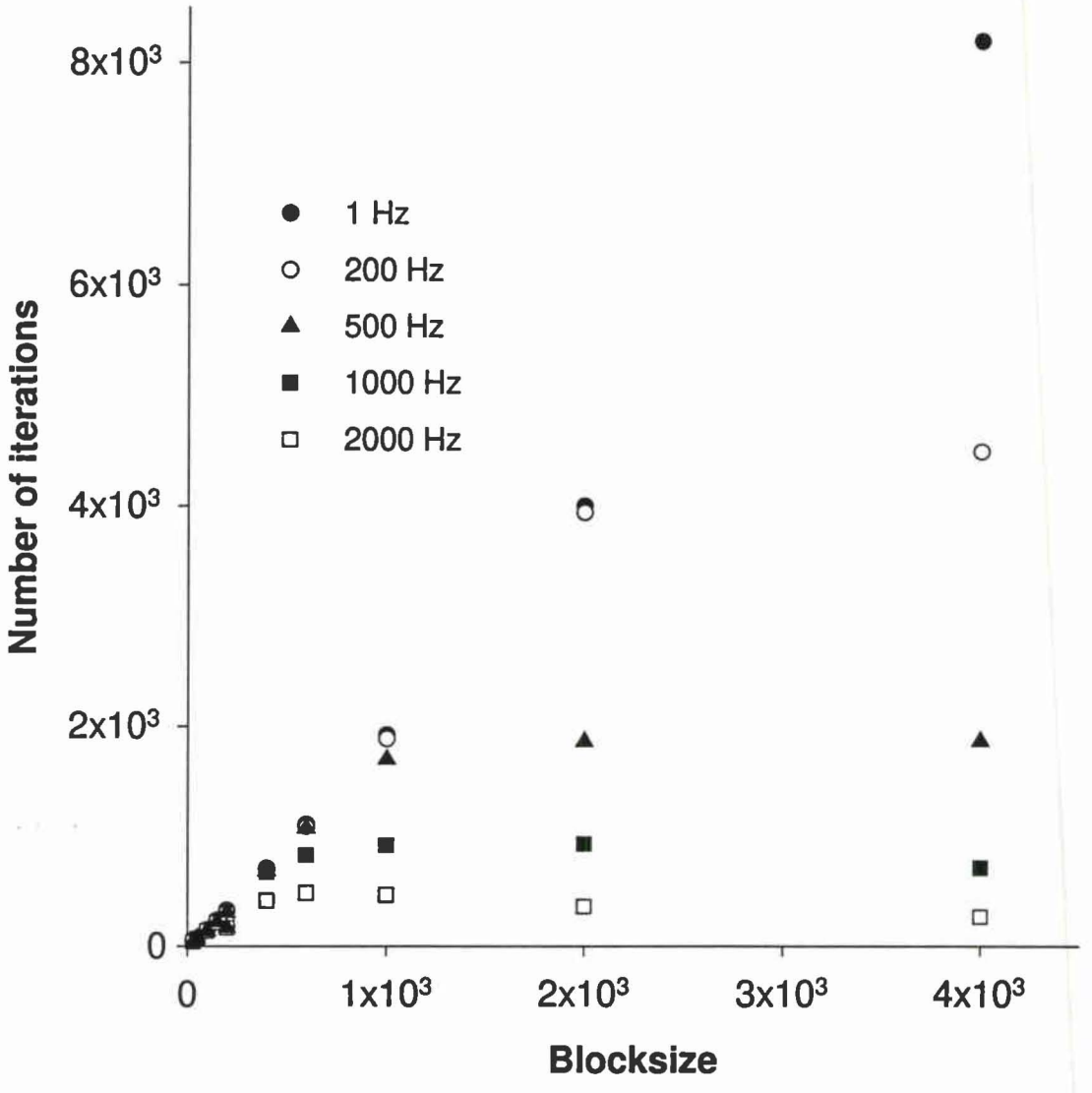

Figure 8.8 The number of Lanczos iterations as a function of blocksize for increasing linewidths. Linewidths ranged between 1 to 2000 Hz. This study scaled the rotor speed inversely with the Floquet dimension, to maintain a constant spectral range.

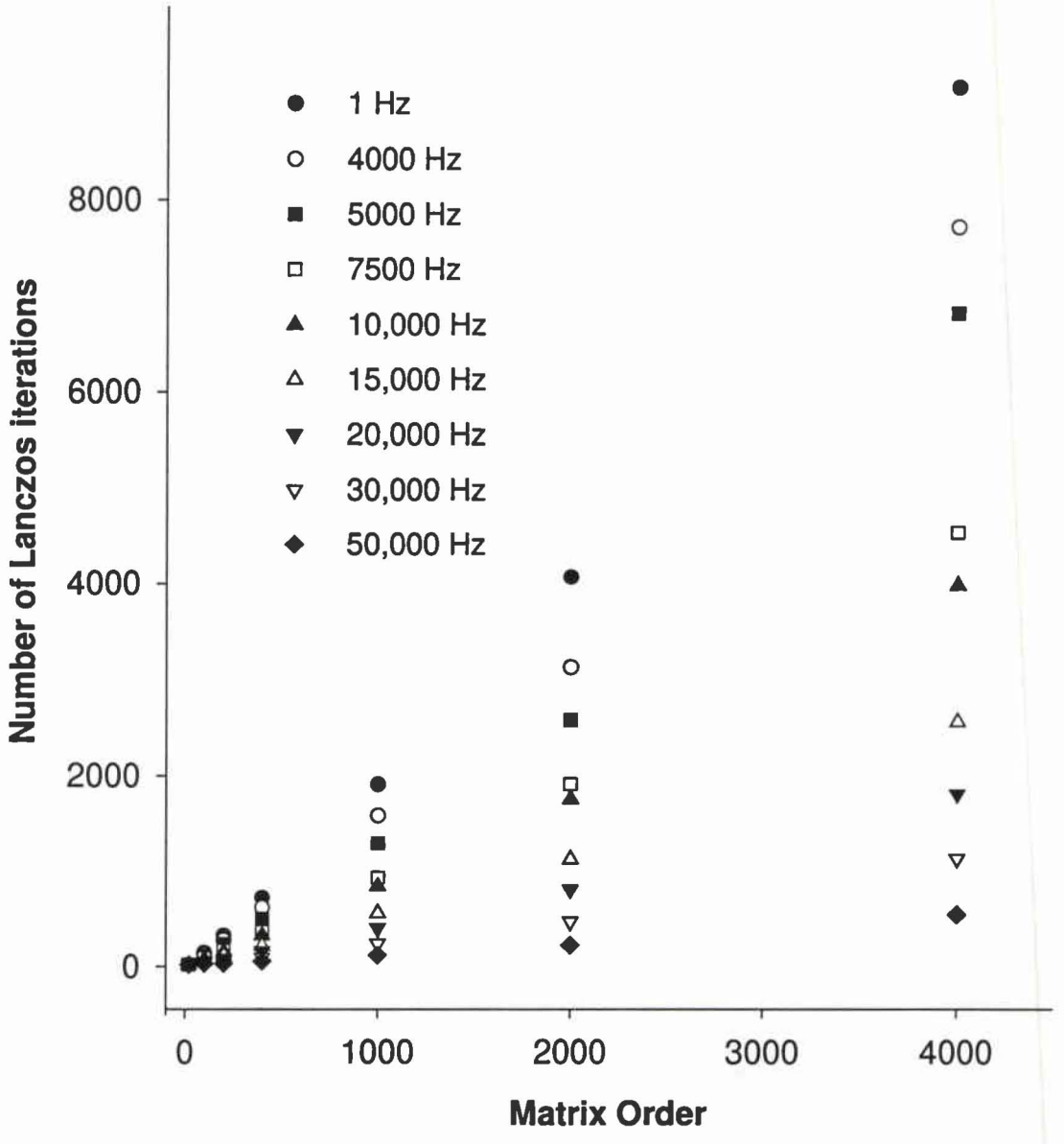

Figure 8.9 The number of Lanczos iterations as a function of blocksize for increasing linewidths. Linewidths ranged between 1 Hz to 50 KHz. This study scaled the tensor components with the Floquet dimension, while maintaining a constant rotor speed, to avoid saturation.

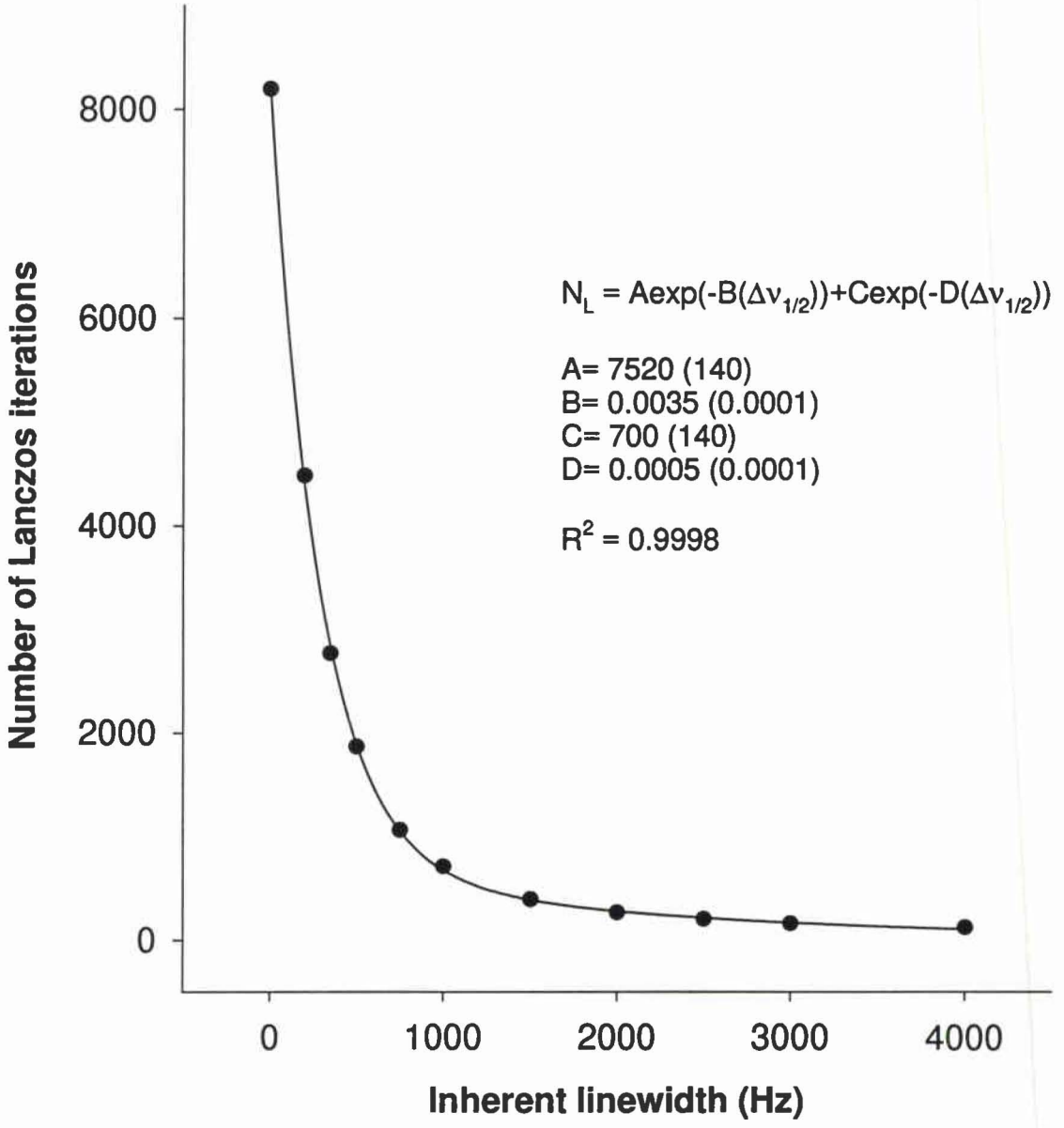

Figure 8.10 The maximum number of Lanczos iterations required to converge a matrix of order 4000, as a function of linewidth. The best-fit curve is based on a biexponential function.

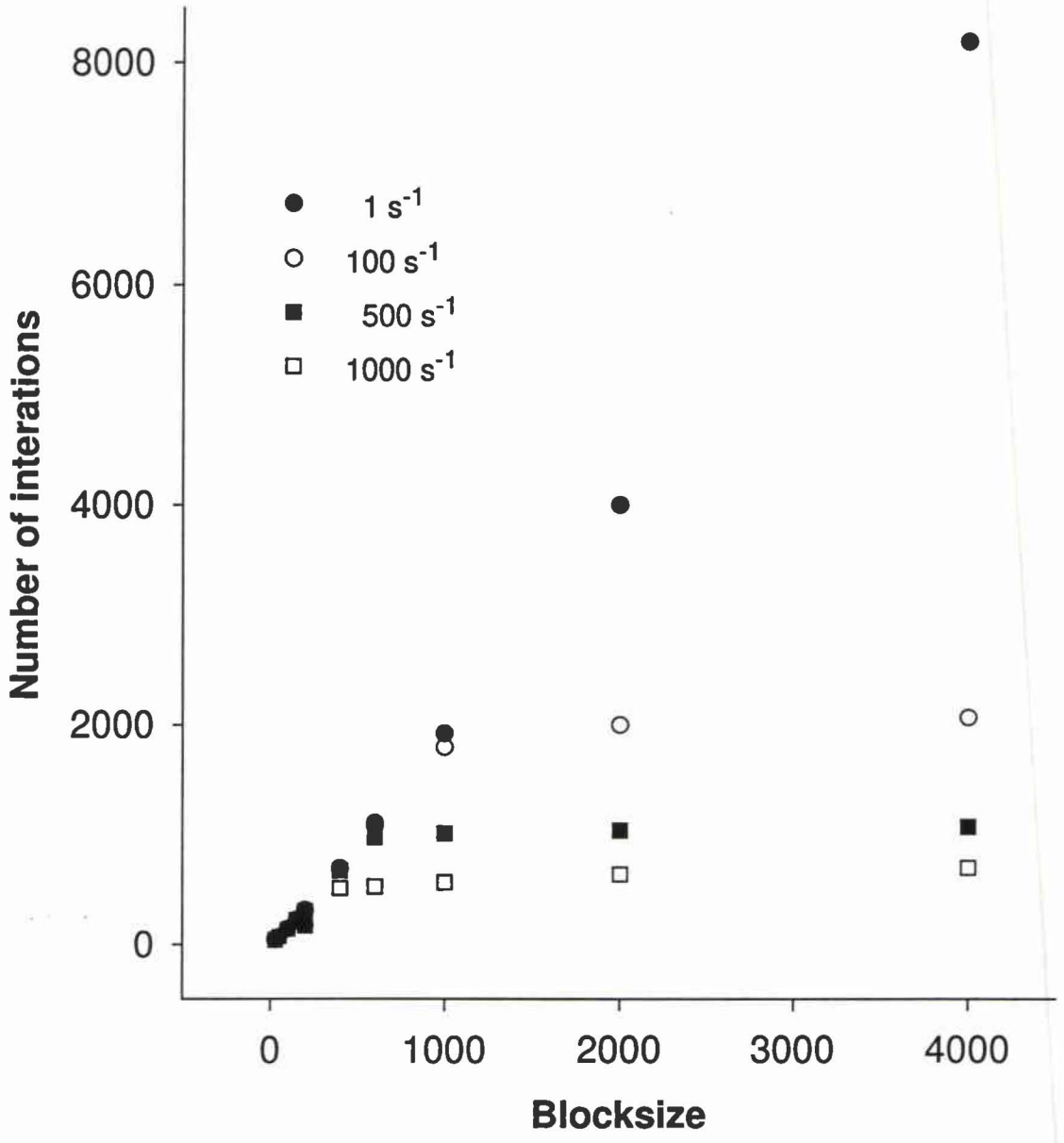

Figure 8.11 The number of Lanczos iterations as a function of blocksize for increasing exchange rates. Exchange rates ranged between 1 to 1000 s^{-1}. This study scaled the rotor speed inversely with the Floquet dimension, to maintain a constant spectral range.

Conclusions

A general method for simulating the effect of chemical exchange on MAS NMR spectra of rotating solids was developed. MAS imparts a periodic time dependence to the spin Hamiltonian. The resulting periodically-time-dependent Liouvillian was converted to a time-independent form via Floquet methods. This much larger Floquet Liouvillian is not tractable by conventional numerical methods on a realistic time scale for large spin systems. Conventional methods scale with the cube of the order of the matrix. The Lanczos algorithm, known to have superior performance over conventional methods (see chapter 7), was employed in the computation of the MAS spectrum, using a direct frequency computation strategy. Spectra of doubly-^{13}C-labelled DMS were successfully simulated, as a two-spin two-site problem, for a series of temperatures starting from the slow- to well within the medium-exchange regime. In this case, simulations using conventional numerical methods were faster than the Lanczos algorithm. A detailed scaling study showed that this advantage is short lived, where the Lanczos algorithm overtakes conventional methods at matrix orders of 50 to100 and larger, which are larger than those used in this particular case. The scaling and convergence behaviour of these calculations was similar to that reported in chapter 7. Therefore, this combined Floquet-Lanczos method will significantly reduce the time required for simulating MAS spectra of larger spin systems.

References

1) Harris, K.D.M.; Aliev, A.E. *Chem.Br.* **1995**, *31*, 132-136.

2) Griffin, R.G.; Ellet, J.D.Jr.; Mehring, M.; Bullitt, J.G.; Waugh, J.S. *J.Chem.Phys.* **1972**, *57*, 2147-2155.

3) Rothwell, W.P.; Waugh, J.S. *J.Chem.Phys.* **1981**, *74*, 2721-2732.

4) Tarbell, D.S.; Weaver, C. *J.Am.Chem.Soc.* **1941**, *63*, 2939-2942.

5) Suwelack, D.; Rothwell, W.P.; Waugh, J.S. *J.Chem.Phys.* **1980**, *73*, 2559-2569.

6) Lausch, M.; Spiess, H.W. *J.Magn.Reson.* **1983**, *54*, 466-479.

7) Lausch, M.; Spiess, H.W. *Chem.Phys.Lett.* **1980**, *71*, 182-186.

8) Yang, Y.; Schuster, M.; Blumich, B.; Spiess, H.W. *Chem.Phys.Lett.* **1987**, *139*, 239-243.

9) Gerardy-Montouillout, V.; Malveau, C.; Tekely, P.; Olender, Z.; Luz, Z. *J.Magn.Reson.* **1996** , *123 A*, 7-15.

10) Frydman, L.; Frydman, B. *Magn.Reson.Chem.* **1990**, *28*, 355-363.

11) Mehring, M.*Principles of High Resolution NMR in Solids*; Springer-Verlag: Berlin, 1983;

12) Munowitz, M.*Coherence and NMR*; John Wiley & Sons: New York, 1988;

13) Harris, R.K.*Nuclear Magnetic Resonance Spectroscopy*; Pitman Books Limited: London, 1983;

14) Pake, G.E. *J.Chem.Phys.* **1948**, *16*, 327-336.

15) Pound, R.V. *Phys.Rev.* **1950**, *79*, 685-702.

16) Spiess, H.W. *J.Chem.Phys.* **1980**, *72*, 6755-6762.

17) Lowe, I.J. *Phys.Rev.Lett.* **1959**, *2*, 285-287.

18) Andrew, E.R.; Newing, R.A. *Proc.Phys.Soc.A* **1958**, *72*, 959-972.

19) Andrew, E.R.; Bradbury, A.; Eades, R.G. *Nature (London)* **1958**, *182* , 1659-1659.

20) Herzfeld, J.; Berger, A.E. *J.Chem.Phys.* **1980**, *73*, 6021-6030.

21) Maricq, M.M.; Waugh, J.S. *J.Chem.Phys.* **1978**, *70*, 3300-3316.

22) Eden, M.; Lee, Y.K.; Levitt, M.H. *J.Magn.Reson.A* **1996**, *120*, 56-71.

23) Shirley, J.H. *Phys.Rev.* **1965**, *138*, B 979-B 987

24) Ding, S.; McDowell, C.A. *Chem.Phys.Lett.* **1998**, *288*, 230-234.

25) Schmidt, A.; Vega, S. *J.Chem.Phys.* **1987**, *87*, 6895-6907.

26) Schmidt, A.; Griffin, R.G.; Raleigh, D.P.; Roberts, J.E.; Smith, S.O.; Vega, S. *J.Chem.Phys.* **1986**, *85*, 4248-4253.

27) Kuwahara, D. *Chem.Phys.Lett.* **1994**, *231*, 414-420.

28) Long, J.R.; Sun, B.Q.; Bowen, A.; Griffin, R.G. *J.Am.Chem.Soc.* **1994**, *116*, 11950-11956.

29) Heaton, N.J. *Chem.Phys.Lett.* **1996**, *252*, 77-84.

30) Heaton, N.J. *Mol.Phys.* **1997**, *92*, 251-263.

31) Wilkinson, J.H.*The Algebraic Eigenvalue Problem*; Clarendon Press: Oxford, 1965;

32) Nakai, T.; McDowell, C.A. *Mol.Phys.* **1996**, *88*, 1263-1275.

33) Nakai, T.; McDowell, C.A. *J.Chem.Phys.* **1991**, *96*, 3452-3466.

34) Dumont, R.S.; Hazendonk, P.; Bain, A.D. *J.Chem.Phys.* **1999**,

35) Dumont, R.S.; Bain, A.D.; Jain, S. *J.Chem.Phys.* **1997**, *106*, 5928-5936.

36) Wassam Jr, W.A. *J.Chem.Phys.* **1985**, *82*, 3371-3385.

37) Smith, B.T.; Boyle, J.M.; Dongarra, J.J.; Garbow, B.S.; Ikebe, Y.Y.; Klema, V.C.; Moler, C.B.*Matrix Eigensystem Routines - EISPACK Guide*; Springer-Verlag: New York, 1976;

38) Moro, G.; Freed, J.H. *J.Chem.Phys.* **1981**, *74*, 3757-3773.

39) Moro, G.; Freed, J.H. *J.Phys.Chem.* **1980**, *84*, 2837-2840.

40) Vasavada, K.V.; Schneider, D.J.; Freed, J.H. *J.Chem.Phys.* **1987**, *86*, 647-661.

41) Golub, G.H.; van Loan, C.F.*Matrix Computations*; Johns Hopkins University Press: Baltimore, 1996;

42) Freund, R.W.; Nachtigal, N.M. *ACM Transactions on Mathematical Software* **1996**, *22*, 46-77.

43) Freund, R.W.; Gutknecht, H.H.; Nachtigal, N.M. *SIAM J.Sci.Comput.* **1993**, *14*, 137

44) Freund, R.W.; Nachtigal, N.M. *SIAM J.Sci.Comput.* **1994**, *15*, 313-337.

45) Saad, Y.; and Schultz, M. *SIAM J.Sci.Comput.* **1986**, *7*, 856

46) Gordon, R.G.; McGinnis, R.P. *J.Chem.Phys.* **1968**, *49*, 2455-2456.

47) Pople, J.A.; Schneider, W.G.; Bernstein, H.J.*High-Resolution Nuclear Magnetic Resonance*; McGraw-Hill Book Company, Inc.: New York, 1959;

48) Gutowsky, H.S.; Holm, C.H. *J.Chem.Phys.* **1956**, *25*, 1228-1234.

49) Bain, A.D.; Duns, G.J. *Can.J.Chem.* **1996**, *74*, 819-824.

50) Binsch, G. *J.Am.Chem.Soc.* **1969**, *91*, 1304-1309.

51) Johnson, C.S. *Advances in Magnetic Resonance* **1965**, *1*, 33-102.

52) Cullum, J.K.; Willoughby, R.A.*Lanczos Algorithms for Large Symmetric Eigenvalue Computations*; Birkhaeuser: Boston, 1985;

53) Dongarra, J.J.; Moler, C.; Bunch, J.R.; Stewart, G.W.*LINPACK User's guide*; SIAM: Philadelphia, 1979;

54) Press, W.H.; Teukolsky, S.A.; Vetterling, W.T.; Flannery, B.P.*Numerical Recipes in FORTRAN: The Art of Scientific Computing*; Press Syndicate of the Cambridge University Press: Cambridge U.K., 1992;

55) Hazendonk, P.; Dumont, R.S.; Grondey, H.; Harrison, P.H.M.; Bain, A.D. *J.Magn.Reson.* **1999** ,

56) Zur, Y.; Vega, S. *J.Chem.Phys.* **1983**, *79*, 548-558.

57) Zur, Y.; Levitt, M.H.; Vega, S. *J.Chem.Phys.* **1983**, *78*, 5293-5310.

58) Krauss, E.M.; Vega, S. *Phys.Rev.A* **1986**, *34*, 333-350.

59) Zax, D.B.; Vega, S. *Phys.Rev.Lett.* **1988**, *62*, 1840-1843.

60) Goelman, G.; Vega, S.; Zax, D.B. *Phys.Rev.A* **1989**, *39*, 5725-5743.

61) Vega, S.; Olejniczak, E.T.; Griffin, R.G. *J.Chem.Phys.* **1984**, *80*, 4832-4840.

62) Maricq, M.M. *Phys.Rev.B* **1982**, *25*, 6622-6632.

63) Kubo, A.; McDowell, C.A. *J.Chem.Phys.* **1990**, *92*, 7156-7170.

64) Schmidt, A.; Vega, S. *J.Chem.Phys.* **1992**, *96*, 2655-2680.

65) Zax, D.B. *J.Chem.Phys.* **1996**, *105*, 6616-6625.

66) Weintraub, O.; Vega, S. *J.Magn.Reson.A* **1993**, *105*, 245-267.

67) Schmidt, A.; Vega, S. *Isr.J.Chem.* **1992**, *32*, 215-230.

68) Luz, Z.; Poupko, R.; Alexander, S. *J.Chem.Phys.* **1993**, *99*, 7544-7553.

69) Levante, T.O.; Baldus, M.; Meier, B.H.; Ernst, R.R. *Mol.Phys.* **1995**, *86*, 1195-1212.

70) Charpentier, T.; Fermon, C. *J.Chim.Phys.* **1998**, *109*, 3116-3130.

71) Reed, M.; Simon, B.*Methods of modern mathematical physics. 1 Functional Analysis*; Academic Press: Toronto, 1980; pp 221-248.

72) Alderman, D.W.; Solum, M.S.; Grant, D.M. *J.Chem.Phys.* **1986**, *84*, 3717-3725.

73) Wang, D.; Hanson, G.R. *J.Magn.Reson.* **1995**, *117 A*, 1-8.

74) Malewski, G.; Mitzinger, L. *Monatsber.Dtsch.Akad.Wiss.Berlin* **1968**, *10*, 74-75.

75) De Jong, A.F.; Kentgens, A.P.M.; Veeman, W.S. *Chem.Phys.Lett.* **1984**, *109*, 337-342.

Chapter 9

Conclusions and Future Work

The main focus of this work has been accurate rate measurement of chemical exchange processes by dynamic NMR in both solution and solid phases. When rate measurements are carried out over large temperature ranges accurate activation parameters are obtained via the Eyring relationship. In solution phase, for small molecules, enthalpies and entropies of activation are readily obtained to within 1 kJ/mol and 6 J/molK, respectively. These statistically significant activation entropies have given important insight into solvent-solute interactions. Experimental barriers, expressed as enthalpies, can be reliably compared with computations. Subtle effects, such as those of substituents, on a barrier can now be compared with theory, independent from their entropic contributions. With spectral assignments and exchange mechanisms from 2D NMR methods it was possible to perform rate measurements by complete lineshape methods on large spin systems and systems exchanging between many conformations. Finally, in an effort to towards extending these methods to the solid state, lineshape simulation of MAS spectra of exchanging multispin systems has been achieved using a combined Floquet-Lanczos approach.

The study into the solvent effect on the barrier in furfural has shown that entropy changes for unimolecular processes are significant and cannot be ignored. In addition, reaction-field methods do not satisfactorily account for this effect; consequently a statistical mechanical approach is necessary. Nevertheless, this study illustrated that the measured activation entropy can be interpreted with confidence and can provide valuable information about the system.

Future dynamic NMR investigations should exploit activation entropies to gain insight into transition state structures and mechanistic information about these processes. This would be particularly useful for large systems such as proteins or natural products, where complex rearrangements of the solvent as the result of conformational changes of the molecule are key in their biological activity. A systematic investigation into activation entropies of dynamic process of small peptides in different solvent systems could be a useful vehicle in the further understanding of the behaviour of bound solvent.

Sparse matrix methods should be extended to simulating spin dynamics in the solid state. The Lanczos method was particularly useful when computing spectra directly in the frequency domain, however, is not easily adapted to time propagation. Chebychev-like propagation methods are probably better suited. In combination with Floquet methods Chebychev-like time propagation techniques could be used to simulate spin dynamics during rotor-synchronised pulse sequences, such as REDOR-based experiments. Dephasing curves could be computed in this manner, especially when dynamic processes and homonuclear coupling need to be considered.

The next stage in simulating MAS spectra should include the quadrupolar coupling term without the use of perturbation methods. Using the current methodology, one must compute the spectrum in a combined Zeeman-Quadrupolar frame, which under MAS conditions is time-dependent. At this stage, in the interest of computational efficiency, it is not clear whether it is worthwhile to continue with Floquet methods, and thus the COMPUTE approach should be explored. With either method it should be possible to simulate spectra of spin-1/2 nuclei coupled to quadrupolar nuclei. More generally simulation of several spin-1/2 nuclei coupled to a quadrupolar nucleus should be pursued, where homonuclear coupling terms, relaxation and chemical exchange are included.

In summary, future work should concentrate on a systematic investigation of the activation entropies on dynamic processes in solution and the development of new sparse matrix methods for time propagation for the simulation of spin dynamics in the solid state.